The Nature of High H I Mass-to-Light Ratio Field Galaxies

Bradley Evan Warren

A thesis submitted for the degree of

Doctor of Philosophy

of The Australian National University

Research School of Astronomy & Astrophysics

February 2005

To my parents, Bruce and Julie.
Without you I could never have come so far.

Disclaimer

I hereby declare that the work in this thesis is that of the candidate alone, except where indicated below or in the text of the thesis. The supervisors of this project, Helmut Jerjen and Bärbel S. Koribalski, have contributed text to the papers resulting from this project.

Chapters 1, 6, 7, and 8 contains text from three papers resulting from this project (Warren et al., 2004, 2005a,b) to which the co-authors, Helmut Jerjen and Bärbel S. Koribalski, have contributed.

Chapter 2 contains three figures (Fig. 2.3, 2.4, and 2.5) which were included in Koribalski et al. (2004).

Bradley E. Warren
February 2005

Acknowledgments

Firstly, I gratefully acknowledge the contribution that my two supervisors have made to this project. My main supervisor Helmut Jerjen has provided constant support for four years, without which I would be completely lost, and made it a pleasure to do this research. My co-supervisor Bärbel Koribalski has always kept me on my toes and has greatly enriched this project, making it possible for me to do the often difficult combination of optical and radio observations.

I am grateful for the assistance of Ken Freeman and Lister Staveley-Smith as advisors to this project, especially for their assistance with observations and their detailed comments on the ESO 215-G?009 paper. I would like to thank Agris Kalnajs for his assistance with the star formation threshold analysis, Frank Briggs for his suggestions for H I flux density calculation, the anonymous referee of the ESO 215-G?009 paper for their useful comments, Erwin de Blok for his help with rotation curve fitting, and everyone who made me welcome during my European trip (especially Erwin de Blok, Walter Huchtmeier, Eline Tolstoy, Mike Irwin and Neil Trentham). I would also like to thank Marilena Salvo and Gayandhi de Silva for their observing assistance.

I would like to personally thank the following friends and family: All of my family back in Melbourne especially my parents, my sister Katrina, and my grandparents. Matt Coleman, Dave Weldrake, Brent Groves and Craig Harrison who have been constant friends from the beginning of this PhD thing. My housemates, Ria Vlavianos and Andrew Davis, for putting up with the "absent minded" astronomer for three and a half years. Sayuri Prior, fellow groupie and music lover, for sharing some beautiful tunes with me and making the last few months much less stressful. Graeme Blackman, Peter Walshe, and Frank Filardo, drivers of the Stromlo bus, without who I would not have been able to get to work for the past four years. Special thanks go to all the friends who have supported me over the years, including Laura and Josh, Jackie, Ewan, Paul, Jörg, Erwin, Leith, Anna and Eduard, José, Brandon and Rekke, Mary, Vicky, Antoine and Genevieve, Laura and Rob, Catherine, and Marilena. Finally I'd like to thank all Mount Stromlo and Siding Spring staff, especially the students, the MSO computing and administration staff, and the SSO lodge and technical staff.

The 2.3-meter Telescope is run by the Australian National University as part of Research School of Astronomy and Astrophysics. The Australia Telescope Compact Array and the Parkes Radio Telescope are part of the Australia Telescope that is funded by the Commonwealth of Australia for operation as a National Facility managed by CSIRO. This research has made use of the NASA/IPAC Extragalactic Database (NED), which is operated by the Jet Propulsion Laboratory, California Institute of Technology, under contract with the National Aeronautics and Space Administration. The Digitized Sky Survey (DSS) was produced at the Space Telescope Science Institute under U.S. Government grant NAG W-2166,

based on photographic data obtained using the UK Schmidt Telescope. Data reduction and analysis in this project was carried out with the IRAF, MIRIAD, GIPSY, AIPS and KARMA packages. All plots in this thesis were produced in SM. This research was done with the support of the Australia Telescope National Facility, CSIRO.

Abstract

This thesis presents a multiwavelength investigation (*BVRI* band photometry and H I line interferometry) of a sample of 41 galaxies, mostly late-type dwarfs, which have been selected on the basis of their H I mass-to-light ratio ($\mathcal{M}_{\rm HI}/L_{\rm B}$). 21 dwarf galaxies were initial selected from the HIPASS Bright Galaxy Catalog (BGC, Koribalski et al., 2004) as they appeared to have a high $\mathcal{M}_{\rm HI}/L_{\rm B}$ when the BGC H I data was compared to optical data from an online extragalactic database (LEDA), while the remaining 20 were low $\mathcal{M}_{\rm HI}/L_{\rm B}$ dwarfs selected as a control sample. We obtained optical and H I follow-up observations with the ANU 2.3-m Telescope and the Australia Telescope Compact Array, respectively.

This study has uncovered a galaxy with some of the most extreme H I properties yet seen, ESO 215-G?009. We find that it is an isolated dwarf irregular galaxy with an old stellar population. We place an upper limit on the current star formation rate of $\sim 2.5 \times 10^{-3}\ \mathcal{M}_{\odot}\,{\rm yr}^{-1}$. The extended H I disk shows regular rotation ($v_{rot} = 51 \pm 8$ km s^{-1}), and at a column density of $\sim 5.0 \times 10^{19}$ atoms cm^{-2} can be traced out to over six times the Holmberg radius of the stellar component (radius at $\mu_B = 26.6$ mag arcsec^{-2}). After foreground star subtraction, we measure a B band apparent magnitude of 16.13 ± 0.07 mag within a radius of 80″. The H I flux density is 122 ± 4 Jy km s^{-1} within a radius of 370″. Given a Galactic extinction of $A_{\rm B} = 0.95 \pm 0.15$ mag, we derive an H I mass-to-light ratio of $22 \pm 4\ \mathcal{M}_{\odot}/L_{\odot,{\rm B}}$ for ESO 215-G?009. To our knowledge this is the highest $\mathcal{M}_{\rm HI}/L_{\rm B}$ ratio for a galaxy to be confirmed by accurate measurement to date.

For the majority of the remaining sample galaxies we found that many of the original predictions of $\mathcal{M}_{\rm HI}/L_{\rm B}$ were overestimates, and that truly high H I mass-to-light ratio objects are rare. Although we only examined a small sample, this and the scarcity of other very high $\mathcal{M}_{\rm HI}/L_{\rm B}$ galaxies in the literature suggests that there are not sufficient numbers of these galaxies to steepen the faint end of mass functions from observations and reconcile them with theoretical dark matter halo mass functions. However, the existence of high $\mathcal{M}_{\rm HI}/L_{\rm B}$ galaxies does have important implications for galaxy models, which can be constrained by extreme objects such as ESO 215-G?009 that appear to be at or close to the limit of their allowed H I mass fraction at a given luminosity. We have discovered a previously uncatalogued companion to the galaxy ESO 121-G020 through H I observations on the ATCA, which contributes to the H I flux density measurement in the HIPASS observations.

We also find that in general high H I mass-to-light ratio galaxies are underluminous rather than having an excess of H I gas, with their baryonic masses being similar to galaxies with the same rotation. There is a general trend for higher $\mathcal{M}_{\rm HI}/L_{\rm B}$ galaxies to have both lower surface brightness (indicating the galaxy has a shallow dark matter potential) and to be more isolated (undergoing less tidal influence from neighbouring galaxies). This implies that high $\mathcal{M}_{\rm HI}/L_{\rm B}$ galaxies

can only form in low density environments and only if they have a shallow dark matter potential.

CONTENTS

LIST OF FIGURES

LIST OF TABLES

"Stars light the sky, and a galaxy of emptiness tonight,
Though I'm happiest when there's no reason for me to be,
With no-ones expectation to weigh heavy on my heart,
And so much hope it sometimes tears me all apart,
Could you please knock me off my feet for a while."

"Galaxy of Emptiness" by Beth Orton

1. INTRODUCTION

Many of the greatest, least understood and most enduring mysteries in observational astronomy today are in the field of galaxies. The formation, evolution, interaction, frequency, mass, content, morphology, structure, and dynamics of galaxies in our Universe are the subject of much ongoing debate many decades after the problems surrounding them were outlined. In particular, the formation and evolution of galaxies into the wide variety of systems that are observed, as well as the number and nature of galaxies which exist is the source of much disagreement, especially between observers and theorist.

Observationally there are many ways to explore these problems. Traditionally to study the origins of galaxies observers have looked towards the farthest galaxies to examine those galaxies which we see still in the process of formation, the regime of far-field cosmology. While this is an enormously important study for both extragalactic and cosmological astronomy, it faces some difficulties due to the very high redshifts of the objects being studied. Only the brightest objects are observable, so we cannot detect the high redshift counterparts for many of the near-field objects that we are familiar with. There is less ability to resolve features within those objects, so we have less physical information on these galaxies than closer ones. And while nearby galaxy have been observed most extensively at optical, infrared and radio wavelengths, the high redshifts of these distant objects means that we are looking at the ultra violet emissions in the optical. So we generally have less of a basis to compare very distant galaxies to nearby object.

The expanding field of near field cosmology takes a different approach by looking at the cosmological evidence which remains in the Local Universe. This includes examination of stars within our own Galaxy for objects that may have merged (the Sagittarius dwarf spheroidal [Ibata, Gilmore, & Irwin, 1994], the RAVE[1] and GAIA[2] surveys), studies of satellites of the Milky Way and other galaxies in the Local Group (Mateo, 1998), and exploration of galaxies in the Local Universe (Karachentsev et al., 2004) some of which are likely to have remained as they are for most of the life of the Universe (such as DDO 154 [Krumm & Burstein, 1984], see § 1.3 below). Dwarf galaxies (faint/low mass galaxies) are particularly good probes of the Local Universe, being more strongly affected by their environment.

[1] http://www.rave-survey.aip.de/rave/
[2] http://www.rssd.esa.int/gaia/

One way to investigate aspects of star formation and galaxy evolution is to study galaxies which appear to have done little of either, those with large quantities of unprocessed neutral hydrogen gas, H I, compared to their stellar content. The high quantities of H I gas in some low luminosity (dwarf) galaxies suggest that star formation within these galaxies has been impaired or halted, has lacked stimulation, or has only recently begun.

This PhD will explore a sample of dwarf galaxies which potentially have a higher H I mass than galaxies of similar luminosity, i.e. they have higher H I mass-to-light ratios ($\mathcal{M}_{\rm HI}/L_{\rm B}$, which compares the H I mass to the B band luminosity in solar units) than is typical. Through a multiwavelength comparison with more normal dwarf galaxies we hope to understand the nature of these objects and find evidence for the physical reasons, whether by environmental or internal processes, why some dwarf galaxies could have maintained an unusual high fraction of H I gas, while others have processed most of their neutral gas into stars.

1.1 A Cosmological Disagreement

The number of low mass dark matter potentials (often referred to as dark matter halos) predicted by models of a CDM dominated Universe far exceeds the quantity of observed low mass galaxies, sometimes by several orders of magnitude (see Kauffmann, White, & Guiderdoni, 1993; Moore et al., 1999; Klypin et al., 1999). Thereby we define a "galaxy" as a dark matter potential that contains baryons. Consequently the low mass end of dark matter halo mass functions generally rises much more steeply than observed galaxy mass functions (Hilker, Mieske, & Infante, 2003; Blanton et al., 2003; but see also Blanton et al., 2004).

While there are some physical processes that could narrow this discrepancy (Klypin et al., 1999; Shapiro, Iliev, & Raga, 2004), they are not enough to reconcile observations and theory. So we are left with the conclusions that the cosmological models have overpredicted the number of low mass dark matter halos present, and/or the observations have failed to find the vast majority of low mass galaxies in the Universe. If the latter were true, then it is important to look at why such galaxies could be missed and how we could detect them (Trentham, Möller, & Ramirez-Ruiz, 2001).

Two reasons why these objects might not have been found yet in optical observations are that they could be very difficult (or even impossible) to see due to low stellar density and content or they do not contain any baryonic matter and are in fact "empty" dark matter halos. Both these possibilities could be dark matter halos in which the star formation from accreted gas has been halted, suppressed, never began, or there were simply no baryons to form stars to begin with. The former objects might be considered as being "dark galaxies," which could be missed in observations biased towards optical wavelengths (Disney, 1976).

The existence of such low mass dark galaxies in large numbers could steepen

the mass functions from observations, which are mostly derived from optical or near-infrared galaxy luminosity functions without consideration of other baryonic matter. Recent large scale observations of neutral hydrogen gas are increasingly allowing mass functions to be derived based on non-stellar properties. Zwaan et al. (2003) produced one of the most extensive H I mass function for a catalogue of the 1000 H I-brightest galaxies in the southern hemisphere (see § 1.5) and found a similar low mass end slope to other observational studies. However the baryonic mass function is still being explored (Salucci & Persic, 1999).

Some methods have been proposed for finding empty dark matter halos, such as the suggestion to use the Milky Way halo microlensing statistics to look for dark matter satellite influence (Widrow & Dubinski, 1998), or to analyse the gravitational lensing of quasars to determine the dark matter sub-halos of the lensing object (Moore et al., 1999; Dalal & Kochanek, 2002). But obviously it is extremely difficult to prove the existence or absence of dark matter halos that do not contain an appreciable amount of baryonic matter in the form of stars and/or H I.

Likewise, to increase the numbers of known optically faint, low surface brightness galaxies that have not retained large amounts of H I, such as dwarf spheroidals, we need very deep, wide field optical observations. This has been shown by the search for such objects in the Local Group in recent decades, with over half the dwarf galaxies of the Local Group having been found since 1971 (Mateo, 1998) as deep wide field observations have become more common. However even with this increase in the number of known low mass Local Group galaxies found with optical studies, Moore et al. (1999) show that this is still well below the predictions of the ΛCDM models.

On the other hand, we may be able to find low mass galaxies that have retained a high proportion of H I gas and thus failed to convert most of their gas into stars. While not entirely "dark", such galaxies would be very faint and hard to detect optically, but may be found through 21cm line observations. Their H I mass-to-light ratio could be significantly higher than the typical ratios seen for late-type galaxies, so that their position in luminosity functions would be lower than on a baryonic mass function. If they existed in significant numbers then they would help correct the discrepancy in two ways, by including more galaxies and by shifting them to higher mass bins than they would be placed in with purely optical results. These are exactly the type of galaxies we wish to study in this project.

Kennicutt (1989) found that a modified Toomre (1964) Q criterion, a simple thin disk gravitational stability condition, could satisfactorily describe a threshold gas surface density above which large scale star formation can occur in active star-forming galaxies. It was proposed in Verde, Oh, & Jimenez (2002) that if angular momentum is conserved during gas contraction, low mass dark matter halos may form Toomre stable disks, and therefore remain faint galaxies with little star formation. If we could find galaxies like these, where the gas density after gravitational collapse is too low for efficient star formation, it may go some

way to explaining the discrepancy between the dark matter halo mass function and the observed galaxy luminosity function.

1.2 The H I Mass-to-Light Ratio

The H I mass-to-luminosity (or simply "light") ratio of a galaxy is a distance independent quantity which compares the H I mass to the luminosity in a particular photometric band. As the B band magnitude of galaxies has been in the past the most commonly available (from photographic studies), the H I mass-to-light ratio is usually expressed with the B band luminosity:

$$\frac{\mathcal{M}_{\rm HI}}{L_{\rm B}} = 1.5 \times 10^{-7} F_{\rm HI}\ 10^{0.4(m_{\rm B}-A_{\rm B})}\ \frac{\mathcal{M}_{\odot}}{L_{\odot,{\rm B}}}, \tag{1.1}$$

where $\mathcal{M}_{\rm HI}$ is the H I mass in $\mathcal{M}_{\odot}$, $L_{\rm B}$ is the B band luminosity in $L_{\odot,{\rm B}}$, $F_{\rm HI}$ is the integrated H I flux density in Jy km s^{-1}, $m_{\rm B}$ is the B band apparent magnitude, and $A_{\rm B}$ is the B band Galactic extinction. Extinction correction from the host galaxy is not taken into account in this calculation (see § 1.4).

For most galaxies $\mathcal{M}_{\rm HI}/L_{\rm B}$ is typically less than 1 $\mathcal{M}_{\odot}/L_{\odot,{\rm B}}$, with late-type galaxies having a larger spread than early-types. Roberts & Haynes (1994) performed a statistical study of physical parameters along the Hubble sequence. For late-type galaxies they found a general trend of lower luminosity, surface brightness and H I mass, and higher $\mathcal{M}_{\rm HI}/L_{\rm B}$ and H I-to-total mass ratio than for early-type spirals. E.g., for the RC3 local Supercluster sample they find a median $\mathcal{M}_{\rm HI}/L_{\rm B}$ of 0.78 $\mathcal{M}_{\odot}/L_{\odot,{\rm B}}$ in type Sm/Im galaxies, with an inner quartile range of 0.44 $\mathcal{M}_{\odot}/L_{\odot,{\rm B}}$ to 1.32 $\mathcal{M}_{\odot}/L_{\odot,{\rm B}}$, and a median $\mathcal{M}_{\rm HI}/\mathcal{M}_{\rm tot}$ of 0.15. However, some low surface brightness dwarf irregular galaxies are know to have H I mass-to-light ratios that are significantly higher than this quartile range.

1.3 Previous and Ongoing Studies of High H I Mass-to-Light Ratio Galaxies

One of the best known dwarf galaxies with a high $\mathcal{M}_{\rm HI}/L_{\rm B}$ is DDO 154 (Krumm & Burstein, 1984), for which Hoffman et al. (1993) measured $\mathcal{M}_{\rm HI}/L_{\rm B} = 11\ \mathcal{M}_{\odot}/L_{\odot,{\rm B}}$. DDO 154, a dwarf galaxy of type Sm, has a very extended H I disk compared to its optical size, stretching to ~6 times the Holmberg radius (Carignan & Purton, 1998). Another example is the Blue Compact Dwarf (BCD) galaxy NGC 2915, which has a moderately high $\mathcal{M}_{\rm HI}/L_{\rm B}$ of 2.7 $\mathcal{M}_{\odot}/L_{\odot,{\rm B}}$ (Meurer, Mackie, & Carignan, 1994; Meurer et al., 1996). The H I disk of this object extends to over five times the Holmberg radius and has distinct spiral arm structure (see Bureau et al., 1999). More recently, the galaxy NGC 3741 ($\mathcal{M}_{\rm HI}/L_{\rm B} \sim 5.8\ \mathcal{M}_{\odot}/L_{\odot,{\rm B}}$) was found to have possibly the most extended H I disk of any galaxy, ~8 times the Holmberg radius (Begum, Chengalur, & Karachentsev, 2005). We do not consider

$\mathcal{M}_{\rm HI}/L_{\rm B}$ ratios in tidal tails or bridges near galaxies, such as H I 1225+01, a tidally disturbed irregular galaxy described in detail by Chengalur, Giovanelli, & Haynes (1995). Likewise, massive gas-rich low surface brightness galaxies such as Malin 1 (Bothun et al., 1987; Impey & Bothun , 1989) are not comparable to low surface brightness dwarf systems with high $\mathcal{M}_{\rm HI}/L_{\rm B}$ ratios (as seen in the comparison of surface brightness and gas surface density by de Blok, McGaugh, & van der Hulst, 1996).

To date the largest study of galaxies with higher than average H I mass-to-light ratios is that of gas-rich low surface brightness dwarf galaxies by van Zee et al. (1997) and van Zee (2000, 2001, and references therein). This study included some galaxies with $\mathcal{M}_{\rm HI}/L_{\rm B}$ up to 7 $\mathcal{M}_{\odot}/L_{\odot,{\rm B}}$, as well as more "normal" higher surface brightness dwarf irregular galaxies (excluding BCDs). van Zee et al. (1997) found that the star formation process in the low surface brightness and normal galaxies was inefficient, with the overall gas density well below the Toomre (1964) instability threshold. They measured some localized H I peaks which approached the threshold and found that these were associated with local star forming regions. Many of the galaxies in the later studies (van Zee, 2000, 2001) are isolated, with no neighbours found within $\sim$ 200 – 400 kpc. van Zee (2001) concluded that unlike Blue Compact Dwarfs, star formation within these galaxies was occurring at a slow, constant rate across the galaxy disk with few major concentrations of activity, and that gas depletion timescales for these galaxies were of the order of 20 Gyr.

1.4 Dust Extinction

One of the most important (although often neglected or mistreated) issues in doing optical observations of galaxies is that of light extinction caused by dust. Any physical property derived from optical measurement, such as $\mathcal{M}_{\rm HI}/L_{\rm B}$ (see eqn. 1.1), needs to be corrected for extinction (especially in bluer bands where it is stronger). Extinction can occur in both the Milky Way (Galactic extinction) or within the host galaxy itself (internal extinction). Galactic extinction is especially strong in the Galactic Plane where it can significantly reduce the light we receive from a galaxy by several orders of magnitude, and sometimes obscure part or all of a galaxy. This can prove a severe problem for observers, such as those wishing to examine the large scale structure of the Local Universe when large areas of the sky are blocked from view in the optical (Kraan-Korteweg & Huchtmeier, 1992). The increasing number of surveys at other wavelengths are improving this situation (such as H I surveys, see § 1.5). But we still wish to know about the stellar properties of galaxies, so some form of compensation is required.

To a degree Galactic extinction is correctable as the dust obscuration of the Milky Way has been traced by several all sky surveys, most notably those of Burstein & Heiles (1978, 1982) and the more recent Schlegel, Finkbeiner, & Davis

(1998, hereafter SFD98) maps. However, there is still a certain degree of uncertainty in this correction, as Willick (1999b) summarise:

> *"Two all-sky Galactic extinction maps are presently available: the older Burstein-Heiles..."* (Burstein & Heiles, 1978, 1982) *"...maps, which are based on 21-cm column density and faint galaxy counts, and the recently completed Schlegel, Finkbeiner, and Davis..."* (SFD98) *"...maps, based on IRAS/DIRBE measurements of diffuse IR emission. The SFD extinctions have been favored in several recent analyses and, indeed, were used in Paper I..."* (Willick, 1999a). *"Unlike BH, the SFD extinctions are based directly on dust emission and have comparatively high spatial resolution. However, it has not been established beyond doubt that they are free of systematic errors, such as could arise from the presence of cold dust invisible to* IRAS. *The BH extinctions are also vulnerable to possible systematic effects, such as a variable dust-to-gas ratio and galaxy count fluctuations. Thus, it seems prudent to use both methods, or linear combinations of them, and see what effect this has on the results."*

The NASA/IPAC Extragalactic Database (NED[3]) also use the above quotation when listing Galactic extinction values for the galaxies in their database. We have chosen to use only the SFD98 values for Galactic extinction to remain consistent with recent publications that favour these newer maps.

The SFD98 maps provide the value of $E(B-V)$ (the difference between the extinction corrections in the B and V bands), which has often been mistaken for the correction need for apparent magnitude values, $A_{\rm G}$ (where the "G" is the photometric band the galaxy is observed in). We believe this is what van Zee et al. (1995) did when calculating their $\mathcal{M}_{\rm HI}/L_{\rm B}$ values, which should have been corrected with $A_{\rm B}$ (see Chapter 6, § 6.5.2). The conversion from $E(B-V)$ to the B band Galactic extinction correction, $A_{\rm B}$, which we use is the one used by NED:

$$A_{\rm B} = 4.32\,E(B-V) \ \ \text{mag}, \tag{1.2}$$

where the factor out the front is different for each photometric band (3.32 in V, 2.68 in R, and 1.94 in I).

While Galactic extinction can be corrected for, internal extinction is much more difficult to quantify. Extinction within galaxies, especially dwarf irregular galaxies, can be very uncertain and there is as yet no reliable method for obtaining such a measurement (Cabanela, 1999; Sidhu & Cabanela, 2003). It is known that the majority of dust within disk galaxies lies in the plane of the disk, so galaxies observed from edge on are more likely to suffer from higher internal extinction. As any correction for internal extinction would be highly speculative we have chosen

[3] http://nedwww.ipac.caltech.edu/

not to apply a correction and make note of the cases where we suspect internal extinction could be high. The issue of dust extinction will be visited several times in this thesis (see in particular Chapters 6, 7, and 8).

1.5 Galaxy Selection Based on H I Properties

While a few galaxies with relatively high $\mathcal{M}_{\rm HI}/L_{\rm B}$ have been found, many more may have gone unnoticed. This is due in part to a bias towards radio follow up of optically selected galaxies. This means that galaxies which are difficult to find optically or have not been considered interesting enough for further study have been ignored. They have also been missed due to the limitations of past blind H I surveys, which have only covered small sky areas or have been very shallow (see for example Zwaan et al., 2003, for other H I mass function studies). Such blind surveys have also generally been focused on known higher density regions such as clusters and nearby groups, and have ignored the field. As high $\mathcal{M}_{\rm HI}/L_{\rm B}$ galaxies are more prominent in H I than the optical, large scale blind H I surveys are needed to find greater numbers of these objects.

The H I Parkes All-Sky Survey (HIPASS) has provided the first ever blind survey of extragalactic neutral hydrogen in the local Universe ($v_{\rm sys}< 12\,700$ km s^{-1}) over the entire southern sky (Barnes et al., 2001). One of its first products is the HIPASS *Bright Galaxy Catalog* (hereafter BGC, Koribalski, 2001; Koribalski et al., 2004), which lists the 1000 H I brightest sources in the southern hemisphere (selected by H I peak flux density). This catalogue gives us the opportunity to select interesting galaxies for detailed examination based on H I and optical properties rather than entirely on optical characteristics, and was the basis for the Zwaan et al. (2003) H I mass function. To study the statistical properties and various correlations of these galaxies we obtained photometric and structural parameters for the BGC's *optical* counterparts from the Lyon-Meudon Extragalactic Database (LEDA, Paturel et al., 1997, and references therein) in 2001/2. First estimates of H I mass-to-light ratios were obtained for BGC galaxies using the BGC H I flux density, the LEDA B band apparent magnitude based on photographic plates, and the SFD98 B band Galactic extinction.

Fig. 1.1 shows the $\log(\mathcal{M}_{\rm HI}/L_{\rm B})$ distribution for the 789 BGC galaxies which had mean photometric B band apparent magnitudes in LEDA as a function of their absolute B magnitude ($M_{\rm B}$). It shows a general trend for low luminosity galaxies in the BGC to have high $\mathcal{M}_{\rm HI}/L_{\rm B}$. The low luminosity and low $\mathcal{M}_{\rm HI}/L_{\rm B}$ region of Fig. 1.1 is underpopulated as optically faint galaxies with little gas (dwarf elliptical galaxies) are not detected by HIPASS (or are below the BGC brightness cutoff). Similarly more massive galaxies with little or no gas (like giant ellipticals) are not present, although we do go to a lower $\mathcal{M}_{\rm HI}/L_{\rm B}$ at the bright end of the plot. We note that overall dwarf galaxies (those with the lowest luminosity) have a large spread in H I mass-to-light ratios. Of the 148 galaxies in the BGC

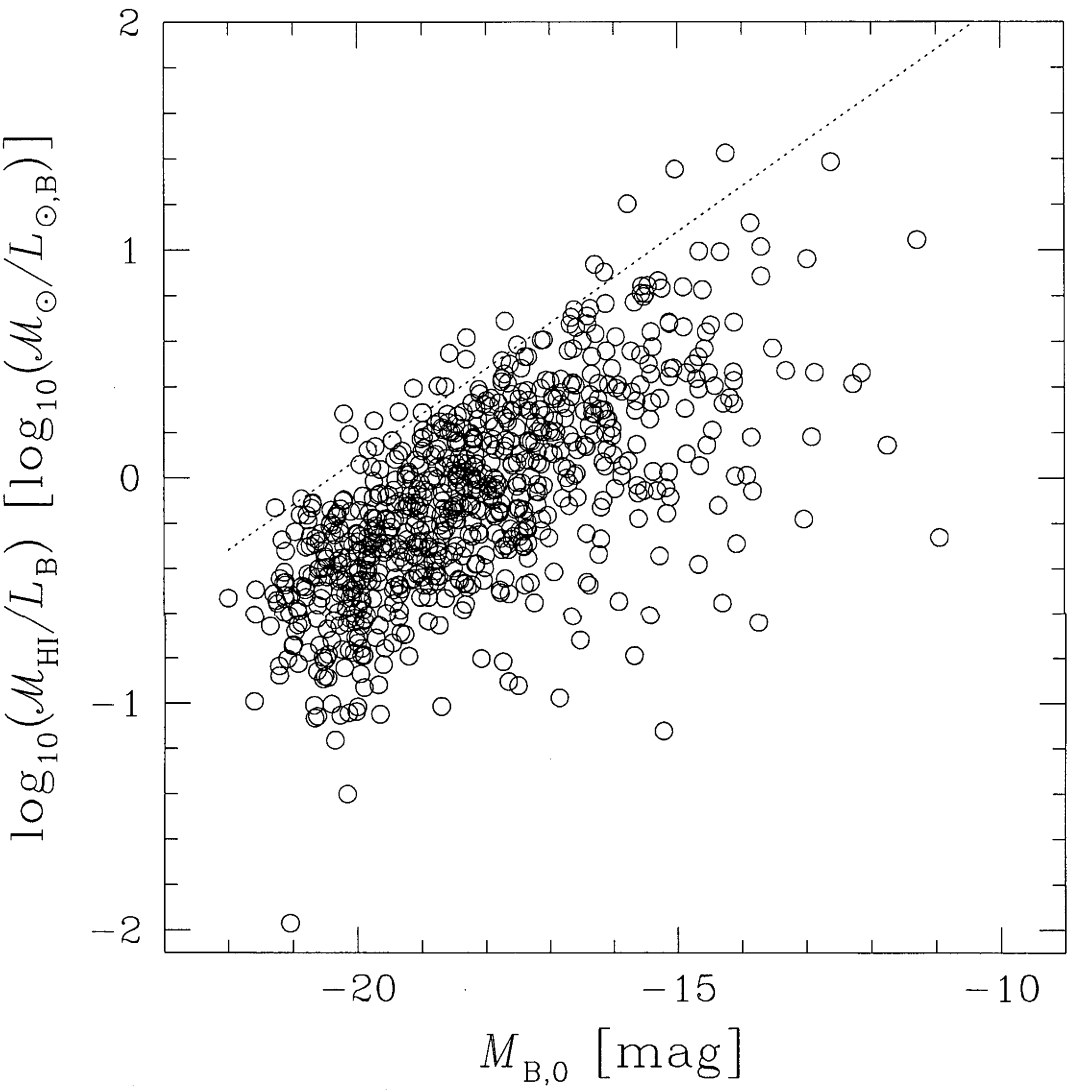

Fig. 1.1: H I mass-to-light ratio versus absolute photographic B magnitude for 789 galaxies in the HIPASS Bright Galaxy Catalog (Koribalski et al., 2004) which have blue apparent magnitudes in LEDA. See text for an explanation of the dotted line.

less luminous than $M_B = -16.5$ mag (hereafter referred to as dwarfs), 50 have $\mathcal{M}_{HI}/L_B \geq 3\ \mathcal{M}_\odot/L_{\odot,B}$. Of these, seven galaxies have initial ratios greater than 10 $\mathcal{M}_\odot/L_{\odot,B}$, and three have ratios in excess of 20 $\mathcal{M}_\odot/L_{\odot,B}$.

The absence of high $\mathcal{M}_{HI}/L_B$ bright galaxies, which should be easily detected in both the optical and at 21cm, suggests that there is a physical limit to the H I mass-to-light ratio for a galaxy of a certain luminosity (which approximates stellar mass). The dotted line plotted in Fig. 1.1 is an upper envelope approximation for $\mathcal{M}_{HI}/L_B$ at a given absolute magnitude, and is given by:

$$\left(\frac{\mathcal{M}_{HI}}{L_B}\right)_{max} \approx 10^{0.2(M_{B,0}+20.4)}\ \frac{\mathcal{M}_\odot}{L_{\odot,B}}, \tag{1.3}$$

At a given absolute magnitude M_B we would not expect the H I mass to light ratio to exceed this value.

To understand the nature of these galaxies, their abundance of neutral hydrogen gas and low stellar content, we have started a multi-wavelength study of the galaxies with the highest estimated H I mass-to-light ratios in the southern sky, selected from the BGC. This PhD thesis describes this study, including the initial selection of the galaxies, basic results, the most important members of the sample, and our investigation of why these galaxies could maintain such high H I mass-to-light ratios, whether by internal processes or external influence, and whether the high ratio is due to an excess of gas or a deficiency of stars.

Chapter 2 looks at the project which spawned this study, an optical investigation of the HIPASS Bright Galaxy Catalog. Chapter 3 describes how a sample was selected from this study. Chapter 4 describes the multiwavelength observations undertaken for this project. Chapter 5 lists the basic radio and optical results for all of our sample galaxies. Chapter 6 investigates the galaxy which has proved to be the most interesting galaxies in the sample, ESO 215-G?009, and looks at why it has retained an extreme proportion of H I gas compared to its stars. Chapter 7 looks at a sub-sample of nine galaxies (including ESO 215-G?009) and investigates whether high $\mathcal{M}_{HI}/L_B$ galaxies can explain the discrepancy between the observed luminosity function and predicted dark matter halo mass functions. Chapter 8 looks at various parameter which correlate with $\mathcal{M}_{HI}/L_B$, and attempts to explain why high $\mathcal{M}_{HI}/L_B$ galaxies exist. And finally Chapter 9 wraps up our discussion on these galaxies, summarises our major conclusions and flags future work in this area.

2. THE OPTICAL PROPERTIES OF THE HIPASS BRIGHT GALAXY CATALOG

The origins of this thesis are in one of the results of a small project completed at the beginning of my PhD, and before going at the main project we will briefly look at this. The aim of that project was to produce a list of optical properties for the 1000 H I sources in the HIPASS Bright Galaxy Catalog. The following chapter discusses this H I catalogue, the process of obtaining the optical data, and some of the results from a comparison of this optical data to the BGC H I properties.

2.1 HIPASS and the BGC

The H I Parkes All-Sky Survey (HIPASS) has provided the first ever blind survey of extragalactic neutral hydrogen (H I) in the Local Universe over the entire southern sky (Staveley-Smith et al., 1996; Barnes et al., 2001). Beginning in 1997, it was completed in March 2000 and the initial public data release was in May 2000. The survey used the then new Multibeam instrument on the 64m Parkes Radio Telescope (in New South Wales, Australia, Fig. 2.1), which has an array of 13 L band receivers. This instrument and the receiver configuration is shown in Fig. 2.2. The survey observed the nearby Universe at 21cm ($v_{\rm sys} < 12\,700$ km s^{-1}) and scanned the sky in 8° strips of declination, revisiting each point on five separate occasions, for an effective integration time of 460 s beam^{-1}. It covered the entire southern sky ($\delta < 2°$), and was later extended to cover the portion of northern sky accessible from Parkes ($\delta < 25°$). The observations have a beam size of $\sim$15.′5, and a velocity resolution of 18 km s^{-1} after smoothing. Details of the Multibeam receiver system, survey strategy, and on-line data analysis can be found in Staveley-Smith et al. (1996) and Barnes et al. (2001). Extensive efforts have been underway since to scientifically mine the rich HIPASS data set. One of most important efforts is the finding and cataloguing of all extragalactic H I sources.

One of two major catalogues to come out of this survey is the HIPASS *Bright Galaxy Catalog* (BGC, Koribalski et al., 2004). The BGC lists the 1000 H I brightest extragalactic sources in the southern hemisphere (and with $v_{\rm sys} < 8\,000$ km s^{-1}), selected by H I peak flux density ($S_{\rm peak} \gtrsim 0.116$ Jy). This catalogue gives us the unique opportunity to select interesting galaxies for detailed examination based on H I and optical properties rather than entirely on optical characteristics. It includes many H I parameters obtained from the HIPASS data, including the inte-

Fig. 2.1: The Parkes Radio Telescope in central western New South Wales, Australia. This image was taken from the Parkes media web site, http://www.parkes.atnf.csiro.au/images/media_images/parkes_photos.html.

grated H I flux density ($F_{\rm HI}$), the systemic velocity ($v_{\rm sys}$), and the widths of the H I line (both w_{50} and w_{20}). For 158 of the galaxies the redshifts in the BGC are the first such measurements. The catalogue provides a clear view of much of the large scale structure in the Local Universe, including details hidden behind the Galactic Plane in optical bands. It contained 91 previously uncatalogued ("new") galaxies, which were explored further in Ryan-Weber et al. (2002). Neither that study or the BGC support the existence of H I galaxies without an optical counterpart, with most of the "new" galaxies being obscured in the optical by the Galactic Plane or bright stars. When calculating approximate distances, the BGC uses the Hubble flow with the velocity relative to the barycentre of the Local Group (except in the case of nine galaxies, see § 3.1). They adopt a Hubble constant of H_0 of 75 $\rm km\,s^{-1}\,Mpc^{-1}$, which we also adopt in this thesis for consistency.

Included where possible with each object in the BGC is the most likely optical counterpart galaxy to the H I source. The counterparts were identified using NED (the NASA/IPAC Extragalactic Database[1]). They searched the database within $6'$ of each source's BGC H I position for optical counterparts, consistent with the Parkes beam size. Where optical velocities were available in NED they were used to identify the most likely counterpart, especially if there were multiple candidates within the seach radius. Improvements were made to the identification of some of these objects in the course of the compilation of the optical properties (see § 2.2). This identification of the optical counterparts allowed us to easily collect further optical parameters of these galaxies for a comparison with the BGC H I results.

[1] http://nedwww.ipac.caltech.edu/

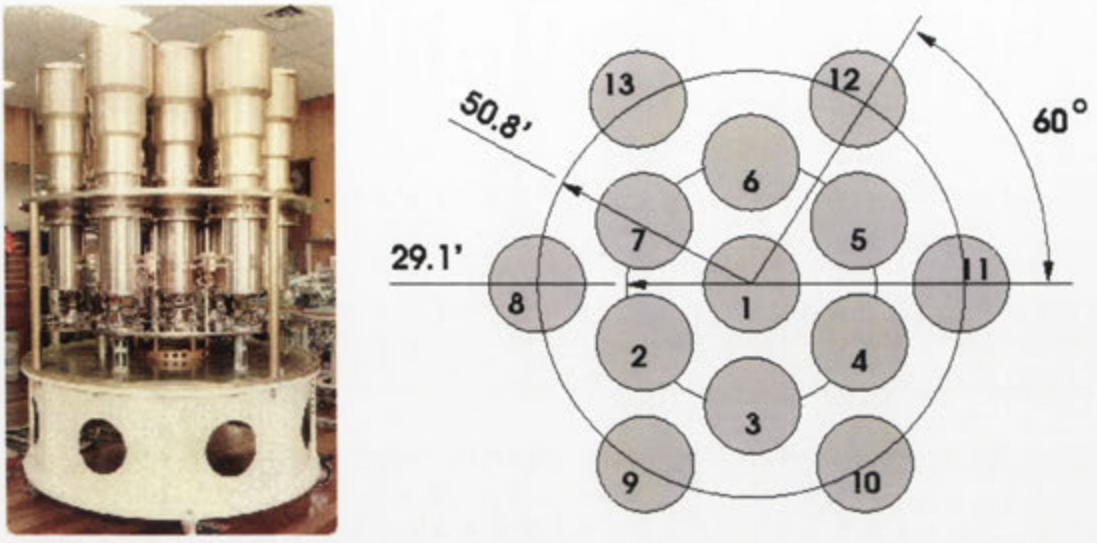

Fig. 2.2: Photo of the Parkes Multibeam instrument (left) and the configuration pattern of the 13 receivers in the instrument (right). The angle between the receivers and the radius on the sky of the inner and outer receiver rings is shown on the configuration diagram. Both images are taken from the Multibeam survey web site, http://www.atnf.csiro.au/research/multibeam/.

2.2 The Optical Properties

As with the identification of optical counterparts, an internet accessible extragalactic database was used to collect the optical data for the identified galaxies in the BGC. An increasing number of databases are now available on the web that contain detailed information on galaxies from various sources, with optical, radio, and other wavelength data available. In 2001 when this project was started, one such database was LEDA, the Lyon-Meudon Extragalactic Database (Paturel et al., 1997, http://cismbdm.univ-lyon1.fr/~leda/), maintained by the CISM at the Lyon Claude-Bernard University. This database, based mostly around the work of the Catalog of Principle Galaxy (PGC, Paturel et al., 1989) and the Third Reference Catalog of Bright Galaxies (RC3, de Vaucouleurs et al., 1991), contained a large collection of mean optical and radio data for thousands of catalogued extragalactic objects. In 2000 this database merged with the Galactic database Hypercat to form the extragalactic half of HyperLEDA (http://www-obs.univ-lyon1.fr/hypercat/), and since 2003 the original version of LEDA is no longer available.

We used LEDA to extract optical parameters for the galaxies in the BGC. It was chosen mainly for the amount of parameters available for each galaxy and its formatting of output for batch jobs, useful when we need the data for up to 1000 galaxies. The database that was used in Koribalski et al. (2004) to find the optical counterparts, NED, was also used here but only to check that names, positions and redshift velocities for some galaxies, not as a source of data for the catalogue. This

Table 2.1. List of Optical Parameters Obtained from LEDA

Parameter (1)	Description (2)
name	Name submitted to LEDA (Returned Automatically)
pgc	PGC/LEDA number
galaxy_name	alternate name
al2000	RA 2000.0 (hours decimal value)
de2000	DEC 2000.0 (degrees decimal value)
al2	galactic longitude (degrees)
ab2	galactic latitude (degrees)
sgl	supergalactic longitude (degrees)
sgb	supergalactic latitude (degrees)
typ	morphological type
t	morphological type code
logd25	$\log_{10}$ of apparent diameter (d25 in 0.′1)
slogd25	actual error on logd25
logr25	$\log_{10}$ of axis ratio (major axis/minor axis)
slogr25	actual error on logr25
brief	mean effective surface brightness (mag arcsec^{-2})
sbrief	actual error on brief
bt	total B magnitude
sbt	actual error on bt
it	total I magnitude
sit	actual error on it
ubt	total $U-B$ color
bvt	total $B-V$ color
ube	effective $U-B$ color
bve	effective $B-V$ color
logs	$\log_{10}$ of central velocity dispersion (σ in km s^{-1})
slogs	actual error on logs
vopt	heliocentric radial velocity from optical measurement (in km s^{-1})
svopt	actual error on vopt
ag	galactic extinction in the B band (SFD98)
ai	extinction due to inclination in B magnitude
incl	inclination between line of sight and polar axis (in degrees)
bri25	mean surface brightness within isophote 25 (mag arcsec^{-2})
logvmopt	$\log_{10}$ of maximum velocity rotation (vm in km s^{-1}) from optical observations (Hα)
slogvmopt	actual error on logvmopt

(1) Name of the parameters downloaded from LEDA.
(2) Description of parameters with units where appropriate.

is because while NED has excellent information for individual objects, including detailed reference lists that LEDA does not provided, the batch job service is less user friendly for large samples. We have found the best use of these two databases is to use one to cross check the data in the other.

The option in LEDA to "Extract mean data for a list of galaxies" allowed a list of galaxy names to be submitted to the database, and returns a table of parameters which is chosen from a list of 77 upon submission. We chose 34 of these parameter, almost all appearing to be based on optical observations and none from H I data, which are listed in Table 2.1. A list of names for the optical counterpart galaxies identified in the BGC was fed into LEDA in this manner (in groups of 50 due to previous restrictions on the number of entries which no longer apply) to obtain the optical data for most of the BGC galaxies.

Not all of the 1000 BGC galaxy identifications returned optical data from LEDA, and several of the returned results were incorrect data. In some cases this is because there was no catalogued optical counterpart identified by the BGC for the H I detection (these are the galaxies identified as "new" in the BGC as mentioned above, see Ryan-Weber et al., 2002), or because there were multiple optical galaxies within the Parkes beam (i.e. a pair or group of galaxies). As in both of these cases we do not have a single optical source to match the H I detection, they were excluded from the final optical catalogue.

For others objects, the counterpart name was not recognised by LEDA, or LEDA returned the wrong galaxy. In order to fix these problems we used NED to check each of the objects which LEDA rejected and obtain alternative catalogued names (many being PGC/LEDA designations to ensure the database would return a result). The alternative names were run through LEDA to obtain the optical data, and the process repeated for those galaxies which were still rejected until the most complete list of available properties possible was obtained.

The optical positions and redshift velocities obtained from LEDA were then compared to the BGC values to confirm the counterpart identification (see § 2.3). Galaxies which had large positional or velocity differences were examined more closely in both NED and LEDA to confirm the identification. A few galaxy identifications in the BGC were found to be incorrect after this comparison, and improved identifications were included in the BGC before its publication. The positional comparison also found several objects which had been confused with another galaxy when submitted to LEDA as the other object was often several times the HIPASS beam size (or even several degrees) away from the H I source. In all but one case this was correctable by using an alternative name for the optical object. For HIPASS J1348–53 however there was no alternative name available. This source was identified in the BGC with the optical galaxy ESO 174-G?001, but as LEDA shortens the names of all ESO(B) Atlas (Lauberts, 1982) galaxies (omitting the "G?00") it was confused with ESO 174-G001 (potentially a third galaxy, ESO 174-GA001, can be confused for the same source by LEDA). As we could not obtain LEDA data for this object it was removed from the final optical catalogue, the only object which was not new or a pair/group to be excluded.

The final catalogue contained the LEDA optical properties of 853 of the 1000 BGC galaxies. Of the remaining objects, 91 were classified as "new" in the BGC, 55 were groups or pairs, and one was ESO 174-G?001. With this list it is possible to make comparisons between the optical and H I properties of a relatively large sample of strong H I sources with known optical counterparts. It is a good starting point to search for gas-rich dwarf galaxies, which we will go into in the next chapter (Chapter 3). But first we will take a look at some of the other results which have emerged from comparing the optical and H I properties.

2.3 Comparison of the Optical and H I properties

After compiling the optical catalogue it was possible to compare the BGC H I data with optical parameters (both how well they match and the physical properties derived from them), as well as look at the general optical properties of an H I selected sample. One of the comparisons we performed of properties derived from the BGC and LEDA parameters, H I mass-to-light ratio versus absolute B magnitude, forms the basis of this thesis project. It is not shown in this section but in the following chapter, and before we get to it we will look at other relationships derived from the optical catalogue.

Fig. 2.3 shows a scatter plot of the positional offsets for each of the BGC galaxies, with the symbol sizes proportional to $\log_{10}$ of the H I peak flux density. Similarly, Fig. 2.4 shows two histograms of the offset between the BGC H I position and the LEDA optical position, with the Right Ascension difference on the left and the Declination difference on the right. All these plots were reproduced in the BGC. Both plots show that there is no systematic positional offset between the BGC H I positions and the position of the optical source, and that there is generally good agreement between the optical and H I positions (much less than the size of the Parkes beam in H I). There is no strong difference in the shape or width of the two distributions in Fig. 2.4, indicating the BGC positions are equally accurate in both RA and Dec. There is no obvious systematic difference at various H I peak flux densities as indicated in Fig. 2.3. The dashed line in this figure at $3'\,14''$ from the centre indicates the radius containing 95% of the galaxy offsets, about two times the approximate positional uncertainty of the HIPASS (Koribalski (priv. comm.)).

There are several reasons why some of the galaxies have offsets much larger than could reasonable be attributed to the size of the Parkes beam. It could be due to a LEDA mix up (which is how ESO 174-G?001 was picked up, see above), the identification of the wrong optical galaxy for the H I source (such as the example of HIPASS J0622–07 shown in the BGC and Chapter 3), contamination from a neighbouring galaxy or a source that is extended compared to the Parkes beam, or in a few cases problems/interference during the HIPASS observations (such as the strong baseline ripple which affects Centaurus A as discussed in the BGC). Or it could be a more physical problem, such as a highly extended H I envelope or optical galaxy, the galaxy could have a peculiar structure (e.g. from galaxy interactions), or the H I could be offset from the optical galaxy (e.g. there is only gas in the outer areas of the disk).

Fig. 2.5 shows a histogram for the velocity difference between the BGC H I sources and the optical counterpart from LEDA. Once again there appears to be no systematic offset in the distribution one way or the other, and the majority of galaxies have velocity differences less than the uncertainties in the LEDA velocities. There are a few galaxies which had very large differences between the BGC H I

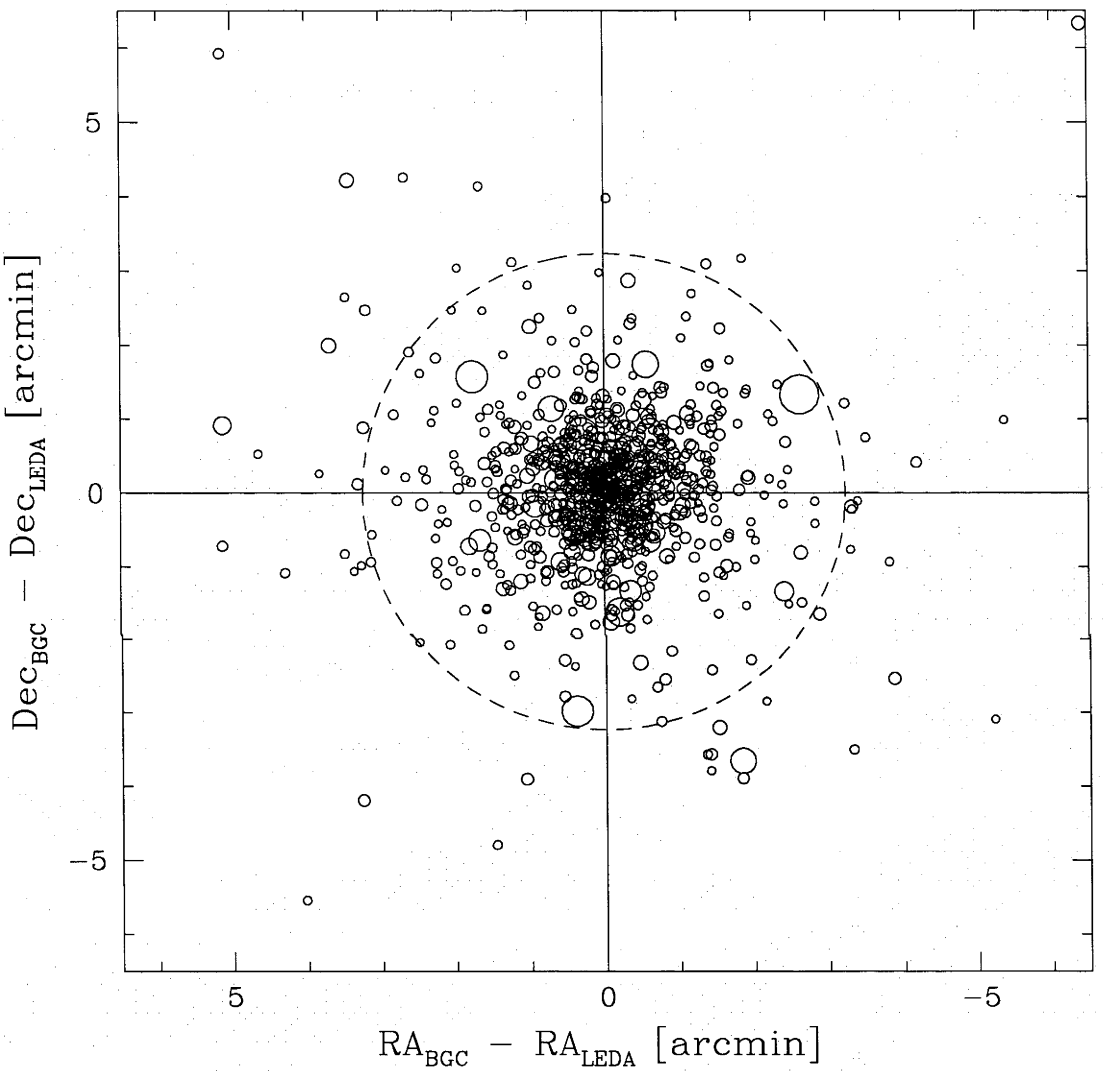

Fig. 2.3: Offsets between the optical (LEDA) and H I (BGC) positions for the 853 BGC galaxies with optical parameters in LEDA. The size of the circles is a function of $\log_{10}$ of the H I peak flux density. 95% of the galaxies have an offset equal to or less than $3'\,14''$, marked by the dashed circle.

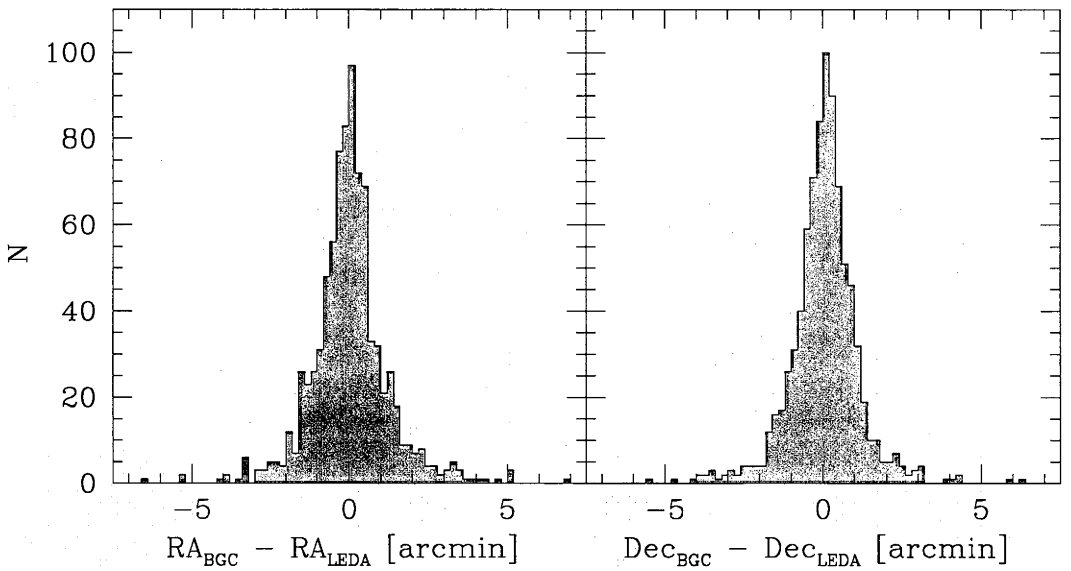

Fig. 2.4: Histograms of the offset between the BGC H I position and the LEDA optical position for the 853 BGC galaxies with optical parameters in LEDA. The left histogram shows offset in Right Ascension, while the right shows Declination.

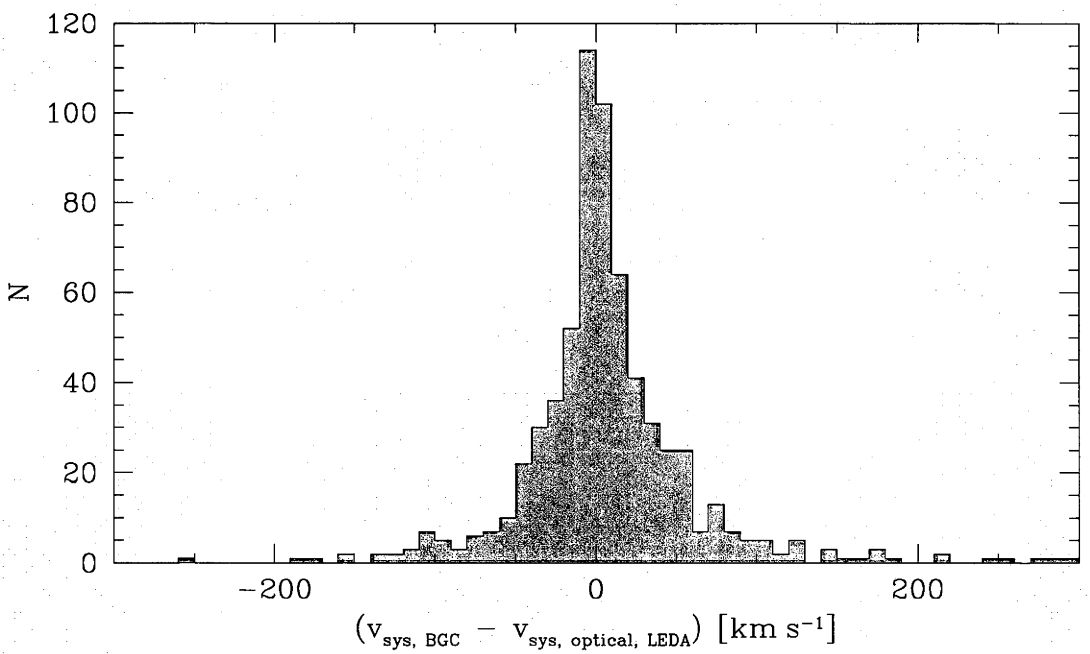

Fig. 2.5: Velocity difference histogram between the BGC H I sources and the optical counterpart from LEDA for the 672 galaxies in the BGC which have optical velocities listed in LEDA.

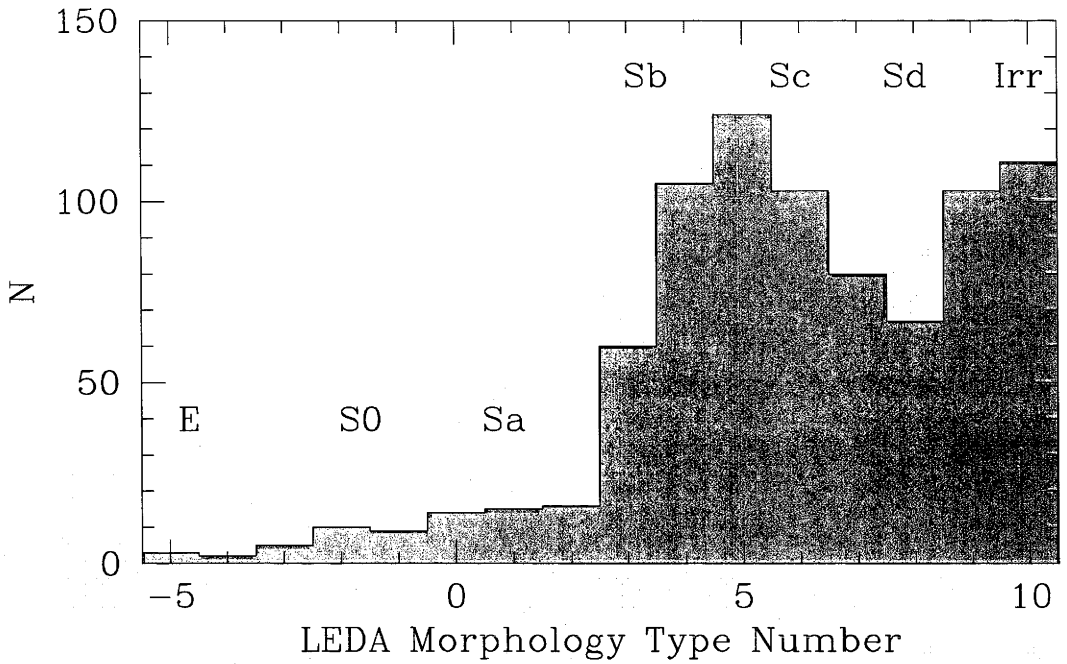

Fig. 2.6: Histogram of the LEDA morphological types of the 827 BGC galaxies which have these classifications in LEDA. The morphology type which corresponds to the number is indicated above the histogram, with –5 being elliptical, –2 being S0, 1 is an Sa, 3 an Sb, 6 an Sc, 8 an Sd, and 10 being irregular. Barred spirals are not distinguished from non-barred in this classification.

systemic velocity and the optical values, 28 greater than $|200\ \mathrm{km\,s^{-1}}|$, sometimes with the optical velocity being several thousand $\mathrm{km\,s^{-1}}$ greater than the BGC value and outside the range of the HIPASS observations. Similar discrepancies were noted for 16 galaxies by the BGC between their velocities and some values supplied by NED, 10 of which match the LEDA discrepancies. A few of the initial cases were found to be incorrect identifications of the optical counterparts which were corrected for the final version of the BGC. But the remainder of velocity discrepancies appear to be due to incorrect optical measurements in one database or the other (see Appendix A in Koribalski et al., 2004). In many cases where there was a large difference with the value from one database then the other would agree with the BGC velocity. In other cases, NED would have alternative velocity measurements which would agree with the BGC value.

Fig. 2.6 shows a histogram of the morphological types of the BGC galaxies. Not surprisingly there is a strong bias toward galaxies of Sb/SBb type or later, which tend to contain higher proportions of neutral hydrogen gas than earlier type spirals (which will have exhausted most of their gas) and ellipticals (which we would not expect to contain much gas, if any). Indeed, some of those classified as earlier types are likely to have been misclassified. Later type galaxies are also more numerous, especially in the field which the HIPASS observations favour due

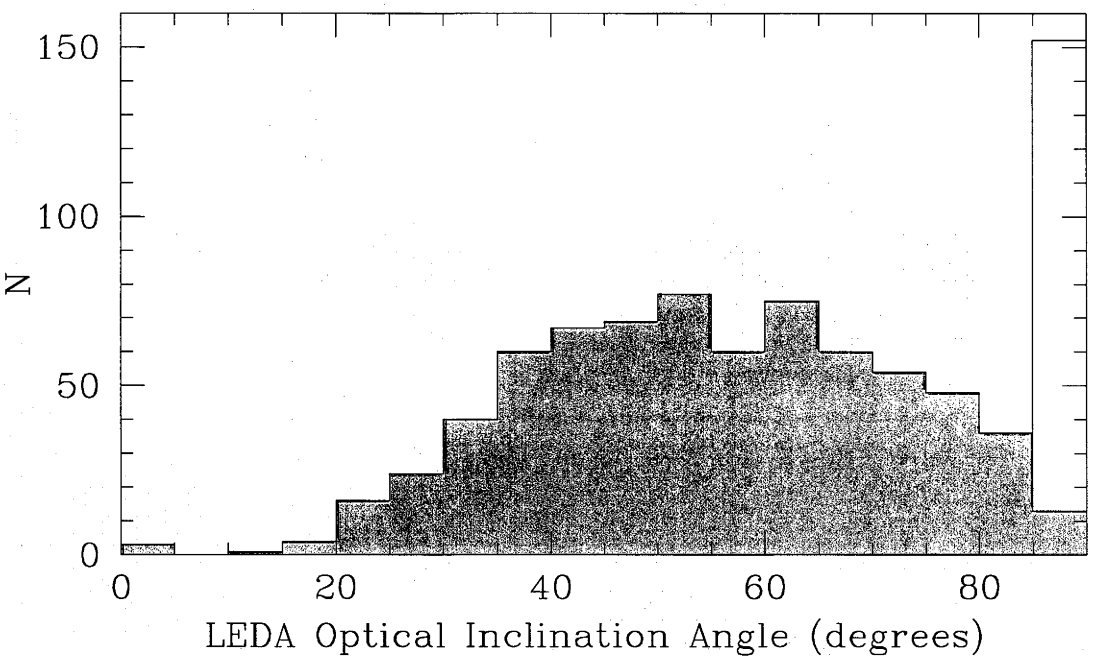

Fig. 2.7: Histogram of the inclination of the 846 BGC galaxies which have this value in LEDA (white histogram), and for all galaxies except those for which $i = 90.^{\circ}0$ (grey histogram, 707 galaxies plotted, see text).

to the H I beam size (remembering that the pairs and groupings were excluded from the optical properties catalogue).

Fig. 2.7 shows a histogram of the inclination of the BGC galaxies (defined as the angle between the line of sight and the polar axis of the galaxy disk). Of the 846 BGC galaxies which had inclinations in LEDA, 139 had values which were exactly $90.^{\circ}0$ (i.e. edge on). These galaxies create a "spike" in the last bin of the histogram. It is likely that these galaxies are all close to edge on but the exact value was not able to be calculated and they were given a default value of 90°. Many of the galaxies may belong to bins of lower inclination. We have plotted the histogram both including (white) and excluding (grey) these galaxies to show their effect on the distribution.

In a large unbiased random sample of disk galaxies we would expect this distribution to follow a sinusoidal curve with few galaxies around 0° and peaking at 90°, as we are more likely to view a galaxy from edge on than face on. The distribution between 0° and 50° approximately follows such a trend, but after that the numbers drop away again, and are back to only a few galaxies again by the time 90° is reached. While the 90° spike accounts for some of this problem, there are not enough galaxies in the spike to fill out the distribution. Instead, the reason for the drop off is in the selection criteria for the BGC. The cutoff for the catalogue was in H I peak flux density. For a galaxy with low inclination the H I line will be narrower and more peaked than a galaxy which is almost edge on as it does

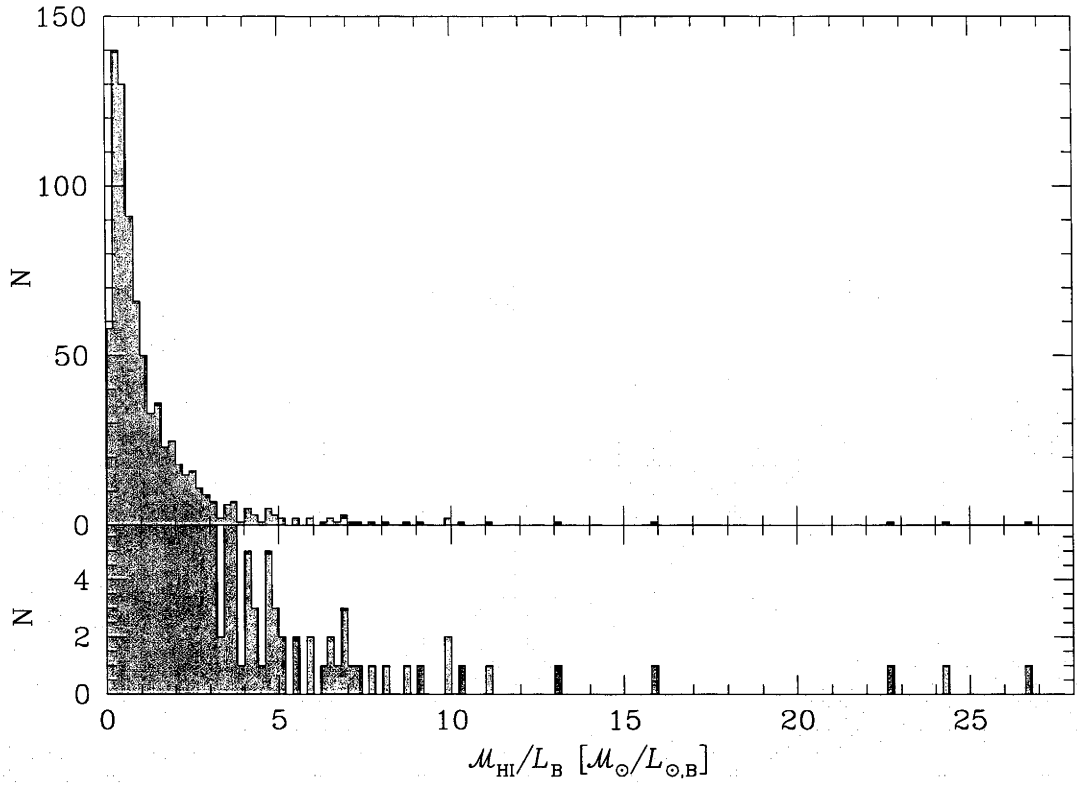

Fig. 2.8: Histogram of the H I mass-to-light ratio for the 789 BGC galaxies with LEDA *B* band apparent magnitudes. Displayed at the top is full histogram, while underneath is a zoomed in version to show the bins with only a few galaxies.

not have as great a spread in velocity. Therefore the BGC preferentially selects galaxies which are more face on.

Fig. 2.8 shows a histogram of the H I mass-to-light ratio ($\mathcal{M}_{HI}/L_B$) for the 789 BGC galaxies with *B* band apparent magnitudes in LEDA (with a zoomed in version plotted beneath to emphasise the small number of galaxies with very high ratios). Typical values of $\mathcal{M}_{HI}/L_B$ are between 0 and 1 $\mathcal{M}_\odot/L_{\odot,B}$ (Roberts & Haynes, 1994). The majority of galaxies in the BGC have low to mid range ratios (between 0 and 2 $\mathcal{M}_\odot/L_{\odot,B}$), but as the catalogue by definition preferentially chooses galaxies with more gas there is a larger spread in ratio than would normally be seen in a random galaxy sample. There is also a long tail to the distribution, which goes out to some extreme ratios above 20 $\mathcal{M}_\odot/L_{\odot,B}$. Fig. 2.9 shows H I mass-to-light ratio histograms for all these galaxies divided into six different morphological types going from ellipticals, through spirals to irregulars (as defined previously in Fig. 2.6). There is a strong trend with morphology, with the early types having a narrow distribution at a low $\mathcal{M}_{HI}/L_B$, while the later type spirals and irregulars have a much broader range and have several galaxies with very high $\mathcal{M}_{HI}/L_B$. The H I mass-to-light ratio is discussed in more detail in Chapter 3.

Finally, Fig. 2.10 shows both the classical Tully Fisher relationship (stellar

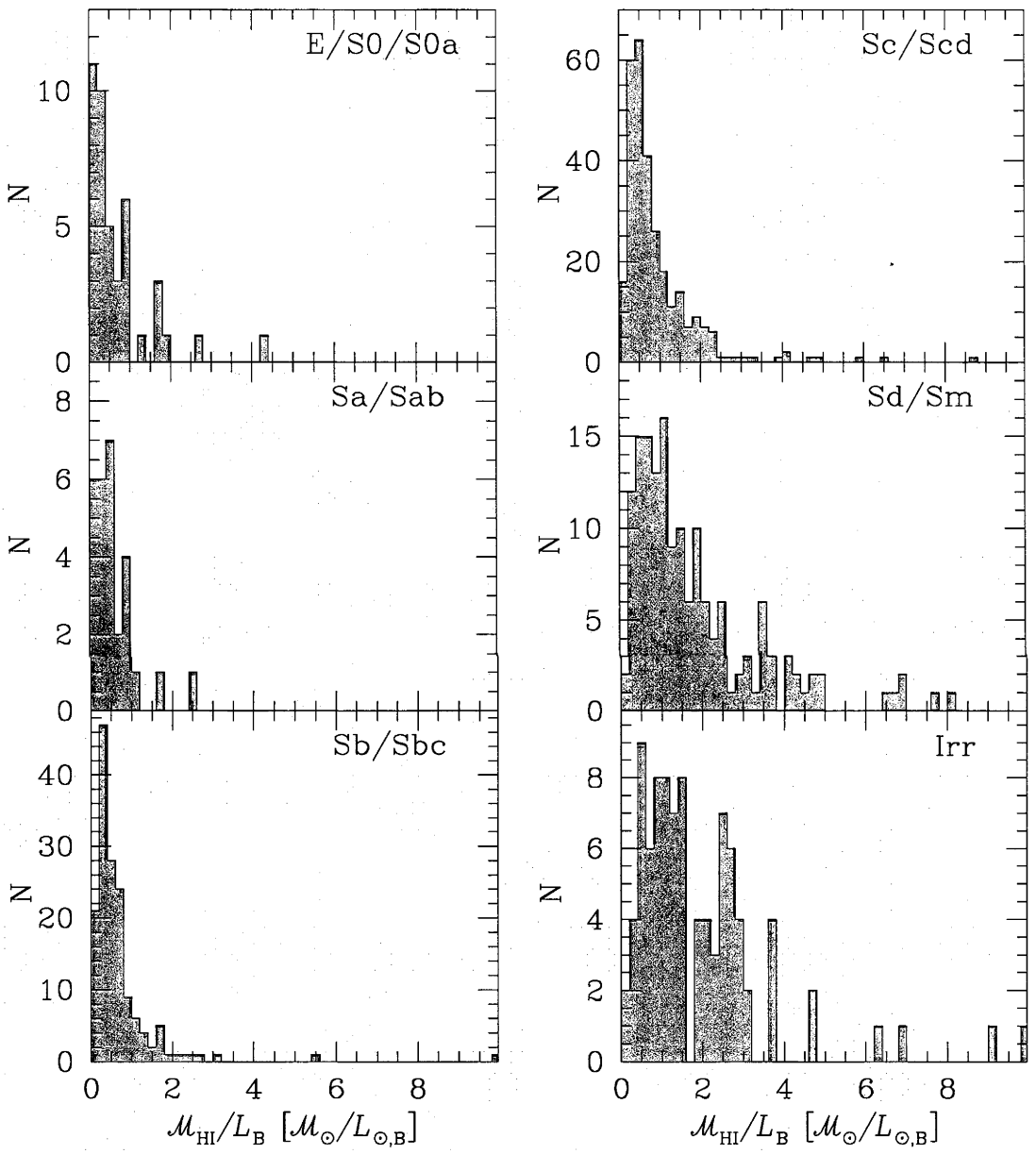

Fig. 2.9: Histogram of the H I mass-to-light ratio ($\mathcal{M}_{HI}/L_B$) for six different morphology types. Types are displayed in the top right corner of each plot and correspond to the types in Fig. 2.6.

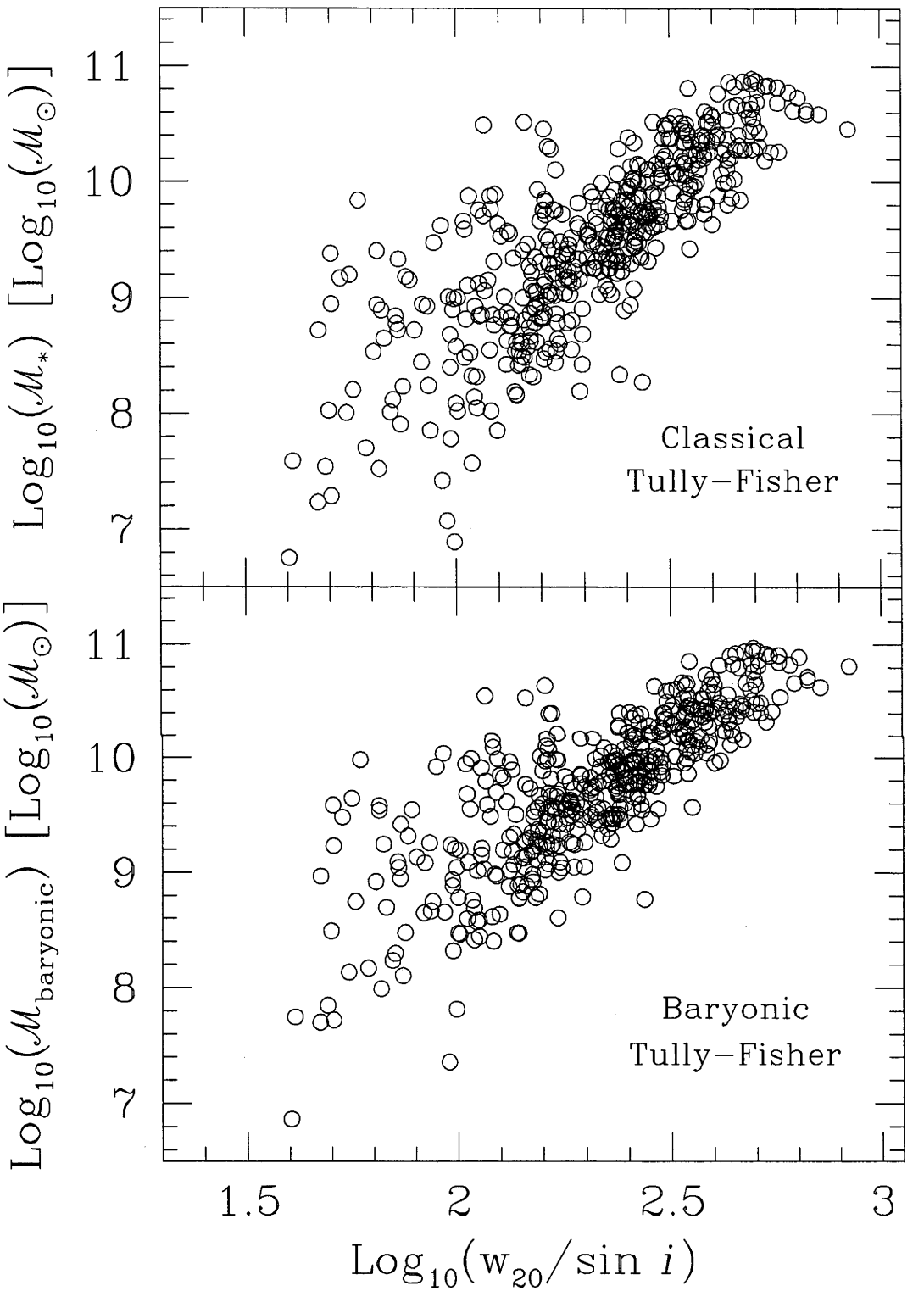

Fig. 2.10: The classical (stellar, top) and baryonic (bottom) Tully Fisher relations (Tully & Fisher, 1977) for the 478 BGC galaxies with LEDA inclinations between 50° and 90°, *B* band apparent magnitudes in LEDA, and SFD98 Galactic extinctions less than 1 mag.

mass versus rotation velocity Tully & Fisher, 1977) and the baryonic Tully Fisher relationship (H I plus stellar mass versus rotation velocity McGaugh et al., 2000). In both cases the rotation velocity is approximated by the velocity width at 20% peak flux density of the H I line (w_{20}), which is corrected for inclination. The plots were limited to galaxies with inclinations between 50° and 90° (including the 90° "spike" seen in Fig. 2.7) as the width of the H I line for galaxies with low inclination tend to be narrow and more strongly affected by internal velocity dispersion, and the inclination correction is more uncertain. We also limited the plot to galaxies with SFD98 Galactic extinction less than 1 mag to avoid the high uncertainties associated with optical results in the Galactic Plane. The stellar mass in both is calculated from the B band luminosity by assuming a stellar mass-to-light ratio ($\mathcal{M}_*/L_{\rm B}$) of 1.5 $\mathcal{M}_\odot/L_{\odot,{\rm B}}$, which is typical of many spiral galaxies but may not be appropriate for all galaxies in the BGC (galaxies with high star formation rates may have lower ratios, while more quiescent galaxies may have a higher ratio). No correction to include molecular hydrogen gas is included as any such addition would be highly speculative.

Both versions of the Tully Fisher relation show a strong trend, with high mass galaxies rotating faster than low mass galaxies. This trend is seen in disk galaxies from many past studies, with the rotation velocity being related to the total mass of the system (by the virial therorem, see Binney & Tremaine, 1987, § 4.3), the relationship therefore implying a link between total mass and luminous/baryonic mass in disk galaxies. The trend in the baryonic mass plot is slightly tighter than the purely stellar mass plot, with the addition of the H I gas moving some of the galaxies that appear to have masses too low for their rotation to higher masses. There is increasing scatter towards the low mass end of both plots, the regime of dwarf galaxies, which is the focus for much of the current work on the Tully Fisher relationship (McGaugh et al., 2000) to see if the currently known correlation for higher mass galaxies continues for dwarfs, deviates, or breaks down.

However, it is the galaxies above the trend, having too high a mass for their rotation (or alternatively, rotating too slowly for their mass), which stand out in both our plots. There are a number of uncertainties which could be contributing to this discrepancy. The distance to the galaxy calculated from the Local Group velocity may be incorrect for many nearby galaxies or galaxies in groups where peculiar motions are of the same order as the redshift. But any large discrepancy here would produce as many galaxies which had masses too low as too high, so this is more likely just to add to the general scatter of the results. Similarly for the LEDA B band magnitudes, which often have very large error bars on them.

A more likely explanation comes from the inclination as further investigation has shown that the LEDA inclinations can be very unreliable. As we have selected only highly inclined galaxies, if the inclination is overestimated by a large amount then we will under-correct the rotation, but if the inclination is underestimated then the galaxy will be excluded from the sample. But the most likely explanation

is that the rotation velocity from the H I line width underestimates the rotation velocity in the outer regions of the galaxy. It has been seen in several disk galaxies that the H I rotation curve is still rising at the last point (Verheijen, 2001; de Blok et al., 1996). So that we cannot be sure the flat part of the rotation curve has been reached, in particular for dwarfs (Begum et al., 2005) where we cannot be certain that they do flatten out as seen in larger galaxies. This may be the case with these galaxies, and it would mean our estimate of rotation velocity is too low.

3. THE SAMPLE GALAXIES

Past studies of gas-rich dwarf galaxies have selected samples based only on optical data (e.g. galaxies with low surface brightness or interesting morphology), or have come from samples of limited area or scope (e.g. from short scanning surveys or from studies of groups). The combination of the H I data from the Bright Galaxy Catalog with the mean optical data from LEDA allows us to select interesting galaxies for further investigation based on H I and optical properties for a relatively large sample of galaxies in the Local Universe. In this chapter we will look at how we selected a sample of dwarf galaxies from the BGC based on their preliminary H I mass-to-light ratios, and at some of the characteristics of those sample objects.

3.1 H I Mass-to-Light Ratio versus Absolute B *Magnitude*

The H I mass-to-light ratio of a galaxy is a distance independent quantity which compares the H I mass to the luminosity in a particular photometric band. It represents the quantity of H I gas in the galaxy relative to the stellar content, and is therefore related to a galaxy's efficiency at converting its neutral gas into stars. As the B band magnitude of galaxies has been in the past the most commonly available (from photographic studies), the H I mass-to-light ratio is usually expressed with the B band luminosity ($\mathcal{M}_{\rm HI}/L_{\rm B}$). The B band is not necessarily the best band to use as it is strongly affected by the current star formation activity (and the luminosity is therefore less representative of the mass of the stars), and it is also subject to higher Galactic extinction than the redder bands. However, until measurements in other bands become widely available for more galaxies, B is the only band in which comparisons with large non optically selected samples are possible.

As the name suggests, the ratio is derived simply by dividing the H I mass ($\mathcal{M}_{\rm HI}$) by the B band luminosity ($L_{\rm B}$). Both of these quantities are dependent on the distance squared, but these cancel each other out so that $\mathcal{M}_{\rm HI}/L_{\rm B}$ is distance independent. This makes it a very useful quantity as for many galaxies the distance is poorly determined. The H I mass in solar units is given by (Roberts, 1975):

$$\mathcal{M}_{\rm HI} = 2.36 \times 10^5 \; D^2 \; F_{\rm HI} \;\; \mathcal{M}_{\odot}, \tag{3.1}$$

where $F_{\rm HI}$ is the integrated H I flux density in Jy km s^{-1}, and D is the galaxy distance in Mpc. Hubble flow distances were calculated from the Local Group

velocities given in the BGC (using our adopted H_0 of 75 km s^{-1} Mpc^{-1}). As stated in the BGC, the distances for nine of the closest galaxies (< 2.2 Mpc) were obtained from other literature sources where they were available (Mateo, 1998; Willick & Batra, 2001), as peculiar velocities are a large component of the total systemic velocity for these close systems and can significantly affect the distances. The B luminosity in solar units is given by:

$$L_{\rm B} = D^2 \; 10^{10-0.4(m_{\rm B}-A_{\rm B}-M_{\rm B,\odot})} \; L_{\odot,{\rm B}}, \tag{3.2}$$

where $m_{\rm B}$ is the B band apparent magnitude, $A_{\rm B}$ is the B band Galactic extinction (from SFD98), and $M_{\rm B,\odot}$ is the absolute Solar B magnitude which is taken as 5.48 mag (Bessell, Castelli, & Plez, 1998).

Therefore, the H I mass-to-light ratio in solar units is given by:

$$\frac{\mathcal{M}_{\rm HI}}{L_{\rm B}} = 1.5 \times 10^{-7} F_{\rm HI} \; 10^{0.4(m_{\rm B}-A_{\rm B})} \; \frac{\mathcal{M}_{\odot}}{L_{\odot,{\rm B}}}, \tag{3.3}$$

where the parameters are as given above. The factor at the front of this equation will be different in photometric bands other than B. Note that a dust extinction correction from the host galaxy (internal extinction) is not included as this correction is highly uncertain, especially for dwarf irregular galaxies (Sidhu & Cabanela, 2003). However it may have an effect on certain galaxies especially disk galaxies seen from edge on (see Chapter 7).

Of the 853 BGC objects with optical counterparts in LEDA, we have the mean photometric B band apparent magnitudes for 789. The integrated H I flux density is available for all the BGC objects, and the Galactic extinction is available for any sky position from SFD98, so the apparent magnitude is the limiting factor for the number of galaxies for which we can calculate $\mathcal{M}_{\rm HI}/L_{\rm B}$. For the same galaxies we can also calculate the absolute B band magnitude (which is equivalent to $L_{\rm B}$) which is given by:

$$M_{\rm B,0} = m_{\rm B} - A_{\rm B} - 5\log_{10}(D) - 25 \;\; {\rm mag}, \tag{3.4}$$

where the parameters are as given above.

One of the most interesting relations to emerge from the comparison of the BGC H I data to the LEDA parameters is a plot of H I mass-to-light ratio against absolute magnitude. Fig. 3.1 shows the $\log_{10}(\mathcal{M}_{\rm HI}/L_{\rm B})$ distribution for the 789 galaxies with B band apparent magnitudes in LEDA as a function of $M_{\rm B}$. This figure forms the basis for the selection of a sample of galaxies for this project and is shown many times in this thesis in various forms (Chapter 1 Fig. 1.1, Chapter 7 Fig. 7.4, Chapter 8 Fig. 8.1 and 8.2).

Overall, dwarf galaxies (which we will define based on low luminosity) have a large spread in H I mass-to-light ratios (similar to what was seen for late-type morphologies in Fig. 2.9). The low luminosity, low $\mathcal{M}_{\rm HI}/L_{\rm B}$ region of the plot is

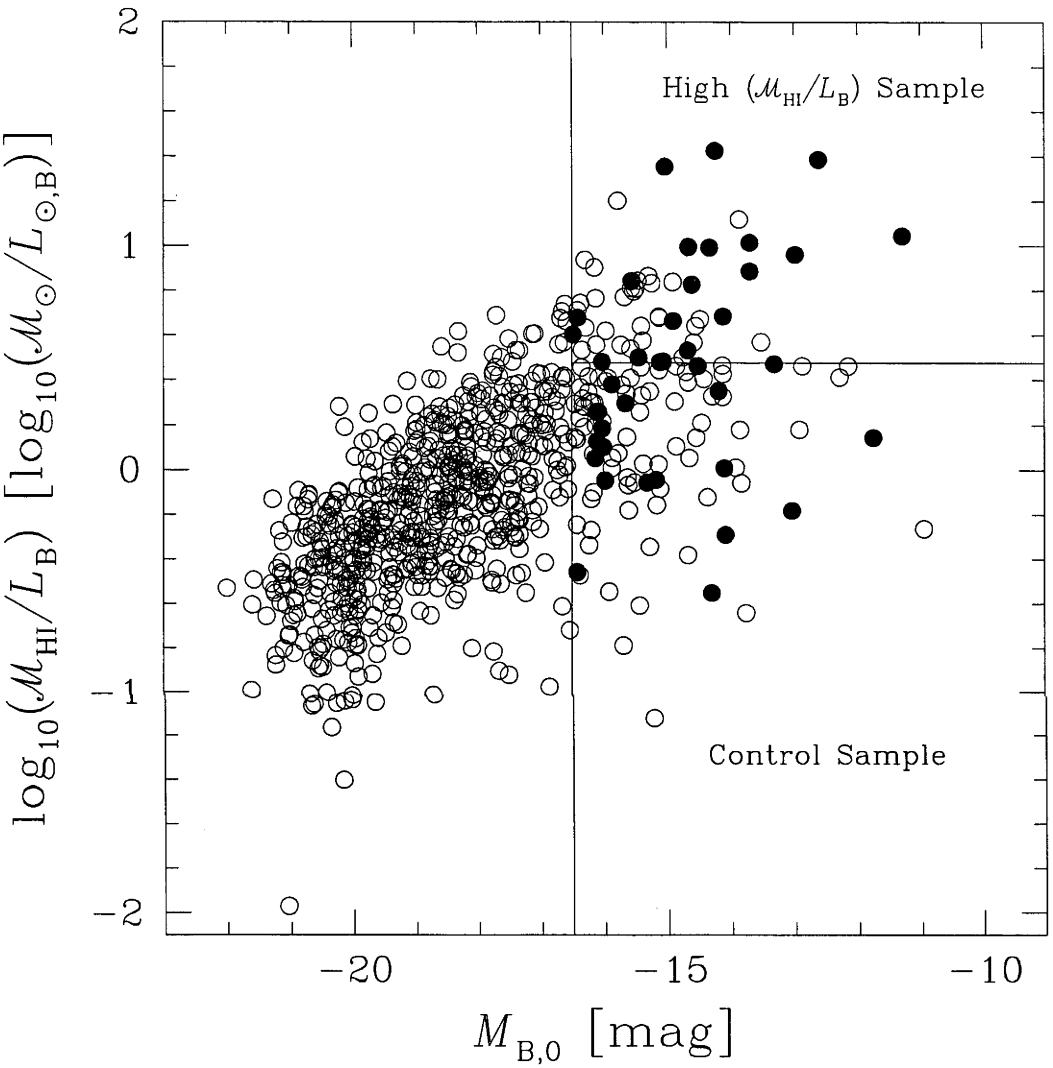

Fig. 3.1: H I mass-to-light ratio versus absolute photographic B magnitude for 789 galaxies in the HIPASS Bright Galaxy Catalog (Koribalski et al., 2004) which have blue apparent magnitudes in LEDA. The lines mark our arbitrarily chosen sample regions. The vertical line shows our magnitude limit ($M_B > -16.5$ mag) for dwarf galaxies. The horizontal line marks the split between high and low $\mathcal{M}_{HI}/L_B$ galaxies ($\mathcal{M}_{HI}/L_B = 3\ \mathcal{M}_\odot/L_{\odot,B}$). The open circles mark the positions of all BGC galaxies with LEDA magnitudes, while the solid circles mark our 41 sample galaxies.

underpopulated as optically faint galaxies with little gas (such as dwarf elliptical galaxies) are harder to detected both optically and in H I, and so are both less likely to be in the BGC and if they are they may not have a catalogued or observed optical counterpart. The lack of high $\mathcal{M}_{\rm HI}/L_{\rm B}$ bright galaxies, which should be easily detected both optically and in H I, suggests that there may be a physical upper limit to the H I mass-to-light ratio for a galaxy of a certain luminosity (stellar mass). A number of the dwarf galaxies in the top right corner of this plot appear to have very high (even extreme) ratios. It is from these galaxies (marked as "High ($\mathcal{M}_{\rm HI}/L_{\rm B}$) Sample" in Fig. 3.1) that we have drawn a sample of dwarf galaxies have high initial H I mass-to-light ratios for detailed follow up observations.

3.2 Selection Criteria

In order to explore the difference in the nature of high H I mass-to-light ratio dwarf galaxies from normal dwarf galaxies, two approximately equal samples of dwarfs were selected from Fig. 3.1. Firstly, we restricted the sample galaxies to those fainter than $M_{\rm B}$ = -16.5 mag, which we define to be dwarf galaxies. This limit was set arbitrarily, and was chosen so that all system in the samples could reasonably be described as low mass galaxies. 148 of the 789 BGC galaxies with LEDA *B* band apparent magnitudes fit this description. These galaxies have a large range in $\mathcal{M}_{\rm HI}/L_{\rm B}$, with 50 having $\mathcal{M}_{\rm HI}/L_{\rm B} \geq 3\ \mathcal{M}_{\odot}/L_{\odot,{\rm B}}$, seven with ratios greater than 10 $\mathcal{M}_{\odot}/L_{\odot,{\rm B}}$, and three have ratios in excess of 20 $\mathcal{M}_{\odot}/L_{\odot,{\rm B}}$.

Next, an arbitrary H I mass-to-light ratio cut off of 3 $\mathcal{M}_{\odot}/L_{\odot,{\rm B}}$ was chosen to separate the high $\mathcal{M}_{\rm HI}/L_{\rm B}$ galaxies from the typical dwarf galaxies. This level is approximately three times the typical ratio seen for late type dwarf galaxies (Roberts & Haynes, 1994) and includes about a third of all dwarfs in the BGC with know optical magnitudes. It is from this region, marked in Fig. 3.1, that we have drawn a sample of 21 high $\mathcal{M}_{\rm HI}/L_{\rm B}$ galaxies for our study. From the remaining dwarfs we drew a sample of 20 low $\mathcal{M}_{\rm HI}/L_{\rm B}$ galaxies as a control sample. The regions of selection are marked in Fig. 3.1, as are the positions of the 41 sample galaxies for this project (solid circles).

Selection of individual galaxies among the high $\mathcal{M}_{\rm HI}/L_{\rm B}$ sample favoured the galaxies with the highest ratios from the BGC and LEDA data. The three galaxies with the highest ratios (ESO 505-G007, ESO 215-G?009, and IC 4212) were all included, as were most of the galaxies over $\mathcal{M}_{\rm HI}/L_{\rm B} = 10\ \mathcal{M}_{\odot}/L_{\odot,{\rm B}}$. The selection of most of the other sample galaxies was essentially random, with some favour given to those galaxies who's sky positions were not too far from other sample objects. This meant there is a slight bias towards galaxies in groups or loose associations. A few galaxies (most notably MCG–04-02-003, see § 3.3 and Chapter 7) were selected because their interesting optical morphology.

3.3 The Galaxies

The sample objects are spread over much of the southern sky, with the main concentrations around $\alpha = 0^h$ (in the area of the Sculptor group), between $\alpha = 5^h$ and 9^h, and around 12^h. The sky distribution of the sample is shown in Fig. 3.2. The details that were available for all 41 sample galaxies from the BGC and LEDA are presented in the tables at the end of this section. Table 3.1 lists the basic details of each galaxy. Table 3.2 lists the H I properties as presented in the BGC (Koribalski et al., 2004). Table 3.3 lists some of the optical properties as obtained from LEDA. Table 3.4 lists some properties derived from both the BGC and LEDA parameters.

Seven of the galaxies (ESO 349-G031, ESO 473-G024, IC 1574, UGCA 015, ESO 347-G017, UGCA 442 and ESO 348-G009) are members of the Sculptor group as seen in Côté et al. (1997). An eighth galaxy, MCG–04-02-003, also appears to be a member given its Local Group velocity and sky position, although it has never been noted as such and its v_{LG} would put it on the far side of the group. ESO 149-G003 is also potentially a member of this group given its v_{LG}, although it is much further south than the other Sculptor members. Potentially there is a problem with the velocity based distance estimates for all of these galaxies (see Jerjen, Freeman, & Binggeli, 1998) which we will discuss in later chapters (see Chapter 7). None of the other galaxies appear to be members of other groups, although some have close companions (see Chapter 8)

As the sample was restricted to dwarfs by optical luminosity and not morphology there are a wide variety of mostly late-type morphologies in this sample, including dwarf irregulars, late-type spirals and some which might be considered BCDs. Fig. 3.3 shows a histogram of the morphological types of our sample objects from LEDA. For comparison to the remainder of the BGC galaxies see Fig. 2.6 in the previous chapter. Our sample is dominated by the late type dwarf galaxies, with 20 irregulars, 10 Sm/SBm, and 5 Sd/SBd. The high $\mathcal{M}_{HI}/L_B$ sample has slightly greater spread of morphological type than the control sample (which are mostly irregulars). One of the most interesting morphologies is that of MCG–04-02-003 (HIPASS J0019–22, an Sm according to LEDA), for which a quick look an optical image shows only a small, bright, centrally concentrated circular region like a BCD. Closer inspection shows that there is in fact a second very low surface brightness disk component extending well beyond this central bulge, which could be easily missed or underestimated with shallow imaging. This faint outer disk is extended north-south and may even have some faint spiral arm structures visible in the bluer bands. A gallery of $4' \times 4'$ DSS images for all 41 galaxies are shown in Fig. 3.4.

The sample also covers a wide range of Galactic dust extinctions, from those in the Sculptor group which are barely affected by extinction as they are close to the South Galactic Pole (ESO 349-G031 has the lowest with $A_B = 0.05 \pm 0.01$ mag,

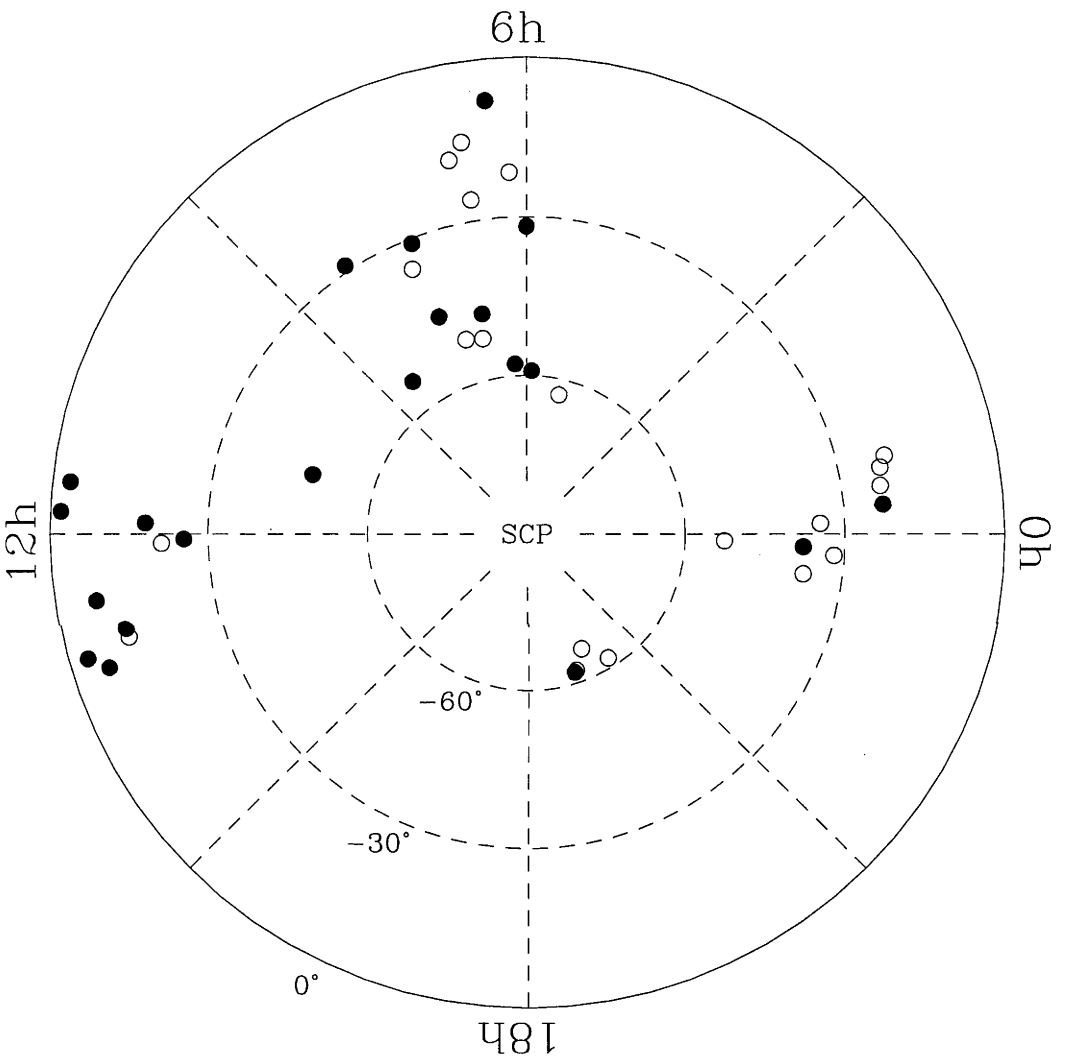

Fig. 3.2: Polar plot of the sky positions of our 41 sample galaxies centred on the South Celestial Pole (SCP). Filled circles mark the positions of the 21 high $\mathcal{M}_{\rm HI}/L_{\rm B}$ galaxies, while the open circles mark the 20 control sample (low $\mathcal{M}_{\rm HI}/L_{\rm B}$) galaxies.

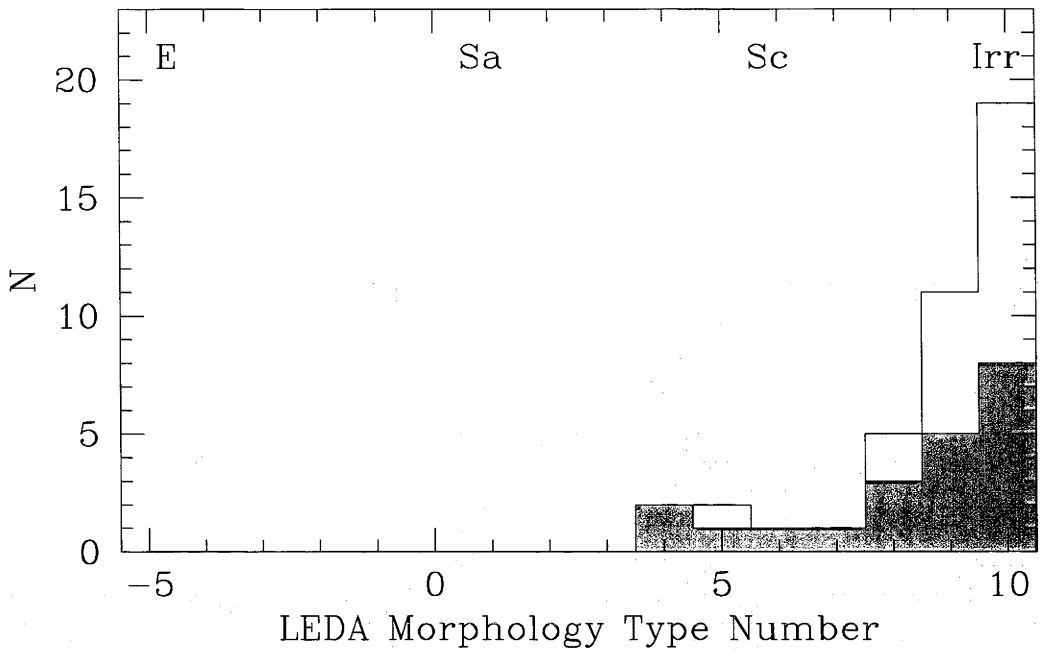

Fig. 3.3: Histogram of the LEDA morphological types for our sample galaxies, showing the 21 high $\mathcal{M}_{\rm HI}/L_{\rm B}$ galaxies (grey) and all 41 sample objects (white). For comparison see the histogram for all 827 BGC galaxies which have LEDA morphological type classifications in Fig. 2.6. The number system for morphology type in LEDA is given with Fig. 2.6.

SFD98, but there are several others almost as low) to WHI B0619–07, which is on the edge of the galactic plane and has $A_{\rm B} = 2.65 \pm 0.42$ mag (SFD98). The latter object, HIPASS J0622–07 in the BGC, is also distinguished by having originally been identified with a different optical source in the BGC (as noted by Koribalski et al., 2004), CGMW 1-0080, which is over 5′ from the position of the H I source. This source is clearly a background galaxy (it has the appearance of a distant large elliptical or edge on disk), and the true optical counterpart was found to be a much closer uncataloged (at the time of examination) irregular galaxy at the position of the H I source. It was recently catalogued independently in the optical by Whiting, Hau, & Irwin (2002) as WHI B0619–07. Therefore the optical data that we obtained from LEDA, which used the background galaxy not the real counterpart, is incorrect. Although this was known at the time of sample selection and it was likely that $\mathcal{M}_{\rm HI}/L_{\rm B}$ was not as high as the value below suggests, the galaxy was kept in the sample as the then uncatalogued object, a dwarf irregular-like galaxy, still appeared to be a promising study.

The three galaxies with the highest estimated H I mass-to-light ratios from the BGC and LEDA data, ESO 505-G007, ESO 215-G?009, and IC 4212, were all included in the sample. All three, with ratios greater than 20 $\mathcal{M}_{\odot}/L_{\odot,{\rm B}}$, are very different galaxies. ESO 505-G007 has the highest ratio (27 ± 9 $\mathcal{M}_{\odot}/L_{\odot,{\rm B}}$), and

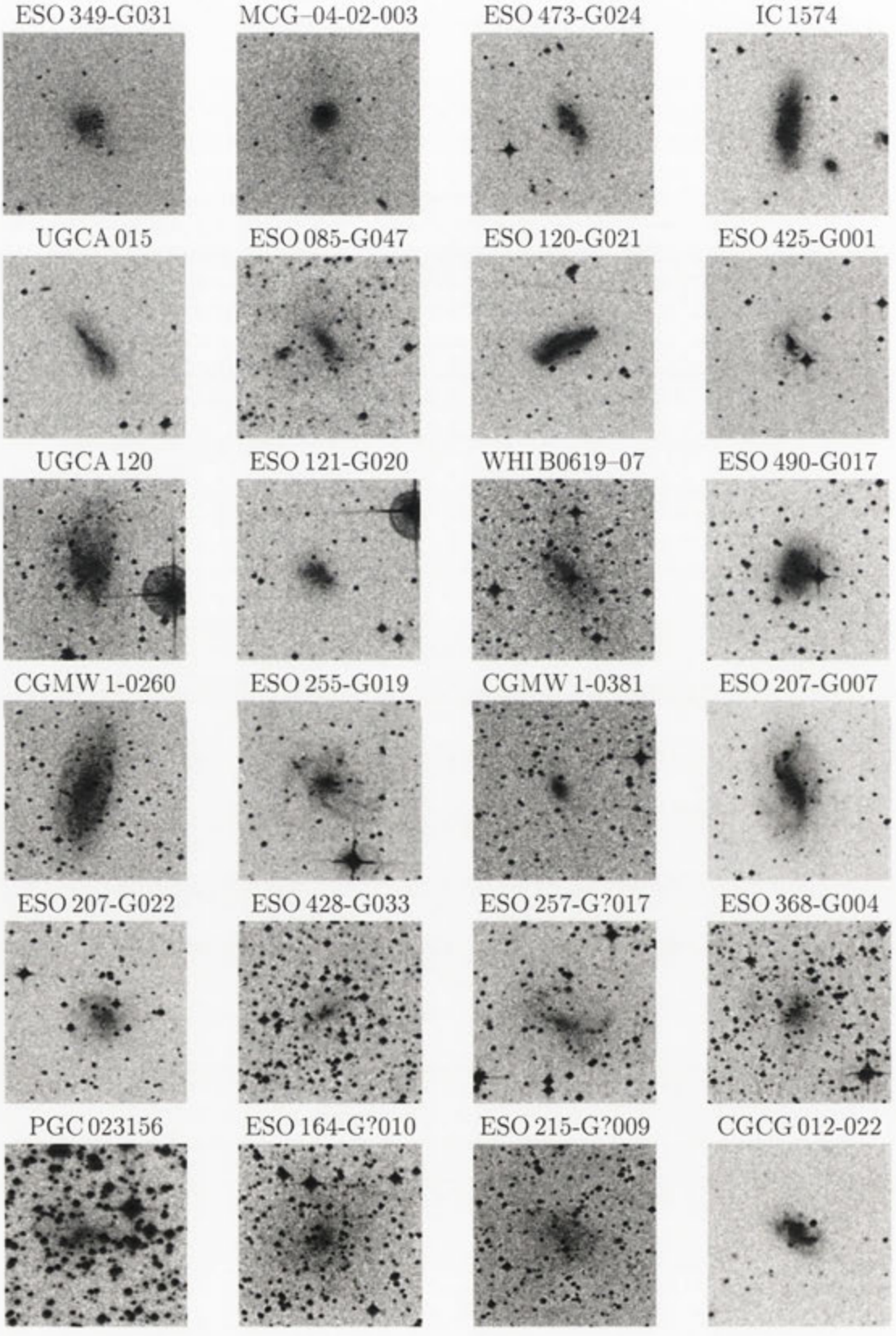

Fig. 3.4: Gallery of DSS images for our 41 sample galaxies. All images are $4' \times 4'$, with the galaxy's optical name above.

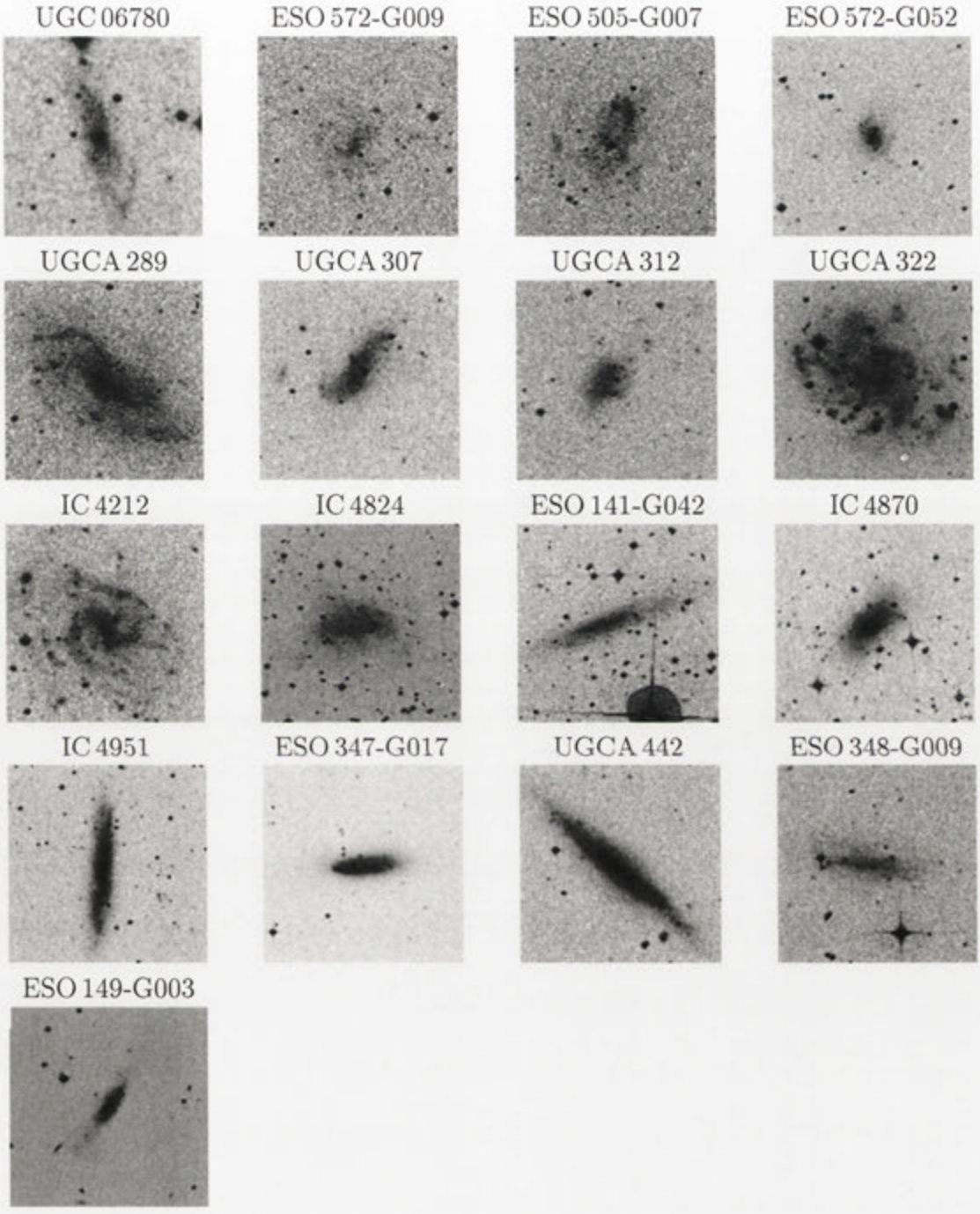

Fig. 3.4: continued

appears to have an unusual irregular morphology, with several large clumps around the central region (with no clear centre) and some ragged spiral arm-like structures. There is another galaxy approximately 7′ to the north, ESO 505-G008, which is potentially a companion to ESO 505-G007. Meanwhile IC 4212 ($\sim 23\ \mathcal{M}_{\odot}/L_{\odot,\mathrm{B}}$) is very clearly a near face on spiral galaxy with two bright, loosely wound arms, several fainter arms, and a small central bar. Both of these galaxies are relatively far away compared to the other objects in our sample. On the other had, ESO 215-G?009 is much closer at about 4.2 Mpc. With $\mathcal{M}_{\mathrm{HI}}/L_{\mathrm{B}} = 24 \pm 12\ \mathcal{M}_{\odot}/L_{\odot,\mathrm{B}}$, the second highest ratio from the BGC, in the optical this galaxy appears as little more than a faint fuzzy patch on the sky (hence the "G?" in its name). A dwarf irregular galaxy with a fairly featureless morphology (there are some potential H II regions around it) it appears to have no nearby neighbouring galaxies either. ESO 215-G?009 was by far the most promising galaxy in the sample, and its isolation and proximity to the Milky Way make it a good candidate for detailed follow-up observations.

Table 3.1. Summary of the Basic Properties for the 41 Sample Galaxies.

Name	Alt. Name	α (J2000.0)	δ (J2000.0)	l	b	A_B (mag)
(1)	(2)	(3)	(4)	(5)	(6)	(7)
ESO 349-G031	Sculptor DIG	$00^h\,08^m\,13\overset{s}{.}0$	$-34°\,34'\,42''$	$351\overset{\circ}{.}6$	$-78\overset{\circ}{.}1$	0.05 ± 0.01
MCG–04-02-003	PGC 001242	$00^h\,19^m\,11\overset{s}{.}4$	$-22°\,40'\,06''$	$62\overset{\circ}{.}5$	$-81\overset{\circ}{.}4$	0.08 ± 0.01
ESO 473-G024	AM 0028–230	$00^h\,31^m\,22\overset{s}{.}5$	$-22°\,45'\,57''$	$75\overset{\circ}{.}7$	$-83\overset{\circ}{.}7$	0.08 ± 0.01
IC 1574	DDO 226	$00^h\,43^m\,03\overset{s}{.}0$	$-22°\,14'\,49''$	$101\overset{\circ}{.}2$	$-84\overset{\circ}{.}7$	0.07 ± 0.01
UGCA 015	DDO 006	$00^h\,49^m\,49\overset{s}{.}0$	$-21°\,00'\,54''$	$118\overset{\circ}{.}9$	$-83\overset{\circ}{.}9$	0.07 ± 0.01
ESO 085-G047	AM 0507–630	$05^h\,07^m\,43\overset{s}{.}0$	$-62°\,59'\,30''$	$272\overset{\circ}{.}8$	$-35\overset{\circ}{.}7$	0.11 ± 0.02
ESO 120-G021	AM 0555–590	$05^h\,53^m\,14\overset{s}{.}0$	$-59°\,03'\,58''$	$267\overset{\circ}{.}7$	$-30\overset{\circ}{.}4$	0.20 ± 0.03
ESO 425-G001		$06^h\,00^m\,10\overset{s}{.}0$	$-31°\,47'\,16''$	$237\overset{\circ}{.}8$	$-24\overset{\circ}{.}1$	0.17 ± 0.03
UGCA 120	ESO 556-G002	$06^h\,11^m\,16\overset{s}{.}0$	$-21°\,35'\,56''$	$228\overset{\circ}{.}4$	$-18\overset{\circ}{.}2$	0.33 ± 0.05
ESO 121-G020	KKs 19	$06^h\,15^m\,54\overset{s}{.}2$	$-57°\,43'\,32''$	$266\overset{\circ}{.}5$	$-27\overset{\circ}{.}3$	0.17 ± 0.03
WHI B0619–07[a]		$06^h\,22^m\,12\overset{s}{.}0$	$-07°\,50'\,21''$	$216\overset{\circ}{.}7$	$-10\overset{\circ}{.}0$	2.65 ± 0.42
ESO 490-G017	MCG–04-16-013	$06^h\,37^m\,57\overset{s}{.}0$	$-26°\,00'\,01''$	$235\overset{\circ}{.}1$	$-14\overset{\circ}{.}3$	0.33 ± 0.05
CGMW 1-0260	IRAS 06357–1458	$06^h\,38^m\,00\overset{s}{.}0$	$-15°\,01'\,29''$	$224\overset{\circ}{.}9$	$-9\overset{\circ}{.}7$	1.46 ± 0.23
ESO 255-G019	UKS 0644–474	$06^h\,45^m\,48\overset{s}{.}0$	$-47°\,31'\,50''$	$256\overset{\circ}{.}8$	$-20\overset{\circ}{.}6$	0.36 ± 0.05
CGMW 1-0381	KKSG 9	$06^h\,46^m\,56\overset{s}{.}0$	$-17°\,56'\,27''$	$228\overset{\circ}{.}5$	$-9\overset{\circ}{.}0$	1.83 ± 0.29
ESO 207-G007	AM 0649–520	$06^h\,50^m\,39\overset{s}{.}0$	$-52°\,08'\,30''$	$261\overset{\circ}{.}8$	$-21\overset{\circ}{.}2$	0.33 ± 0.05
ESO 207-G022	KK 58	$07^h\,09^m\,10\overset{s}{.}0$	$-51°\,28'\,01''$	$262\overset{\circ}{.}1$	$-18\overset{\circ}{.}3$	0.56 ± 0.09
ESO 428-G033		$07^h\,25^m\,49\overset{s}{.}5$	$-30°\,55'\,09''$	$244\overset{\circ}{.}2$	$-6\overset{\circ}{.}9$	1.10 ± 0.18
ESO 257-G?017	AM 0726–453	$07^h\,27^m\,33\overset{s}{.}0$	$-45°\,41'\,04''$	$257\overset{\circ}{.}8$	$-13\overset{\circ}{.}2$	0.62 ± 0.10
ESO 368-G004	KKs 22	$07^h\,32^m\,54\overset{s}{.}0$	$-35°\,29'\,19''$	$249\overset{\circ}{.}0$	$-7\overset{\circ}{.}7$	1.94 ± 0.31
PGC 023156	AM 0813–284	$08^h\,15^m\,42\overset{s}{.}0$	$-28°\,51'\,21''$	$248\overset{\circ}{.}0$	$3\overset{\circ}{.}4$	1.70 ± 0.27
ESO 164-G?010	UKS 0824–538	$08^h\,26^m\,12\overset{s}{.}0$	$-54°\,02'\,00''$	$269\overset{\circ}{.}9$	$-9\overset{\circ}{.}2$	1.55 ± 0.25
ESO 215-G?009	KKs 40	$10^h\,57^m\,29\overset{s}{.}4$	$-48°\,10'\,40''$	$284\overset{\circ}{.}1$	$10\overset{\circ}{.}5$	0.95 ± 0.15
CGCG 012-022	MCG+00-30-011	$11^h\,33^m\,45\overset{s}{.}0$	$-03°\,26'\,16''$	$268\overset{\circ}{.}4$	$54\overset{\circ}{.}2$	0.15 ± 0.02
UGC 06780	MCG+00-30-024	$11^h\,48^m\,50\overset{s}{.}0$	$-02°\,01'\,56''$	$273\overset{\circ}{.}1$	$57\overset{\circ}{.}2$	0.09 ± 0.01
ESO 572-G009	PGC 037270	$11^h\,53^m\,23\overset{s}{.}0$	$-18°\,10'\,00''$	$284\overset{\circ}{.}1$	$42\overset{\circ}{.}6$	0.16 ± 0.03
ESO 505-G007	AM 1200–251	$12^h\,03^m\,31\overset{s}{.}0$	$-25°\,28'\,36''$	$289\overset{\circ}{.}5$	$36\overset{\circ}{.}2$	0.36 ± 0.06
ESO 572-G052	PGC 038364	$12^h\,06^m\,03\overset{s}{.}0$	$-21°\,11'\,54''$	$289\overset{\circ}{.}0$	$40\overset{\circ}{.}5$	0.26 ± 0.04
UGCA 289	MCG–01-32-028	$12^h\,35^m\,38\overset{s}{.}0$	$-07°\,52'\,35''$	$296\overset{\circ}{.}1$	$54\overset{\circ}{.}8$	0.12 ± 0.02
UGCA 307	MCG–02-33-047	$12^h\,53^m\,57\overset{s}{.}0$	$-12°\,06'\,30''$	$303\overset{\circ}{.}9$	$50\overset{\circ}{.}8$	0.24 ± 0.04
UGCA 312	PGC 044549	$12^h\,59^m\,06\overset{s}{.}0$	$-12°\,13'\,40''$	$305\overset{\circ}{.}9$	$50\overset{\circ}{.}6$	0.18 ± 0.03
UGCA 322	MCG+00-33-028	$13^h\,04^m\,30\overset{s}{.}0$	$-03°\,34'\,22''$	$309\overset{\circ}{.}3$	$59\overset{\circ}{.}1$	0.13 ± 0.02
IC 4212	UGCA 333	$13^h\,12^m\,03\overset{s}{.}0$	$-06°\,59'\,29''$	$312\overset{\circ}{.}0$	$55\overset{\circ}{.}5$	0.19 ± 0.03
IC 4824	ESO 141-G033	$19^h\,13^m\,14\overset{s}{.}0$	$-62°\,05'\,18''$	$334\overset{\circ}{.}2$	$-26\overset{\circ}{.}3$	0.24 ± 0.04
ESO 141-G042	UKS 1911–624	$19^h\,16^m\,11\overset{s}{.}0$	$-62°\,21'\,42''$	$334\overset{\circ}{.}0$	$-26\overset{\circ}{.}7$	0.25 ± 0.04
IC 4870	ESO 105-IG011	$19^h\,37^m\,37\overset{s}{.}0$	$-65°\,48'\,40''$	$330\overset{\circ}{.}3$	$-29\overset{\circ}{.}3$	0.49 ± 0.08
IC 4951	PGC 064181	$20^h\,09^m\,31\overset{s}{.}0$	$-61°\,50'\,47''$	$334\overset{\circ}{.}9$	$-32\overset{\circ}{.}9$	0.17 ± 0.03
ESO 347-G017	MCG–06-51-005	$23^h\,26^m\,57\overset{s}{.}0$	$-37°\,20'\,45''$	$357\overset{\circ}{.}8$	$-69\overset{\circ}{.}5$	0.07 ± 0.01
UGCA 442	ESO 471-G006	$23^h\,43^m\,45\overset{s}{.}0$	$-31°\,57'\,29''$	$10\overset{\circ}{.}7$	$-74\overset{\circ}{.}5$	0.07 ± 0.01
ESO 348-G009	AM 2346–380	$23^h\,49^m\,23\overset{s}{.}5$	$-37°\,46'\,19''$	$349\overset{\circ}{.}8$	$-73\overset{\circ}{.}2$	0.06 ± 0.01
ESO 149-G003	AM 2349–525	$23^h\,52^m\,02\overset{s}{.}0$	$-52°\,34'\,43''$	$322\overset{\circ}{.}5$	$-62\overset{\circ}{.}3$	0.06 ± 0.01

(1) The Most commonly used name of this galaxy (the identified optical counterpart name).
(2) gives an alternative (optical) name where available.
(3) J2000.0 right ascension as given in RC3 (de Vaucouleurs et al., 1991).
(4) J2000.0 declination as given in RC3 (de Vaucouleurs et al., 1991).
(5) Galactic longitude.
(6) Galactic latitude.
(7) SFD98 Galactic dust extinction value in the B band.

[a]Galaxy misidentified as CGMW 1-0080 in BGC

Table 3.2. Summary of the BGC H I Properties for the 41 Sample Galaxies.

Name	HIPASS Name	S_{peak} (Jy)	F_{HI} (Jy km s^{-1})	v_{sys} (km s^{-1})	w_{50} (km s^{-1})	w_{20} (km s^{-1})	v_{LG} (km s^{-1})	D (Mpc)	$\log_{10}(\mathcal{M}_{HI})$ ($\log_{10}(\mathcal{M}_{\odot})$)
(1)	(2)	(3)	(4)	(5)	(6)	(7)	(8)	(9)	(10)
ESO 349-G031	HIPASS J0008–34	0.166 ± 0.016	5.8 ± 1.6	221 ± 6	30	79	212	2.8	7.04
MCG–04-02-003	HIPASS J0019–22	0.191 ± 0.016	16.0 ± 2.5	669 ± 3	119	131	709	9.5	8.53
ESO 473-G024	HIPASS J0031–22	0.160 ± 0.016	7.2 ± 1.8	540 ± 4	45	61	572	7.6	7.99
IC 1574	HIPASS J0043–22	0.146 ± 0.015	5.4 ± 1.5	363 ± 4	39	55	390	5.2	7.54
UGCA 015	HIPASS J0049–20	0.144 ± 0.018	3.9 ± 1.5	294 ± 4	25	41	322	4.3	7.23
ESO 085-G047	HIPASS J0507–63	0.238 ± 0.019	13.4 ± 2.4	1465 ± 3	61	75	1222	16.3	8.92
ESO 120-G021	HIPASS J0553–59	0.135 ± 0.016	14.4 ± 2.7	1308 ± 5	120	141	1049	14.0	8.82
ESO 425-G001	HIPASS J0600–31	0.120 ± 0.015	10.0 ± 2.4	1353 ± 6	90	117	1121	14.9	8.72
UGCA 120	HIPASS J0611–21	0.394 ± 0.023	32.5 ± 3.6	860 ± 3	87	112	647	8.6	8.76
ESO 121-G020	HIPASS J0615–57	0.210 ± 0.021	14.1 ± 2.9	577 ± 5	65	96	311	4.1	7.76
WHI B0619–07[a]	HIPASS J0622–07	0.387 ± 0.023	51.9 ± 4.6	754 ± 2	156	176	578	7.7	8.86
ESO 490-G017	HIPASS J0638–26	0.163 ± 0.025	7.9 ± 3.0	503 ± 6	47	68	264	3.5	7.37
CGMW 1-0260	HIPASS J0638–15	0.151 ± 0.018	16.5 ± 3.1	748 ± 5	187	206	539	7.2	8.30
ESO 255-G019	HIPASS J0645–47	0.291 ± 0.023	28.5 ± 3.9	1058 ± 3	129	143	785	10.5	8.87
CGMW 1-0381	HIPASS J0646–17	0.264 ± 0.037	31.4 ± 6.9	693 ± 6	182	202	471	6.3	8.47
ESO 207-G007	HIPASS J0650–52	0.188 ± 0.018	22.7 ± 3.3	1083 ± 3	149	165	806	10.7	8.79
ESO 207-G022	HIPASS J0709–51	0.175 ± 0.016	7.3 ± 1.7	1059 ± 3	42	59	777	10.4	8.27
ESO 428-G033	HIPASS J0725–30B	0.161 ± 0.018	12.8 ± 2.7	1727 ± 4	96	111	1459	19.5	9.06
ESO 257-G?017	HIPASS J0727–45	0.190 ± 0.018	16.3 ± 2.8	1016 ± 4	97	115	731	9.7	8.56
ESO 368-G004	HIPASS J0732–35	0.252 ± 0.021	15.1 ± 2.8	1397 ± 4	61	83	1119	14.9	8.90
PGC 023156	HIPASS J0815–28	0.143 ± 0.021	21.4 ± 4.4	1705 ± 10	162	215	1427	19.0	9.26
ESO 164-G?010	HIPASS J0826–54	0.135 ± 0.017	16.6 ± 3.3	1051 ± 4	147	157	755	10.1	8.60
ESO 215-G?009	HIPASS J1057–48	1.607 ± 0.084	104.4 ± 11.5	598 ± 2	67	83	312	4.2	8.63
CGCG 012-022	HIPASS J1133–03	0.139 ± 0.013	14.2 ± 2.2	1609 ± 4	135	153	1433	19.1	9.09
UGC 06780	HIPASS J1148–02	0.170 ± 0.016	26.6 ± 3.5	1730 ± 3	224	236	1568	20.9	9.44
ESO 572-G009	HIPASS J1153–18	0.170 ± 0.016	8.5 ± 1.9	1745 ± 3	42	57	1531	20.4	8.92
ESO 505-G007	HIPASS J1203–25	0.296 ± 0.023	20.5 ± 3.2	1785 ± 4	67	95	1557	20.8	9.32
ESO 572-G052	HIPASS J1206–21	0.165 ± 0.015	4.8 ± 1.4	1794 ± 4	38	56	1578	21.0	8.70
UGCA 289	HIPASS J1235–07	0.176 ± 0.016	26.1 ± 3.2	986 ± 3	165	184	831	11.1	8.88
UGCA 307	HIPASS J1253–12	0.382 ± 0.025	27.2 ± 3.6	824 ± 3	68	97	667	8.9	8.71
UGCA 312	HIPASS J1259–12	0.185 ± 0.015	13.9 ± 2.2	1308 ± 5	73	114	1154	15.4	8.89
UGCA 322	HIPASS J1304–03	0.397 ± 0.025	38.2 ± 4.2	1362 ± 3	110	132	1243	16.6	9.39
IC 4212	HIPASS J1311–06	0.346 ± 0.023	47.5 ± 4.6	1484 ± 2	161	178	1358	18.1	9.57
IC 4824	HIPASS J1913–62	0.270 ± 0.020	17.0 ± 2.7	947 ± 3	68	87	830	11.1	8.69

Table 3.2 (cont'd)

Name	HIPASS Name	S_{peak} (Jy)	F_{HI} (Jy km s^{-1})	v_{sys} (km s^{-1})	w_{50} (km s^{-1})	w_{20} (km s^{-1})	v_{LG} (km s^{-1})	D (Mpc)	$\log_{10}(\mathcal{M}_{HI})$ ($\log_{10}(\mathcal{M}_{\odot})$)
(1)	(2)	(3)	(4)	(5)	(6)	(7)	(8)	(9)	(10)
ESO 141-G042	HIPASS J1916–62	0.142 ± 0.017	13.2 ± 2.7	909 ± 4	105	123	791	10.5	8.54
IC 4870	HIPASS J1937–65	0.330 ± 0.022	24.7 ± 3.2	879 ± 3	76	98	749	10.0	8.76
IC 4951	HIPASS J2009–61	0.261 ± 0.018	23.9 ± 2.9	814 ± 2	119	135	707	9.4	8.70
ESO 347-G017	HIPASS J2326–37	0.133 ± 0.013	8.4 ± 1.7	692 ± 4	65	83	688	9.2	8.22
UGCA 442	HIPASS J2343–31	0.557 ± 0.033	50.1 ± 5.3	267 ± 2	94	112	282	3.8	8.22
ESO 348-G009	HIPASS J2349–37	0.169 ± 0.015	13.4 ± 2.2	648 ± 4	81	109	633	8.4	8.35
ESO 149-G003	HIPASS J2352–52	0.158 ± 0.014	6.9 ± 1.6	576 ± 5	39	70	491	6.5	7.84

(1) Optical galaxy name (as in Table 3.1).
(2) HIPASS designation.
(3) H I peak flux density.
(4) Total integrated H I flux density.
(5) Systemic heliocentric velocity of the H I line.
(6) H I line width at 50% of the peak flux density.
(7) H I line width at 20% of the peak flux density.
(8) Velocity relative to the barycentre of the Local Group (Local Group velocity) derived from systemic velocity.
(9) Approximate distance derived from the Local Group velocity (using $H_0 = 75$ km s^{-1} Mpc^{-1}).
(10) $\log_{10}$ of the H I mass (derived from the total flux density and the distance).

[a]Galaxy misidentified as CGMW 1-0080 in BGC

Table 3.3. Summary of the Optical Properties Returned by LEDA for the 41 Sample Galaxies.

Name	Morphology	m_B (mag)	$\langle\mu\rangle_{eff,B}$ (mag arcsec^{-2})	$v_{sys,opt}$ (km s^{-1})	Inclination (degrees)	A_B (mag)
(1)	(2)	(3)	(4)	(5)	(6)	(7)
ESO 349-G031	Irr	15.6 ± 0.2	24.2 ± 0.3		56	0.05 ± 0.01
MCG-04-02-003	Sm	15.8 ± 0.2		670 ± 60	30	0.08 ± 0.01
ESO 473-G024	Irr	16.2 ± 0.2	24.6 ± 0.3	540 ± 60	86	0.08 ± 0.01
IC 1574	Irr	14.6 ± 0.3	24.1 ± 0.4	360 ± 60	90	0.07 ± 0.01
UGCA 015	Irr	15.2 ± 0.2	24.4 ± 0.3		90	0.07 ± 0.01
ESO 085-G047	SBm	15.3 ± 0.4	24.7 ± 0.3	1470 ± 40	70	0.11 ± 0.02
ESO 120-G021	Irr	16.0 ± 0.2	24.9 ± 0.3	1360 ± 60	71	0.20 ± 0.03
ESO 425-G001	Sbc	15.9 ± 0.5	24.7 ± 0.3		57	0.17 ± 0.03
UGCA 120	Irr	14.4 ± 0.2	25.1 ± 0.3		36	0.33 ± 0.05
ESO 121-G020	Irr	17.0 ± 0.4	24.1 ± 0.3		76	0.17 ± 0.03
CGMW 1-0080[a]	Sc	18.2 ± 0.1		800 ± 60	54	2.65 ± 0.42
ESO 490-G017	Irr	13.8 ± 0.2	22.4 ± 0.3	500 ± 60	34	0.33 ± 0.05
CGMW 1-0260	Sd	14.3 ± 0.1		750 ± 40	90	1.46 ± 0.23
ESO 255-G019	Sm	15.9 ± 0.8	24.9 ± 0.3		42	0.36 ± 0.05
CGMW 1-0381	Sc	16.3 ± 0.1			57	1.83 ± 0.29
ESO 207-G007	SBm	14.5 ± 0.2	23.8 ± 0.3		72	0.33 ± 0.05
ESO 207-G022	Irr	15.3 ± 0.2			38	0.56 ± 0.09
ESO 428-G033	Sbc	17.9 ± 0.5	25.1 ± 0.3		58	1.10 ± 0.18
ESO 257-G?017	Sm	16.9 ± 0.2	25.3 ± 0.3	1010 ± 60	67	0.62 ± 0.10
ESO 368-G004	Irr	16.7 ± 1.0			60	1.94 ± 0.31
PGC 023156	SBm	17.5 ± 0.1		1700 ± 60	79	1.70 ± 0.27
ESO 164-G?010	Sm	16.9 ± 0.3		1050 ± 60	33	1.55 ± 0.25
ESO 215-G?009	Irr	16.4 ± 0.4			63	0.95 ± 0.15
CGCG 012-022	SBd	15.5 ± 0.3		1620 ± 60	57	0.15 ± 0.02
UGC 06780	Scd	15.3 ± 0.2		1740 ± 40	67	0.09 ± 0.01
ESO 572-G009	Irr	17.4 ± 0.2	25.3 ± 0.3		38	0.16 ± 0.03
ESO 505-G007	Irr	17.7 ± 0.2			48	0.36 ± 0.06
ESO 572-G052	Irr	15.9 ± 0.1	23.8 ± 0.3		51	0.26 ± 0.04
UGCA 289	SBd	14.9 ± 0.3		990 ± 60	80	0.12 ± 0.02
UGCA 307	Irr	14.9 ± 0.3		820 ± 60	90	0.24 ± 0.04
UGCA 312	Irr	15.0 ± 0.3			52	0.18 ± 0.03
UGCA 322	SBd	14.7 ± 0.2		1350 ± 40	49	0.13 ± 0.02
IC 4212	SBc	16.4 ± 1.1		1490 ± 60	47	0.19 ± 0.03
IC 4824	Irr	16.8 ± 0.2	22.8 ± 0.3	1020 ± 70	90	0.24 ± 0.04
ESO 141-G042	SBm	14.4 ± 0.2	24.3 ± 0.3	1010 ± 80	90	0.25 ± 0.04
IC 4870	Irr	14.4 ± 0.4	21.4 ± 0.3	870 ± 40	68	0.49 ± 0.08
IC 4951	SBd	13.9 ± 0.2	22.3 ± 0.3	800 ± 40	90	0.17 ± 0.03
ESO 347-G017	SBm	14.7 ± 0.8	24.1 ± 0.3	690 ± 60	90	0.07 ± 0.01
UGCA 442	SBm	13.8 ± 0.3	22.9 ± 0.3	230 ± 50	90	0.07 ± 0.01
ESO 348-G009	Irr	16.7 ± 0.7			90	0.06 ± 0.01
ESO 149-G003	Irr	15.0 ± 0.1	23.7 ± 0.3	590 ± 40	90	0.06 ± 0.01

(1) Optical galaxy name (as in Table 3.1).
(2) Morphological type assigned to the galaxy.
(3) Total apparent B band magnitude.
(4) Mean effective surface brightness in the B band (the average surface brightness out to the half light radius).
(5) Heliocentric radial velocity (systemic velocity) from optical measurement.
(6) Inclination of the galaxies disk (the angle between the line of sight and the polar axis).
(7) SFD98 Galactic dust extinction value in the B band.
No extinction correction was applied to either m_B or $\langle\mu\rangle_{eff,B}$.

[a]Incorrect optical counterpart

Table 3.4. Summary of Properties Derived from the BGC and LEDA Data for the 41 Sample Galaxies.

Name	$\mathcal{M}_{HI}$	M_B	(L_B)	$\mathcal{M}_{HI}/L_B$	Sample
	($\times 10^7\ \mathcal{M}_\odot$)	mag	($\times 10^7\ L_{\odot,B}$)	$\mathcal{M}_\odot/L_{\odot,B}$	
(1)	(2)	(3)	(4)	(5)	(6)
ESO 349-G031	1.1 ± 0.3	−11.8 ± 0.2	0.82 ± 0.15	1.4 ± 0.6	low
MCG–04-02-003	34 ± 5	−14.1 ± 0.2	6.8 ± 1.3	4.8 ± 1.6	high
ESO 473-G024	10 ± 2	−13.3 ± 0.2	3.3 ± 0.6	3.0 ± 1.3	low
IC 1574	3.4 ± 0.9	−14.1 ± 0.3	6.8 ± 1.9	0.5 ± 0.3	low
UGCA 015	1.7 ± 0.7	−13.0 ± 0.2	2.5 ± 0.5	0.7 ± 0.4	low
ESO 085-G047	84 ± 15	−15.9 ± 0.4	36 ± 13	2.4 ± 1.3	low
ESO 120-G021	67 ± 12	−14.9 ± 0.2	14 ± 3	4.6 ± 1.7	high
ESO 425-G001	52 ± 13	−15.1 ± 0.5	17 ± 8	3.0 ± 2.1	high
UGCA 120	57 ± 6	−15.7 ± 0.2	30 ± 5	2.0 ± 0.6	low
ESO 121-G020	5.6 ± 1.2	−11.3 ± 0.4	0.52 ± 0.19	11 ± 6	high
CGMW 1-0080[a]	73 ± 6	−13.9 ± 0.4	5 ± 2	13 ± 6	high
ESO 490-G017	2.3 ± 0.9	−14.3 ± 0.2	8.2 ± 1.5	0.28 ± 0.15	low
CGMW 1-0260	20 ± 4	−16.4 ± 0.3	56 ± 16	0.35 ± 0.16	low
ESO 255-G019	74 ± 10	−14.6 ± 0.8	11 ± 8	7 ± 6	high
CGMW 1-0381	29 ± 6	−14.5 ± 0.3	10 ± 3	2.9 ± 1.4	low
ESO 207-G007	61 ± 9	−16.0 ± 0.2	39 ± 7	1.5 ± 0.5	low
ESO 207-G022	19 ± 4	−15.3 ± 0.2	21 ± 4	0.9 ± 0.4	low
ESO 428-G033	115 ± 24	−14.7 ± 0.5	12 ± 5	10 ± 7	high
ESO 257-G?017	36 ± 6	−13.7 ± 0.2	4.7 ± 0.9	8 ± 3	high
ESO 368-G004	79 ± 15	−16.1 ± 1.0	∼ 43	∼ 1.8	low
PGC 023156	180 ± 40	−15.6 ± 0.3	27 ± 7	7 ± 3	high
ESO 164-G?010	40 ± 8	−14.7 ± 0.4	12 ± 4	3.4 ± 1.9	high
ESO 215-G?009	43 ± 5	−12.6 ± 0.4	1.7 ± 0.6	24 ± 12	high
CGCG 012-022	122 ± 19	−16.0 ± 0.3	39 ± 11	3.0 ± 1.3	high
UGC 06780	270 ± 40	−16.4 ± 0.2	56 ± 10	4.8 ± 1.5	high
ESO 572-G009	83 ± 19	−14.3 ± 0.2	8.2 ± 1.5	10 ± 4	high
ESO 505-G007	210 ± 30	−14.2 ± 0.2	7.4 ± 1.4	27 ± 9	high
ESO 572-G052	50 ± 15	−16.0 ± 0.1	39 ± 4	1.3 ± 0.5	low
UGCA 289	76 ± 9	−15.5 ± 0.3	25 ± 7	3.2 ± 1.3	high
UGCA 307	51 ± 7	−15.1 ± 0.3	17 ± 5	3.0 ± 1.2	high
UGCA 312	78 ± 12	−16.1 ± 0.3	43 ± 12	1.8 ± 0.8	low
UGCA 322	250 ± 30	−16.5 ± 0.2	62 ± 11	4.0 ± 1.2	high
IC 4212	370 ± 40	−15.0 ± 1.1	∼ 16	∼ 23	high
IC 4824	49 ± 8	−13.7 ± 0.2	4.7 ± 0.9	10 ± 4	high
ESO 141-G042	34 ± 7	−16.0 ± 0.2	39 ± 7	0.9 ± 0.3	low
IC 4870	58 ± 8	−16.1 ± 0.4	43 ± 16	1.3 ± 0.7	low
IC 4951	50 ± 6	−16.1 ± 0.2	43 ± 8	1.1 ± 0.3	low
ESO 347-G017	17 ± 3	−15.2 ± 0.8	19 ± 14	0.9 ± 0.8	low
UGCA 442	17.1 ± 1.8	−14.2 ± 0.3	7.4 ± 2.0	2.3 ± 0.9	low
ESO 348-G009	22 ± 4	−13.0 ± 0.7	2.5 ± 1.6	9 ± 7	high
ESO 149-G003	6.9 ± 1.6	−14.1 ± 0.1	6.8 ± 0.6	1.0 ± 0.3	low

(1) Optical galaxy name (as in Table 3.1).
(2) H I mass of the galaxy as given by Eqn. 3.1 (the $\log_{10}$ of which is listed in the BGC).
(3) Absolute B band magnitude as given by Eqn. 3.4.
(4) B band luminosity as given by Eqn. 3.2.
(5) H I mass-to-light ratio as given by Eqn. 3.3.
(6) Sample to which the galaxy belongs ("high" for the high $\mathcal{M}_{HI}/L_B$ galaxies, "low" for the control sample).

[a]Incorrect optical counterpart

4. OBSERVATIONS AND DATA REDUCTION

In order to explore the physical nature of any galaxy it is a necessity to extend observations beyond the optical regime. This is particularly so for any galaxy where neutral hydrogen gas makes up a significant proportion of the baryons, such as in our sample of high H I mass-to-light ratio galaxies. The combination of the BGC and LEDA data gives us a good starting point for follow up investigations. However, many of these galaxies were only observed for the first time in H I as part of the HIPASS observations, and optical information on them is often very limited or of poor quality. We wish to extend our knowledge of both the optical and H I for our sample galaxies. In this chapter we will outline the observations done for this thesis project and the data reduction process.

4.1 Observing Program

The optical observations available in LEDA are generally shallow, inhomogeneous, and are the weighted mean of several results which may be in disagreement. Many come from photographic measurements, or from digitised scans of photographic plates, the accuracy of which is much less than is possible with modern CCD photometry. In addition, only one photometric band, B where photographic plates are most sensitive, is widely available for our sample galaxies (only four galaxies have U and V band observations listed in LEDA, and two others have I band observations). We need deep, multiband optical photometry using CCDs in order to obtain improved photometric measurements. With these we can confirm $\mathcal{M}_{\rm HI}/L_{\rm B}$, examine in detail the structure of the galaxy's stellar component, and explore the recent star formation history of the galaxy.

The BGC H I measurements of H I flux density and other parameters are for the most part very reliable, although a the occational individual results may be affected by such things as contamination from neighbours. As the HIPASS observations were performed on a single dish telescope the spatial resolution is relatively large compared to the optical size of most galaxies ($\sim$15.5). This allowed the survey to cover the whole Southern sky, but means we have little information on the spatial structure of the galaxies in H I, most of which are far smaller than the Parkes beam. Also, there may be other galaxies within the Parkes beam which may contribute to the H I flux density measurements, either in part or in full. There may even be cases of sources which do not correspond to the optical counterpart listed in the

Fig. 4.1: The ANU 2.3-meter Telescope at Siding Spring Observatory near Coonabarabran, New South Wales, Australia. This image was taken by the author.

BGC (such as WHI B0619–07, originally identified with a background galaxy, see Chapter 3). The velocity resolution is also limited in order to accommodate the the limited number of channels over the wide bandpass of the survey. So in the radio we would like to have H I line observations with both higher spatial and velocity resolution in order to confirm the BGC results, verify that the optical counterpart is the correct galaxy and the only source of H I for that measurement, look at the spatial structure of the neutral gas and compare it to the optical structure, and where we have sufficient resolution produce rotation curves.

Two telescopes were used for observations of our sample galaxies. Optical observations were obtained with the Australian National University (ANU) 2.3-meter Telescope at the Siding Spring Observatory near Coonabarabran, New South Wales, Australia (occasionally called the Advanced Technology Telescope, ATT, but which we will refer to simply as the 2.3m). The telescope is shown in Fig. 4.1. The 2.3m is a single mirror telescope with two Nasmyth foci (with an optical imager at one and a spectrograph at the other) and a Cassergrain focus (which usually holds an infrared instrument). The main observations we obtained on the 2.3m were deep optical broad band photometry in four bands (*BVRI*, between 30 and 60 minutes in each band).

Radio observations were obtained with the Australia Telescope Compact Array (ATCA) at the Paul Wild Observatory outside Narrabri, New South Wales, Australia, which is shown in Fig. 4.2. The ATCA is an interferometer with an array of six 22-meter dishes, five of which move along a 3km east-west track, the sixth siting in a fixed position 3km to the west of the end of the track. Recently (in 2002) a short northern spur track was added to the east-west track. On the

Fig. 4.2: The Australia Telescope Compact Array at the Paul Wild Observatory outside Narrabri, New South Wales, Australia. This image was taken by the author during the first observing period using the Northern Spur track in August 2002 (the birds are galahs).

ATCA we initially obtained H I snapshot observations for 40 galaxies, all except ESO 215-G?009. The snapshots consisted of observing the galaxies in small groups (four to six galaxies per group) and observing each for a total of approximately 2 hours spread over a 12 hour observation (spending 10 minutes on each galaxy before moving to the next, and then repeating for the observing time). The snapshots were done on relatively short array configurations. Approximately half the sample (21 galaxies) were observed on purely east-west configurations (EW352 and EW367B). For galaxies north of $\delta \sim -30°$ the beam shape on east-west arrays becomes highly elongated and gives poor resolution in the north-south direction. So for the remaining 19 galaxies which were all between $\delta \sim -30°$ and 0° we used hybrid array configurations which have two of the antennas on the northern spur track (H75B and H168B). These configurations have the disadvantage of having a large beam in H I due to the short baselines.

For ESO 215-G?009, which was our most promising candidate, we decided to begin with a full 12 hour observation of the galaxy. This was also done on a short array (EW352), but was later extended to two additional 12 hour runs on arrays with longer baselines (750A and 6A). The full details of the observations for this galaxy are in Chapter 6. After the snapshots, full 12 hour observations were also done on two arrays for a further three galaxies (ESO 121-G020, ESO 428-G033, and ESO 348-G009 on 750D and 1.5B), and additional observations were obtained for another three (MCG–04-02-003, ESO 505-G007, and IC 4212 on hybrid arrays) when the opportunity presented itself. Table 4.1 summarises the observing details for each of the 41 galaxies in both optical (columns (2) to (4)) and radio (columns

(5) to (8)).

4.2 Optical Observations and Reduction

Optical *BVRI* band (Cousins filters) images were taken as a series of 300 s or 600 s exposures during ten observing runs between April 2002 and February 2004 using the Nasmyth Imager (SITe 1124 × 1024 thinned CCD). The imager has a circular field of view with a diameter of 6.′62 and a pixel size of 0.″59. Most observations were taken at low airmass. Twilight sky flat fields in all bands and bias images were obtained at the time of observation. Several Landolt (1992) standard stars were taken together with shallow 120 s *BVRI* images of the galaxy field on photometric nights to perform the photometric calibration of the deeper images. Unfortunately the calibration for four galaxies (CGMW 1-0260, CGMW 1-0381, ESO 347-G017, and UGCA 442) was not possible as the calibration images taken were affected by non-photometric conditions (light cirrus clouds) at the time of observations as a careful analysis revealed. In the case of a fifth galaxy, ESO 121-G020 we obtained the calibration from another observer (Salvo, priv. comm., on a new imager CCD at the 2.3m). *B* band images for all galaxies with calibrations were obtained, although some observations in other bands were missed or rejected in the reduction process due to poor data.

Data reduction and analysis was carried out with IRAF using standard procedures. After overscan subtraction, bias subtraction, and flatfielding, individual deep images were registered to each other and the sky level was subtracted. The images for each band were then combined into a master image (to increase signal-to-noise, remove cosmic rays, etc.) and the photometric calibration applied.

Foreground stars were removed around and on each galaxy by replacing them with the surrounding sky so that only the galaxy remained. Special care was taken to restore the light distribution under any stars superimposed onto the galaxies, using the mirror image from across the galaxies center. Appendix A contains all the available *BVRI* images that are available with full calibration for the sample galaxies, showing the images both before and after star subtraction. For the four galaxies with no calibration only the *B* band image with stars is shown.

4.3 Radio Observations and Reduction

H I line and 20-cm radio continuum observations of the galaxies were obtained between June 2002 and June 2003. As mentioned above all galaxies except ESO 215-G?009 were observed in snapshot mode, with just under half observed on hybrid arrays. For each of these we have between 1 and 3 hours of time on source spread over ∼12 hour (in 10 min intervals). The galaxies ESO 121-G020, ESO 428-G033, ESO 215-G?009, and ESO 348-G009 were all observed for at least two ∼ 12 hour observations on different east-west array configurations, with ESO 215-G?009 having

the most extensive observations of three ~12 hour sessions. For MCG–04-02-003, ESO 505-G007, and IC 4212 we have an additional ~9 to 12 hour observations on a hybrid array on top of the snapshots (although snapshots for IC 4212 were not used in the final data set due to Solar interference). The arrays used, observing time, central frequency and phase calibration source for each observation are in Table 4.1. The bandwidth for all observations is 8 MHz, divided into 512 channels. The channel width is 3.3 $\mathrm{km\,s^{-1}}$, and the velocity resolution is ~4 $\mathrm{km\,s^{-1}}$. The primary calibrator in all cases was the ATCA's primary calibrator, PKS 1934–638 (which also happens to be the phase calibrator for four of the galaxies).

Data reduction and analysis was performed with the *MIRIAD*, *AIPS*, GIPSY, and KARMA packages using standard procedures. Channels with Galactic H I emission were discarded where appropriate. After continuum subtraction, the H I data were Fourier-transformed using 'natural' weighting and a channel width of 4 $\mathrm{km\,s^{-1}}$. The data were cleaned and restored with a synthesized beam (the size of which is in Chapter 5, Table 5.1 for each galaxy) and primary beam correction was applied. H I 0th moment maps (the H I distribution), 1st order maps (mean velocity field), and 2nd order maps (velocity dispersion) were obtained for all galaxies using cutoffs of between 3 and 4σ. These are shown in Appendix A along with the H I spectrum of the galaxy.

Table 4.1. Summary of Observations for each Galaxy.

Name	Optical			Radio			
	Band	Exposure Time (seconds)	Seeing (arcsec)	Arrays	Time (hours)	Central Freq. (MHz)	Phase Cal.
(1)	(2)	(3)	(4)	(5)	(6)	(7)	(8)
ESO 349-G031	*B*	3000 (10 × 300)	1.″9	EW352	∼ 1.9	1417	PKS 0008–421
	V	2400 (8 × 300)	1.″7				
	R	1800 (6 × 300)	1.″7				
	I	1800 (6 × 300)	1.″6				
MCG–04-02-003	*B*	3000 (10 × 300)	2.″2	H75B	∼ 1.5	1417	PKS 0023–263
	V	2400 (8 × 300)	2.″0	H168B	∼ 8.6	1417	PKS 0023–263
	R	1800 (6 × 300)	1.″9				
	I	1800 (6 × 300)	2.″2				
ESO 473-G024	*B*	3000 (10 × 300)	2.″5	H75B	∼ 1.5	1417	PKS 0023–263
	V	2400 (8 × 300)	3.″3	H168B	∼ 1.0	1417	PKS 0023–263
	R	1800 (6 × 300)	3.″3				
	I	1800 (6 × 300)	2.″0				
IC 1574	*B*	3000 (10 × 300)	2.″0	H75B	∼ 1.5	1417	PKS 0023–263
	V	2400 (8 × 300)	1.″9	H168B	∼ 1.0	1417	PKS 0023–263
	R	1800 (6 × 300)	2.″3				
	I	1800 (6 × 300)	2.″3				
UGCA 015	*B*	3000 (10 × 300)	2.″2	H75B	∼ 1.3	1417	PKS 0023–263
	V	2400 (8 × 300)	2.″5	H168B	∼ 1.0	1417	PKS 0023–263
	R	1800 (6 × 300)	1.″7				
	I	1800 (6 × 300)	2.″1				
ESO 085-G047	*B*	3000 (5 × 600)	2.″7	EW352	∼ 3.0	1414	PKS 0537–441
ESO 120-G021	*B*	3000 (10 × 300)	2.″2	EW352	∼ 2.2	1414	PKS 0537–441
	V	2400 (8 × 300)	1.″5				
	R	1800 (6 × 300)	2.″0				
	I	1800 (6 × 300)	2.″1				
ESO 425-G001	*B*	3000 (5 × 600)	2.″9	EW352	∼ 0.8	1414	PKS 0614–349
				EW367B	∼ 0.8	1414	PKS 0614–349
UGCA 120	*B*	3000 (5 × 600)	2.″2	H75B	∼ 2.2	1417	PKS 0704–231
ESO 121-G020	*B*	3000 (10 × 300)	2.″1	750D	∼ 10.5	1417	PKS 0407–658
				1.5B	∼ 10.9	1417	PKS 0407–658
	R	1800 (6 × 300)	1.″9	EW352	∼ 2.4	1416	PKS 0537–441
WHI B0619–07	*B*	3000 (10 × 300)	1.″5	H75B	∼ 1.8	1417	PKS 0704–231
	V	2400 (8 × 300)	1.″4				
	R	1800 (6 × 300)	1.″4				
	I	1800 (6 × 300)	1.″3				
ESO 490-G017	*B*	3000 (5 × 600)	2.″0	H75B	∼ 2.0	1417	PKS 0704–231
CGMW 1-0260				H75B	∼ 2.0	1417	PKS 0704–231
ESO 255-G019	*B*	3000 (5 × 600)	1.″9	EW352	∼ 0.8	1414	PKS 0614–349
				EW367B	∼ 0.8	1414	PKS 0614–349
CGMW 1-0381				H75B	∼ 2.0	1417	PKS 0704–231
ESO 207-G007	*B*	3000 (5 × 600)	2.″0	EW352	∼ 2.0	1416	PKS 0537–441
	V	2400 (4 × 600)	2.″1				

Table 4.1 (cont'd)

Name	Optical			Radio			
	Band	Exposure Time (seconds)	Seeing (arcsec)	Arrays	Time (hours)	Central Freq. (MHz)	Phase Cal.
(1)	(2)	(3)	(4)	(5)	(6)	(7)	(8)
	R	1800 (3 × 600)	2.″0				
ESO 207-G022	*B*	3000 (5 × 600)	1.″9	EW352	~ 2.0	1416	PKS 0537–441
	V	2400 (4 × 600)	1.″8				
ESO 428-G033	*B*	3000 (5 × 600)	2.″2	750D	~ 10.6	1412	PKS 0614–349
	V	2400 (4 × 600)	2.″0	1.5B	~ 10.3	1412	PKS 0614–349
	R	1800 (3 × 600)	1.″9	EW352	~ 1.1	1414	PKS 0614–349
	I	1800 (3 × 600)	3.″0	EW367B	~ 0.8	1414	PKS 0614–349
ESO 257-G?017	*B*	3000 (5 × 600)	1.″8	EW352	~ 0.8	1414	PKS 0614–349
				EW367B	~ 0.8	1414	PKS 0614–349
ESO 368-G004	*B*	3000 (5 × 600)	1.″9	EW352	~ 1.0	1414	PKS 0614–349
				EW367B	~ 0.8	1414	PKS 0614–349
PGC 023156	*B*	3000 (5 × 600)	1.″8	EW352	~ 1.0	1414	PKS 0614–349
				EW367B	~ 0.7	1414	PKS 0614–349
ESO 164-G?010	*B*	3000 (5 × 600)	2.″0	EW352	~ 2.7	1416	PKS 0537–441
ESO 215-G?009	*B*	3000 (10 × 300)	1.″9	EW352	~ 11.6	1417	PKS 1215–457
	V	2400 (8 × 300)	1.″9	750A	~ 10.6	1417	PKS 1215–457
	R	1800 (6 × 300)	1.″8	6A	~ 11.5	1417	PKS 1215–457
	I	1800 (6 × 300)	2.″0				
CGCG 012-022	*B*	3000 (5 × 600)	1.″9	H75B	~ 1.0	1412	PKS 1127–145
	V	2400 (4 × 600)	2.″1				
	R	1800 (3 × 600)	1.″8				
	I	1800 (3 × 600)	1.″9				
UGC 06780	*B*	3000 (5 × 600)	2.″2	H75B	~ 1.0	1412	PKS 1127–145
	V	2400 (4 × 600)	2.″1				
	R	1800 (3 × 600)	2.″3				
	I	1800 (3 × 600)	2.″0				
ESO 572-G009	*B*	1800 (3 × 600)	1.″9	H75B	~ 1.0	1412	PKS 1127–145
	V	2400 (8 × 300)	2.″7				
	R	1800 (6 × 300)	2.″2				
ESO 505-G007	*B*	3000 (10 × 300)	2.″0	H75B	~ 1.0	1412	PKS 1127–145
	V	1800 (6 × 300)	2.″2	H168B	~ 1.9	1412	PKS 1127–145
	R	1800 (6 × 300)	2.″2	H75B	~ 9.2	1412	PKS 1151–348
ESO 572-G052	*B*	3000 (5 × 600)	1.″8	H75B	~ 1.0	1412	PKS 1127–145
	V	2400 (4 × 600)	1.″9				
	I	1800 (3 × 600)	1.″7				
UGCA 289	*B*	3000 (5 × 600)	2.″3	H75B	~ 1.4	1415	PKS 1245–197
	V	2400 (4 × 600)	2.″1				
	R	1800 (3 × 600)	2.″1				
UGCA 307	*B*	3000 (5 × 600)	2.″0	H75B	~ 1.3	1415	PKS 1245–197
	V	2400 (4 × 600)	1.″9				
	R	1800 (3 × 600)	2.″0				
	I	1800 (3 × 600)	2.″2				

Table 4.1 (cont'd)

Name	Optical			Radio			
	Band	Exposure Time (seconds)	Seeing (arcsec)	Arrays	Time (hours)	Central Freq. (MHz)	Phase Cal.
(1)	(2)	(3)	(4)	(5)	(6)	(7)	(8)
UGCA 312	*B*	3000 (5 × 600)	2.″1	H75B	∼ 1.3	1415	PKS 1245–197
	V	2400 (4 × 600)	1.″9				
	R	1800 (3 × 600)	2.″0				
UGCA 322	*B*	3000 (5 × 600)	2.″5	H75B	∼ 1.4	1415	PKS 1245–197
IC 4212	*B*	3000 (5 × 600)	2.″9	H75B	∼ 8.8	1413	PKS 1308–220
	V	2400 (4 × 600)	2.″3				
	R	1800 (3 × 600)	1.″9				
IC 4824	*B*	3000 (10 × 300)	1.″7	EW352	∼ 0.7	1416	PKS 1934–638
	V	2400 (8 × 300)	1.″6	EW367B	∼ 1.8	1416	PKS 1934–638
	R	1800 (6 × 300)	1.″5				
	I	1800 (6 × 300)	1.″5				
ESO 141-G042	*B*	3000 (10 × 300)	1.″7	EW352	∼ 0.7	1416	PKS 1934–638
				EW367B	∼ 1.8	1416	PKS 1934–638
IC 4870	*B*	3000 (10 × 300)	2.″1	EW352	∼ 0.7	1416	PKS 1934–638
				EW367B	∼ 1.8	1416	PKS 1934–638
IC 4951	*B*	3000 (10 × 300)	2.″8	EW352	∼ 0.7	1416	PKS 1934–638
	V	2400 (8 × 300)	2.″2	EW367B	∼ 1.8	1416	PKS 1934–638
	R	1800 (6 × 300)	1.″9				
ESO 347-G017				EW352	∼ 1.7	1417	PKS 0008–421
UGCA 442				EW352	∼ 1.8	1417	PKS 0008–421
ESO 348-G009	*B*	3000 (10 × 300)	1.″7	750D	∼ 10.6	1417	PKS 0008–421
	V	2400 (8 × 300)	1.″4	1.5B	∼ 9.8	1417	PKS 0008–421
	R	1800 (6 × 300)	1.″5	EW352	∼ 1.7	1417	PKS 0008–421
	I	1800 (6 × 300)	1.″4				
ESO 149-G003	*B*	3000 (10 × 300)	2.″2	EW352	∼ 2.2	1417	PKS 0008–421
	V	2400 (8 × 300)	1.″9				
	R	1800 (6 × 300)	1.″9				
	I	1800 (6 × 300)	2.″0				

(1) Galaxy name.
(2) Broad band filters used for the optical observations (Cousins filters).
(3) Total observing time in each of the optical bands including the number of individual exposures.
(4) Seeing in the final optical images in each band.
(5) Array configurations on the ATCA on which each galaxy was observed in the radio.
(6) Approximate time on source for each array.
(7) Central frequency of the radio H I line observations for each galaxies.
(8) Radio phase calibration source used throughout the observations of each galaxy.

5. RESULTS FROM THE OBSERVATIONS

The observations planed for this project were extensive and ambitious, and a large amount of the time for this project was devoted to obtaining and reducing the data required for all 41 galaxies. For all galaxies it was possible to at least get H I snapshot observations, and for several galaxies we have deeper observations. Weather was the main limiting factor in the optical and it was not possible to get observations in all photometric bands for all galaxies, although the vast majority of optical observations were obtained. In this chapter we present the main observational results of this thesis, the H I line data and *BVRI* optical photometry. The H I moment maps, H I spectra, optical images, and surface brightness profiles associated with these results are presented in Appendix A, organised by galaxy. We provide a brief discussion here of 32 sample galaxies that are not discussed in detail later in the thesis (the other nine are examined in Chapters 6 and 7). The subsequent three chapters will analyse these results, derive physical parameters from them, and go into further details about some individual galaxies.

5.1 H I Line Observation Results

As shown in the previous chapter (Table 4.1) we were able to obtain at least H I snapshot data for all 41 galaxies in our sample, and deeper observations for seven galaxies. Table 5.1 lists the results of the 21cm observations for the sample galaxies. Column (1) gives the galaxy name. Column (2) gives the beam size of the H I observations (major and minor axes). Column (3) gives the H I peak flux density. Column (4) gives the total integrated H I flux density. Column (5) gives the systemic velocity from the H I line. Column (6) gives the velocity width of the H I line at 50% of the peak flux density. Column (7) gives the velocity width of the H I line at 20% of the peak flux density.

5.2 Optical Photometry Results

Table 5.1. ATCA Radio Results for all 41 Galaxy.

Name (1)	Beam (H I) (arcsec) (2)	S_{peak} (Jy (3)	F_{HI} (Jy km s^{-1}) (4)	v_{sys} (km s^{-1}) (5)	w_{50} (km s^{-1}) (6)	w_{20} (km s^{-1}) (7)
ESO 349-G031	238 × 115	0.20 ± 0.02	4.3 ± 0.8	227 ± 2	31 ± 2	40 ± 4
MCG–04-02-003	193 × 129	0.232 ± 0.009	16.2 ± 0.6	670 ± 2	112 ± 2	126 ± 2
ESO 473-G024	359 × 205	0.17 ± 0.02	5.7 ± 0.9	542 ± 3	37 ± 2	50 ± 3
IC 1574	354 × 221	0.17 ± 0.02	5.0 ± 0.9	361 ± 1	45 ± 2	59 ± 2
UGCA 015	350 × 211	0.16 ± 0.02	2.6 ± 0.6	301 ± 2	17 ± 2	32 ± 4
ESO 085-G047	218 × 104	0.32 ± 0.02	14.7 ± 1.1	1445 ± 2	61 ± 2	76 ± 2
ESO 120-G021	179 × 120	0.18 ± 0.02	10.6 ± 1.2	1299 ± 2	108 ± 3	132 ± 4
ESO 425-G001	235 × 130	0.14 ± 0.03	6.7 ± 1.7	1341 ± 2	86 ± 2	110 ± 4
UGCA 120	507 × 354	0.42 ± 0.02	33.4 ± 1.4	859 ± 1	83 ± 2	107 ± 2
ESO 121-G020	32 × 30	0.248 ± 0.006	8.8 ± 0.3	588 ± 2	56 ± 2	78 ± 7
ATCA J061608–574552[a]	32 × 30	0.115 ± 0.006	2.5 ± 0.2	567 ± 4	38 ± 3	72 ± 16
WHI B0619–07	478 × 356	0.40 ± 0.03	52.0 ± 3.0	759 ± 1	160 ± 2	176 ± 2
ESO 490-G017	508 × 354	0.21 ± 0.02	7.7 ± 1.0	499 ± 2	45 ± 2	61 ± 2
CGMW 1-0260	484 × 351	0.13 ± 0.02	11.7 ± 1.5	754 ± 2	188 ± 2	204 ± 2
ESO 255-G019	163 × 114	0.39 ± 0.03	28.0 ± 2.0	1050 ± 1	125 ± 2	141 ± 2
CGMW 1-0381	497 × 352	0.18 ± 0.02	27.0 ± 2.0	692 ± 2	181 ± 2	208 ± 2
ESO 207-G007	125 × 101	0.27 ± 0.03	16.4 ± 1.9	1070 ± 1	125 ± 2	148 ± 4
ESO 207-G022	131 × 112	0.20 ± 0.03	5.4 ± 1.3	1059 ± 1	34 ± 2	46 ± 6
ESO 428-G033	45 × 30	0.292 ± 0.005	14.6 ± 0.3	1720 ± 3	91 ± 2	115 ± 5
ESO 257-G?017	176 × 126	0.24 ± 0.03	15.2 ± 1.9	1015 ± 2	101 ± 2	115 ± 4
ESO 368-G004	209 × 133	0.35 ± 0.03	14.5 ± 1.6	1383 ± 2	61 ± 2	87 ± 2
PGC 023156	274 × 112	0.15 ± 0.03	13.0 ± 2.0	1693 ± 2	140 ± 2	163 ± 6
ESO 164-G?010	119 × 102	0.19 ± 0.03	11.2 ± 1.8	1052 ± 2	143 ± 2	158 ± 3
ESO 215-G?009	38 × 35	2.128 ± 0.005	122 ± 4	597 ± 1	64 ± 2	90 ± 4
CGCG 012-022	503 × 345	0.17 ± 0.03	13.0 ± 2.0	1601 ± 1	127 ± 2	141 ± 2
UGC 06780	505 × 342	0.18 ± 0.03	21.0 ± 3.0	1723 ± 2	214 ± 2	226 ± 3
ESO 572-G009	477 × 327	0.25 ± 0.03	7.2 ± 1.3	1743 ± 2	36 ± 2	49 ± 2
ESO 505-G007	241 × 214	0.347 ± 0.009	22.9 ± 0.6	1776 ± 2	69 ± 3	88 ± 3
ESO 572-G052	495 × 329	0.19 ± 0.03	6.0 ± 1.3	1791 ± 2	34 ± 2	45 ± 2
UGCA 289	464 × 349	0.20 ± 0.02	22.8 ± 1.7	980 ± 2	156 ± 2	172 ± 2
UGCA 307	457 × 343	0.36 ± 0.02	22.8 ± 1.3	821 ± 1	66 ± 2	84 ± 2
UGCA 312	459 × 343	0.23 ± 0.02	12.9 ± 1.2	1303 ± 2	55 ± 2	102 ± 2
UGCA 322	476 × 356	0.42 ± 0.03	38.0 ± 2.0	1357 ± 2	110 ± 2	128 ± 2
IC 4212	444 × 357	0.342 ± 0.009	46.0 ± 1.0	1476 ± 1	158 ± 2	172 ± 2
IC 4824	142 × 126	0.33 ± 0.02	18.0 ± 1.2	937 ± 2	68 ± 2	82 ± 2
ESO 141-G042	138 × 128	0.17 ± 0.02	10.9 ± 1.3	896 ± 2	99 ± 2	126 ± 4
IC 4870	139 × 124	0.42 ± 0.02	20.1 ± 1.1	875 ± 1	72 ± 2	96 ± 2
IC 4951	133 × 102	0.25 ± 0.03	21.0 ± 2.0	800 ± 2	119 ± 2	127 ± 4
ESO 347-G017	234 × 104	0.18 ± 0.02	8.4 ± 1.1	700 ± 2	68 ± 6	99 ± 4
UGCA 442	276 × 107	0.67 ± 0.02	53.8 ± 1.4	277 ± 2	94 ± 2	106 ± 2
ESO 348-G009	44 × 27	0.271 ± 0.005	15.7 ± 0.3	645 ± 1	97 ± 2	109 ± 4
ESO 149-G003	147 × 116	0.21 ± 0.02	5.6 ± 0.8	590 ± 2	35 ± 4	74 ± 4

(1) Galaxy name.
(2) Beam size of the H I observations (major and minor axes).
(3) H I peak flux density.
(4) Total integrated H I flux density.
(5) Systemic velocity from the H I line.
(6) Velocity width of the H I line at 50% of the peak flux density.
(7) Velocity width of the H I line at 20% of the peak flux density.

[a]Companion to ESO 121-G020. See Chapter 7

Table 5.2. *B* Band Optical Results from the 2.3m Telscope for each Galaxy.

Name	m_B [a] (mag)	$\mu_{0,B}$ [a] (mag arcsec^{-2})	$\langle\mu\rangle_{eff,B}$ [a] (mag arcsec^{-2})	$r_{eff,B}$ (arcsec)	$r_{H,0,B}$ (arcsec)	A_B (mag)
(1)	(2)	(3)	(4)	(5)	(6)	(7)
ESO 349-G031	15.71 ± 0.06	24.05 ± 0.04	24.53 ± 0.05	23.2 ± 0.8	41.8 ± 0.6	0.05
MCG–04-02-003	15.32 ± 0.06	22.34 ± 0.02	23.77 ± 0.04	19.6 ± 0.7	51.0 ± 2.0	0.08
ESO 473-G024	16.38 ± 0.06	24.63 ± 0.04	25.30 ± 0.04	24.3 ± 0.8	32.4 ± 0.8	0.08
IC 1574	14.90 ± 0.03	23.36 ± 0.02	24.12 ± 0.02	27.8 ± 0.6	61.0 ± 2.0	0.07
UGCA 015	15.30 ± 0.05	23.49 ± 0.03	24.46 ± 0.02	27.1 ± 0.6	50.4 ± 1.2	0.07
ESO 085-G047	14.18 ± 0.04	22.50 ± 0.02	24.25 ± 0.02	41.2 ± 0.8	84.0 ± 2.0	0.11
ESO 120-G021	14.96 ± 0.05	23.29 ± 0.03	23.91 ± 0.02	24.6 ± 0.5	52.1 ± 1.2	0.20
ESO 425-G001	14.97 ± 0.05	21.75 ± 0.01	24.11 ± 0.04	26.8 ± 0.7	57.0 ± 2.0	0.17
UGCA 120	12.98 ± 0.04	22.05 ± 0.01	23.25 ± 0.02	45.0 ± 0.9	105.6 ± 0.6	0.33
ESO 121-G020	15.27 ± 0.05	23.36 ± 0.03	23.95 ± 0.02	21.7 ± 0.4	47.0 ± 2.0	0.17
ATCA J061608–574552[b]	17.01 ± 0.06	22.81 ± 0.04	23.34 ± 0.02	7.4 ± 0.3	18.6 ± 0.6	0.17
WHI B0619–07	14.63 ± 0.06	23.45 ± 0.01	24.69 ± 0.03	41.0 ± 1.1	108.0 ± 5.0	2.65
ESO 490-G017	12.98 ± 0.04	21.95 ± 0.02	22.78 ± 0.03	36.4 ± 0.8	105.0 ± 1.2	0.33
CGMW 1-0260						1.46
ESO 255-G019	14.14 ± 0.05	22.70 ± 0.02	24.35 ± 0.03	44.1 ± 0.9	95.0 ± 0.6	0.36
CGMW 1-0381						1.83
ESO 207-G007	13.71 ± 0.03	22.24 ± 0.03	23.56 ± 0.02	37.1 ± 0.6	91.5 ± 0.6	0.33
ESO 207-G022	14.52 ± 0.06	23.34 ± 0.02	24.27 ± 0.03	35.7 ± 1.0	79.2 ± 0.6	0.56
ESO 428-G033	16.90 ± 0.10	23.33 ± 0.11	24.69 ± 0.02	14.4 ± 0.5	37.2 ± 1.2	1.10
ESO 257-G?017	15.82 ± 0.10	24.67 ± 0.07	25.35 ± 0.03	32.1 ± 1.2	59.6 ± 0.6	0.62
ESO 368-G004	16.07 ± 0.07	23.45 ± 0.04	24.72 ± 0.02	21.4 ± 0.6	60.0 ± 10.0	1.94
PGC 023156	16.91 ± 0.10	24.26 ± 0.06	24.97 ± 0.01	16.3 ± 0.4	32.0 ± 2.0	1.70
ESO 164-G?010	13.91 ± 0.07	22.58 ± 0.02	23.61 ± 0.01	34.7 ± 0.5	74.0 ± 2.0	1.55
ESO 215-G?009	16.13 ± 0.07	24.97 ± 0.03	25.48 ± 0.02	29.7 ± 0.6	57.6 ± 0.6	0.95
CGCG 012-022	15.06 ± 0.02	22.63 ± 0.02	23.43 ± 0.04	18.9 ± 0.5	45.6 ± 0.7	0.15
UGC 06780	13.91 ± 0.08	21.53 ± 0.01	24.19 ± 0.05	45.0 ± 2.0	99.6 ± 0.6	0.09
ESO 572-G009	16.79 ± 0.05	24.96 ± 0.05	26.03 ± 0.02	28.1 ± 0.7	30.6 ± 1.2	0.16
ESO 505-G007	14.20 ± 0.06	23.99 ± 0.04	24.00 ± 0.01	36.4 ± 0.7	82.8 ± 1.2	0.36
ESO 572-G052	15.91 ± 0.06	22.33 ± 0.02	23.72 ± 0.03	14.6 ± 0.4	34.0 ± 2.0	0.26
UGCA 289	13.83 ± 0.03	23.46 ± 0.02	24.49 ± 0.02	54.2 ± 0.9	104.4 ± 1.2	0.12
UGCA 307	14.59 ± 0.03	23.39 ± 0.03	24.25 ± 0.03	34.0 ± 0.6	69.6 ± 1.2	0.24
UGCA 312	15.16 ± 0.02	23.85 ± 0.02	24.47 ± 0.02	29.1 ± 0.4	55.0 ± 2.0	0.18
UGCA 322	13.22 ± 0.03	23.69 ± 0.04	24.09 ± 0.01	59.5 ± 0.4	115.8 ± 0.6	0.13
IC 4212	14.11 ± 0.04	22.38 ± 0.02	24.42 ± 0.02	46.0 ± 1.0	98.4 ± 0.6	0.19

Table 5.2 (cont'd)

Name	m_B [a] (mag)	$\mu_{0,B}$ [a] (mag arcsec^{-2})	$\langle\mu\rangle_{eff,B}$ [a] (mag arcsec^{-2})	$r_{eff,B}$ (arcsec)	$r_{H,0,B}$ (arcsec)	A_B (mag)
(1)	(2)	(3)	(4)	(5)	(6)	(7)
IC 4824	14.48 ± 0.11	23.82 ± 0.02	24.19 ± 0.04	34.9 ± 1.5	78.6 ± 0.8	0.24
ESO 141-G042	13.70 ± 0.09	22.88 ± 0.01	24.27 ± 0.03	51.8 ± 1.6	113.0 ± 0.6	0.25
IC 4870	14.79 ± 0.06	22.38 ± 0.02	23.94 ± 0.05	27.1 ± 1.1	70.0 ± 2.0	0.49
IC 4951	14.09 ± 0.02	21.36 ± 0.01	23.15 ± 0.03	25.9 ± 0.5	74.4 ± 0.6	0.17
ESO 347-G017						0.07
UGCA 442						0.07
ESO 348-G009	14.82 ± 0.07	23.78 ± 0.04	24.79 ± 0.03	39.5 ± 0.9	72.0 ± 0.6	0.06
ESO 149-G003	14.79 ± 0.03	21.71 ± 0.01	23.12 ± 0.04	18.5 ± 0.5	51.2 ± 1.2	0.06

(1) Galaxy name.
(2) Total apparent B band magnitude.
(3) Central B band surface brightness.
(4) Effective B band surface brightness, the average surface brightness out to the half light radius.
(5) Half light (effective) radius in the B band.
(6) Radii out to $\mu = 26.6$ mag arcsec^{-2} in the B band (which is the Holmberg radius, extinction corrected).
(7) B band Galactic extinction from SFD98 ($\pm$16%).

[a]Correction for Galactic extinction not applied.

[b]Companion to ESO 121-G020. See Chapter 7

Due to weather problems not all optical data for all galaxies was obtained. B band photometry was taken for all galaxies, but for four objects (CGMW 1-0260, CGMW 1-0381, ESO 347-G017, and UGCA 442) the calibration images obtained at the time of observation were later rejected (in all four photometric bands) due to non photometric conditions. Subsequent attempts to obtain new calibration data were only sucessful for one additional galaxy field, ESO 121-G020 (see § 4.2). In addition, some images are absent in the other three bands also (either not able to be observed during the observing runs, or rejected later due to problems with the images, especially in I). In total we have B band images for 38 galaxies, V band for 24 galaxies, R band for 24 galaxies, and I band for 16 galaxies.

Table 5.2 lists the results of the optical B band photometry taken on the 2.3m Telescope for the sample galaxies where they were available. No Galactic extinction correction was applied to the apparent magnitude and surface brightness. Column (1) gives the galaxy name. Column (2) gives the total apparent B band magnitude. Column (3) gives the central B band surface brightness. Column (4) gives the effective B band surface brightness, the average surface brightness out to the half light radius. Column (5) gives this half light (effective) radius in the B band. Column (6) gives the radii out to $\mu = 26.6$ mag arcsec^{-2} in the B band (which is the Holmberg radius, extinction corrected). Column (7) gives the B band Galactic extinction from SFD98 ($\pm$16%).

Tables 5.3, 5.4, and 5.5 are very similar to Table 5.2, and lists the results of the optical photometry taken on the 2.3m Telescope for the 41 galaxies in the V, R, and I bands, respectively. The Holmberg radius was excluded as it is only measured in B. Again, no Galactic extinction correction was applied to the apparent magnitude and surface brightness. For all three tables, column (1) gives the galaxy name. Column (2) gives the total apparent magnitude. Column (3) gives the central surface brightness. Column (4) gives the effective surface brightness, the average surface brightness out to the half light radius. Column (5) gives this half light (effective) radius. Column (6) gives the Galactic extinction correction from SFD98.

5.3 Comparison to BGC and LEDA values

We have ATCA H I observations for all 41 sample galaxies, including H I flux density. Fig. 5.1 plots our H I flux density from the ATCA against that from the BGC, with the line showing where the two are equal. The two measurements are in very good agreement, with the vast majority of values agreeing within the uncertainty ranges. There is a slight systematic trend for the ATCA measurements to sit lower than the BGC flux densities. Such a trend is consistent with what we might expect from an interferometry array like the ATCA versus a single dish like Parkes. One of the galaxies which has a lower flux density is ESO 121-G020, which was found to have a companion, ATCA J061608–574552, but the combined

Table 5.3. *V* Band Optical Results from the 2.3m Telscope for each Galaxy.

Name (1)	m_V [a] (mag) (2)	$\mu_{0,V}$ [a] (mag arcsec^{-2}) (3)	$\langle\mu\rangle_{eff,V}$ [a] (mag arcsec^{-2}) (4)	$r_{eff,V}$ (arcsec) (5)	A_V (mag) (6)
ESO 349-G031	15.46 ± 0.07	23.68 ± 0.03	24.26 ± 0.03	23.0 ± 0.8	0.04
MCG-04-02-003	14.91 ± 0.05	21.89 ± 0.01	22.98 ± 0.04	16.4 ± 0.6	0.06
ESO 473-G024	15.44 ± 0.07	23.73 ± 0.03	24.46 ± 0.03	25.4 ± 0.7	0.06
IC 1574	14.15 ± 0.03	22.84 ± 0.02	23.65 ± 0.02	31.7 ± 0.4	0.05
UGCA 015	15.35 ± 0.05	23.97 ± 0.02	24.83 ± 0.02	31.5 ± 0.7	0.06
ESO 085-G047					0.09
ESO 120-G021	15.26 ± 0.06	23.41 ± 0.05	23.98 ± 0.02	22.2 ± 0.5	0.15
ESO 425-G001					0.13
UGCA 120					0.26
ESO 121-G020					0.13
ATCA J061608–574552[b]					0.13
WHI B0619–07	14.63 ± 0.08	23.18 ± 0.02	24.17 ± 0.03	32.2 ± 0.8	1.95
ESO 490-G017					0.26
CGMW 1-0260					1.11
ESO 255-G019					0.28
CGMW 1-0381					1.47
ESO 207-G007	13.28 ± 0.03	21.59 ± 0.02	22.93 ± 0.02	33.8 ± 0.5	0.26
ESO 207-G022	14.36 ± 0.07	22.98 ± 0.02	23.68 ± 0.03	29.2 ± 0.8	0.44
ESO 428-G033	16.13 ± 0.10	23.12 ± 0.02	24.23 ± 0.05	16.7 ± 0.8	0.85
ESO 257-G?017					0.47
ESO 368-G004					1.49
PGC 023156					1.29
ESO 164-G?010					1.19
ESO 215-G?009	14.89 ± 0.06	23.65 ± 0.03	24.14 ± 0.02	28.3 ± 0.7	0.73
CGCG 012-022	14.77 ± 0.02	22.05 ± 0.01	22.89 ± 0.02	16.8 ± 0.3	0.11
UGC 06780	13.76 ± 0.06	20.99 ± 0.01	23.48 ± 0.05	35.1 ± 1.0	0.07
ESO 572-G009	15.65 ± 0.07	23.69 ± 0.02	25.12 ± 0.02	31.1 ± 0.8	0.12
ESO 505-G007	14.48 ± 0.05	23.89 ± 0.04	23.96 ± 0.01	31.3 ± 0.6	0.28
ESO 572-G052	15.51 ± 0.11	21.89 ± 0.02	23.40 ± 0.06	15.1 ± 0.8	0.20
UGCA 289	13.42 ± 0.02	22.90 ± 0.02	23.92 ± 0.02	50.4 ± 0.4	0.09
UGCA 307	14.34 ± 0.03	22.31 ± 0.09	23.87 ± 0.03	32.2 ± 0.5	0.18
UGCA 312	15.33 ± 0.02	23.52 ± 0.02	23.83 ± 0.02	20.0 ± 0.3	0.14
UGCA 322					0.10
IC 4212	13.69 ± 0.05	22.00 ± 0.03	23.98 ± 0.01	45.7 ± 0.9	0.14
IC 4824	14.18 ± 0.03	23.14 ± 0.02	23.93 ± 0.02	35.6 ± 0.5	0.18
ESO 141-G042					0.19
IC 4870					0.37
IC 4951	13.71 ± 0.03	20.92 ± 0.02	22.70 ± 0.03	25.0 ± 0.6	0.13
ESO 347-G017					0.06
UGCA 442					0.06
ESO 348-G009	14.68 ± 0.06	23.42 ± 0.03	24.40 ± 0.03	35.1 ± 1.0	0.04
ESO 149-G003	14.83 ± 0.03	21.68 ± 0.01	22.81 ± 0.02	15.7 ± 0.3	0.04

(1) Galaxy name.
(2) Total apparent *V* band magnitude.
(3) Central *V* band surface brightness.
(4) Effective *V* band surface brightness, the average surface brightness out to the half light radius.
(5) Half light (effective) radius in the *V* band.
(6) *V* band Galactic extinction from SFD98 (±16%).

[a] Correction for Galactic extinction not applied.

[b] Companion to ESO 121-G020. See Chapter 7

Table 5.4. *R* Band Optical Results from the 2.3m Telscope for each Galaxy.

Name	m_R [a] (mag)	$\mu_{0,R}$ [a] (mag arcsec^{-2})	$\langle\mu\rangle_{eff,R}$ [a] (mag arcsec^{-2})	$r_{eff,R}$ (arcsec)	A_R (mag)
(1)	(2)	(3)	(4)	(5)	(6)
ESO 349-G031	15.29 ± 0.04	23.41 ± 0.03	23.96 ± 0.02	21.6 ± 0.4	0.03
MCG-04-02-003	14.40 ± 0.05	21.60 ± 0.01	22.68 ± 0.05	18.1 ± 0.7	0.05
ESO 473-G024	15.19 ± 0.03	23.51 ± 0.03	24.18 ± 0.02	25.1 ± 0.4	0.05
IC 1574	14.17 ± 0.04	22.79 ± 0.01	23.49 ± 0.02	29.2 ± 0.5	0.04
UGCA 015	14.66 ± 0.07	22.97 ± 0.03	23.87 ± 0.01	27.7 ± 0.5	0.05
ESO 085-G047					0.07
ESO 120-G021	14.26 ± 0.02	22.46 ± 0.02	23.07 ± 0.02	23.0 ± 0.3	0.12
ESO 425-G001					0.11
UGCA 120					0.21
ESO 121-G020	14.62 ± 0.04	22.71 ± 0.03	23.29 ± 0.02	21.6 ± 0.5	0.11
ATCA J061608–574552[b]	16.36 ± 0.06	22.07 ± 0.02	22.72 ± 0.02	7.5 ± 0.2	0.11
WHI B0619–07	14.85 ± 0.09	23.16 ± 0.04	24.15 ± 0.04	28.8 ± 1.2	1.57
ESO 490-G017					0.21
CGMW 1-0260					0.90
ESO 255-G019					0.22
CGMW 1-0381					1.18
ESO 207-G007	12.90 ± 0.02	21.06 ± 0.03	22.41 ± 0.02	31.8 ± 0.4	0.21
ESO 207-G022					0.36
ESO 428-G033	15.61 ± 0.08	22.56 ± 0.02	23.48 ± 0.05	15.0 ± 0.9	0.68
ESO 257-G?017					0.39
ESO 368-G004					1.20
PGC 023156					1.04
ESO 164-G?010					0.96
ESO 215-G?009	14.38 ± 0.05	23.16 ± 0.02	23.64 ± 0.03	28.4 ± 0.5	0.59
CGCG 012-022	14.41 ± 0.02	21.65 ± 0.02	22.49 ± 0.03	16.5 ± 0.3	0.09
UGC 06780	13.46 ± 0.06	20.51 ± 0.01	22.98 ± 0.04	32.1 ± 0.9	0.06
ESO 572-G009	15.40 ± 0.04	23.42 ± 0.03	24.75 ± 0.01	29.6 ± 0.5	0.10
ESO 505-G007	13.97 ± 0.04	23.46 ± 0.04	23.66 ± 0.02	34.6 ± 0.5	0.22
ESO 572-G052					0.16
UGCA 289	12.88 ± 0.03	22.23 ± 0.01	23.30 ± 0.02	48.5 ± 0.5	0.07
UGCA 307	14.01 ± 0.08	22.02 ± 0.06	23.54 ± 0.03	32.1 ± 0.8	0.14
UGCA 312	15.12 ± 0.04	23.25 ± 0.03	23.54 ± 0.02	19.3 ± 0.3	0.11
UGCA 322					0.08
IC 4212	13.29 ± 0.06	21.53 ± 0.02	23.53 ± 0.02	44.5 ± 0.9	0.12
IC 4824	13.82 ± 0.05	22.82 ± 0.01	23.47 ± 0.02	34.0 ± 0.5	0.14
ESO 141-G042					0.15
IC 4870					0.30
IC 4951	13.39 ± 0.03	20.61 ± 0.01	22.40 ± 0.04	25.3 ± 0.7	0.11
ESO 347-G017					0.05
UGCA 442					0.05
ESO 348-G009	14.48 ± 0.05	23.13 ± 0.03	24.03 ± 0.03	32.4 ± 0.8	0.04
ESO 149-G003	14.44 ± 0.05	21.32 ± 0.02	22.44 ± 0.04	15.9 ± 0.6	0.11

(1) Galaxy name.
(2) Total apparent *R* band magnitude.
(3) Central *R* band surface brightness.
(4) Effective *R* band surface brightness, the average surface brightness out to the half light radius.
(5) Half light (effective) radius in the *R* band.
(6) *R* band Galactic extinction from SFD98 (±16%).

[a]Correction for Galactic extinction not applied.

[b]Companion to ESO 121-G020. See Chapter 7

Table 5.5. *I* Band Optical Results from the 2.3m Telscope for each Galaxy.

Name	m_I [a] (mag)	$\mu_{0,I}$ [a] (mag arcsec^{-2})	$\langle\mu\rangle_{eff,I}$ [a] (mag arcsec^{-2})	$r_{eff,I}$ (arcsec)	A_I (mag)
(1)	(2)	(3)	(4)	(5)	(6)
ESO 349-G031	14.82 ± 0.09	23.26 ± 0.07	23.73 ± 0.01	24.2 ± 0.6	0.02
MCG–04-02-003	13.60 ± 0.06	21.17 ± 0.01	22.76 ± 0.05	27.1 ± 1.0	0.04
ESO 473-G024	14.76 ± 0.07	23.42 ± 0.08	24.35 ± 0.02	33.0 ± 0.9	0.04
IC 1574	13.72 ± 0.05	22.45 ± 0.02	23.07 ± 0.03	29.6 ± 0.6	0.03
UGCA 015	14.39 ± 0.11	23.48 ± 0.06	23.86 ± 0.02	31.2 ± 0.9	0.03
ESO 085-G047					0.050±
ESO 120-G021	14.19 ± 0.05	22.18 ± 0.04	22.73 ± 0.02	20.4 ± 0.3	0.09
ESO 425-G001					0.08
UGCA 120					0.15
ESO 121-G020					0.08
ATCA J061608–574552[b]					0.08
WHI B0619–07	13.32 ± 0.06	21.73 ± 0.03	22.36 ± 0.03	25.7 ± 0.5	1.14
ESO 490-G017					0.15
CGMW 1-0260					0.65
ESO 255-G019					0.16
CGMW 1-0381					0.86
ESO 207-G007					0.15
ESO 207-G022					0.26
ESO 428-G033	15.04 ± 0.09	22.01 ± 0.03	22.95 ± 0.04	15.2 ± 0.7	0.50
ESO 257-G?017					0.28
ESO 368-G004					0.87
PGC 023156					0.75
ESO 164-G?010					0.70
ESO 215-G?009	13.76 ± 0.06	22.91 ± 0.04	23.40 ± 0.03	33.9 ± 0.8	0.43
CGCG 012-022	13.94 ± 0.03	21.22 ± 0.01	22.18 ± 0.02	17.8 ± 0.3	0.06
UGC 06780	12.89 ± 0.07	20.14 ± 0.01	22.60 ± 0.05	34.9 ± 1.3	0.04
ESO 572-G009					0.07
ESO 505-G007					0.16
ESO 572-G052	14.80 ± 0.04	21.20 ± 0.02	22.61 ± 0.03	14.5 ± 0.5	0.12
UGCA 289					0.05
UGCA 307	13.36 ± 0.02	21.71 ± 0.02	23.10 ± 0.02	35.3 ± 0.5	0.10
UGCA 312					0.08
UGCA 322					0.06
IC 4212					0.08
IC 4824	13.13 ± 0.05	22.19 ± 0.03	22.69 ± 0.03	32.6 ± 0.6	0.10
ESO 141-G042					0.11
IC 4870					0.22
IC 4951					0.08
ESO 347-G017					0.03
UGCA 442					0.03
ESO 348-G009	13.75 ± 0.10	22.75 ± 0.03	23.72 ± 0.02	39.3 ± 1.1	0.03
ESO 149-G003	13.86 ± 0.09	21.20 ± 0.03	22.62 ± 0.07	22.6 ± 1.2	0.03

(1) Galaxy name.
(2) Total apparent *I* band magnitude.
(3) Central *I* band surface brightness.
(4) Effective *I* band surface brightness, the average surface brightness out to the half light radius.
(5) Half light (effective) radius in the *I* band.
(6) *I* band Galactic extinction from SFD98 (±16%).

[a]Correction for Galactic extinction not applied.

[b]Companion to ESO 121-G020. See Chapter 7

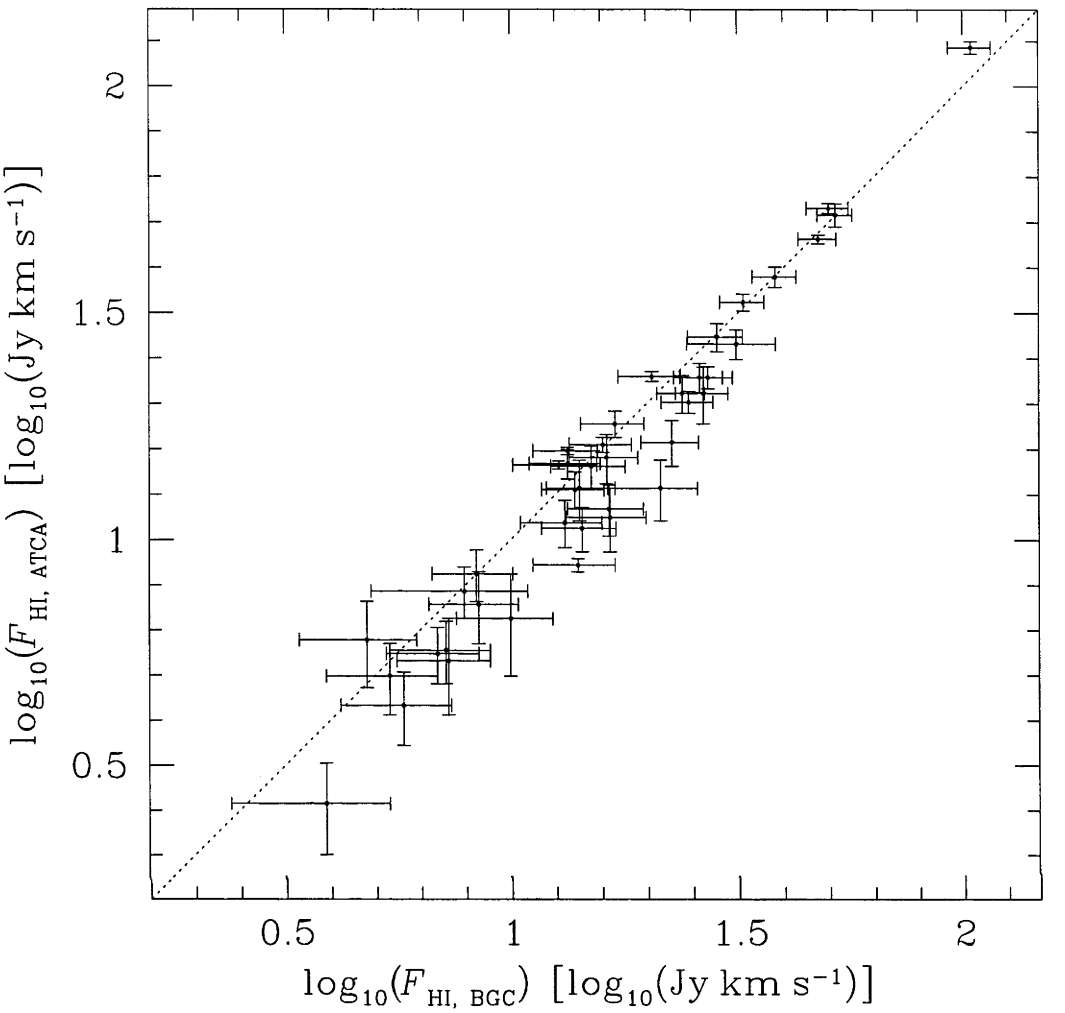

Fig. 5.1: The H I flux density as measured on the ATCA versus the H I flux density as given in the BGC. The line marks where both values are equal.

flux density of these two galaxies agrees with the BGC (see Chapter 7, § 7.2.1). The other ATCA flux densities which do not agree with the BGC measurement also follow this trend, the only exception being the galaxy with the highest H I flux density, ESO 215-G?009 (see Chapter 6, § 6.4.1).

Fig. 5.2 shows a similar plot for the B band apparent magnitude from the 2.3m telescope versus the LEDA value. Unlike the H I results, many of the 2.3m measurements do not agree with those LEDA provides, with most being significantly brighter, sometimes by several magnitudes. Only ten values agree with the LEDA data within the uncertainties (some of the LEDA values having enormous uncertainties of $\sim$ 1 mag or greater). This has a strong effect on $\mathcal{M}_{\rm HI}/L_{\rm B}$, shifting it down significantly for most of the sample. At this point we could ask whether this could be a systematic effect caused by problems with our observations.

The most likely problem is with the photometric calibration, which was done using shallow images of the galaxy fields taken on photometric nights with Landolt (1992) standard star fields. As good photometric nights at Siding Springs are not always available during observing runs (our average run was about five nights on the 2.3m) these calibrations tended to be done all on the same night when the conditions were favourable. If there would be something wrong with the conditions that was not noticed on that night (e.g. light cirrus clouds) then this could create a systematic error in the calibration. However, the calibrations were not done for all galaxies in a single night (this is not possible due to the sky positions of the galaxies and the time it takes to do the calibration) but on several nights in different observing runs. There is no particular correlation between which run the calibration was done and whether our result agrees with LEDA, so the problem must lie with the values that the database provides. We will discuss this problem in later chapters (see Chapter 7, § 7.4.2, and Chapter 8, § 7.4.2).

5.4 Galaxy Comments

We present here some comments on a few of the sample galaxies not discussed in the following two chapters. The galaxy ESO 215-G?009 is presented in the next chapter in detail (Chapter 6), while it and eight other galaxies (MCG–04-02-003, ESO 473-G024, ESO 121-G020, ESO 428-G033, ESO 572-G009, ESO 505-G007, IC 4212, and ESO 348-G009) are discussed in the chapter after that (Chapter 7). The 32 here were only observed at 21cm in snapshot mode, and includes the four galaxies for which we have no optical calibration. The page references refer to the images in Appendix A.

ESO 349-G031 (page 145, also known as the Sculptor Dwarf Irregular Galaxy), **IC 1574** (page 157), and **UGCA 015** (page 161) are some of the several known members of the Sculptor Group in our sample (see Côté et al., 1997). All three were control sample galaxies. In all three cases our values of both $F_{\rm HI}$ and $m_{\rm B}$ agreed with the BGC and LEDA measurements, respectively. ESO 349-G031 has a mottled irregular appearence, while both IC 1574 and UGCA 015 appear to be edge on disks, the latter appearing to have an irregular or warped structure. The optical field around IC 1574 contains several other diffuse objects, which could be background galaxies, other Sculptor members, or possibly even satellites of IC 1574. The beam of our ATCA observations is too large to determine if there is any H I asociated with them at the same velocity as IC 1574, and there were no other sources in the H I cube. **ESO 347-G017** (page 254) and **UGCA 442** (page 256) are also Sculptor members, although we have no optical calibration for these two. **ESO 149-G003** (page 261) may also belong to the Sculptor group given its Local Group velocity, although it is $\sim$15° south of the main group.

WHI B0619–07 (page 178) was the galaxy which was uncatalogued at the time the BGC was compiled, and as such was misidentified as another optical

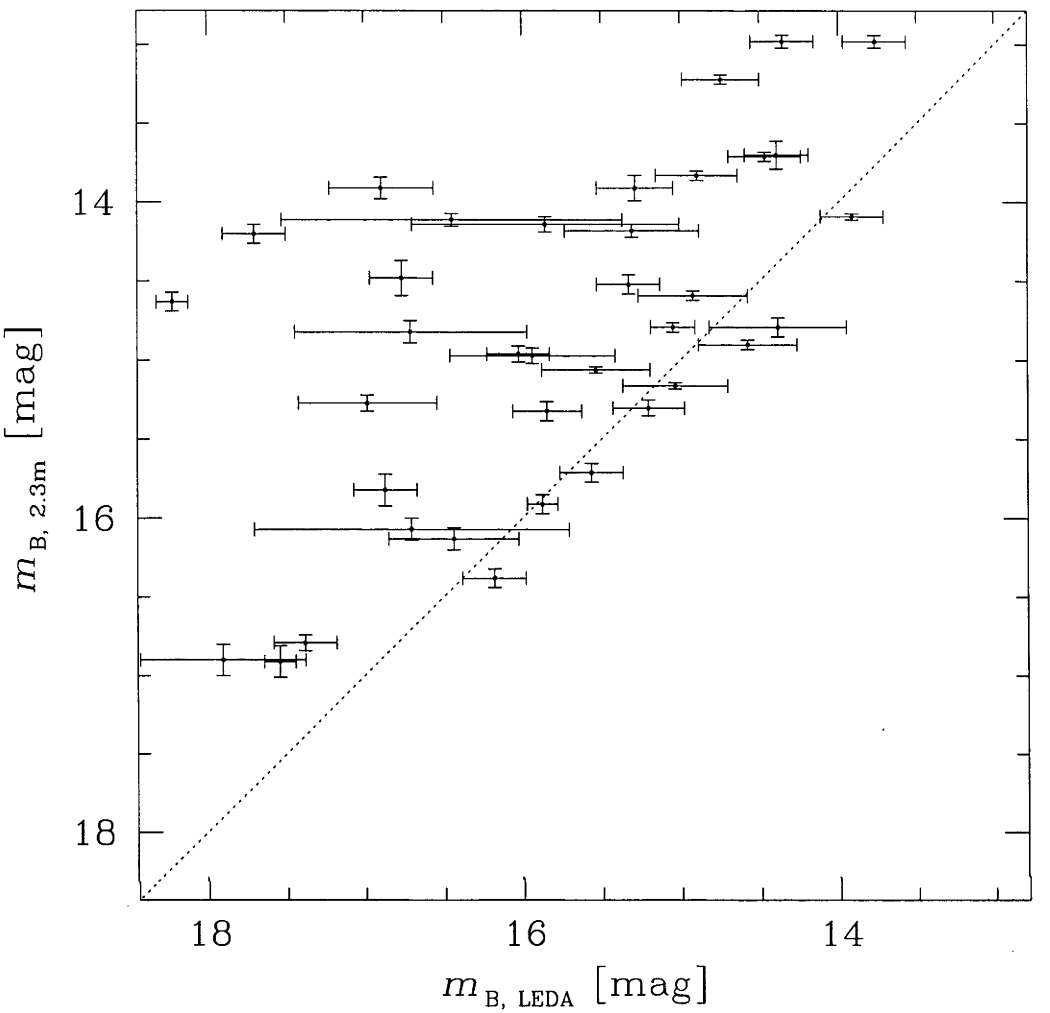

Fig. 5.2: The B band apparent magnitude as measured on the 2.3m telescope versus the B band apparent magnitude provided by LEDA. The line marks where both values are equal.

counterpart, CGMW 1-0080 which appears to be very distant or very compact (as shown in the BGC). The new counterpart has a much brighter B apparent magnitude than CGMW 1-0080, and the $\mathcal{M}_{HI}/L_B$ drops to the level of the control sample as a result.

The H I structure of **CGMW 1-0381** (page 188) is possibly one of the more interesting in this sample, especially when compared to the optical galaxy. Despite the very large beam from the H75B array configuration that the galaxy was observed on and the relatively low signal-to-noise, CGMW 1-0381 is clearly extended in the north-east to south-west direction, and is much larger than the optical counterpart at it's centre. Unfortunately this was one of the galaxies for which we were forced to reject the optical photometric calibrations, so we cannot recalculate

$\mathcal{M}_{\rm HI}/L_{\rm B}$. The optical image taken on the 2.3m does not show any more extended stellar structure than was visible in the DSS image. However, the galaxy is in the Galactic plane and suffers from a relatively high extinction (1.83 ± 0.29 mag, SFD98), and large parts of the galaxy could be blocked by the Galactic dust or obscured by foreground stars.

6. ESO215–G?009: AN EXTREME H I-RICH DWARF IRREGULAR GALAXY

Of the 41 galaxies examined in this project one stood out from the very beginning, ESO 215-G?009. Aside from its unusual name, this galaxy had the second highest preliminary $\mathcal{M}_{\rm HI}/L_{\rm B}$ of all the BGC galaxies, $\mathcal{M}_{\rm HI}/L_{\rm B} = 24 \pm 12\ \mathcal{M}_{\odot}/L_{\odot,{\rm B}}$. Importantly it is also relatively close and has no apparent nearby neighbours. Morphologically it appears as a low surface brightness dwarf irregular galaxy, little more than a faint fuzzy blob while having one of the highest H I peak flux densities in the BGC (and therefore the southern hemisphere). Overall this looked like the most promising candidate for a true high H I mass-to-light ratio galaxy, and the most extensive observations of any object in this project were performed on ESO 215-G?009 to find its true nature. In this chapter we present the results of a detailed examination of the galaxy ESO 215-G?009, which were published as Warren, Jerjen, & Koribalski (2004).

6.1 The Galaxy ESO 215-G?009

ESO 215-G?009 (HIPASS J1057–48) was first catalogued on ESO(B) Atlas photographic plates (Lauberts, 1982) and classified "G?", a *potential* galaxy. It is necessary to retain the full original designation for ESO galaxies (including question marks and other designations) because of confusions that can sometimes arise between objects (such as with ESO 174-G?001, ESO 174-G001 and ESO 174-GA001, see § 2.2). ESO 215-G?009 is a dwarf irregular galaxy with a very low surface brightness. Because of its low Galactic latitude, $b = 10\overset{\circ}{.}5$, the Galactic extinction, $A_{\rm B} = 0.95 \pm 0.15$ mag (SFD98), is relatively high. Foreground star density in the field surrounding the galaxy is also high. No optical velocity is available to date. Lauberts & Valentijn (1989) measured a total blue magnitude of $m_{\rm B} = 16.03 \pm 0.09$ mag from photographic plates. No previous H I observations are available other than those derived from HIPASS. Huchtmeier, Karachentsev, and Karachentseva (2001) published an $\mathcal{M}_{\rm HI}/L_{\rm B}$ for this galaxy (under the name KKs40) which was calculated using the H I flux density from an early public data release of HIPASS and the Lauberts & Valentijn (1989) photographic blue magnitude. They found a high $\mathcal{M}_{\rm HI}/L_{\rm B}$ of $\sim 12\ \mathcal{M}_{\odot}/L_{\odot,{\rm B}}$, already quite high and comparable to DDO 154. Unfortunately their H I flux density is an underestimate as the public data release spectrum is off centre and does not cover the entire galaxy.

Table 6.1. Properties of ESO 215-G?009.

Property (1)	Previous Value (2)	Reference (3)	This Thesis (4)
Names	ESO 215-G?009	Lauberts (1982)	
	HIPASS J1057–48	BGC	
	PGC 490287	LEDA	
	KKs40	Karachentseva et al. (2000)	
Center position	$10^h\,57^m\,29\overset{s}{.}37$	Lauberts (1982)	Opt: $10^h\,57^m\,29\overset{s}{.}9$
α, δ(J2000.0)	$-48°\,10'\,40\overset{''}{.}1$ ($\pm 8''$)		$-48°\,10'\,43''$ ($\pm 2''$)
			H I: $10^h\,57^m\,30\overset{s}{.}0$
			$-48°\,10'\,47''$ ($\pm 10''$)
Galactic coordinates l, b	$284\overset{°}{.}1$, $10\overset{°}{.}5$		
systemic velocity, v_{sys}	598 ± 1 km s^{-1}	BGC	597 ± 1 km s^{-1}
50% velocity width, w_{50}	67 ± 2 km s^{-1}	BGC	
20% velocity width, w_{20}	83 ± 3 km s^{-1}	BGC	
Local group velocity, v_{LG}	312 ± 1 km s^{-1}	BGC	311 ± 1 km s^{-1}
Distance, D	4.2 Mpc		
apparent R mag., m_R	15.02 ± 0.09 mag	Lauberts & Valentijn (1989)	14.38 ± 0.11 mag
apparent B mag., m_B	16.03 ± 0.09 mag	Lauberts & Valentijn (1989)	16.13 ± 0.07 mag
	16.43 ± 0.41 mag	LEDA	
extinction, A_B	0.95 ± 0.15 mag	Schlegel et al. (1998)	
	0.84 mag	Burstein & Heiles (1982)	
absolute B mag., $M_{B,0}$	-12.64 ± 0.4 mag		-12.9 ± 0.2 mag
H I flux density, F_{HI}	104.4 ± 11.5 Jy km s^{-1}	BGC	122 ± 4 Jy km s^{-1}
H I mass, $\mathcal{M}_{HI}$	$(4.3 \pm 0.5) \times 10^8\ \mathcal{M}_\odot$	BGC	$(5.1 \pm 0.2) \times 10^8\ \mathcal{M}_\odot$
$\mathcal{M}_{HI}/L_B$	$24 \pm 12\ \mathcal{M}_\odot/L_{\odot,B}$	BGC + LEDA	$22 \pm 4\ \mathcal{M}_\odot/L_{\odot,B}$

(1) Property of ESO 215-G?009.
(2) Literature value for this property.
(3) Literature reference for this property.
(4) Values derived from our results for ESO 215-G?009.

Table 6.1 summarises the properties of ESO 215-G?009 from previous studies, values derived from those quantities, and some of the results of this study. Koribalski et al. (2004) measured a systemic velocity of $v_{sys} = 598 \pm 1$ km s^{-1}, a velocity width of $w_{20} = 83 \pm 3$ km s^{-1}, and an integrated H I flux density of $F_{HI} = 104.4 \pm 11.5$ Jy km s^{-1}. We adopt a distance to ESO 215-G?009 of $D = 4.2$ Mpc from the Local Group velocity of 312 ± 1 km s^{-1} using $D = v_{LG}/H_0$ (see also § 6.5.3).

The proximity and isolation of ESO 215-G?009 make it an excellent candidate for a study of the nature of high H I mass-to-light ratio galaxies and of galaxy evolution in general. Using deep optical *BVRI* band images and H I data of ESO 215-G?009 we will examine the stellar and H I distribution, stellar population, isolation and the H I kinematics to search for the physical reasons why ESO 215-G?009 could maintain such a high fraction of H I gas, while other galaxies processed most of their gas into stars.

6.2 Observations and Data Reduction

As we set out in Chapter 4, ESO 215-G?009 and all the other galaxies were observed in two different wavelength regimes. Optical photometry was obtained with the ANU 2.3-meter Telescope at the Siding Springs Observatory. H I line and radio continuum data were obtained with the Australia Telescope Compact Array.

6.2.1 Optical Photometry

Optical *BVRI* band (Cousins filters) images were taken as a series of 300 s exposures in April/June 2002 and May 2003 using the 2.3m Nasmyth Imager. The total exposure time in the four bands is 50, 40, 30, and 30 minutes, respectively. The typical seeing in the final images for the different bands was $\sim$1.″9, 1.″9, 1.″8, and 2.″0, respectively, and most observations were taken at low airmass. Twilight sky flat fields in all bands and bias images were obtained at the same time. Several Landolt (1992) standard stars were taken together with shallow 120 s *BVRI* images of the galaxy field on a photometric night to perform the photometric calibration of the deeper images.

Data reduction and analysis was carried out with IRAF using standard procedures as described in Chapter 4. Foreground stars were removed by replacing them with the surrounding sky so that only the galaxy remained. Special care was taken to restore the light distribution under stars superposed onto the galaxy, using the mirror image from across the galaxies centre. Fig. 6.1 shows the resulting *BVRI* images before and after star subtraction. We measured the luminosity-weighted centre of the galaxy (averaged between the four bands) to be at α, δ(J2000) = $10^{\rm h}\,57^{\rm m}\,29.^{\rm s}9$, $-48°\,10'\,43''$ ($\pm 2''$), consistent with Lauberts (1982, see Table 6.1).

6.2.2 Radio Observations

H I line and 20 cm radio continuum observations of ESO 215-G?009 were obtained in three $\sim$12 h observations in June/October 2002 and March 2003 with the EW352, 750A and 6A arrays, respectively. The band was centred at a frequency of 1417 MHz with a bandwidth of 8 MHz, divided into 512 channels. The channel width is 3.3 km s^{-1}, and the velocity resolution is $\sim$4 km s^{-1}. The primary and secondary calibrators were PKS 1934–638 (14.88 Jy) and PKS 1215–457 (4.8 Jy), respectively.

Data reduction and analysis was performed with the *MIRIAD*, *AIPS*, and KARMA packages using standard procedures (see Chapter 4). Channels with Galactic emission were discarded. After continuum subtraction, the H I data were Fourier-transformed using "natural" weighting and a channel width of 4 km s^{-1}. The data were cleaned and restored with a synthesised beam of $38'' \times 35''$. We measure an r.m.s. noise of 1.6 mJy per channel, close to the theoretical value. Primary beam correction was applied. H I moment maps were obtained using

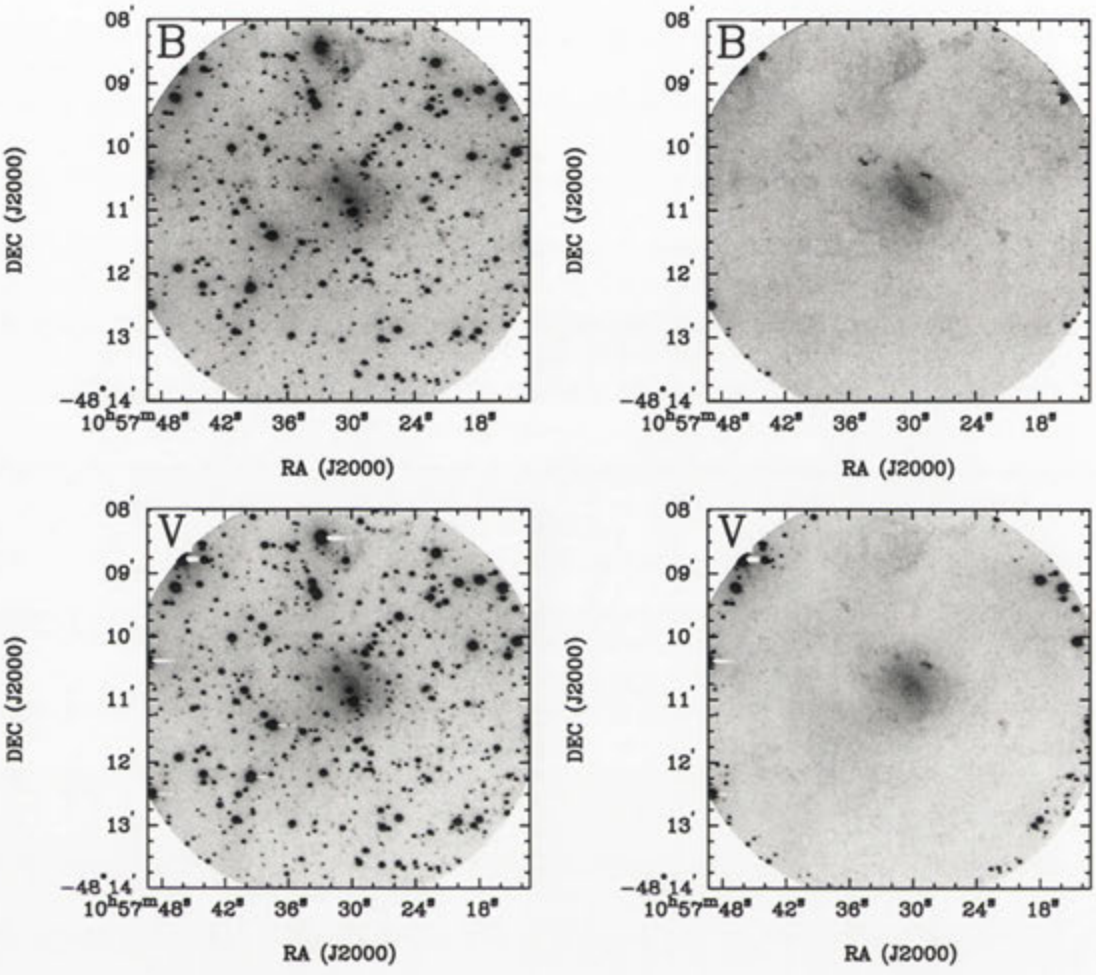

Fig. 6.1: Deep *BVRI* images of ESO 215-G?009 before and after subtraction of the foreground stars. East is to the left and North is up for all images in this thesis.

cutoffs of 4 mJy beam^{-1} (H I distribution) and 6 mJy beam^{-1} (mean velocity field and dispersion).

Low resolution 20 cm radio continuum maps were produced using multi-frequency synthesis and "natural" weighting resulting in a synthesised beam of $18'' \times 17''$ and an r.m.s. of $\sim$0.13 mJy. Primary beam correction was applied. We do not find any radio continuum emission associated with ESO 215-G?009. We estimate the 20 cm flux density to be less than 1 mJy over the optical extent of the galaxy. To obtain the star formation rate we used the relation by Condon (1992) and Haarsma et al. (2000):

$$SFR_{20\,\mathrm{cm}} = 0.14\ D^2\ S_{20\,\mathrm{cm}}\ \ \mathcal{M}_\odot\,\mathrm{yr}^{-1}, \tag{6.1}$$

where D is the distance in Mpc and $S_{20\,\mathrm{cm}}$ is the 20 cm radio continuum flux density in Jy. We calculate an upper limit to the star formation rate for ESO 215-G?009 is $\sim 2.5 \times 10^{-3}\ \mathcal{M}_\odot\,\mathrm{yr}^{-1}$.

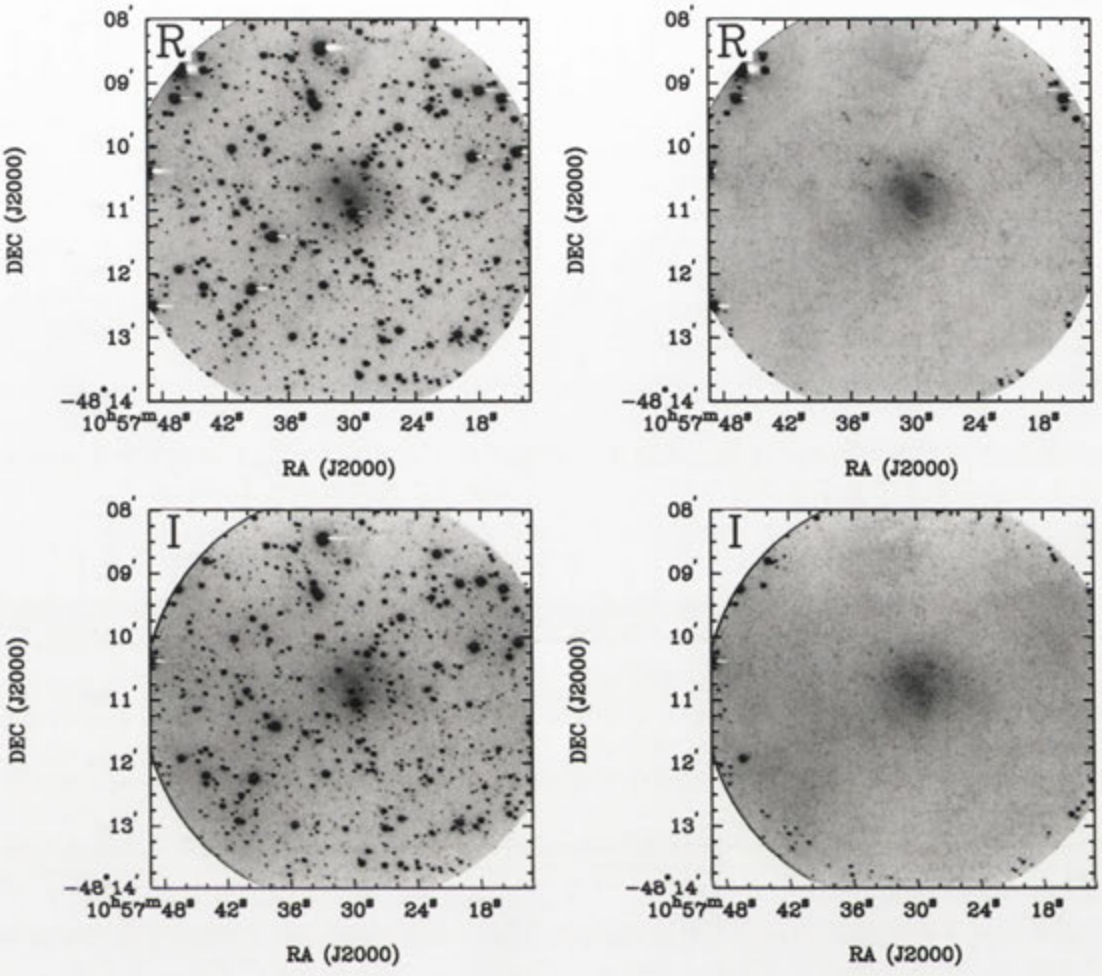

Fig. 6.1: continued

6.3 Optical Properties

Fig. 6.1 shows the deep *BVRI* band images of ESO 215-G?009 before and after subtraction of the foreground stars. A growth curve of the galaxy was measured for the star-subtracted images from the centre in 2 pixel (∼1.″2) circular aperture rings to obtain the total intensity. We are confident that the sky background subtraction was successful as the growth curves for all bands flattened out beyond the galaxy at around the same radius. From these the empirical apparent magnitude, effective radius and effective surface brightness for each band were calculated. The main error for the apparent magnitude is the uncertainty in the background sky level. The derived B band magnitude of $m_{\rm B} = 16.13 \pm 0.07$ mag (within 80″ of the centre) is consistent with Lauberts & Valentijn (1989, see Table 6.1). The R band magnitude of $m_{\rm R} = 14.38 \pm 0.11$ mag is however 0.64 mag brighter than that from Lauberts & Valentijn (1989). From $m_{\rm B}$ and our adopted distance, ESO 215-G?009 has an absolute magnitude of $M_{\rm B} = -12.9 \pm 0.2$ mag. We derive a B band luminosity of $L_{\rm B} = (2.3 \pm 0.4) \times 10^7\ L_{\odot,{\rm B}}$, a factor of ∼80 below the median B

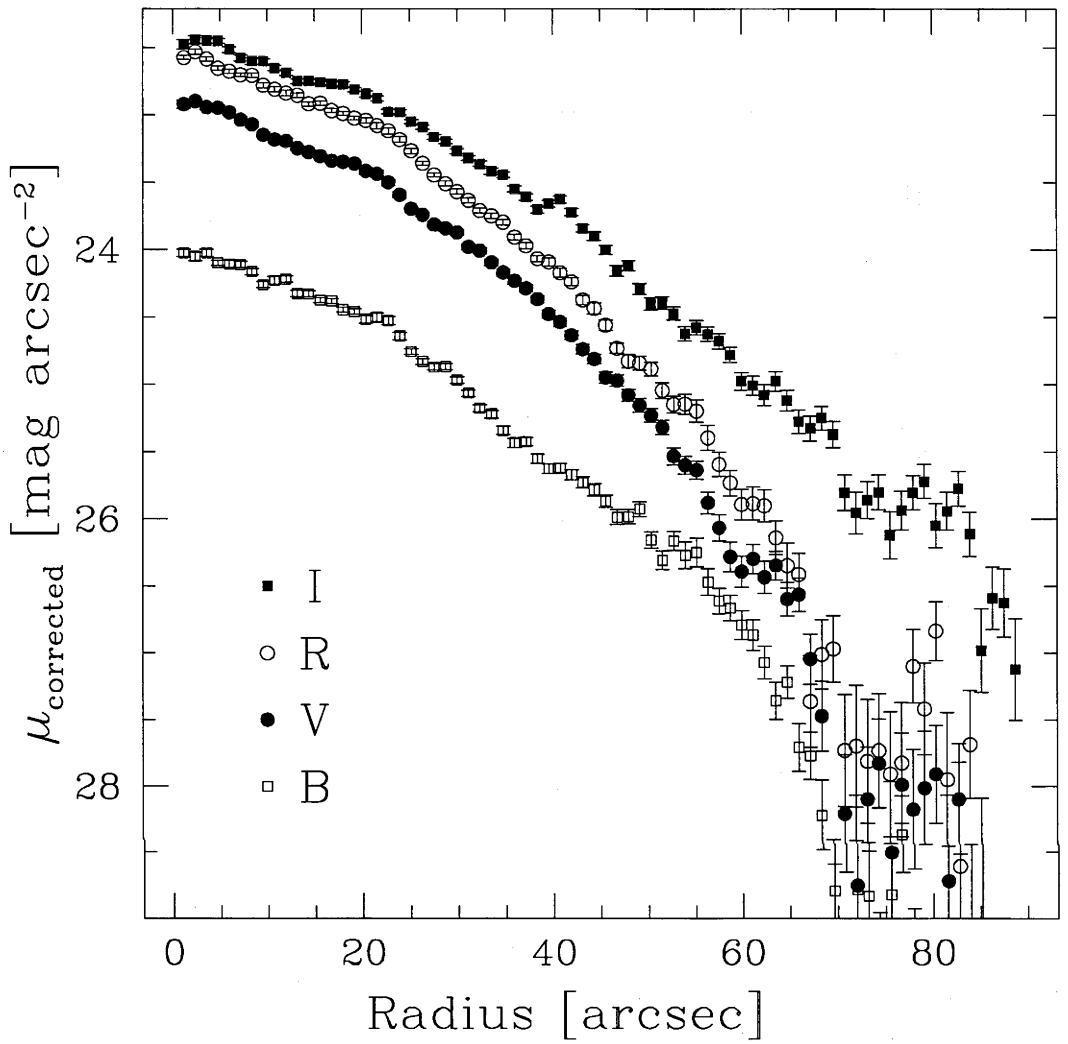

Fig. 6.2: *BVRI* surface brightness profiles of ESO 215-G?009, corrected for Galactic extinction.

luminosity of 1.9×10^9 $L_{\odot,B}$ for Sm/Im galaxies in Roberts & Haynes (1994).

We then obtain surface brightness profiles from all four bands, shown in Fig. 6.2. A Sérsic profile (Sérsic, 1968), which is a generalised version of an exponential profile, was fitted to all the surface brightness profiles. The Sérsic law, in terms of surface brightness $\mu(r)$, is defined by:

$$\mu(r) = \mu_0 + 1.086(r/r_0)^n \text{ mag arcsec}^{-2}, \tag{6.2}$$

where r is the radius from the centre in arcsec, μ_0 is the central surface brightness in mag arcsec^{-2}, r_0 is the scale radius in arcseconds, and n is the shape parameter (where $n = 1$ gives an exponential profile). These profiles are not normally fitted to dwarf irregular galaxies as they commonly have clumpy H II regions on top of an exponential disk, but as ESO 215-G?009 is much smoother than most late-

Table 6.2. *BVRI* Photometry Results for ESO 215-G?009.

Band	m_T [a] (mag)	$m_{\text{Sérsic}}$ [a] (mag)	μ_0 [a] (mag arcsec^{-2})	$\langle\mu\rangle_{eff}$ [a] (mag arcsec^{-2})	r_{eff} (arcsec)	$r_{26.6}$ (arcsec)	A_G (mag)
(1)	(2)	(3)	(4)	(5)	(6)	(7)	(8)
B	16.13 ± 0.07	16.03 ± 0.07	24.97 ± 0.03	25.48 ± 0.02	29.7 ± 0.6	57.6 ± 0.6	0.95 ± 0.15
V	14.89 ± 0.06	14.83 ± 0.06	23.65 ± 0.03	24.14 ± 0.02	28.3 ± 0.6	65 ± 2	0.73 ± 0.12
R	14.38 ± 0.11	14.31 ± 0.11	23.16 ± 0.02	23.64 ± 0.03	28.4 ± 0.6	68 ± 2	0.59 ± 0.09
I	13.76 ± 0.13	13.70 ± 0.13	22.91 ± 0.04	23.40 ± 0.04	33.9 ± 0.6	85 ± 10	0.43 ± 0.07

(1) Cousins broad band filters used.
(2) Empirically derived total apparent magnitude.
(3) Total apparent magnitude as extrapolated from the Sérsic profile fit.
(4) Central surface brightness.
(5) Effective surface brightness, the average surface brightness out to the half light radius
(6) Half light (effective) radius.
(7) Radii out to $\mu = 26.6$ mag arcsec^{-2} (which is the Holmberg radius in the *B* band, extinction corrected).
(8) Galactic extinction correction from SFD98.

[a]Galactic extinction not applied.

type galaxies it is well described by a Sérsic model. The Sérsic fits were used to extrapolate beyond the detection limit to get the total apparent magnitude. The magnitudes are consistent with the empirical magnitudes derived from the total counts above the sky level, and the empirical values are adopted for the remainder of the chapter. The radial extent of ESO 215-G?009 at an extinction corrected *B* band surface brightness of 26.6 mag arcsec^{-2} (the Holmberg radius) is $57\farcs6 \pm 0\farcs6$.

To the north in the optical images ($\sim$2.5 from the centre) there is a diffuse patch of stars that may be related to star formation in the galaxy, which is on the eastern edge of the strongest peak in the H I distribution. Unfortunately there is also a strong concentration of foreground stars on the eastern side of this patch, including the brightest star in the field, which makes the star subtraction here more difficult and increases the uncertainty for any luminosity determination.

Table 6.2 gives a summary of the photometric results obtained from these profiles. No Galactic extinction correction was applied to the apparent magnitude and surface brightness. We obtained six colours from the photometry, which are shown at the end of Table 6.3 (discussed in § 6.5.6). From these colours it seems that ESO 215-G?009 is very red for a late-type galaxy, suggesting that the stellar population is older than that typically seen in dwarf irregulars (see discussion in § 6.5.4). Fig. 6.3 shows the colour profiles for each of these six colour combinations.

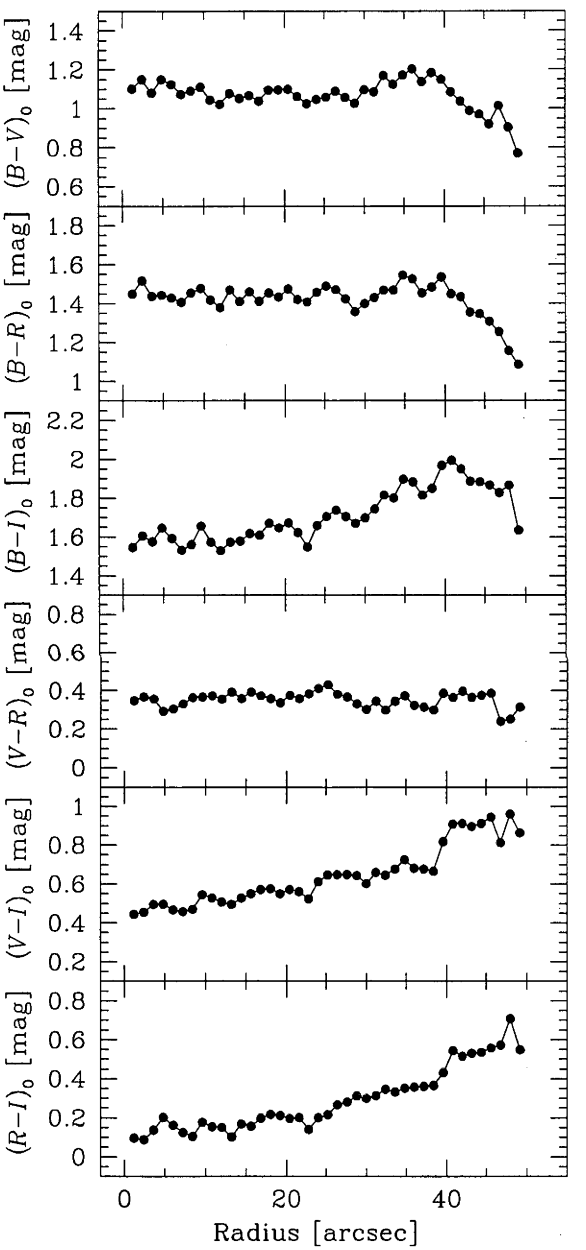

Fig. 6.3: Color profiles for ESO 215-G?009, corrected for Galactic extinction.

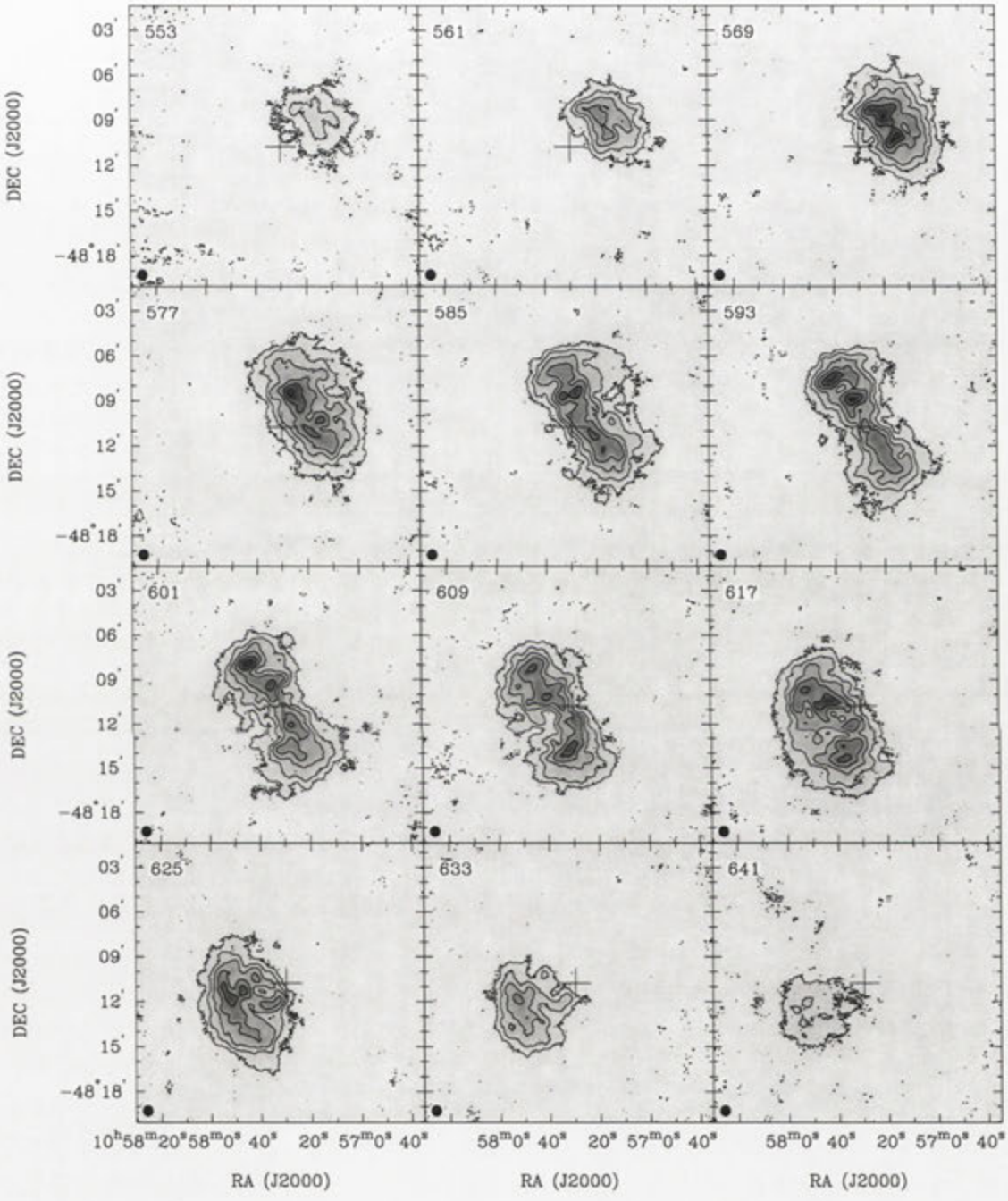

Fig. 6.4: H I channel maps of ESO 215-G?009. For display purposes we show channels smoothed to a velocity resolution of 8 km s^{-1}. The contour levels are ± 3.15 ($\sim 3\sigma$), 8.4, 15.75, 26.25, 42, and 63 mJy beam^{-1}. The grey scale ranges from –6 to 95 mJy beam^{-1}. Negative contours are marked with dashed lines. The cross marks the dynamical centre of the galaxy. The synthesised beam is displayed in the bottom left corner of each panel. The central heliocentric velocity for each panel is displayed in the top left corner.

6.4 Radio Properties

6.4.1 H I Structure

Fig. 6.4 shows the H I channel maps of ESO 215-G?009. H I line emission was detected in the velocity range 547 to 647 km s^{-1}. The emission has a resemblance to a slowly rotating gas disk, except that the pattern is not as sharply defined as might be seen in a larger disk (see the example in Giovanelli & Haynes, 1988). In addition, the structure throughout the channels is not evenly distributed, but instead has several concentrations and voids. In particular, to the north of the galaxy centre the gas has two strong peaks close to the systemic velocity, and to the south east of the centre a depression is visible around 609 km s^{-1}. We find no companion galaxies within the ATCA primary beam (33′) and the velocity range of 200 – 1300 km s^{-1}.

Fig. 6.5 shows the H I spectra of ESO 215-G?009 as obtained from the HIPASS BGC and the ATCA. There is a resemblance to a double horn profile, characteristic of a rotating disk, although the central dip is not pronounced (which may be partially due to the low inclination of the source). Notably the ATCA spectrum is inconsistent with the single-dish result and measures a higher flux density. The HIPASS BGC flux density may be underestimated because of the large extent and high peak flux density of the source (see Barnes et al., 2001).

Fig. 6.6 shows the integrated H I distribution, the mean H I velocity field and the H I velocity dispersion of ESO 215-G?009. From the H I distribution we measure the dimensions of the H I disk as $730'' \times 640''$ ($\pm 40''$) at a position angle of $PA \sim 120°$. Fig. 6.7 shows the azimuthally averaged radial H I density profile of ESO 215-G?009. The profile was measured with rings $10''$ wide assuming an inclination of 36° and PA = 119° (§ 6.4.2). Here 1 Jy beam^{-1} km s^{-1} corresponds to a column density of 8.32×10^{20} atoms cm^{-2}. H I can be traced out to a column density of $\sim 5.0 \times 10^{19}$ atoms cm^{-2} at a radius of $370'' \pm 20''$. We obtain an H I flux density of $F_{\rm HI} = 122 \pm 4$ Jy km s^{-1}. This is higher than the $F_{\rm HI} = 104.4 \pm 11.5$ Jy km s^{-1} obtained in the BGC (Koribalski et al., 2004). Using the adopted distance of 4.2 Mpc we derive an H I mass of $\mathcal{M}_{\rm HI} = (5.1 \pm 0.2) \times 10^8\ \mathcal{M}_\odot$. This is less than half the median H I mass of $1.27 \times 10^9\ \mathcal{M}_\odot$ for Sm/Im galaxies in Roberts & Haynes (1994), but is still well within the range of H I masses seen in this sample (see Table 6.3).

6.4.2 H I Gas Dynamics

Overall the mean H I velocity field (Fig. 6.6c) is remarkably regular, especially for a late-type galaxy, in which the velocity field is usually extensively disturbed (see examples in Côté, Carignan, & Freeman, 2000; Stil & Israel, 2002b). There are few asymmetries between the two sides of the galaxy. The last contour on the approaching side is closed, while the receding side contours are still open, which

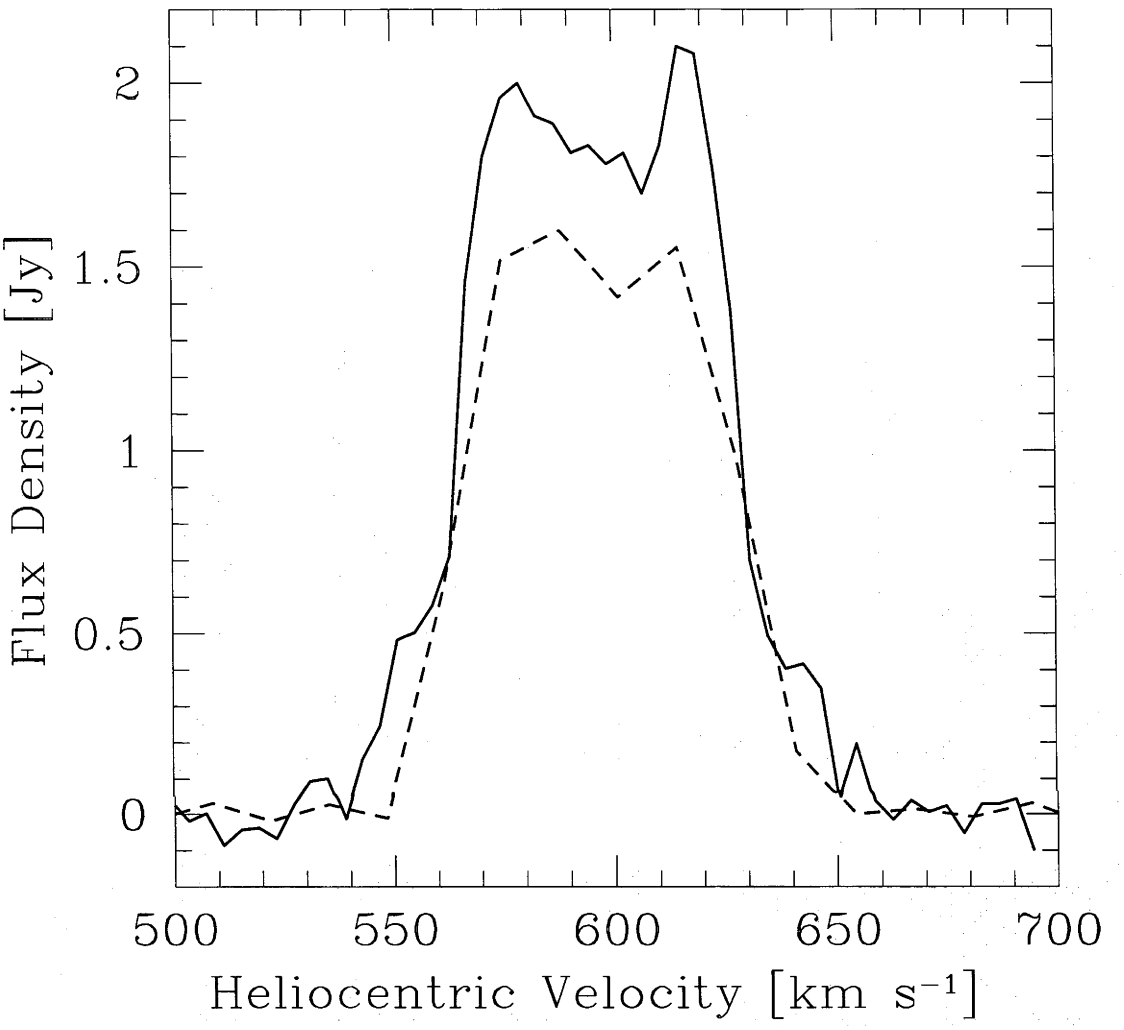

Fig. 6.5: Global H I spectra of ESO 215-G?009 as obtained from HIPASS (dashed lines) and the ATCA (solid line).

suggests the rotation curve on the approaching side may turn down. There is also some asymmetry across the major axis of the galaxy, most clearly seen in the channel maps (Fig. 6.4) around $v_{hel} \sim 609$ km s^{-1}, where the southern portion of the galaxy curves around more than the northern portion. However, on the whole this is one of the most symmetric and undisturbed velocity fields of a low-mass, late-type galaxy.

Through most of the galaxy the velocity dispersion (see Fig. 6.6d) is between about 4 to 10 km s^{-1}. In the central region around the stellar component of the galaxy, and extending to the north toward the strongest H I concentration, the velocity dispersion is largest. This is reflected in Fig. 6.8, which shows the azimuthally averaged radial H I velocity dispersion profile of ESO 215-G?009. The velocity dispersion is highest in the centre of the galaxy where the profile is peaked.

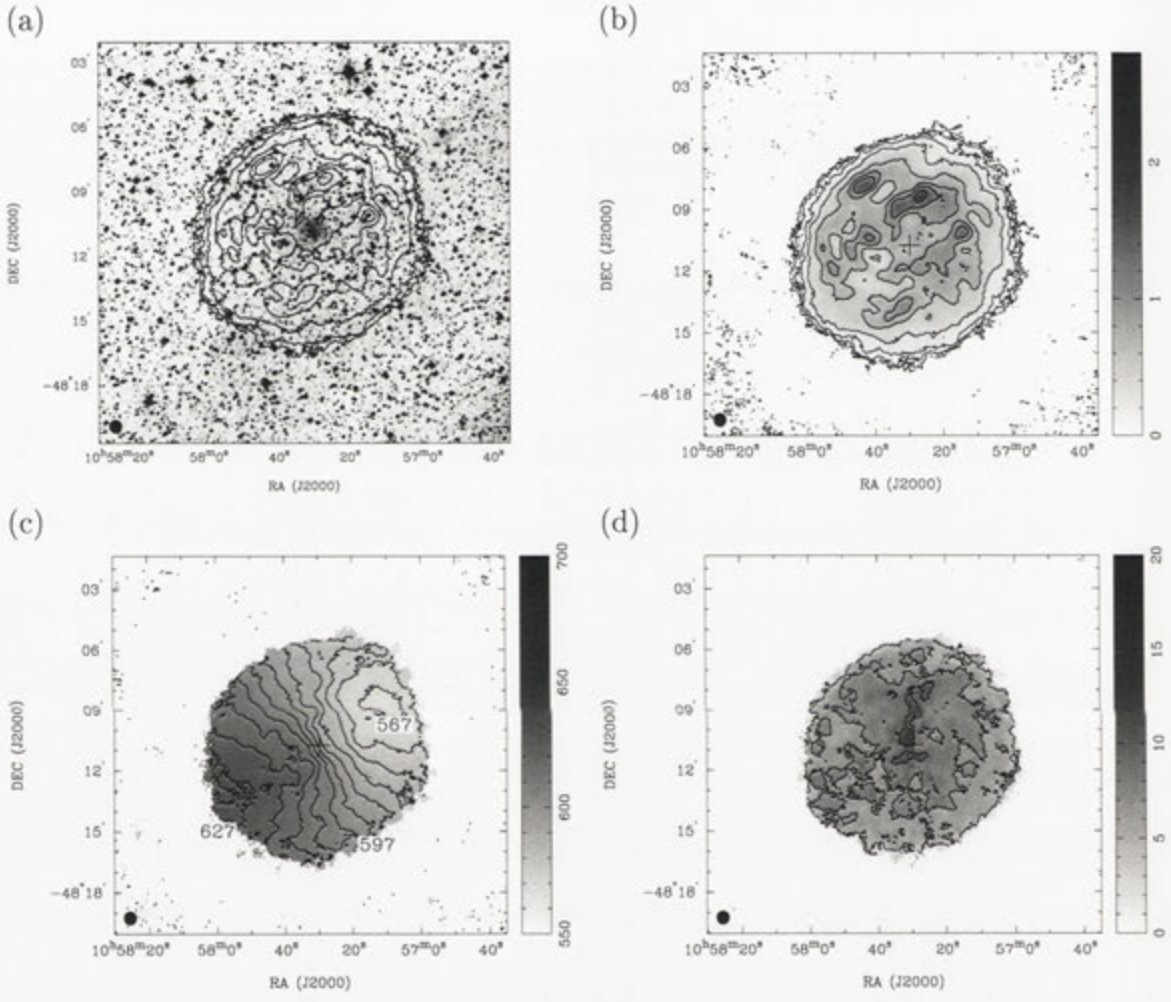

Fig. 6.6: H I moment maps of ESO 215-G?009. (a) Integrated H I intensity distribution overlaid onto an optical DSS II R band image. The contour levels are 0.073, 0.145, 0.29, 0.58, 0.87, 1.16 and 1.57 Jy beam^{-1} km s^{-1} (which corresponds to column densities of 6, 12, 24, 48, 72, 96 and 130 $\times$ 10^{19} atoms cm^{-2}, respectively). (b) As in (a) but overlaid onto itself, and with the additional contours of $\pm$0.036 Jy beam^{-1} km s^{-1} ($\pm$3 $\times 10^{19}$ atoms cm^{-2}). Negative contours are dashed. (c) Mean H I velocity field. The contours levels range from 567 to 627 km s^{-1} in steps of 6 km s^{-1}. (d) H I velocity dispersion. The contours levels are 4, 7, and 10 km s^{-1}. The cross in (b), (c), and (d) marks the dynamical centre of the galaxy. The synthesised beam is displayed in the bottom left corner of each panel.

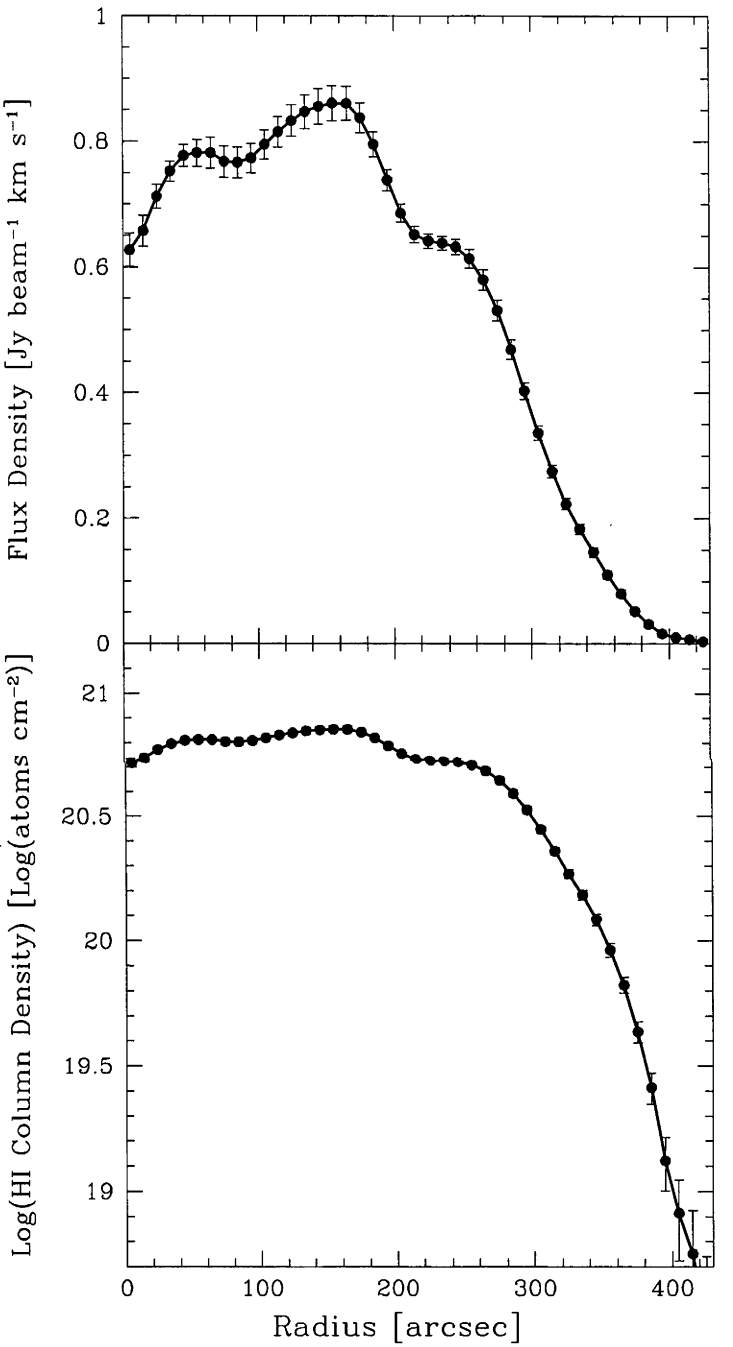

Fig. 6.7: Azimuthally averaged H I radial profiles of ESO 215-G?009 in (a) flux density, and (b) column density. The profile was measured in 10″ steps, and corrected for an inclination of 36°. Error bars reflect Poisson statistical uncertainties.

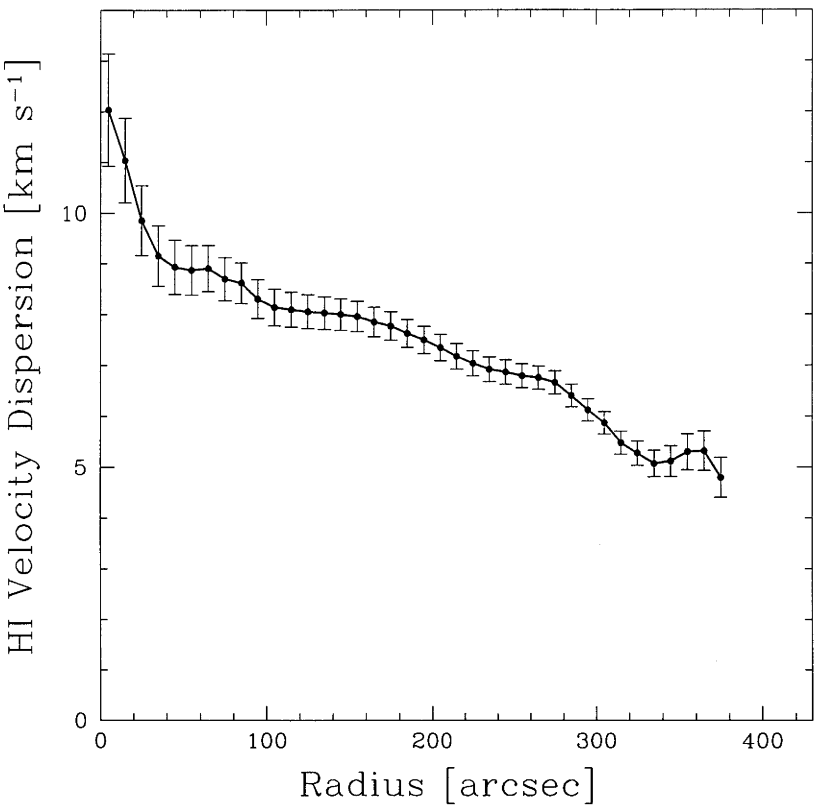

Fig. 6.8: Azimuthally averaged H I velocity dispersion radial profile of ESO 215-G?009. The profile was measured in 10″ steps and corrected for an inclination of 36°. Error bars reflect Poisson statistical uncertainties.

In the outer galaxy the dispersion is lower with a slightly declining profile. Fig. 6.9 shows an H I position-velocity diagram along the major axis of ESO 215-G?009, emphasizing the symmetry between the approaching and receding sides of the galaxy. On the receding side there are two gaps in the gas distribution accompanied by a large spread in velocity. These features could be expanding bubbles which have been recognised in other face-on galaxies (such as the large H I "superbubble" in M101, Kamphuis, Sancisi, & van der Hulst, 1991). They correspond to the low density regions in Fig. 6.6b to the south east. There is no evidence of a central H I bar in Fig. 6.9; however, a weak bar on the scale of the optical component of the galaxy would be difficult to pick up from this diagram with our current resolution.

We obtained a rotation curve from the mean H I velocity field of ESO 215-G?009 using the tilted ring algorithm in AIPS (Begeman, 1989ROCUR). Using all data within a radius of 6′, we derive the dynamical centre of the galaxy at α, δ(J2000) = $10^{\rm h}\,57^{\rm m}\,30\overset{\rm s}{.}0$, −48° 10′ 47″ (±10″), and its systemic heliocentric velocity, $v_{\rm sys}$ = 597 ± 1 km s^{-1}. This is consistent with Koribalski et al. (2004), and the position agrees with that derived from the centre of the stellar component. The centre and systemic velocity were fixed for the fitting of the remaining parameters for which

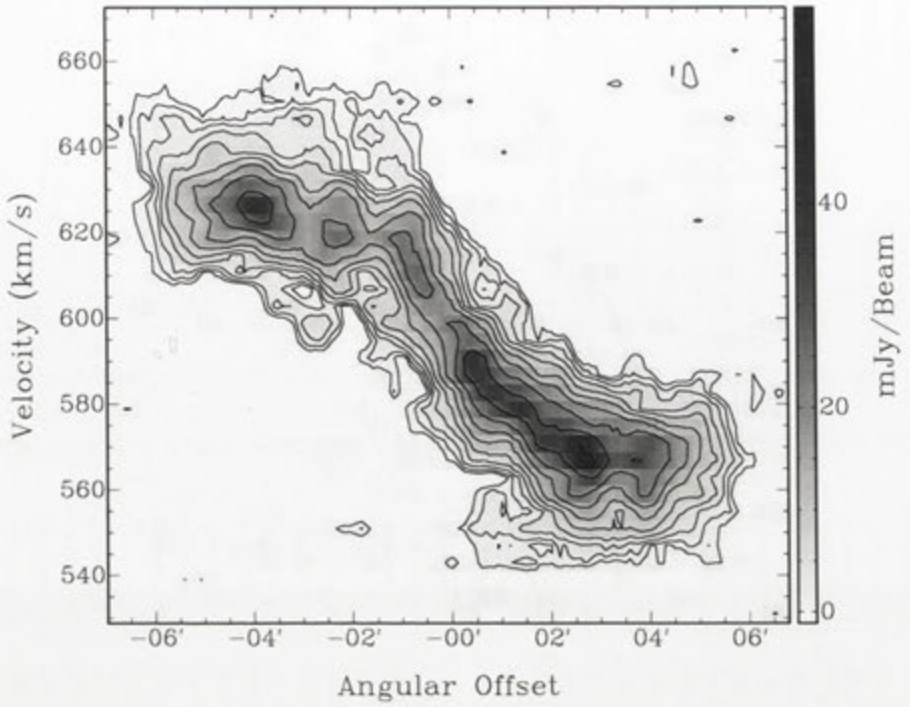

Fig. 6.9: H I position velocity diagram along the major axis of ESO 215-G?009 at a position angle of 119°. The slice is averaged over a width of ∼40″ (slightly larger than the beam size of the H I observations). Contour levels are ±2.0, 2.8, 4.0, 5.7, 8.0, 11.3, 16.0, 22.6, 32.0, and 45.3 mJy beam^{-1}. Negative contours are in light grey.

we used 12 rings of 35″ width.

We found the position angle of ESO 215-G?009 to be constant with radius and over both receding and approaching sides at $PA = 119° \pm 2°$, and thus it was fixed for the remainder of the fitting. The inclination angle i varied between 34° and 44° beyond 180″ but remained mostly around 36° and was fixed at this angle to fit the rotation curve. The resulting rotation curve is shown in Fig. 6.10.

Individual analysis of the approaching and receding sides of the galaxy revealed some differences. The inclination for the best fit to the outer part of the galaxy on the receding side was $i = 40° \pm 6°$ (beyond 150″), while for the approaching side it was $i = 31° \pm 4°$. Fig. 6.10 includes the rotation curves for both sides fitted with the same inclination angle as the overall fit, 36°. There is a slight turn down on the approaching side, while the receding side continues rising slightly. Overall the three rotation curves are reasonably flat beyond 150″.

With $i = 36° \pm 10°$ we find a rotational velocity of $v_{\rm max} = 51 \pm 8$ km s^{-1} out to a radius of 370″ ± 20″ (∼7.5 kpc). We derive a total dynamical mass of $\mathcal{M}_{\rm tot} = (4.5 \pm 1.6) \times 10^9\ \mathcal{M}_\odot$. This gives an H I to dynamical mass ratio of $\mathcal{M}_{\rm HI}/\mathcal{M}_{\rm tot} = 0.11 \pm 0.04$, at the low end of what Roberts & Haynes (1994) found for Sm/Im galaxies (median value 0.15).

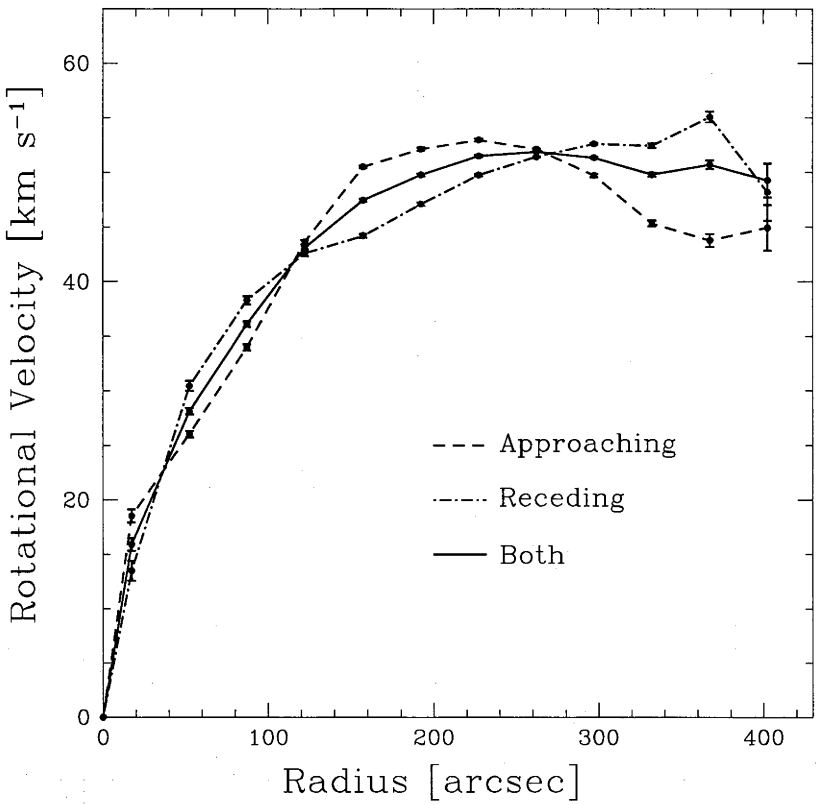

Fig. 6.10: Rotation curve of ESO 215-G?009 as derived from the mean H I velocity field. The three curves correspond to the approaching side (dashed line), receding side (dot-dashed line), and both sides (solid line). For the final ROCUR fit the inclination angle was fixed at 36°, and the position angle at 119°. For details see § 6.4.2.

6.5 Discussion

6.5.1 Comparing Optical and H I Properties

Using Eqn. 1.1, we can now recalculate $\mathcal{M}_{\rm HI}/L_{\rm B}$ using the ATCA integrated H I flux density of 122 ± 4 Jy km s^{-1}, the B band apparent magnitude of 16.13 ± 0.07 mag, and the SFD98 Galactic extinction of 0.95 ± 0.15 mag. We derive an H I mass-to-light ratio for ESO 215-G?009 of $22 \pm 4\ \mathcal{M}_{\odot}/L_{\odot,\rm B}$. A large portion of the uncertainty is due to the uncertainty in the Galactic extinction. This is in good agreement with the preliminary ratio from the BGC of $24 \pm 12\ \mathcal{M}_{\odot}/L_{\odot,\rm B}$. To our knowledge ESO 215-G?009 has one of the highest (if not the highest) $\mathcal{M}_{\rm HI}/L_{\rm B}$ to be confirmed by accurate measurement to date for any galaxy system, being approximately double the $\mathcal{M}_{\rm HI}/L_{\rm B}$ of DDO 154 (Hoffman et al., 1993). Using $\mathcal{M}_{\rm tot} = (4.5 \pm 1.6) \times 10^9\ \mathcal{M}_{\odot}$ and $L_{\rm B} = (2.3 \pm 0.4) \times 10^7\ L_{\odot,\rm B}$, the dynamical mass-to-light ratio is $\mathcal{M}_{\rm tot}/L_{\rm B} = 200 \pm 110\ \mathcal{M}_{\odot}/L_{\odot,\rm B}$, making ESO 215-G?009 an extremely dark matter dominated galaxy. If we assume a stellar mass-to-light ratio

Table 6.3. Comparison of ESO 215-G?009 Properties with those of other Late-Type Dwarf Galaxies.

Property	ESO 215-G?009 (This Thesis)	Late-Type Dwarf Galaxies	Reference	Sample
(1)	(2)	(3)	(4)	(5)
M_B (mag)	-12.9 ± 0.2	-16.8 to -18.6	Roberts & Haynes (1994)	Sm/Im[a]
		-11.5 to -18.3	Lee et al. (2003)	Field dI's
		-12.8 to -17.6	Stil & Israel (2002a)	Im & Sm
$\mu_{B,0}$ (mag arcsec^{-2})	24.97 ± 0.03	24.33 to 20.31	Barazza et al. (2001)	Sm/Im/BCD
L_B ($\times 10^7$ $L_{\odot,B}$)	2.3 ± 0.4	80 to 410	Roberts & Haynes (1994)	Sm/Im[a]
v_{max} (km s^{-1})	51 ± 8	33 to 89	Stil & Israel (2002b)	Im & Sm
$\mathcal{M}_{HI}$ ($\times 10^8$ $\mathcal{M}_\odot$)	5.1 ± 0.2	4.3 to 26.9	Roberts & Haynes (1994)	Sm/Im[a]
		0.098 to 17.4	Lee et al. (2003)	Field dI's
		0.04 to 16.56	Stil & Israel (2002a)	Im & Sm
$\mathcal{M}_{HI}/L_B$ ($\mathcal{M}_\odot/L_{\odot,B}$)	22 ± 4	0.44 to 1.32	Roberts & Haynes (1994)	Sm/Im[a]
		0.15 to 4.2	Lee et al. (2003)	Field dI's
		0.1 to 2.8	Stil & Israel (2002a)	Im & Sm
$\mathcal{M}_{tot}$ ($\times 10^9$ $\mathcal{M}_\odot$)	4.5 ± 1.6	4 to 18	Roberts & Haynes (1994)	Sm/Im[a]
$\mathcal{M}_{HI}/\mathcal{M}_{tot}$	0.11 ± 0.04	0.09 to 0.24	Roberts & Haynes (1994)	Sm/Im[a]
$\mathcal{M}_{tot}/L_B$ ($\mathcal{M}_\odot/L_{\odot,B}$)	200 ± 110	3.1 to 7.9	Roberts & Haynes (1994)	Sm/Im[a]
$(B-V)_0$ (mag)	1.02 ± 0.21	0.35 to 0.51	Roberts & Haynes (1994)	Sm/Im[a]
		-0.18 to 0.73	Stil & Israel (2002a)	Im & Sm
		0.07 to 0.71	Barazza et al. (2001)	Sm/Im/BCD
$(B-R)_0$ (mag)	1.39 ± 0.22	0.61 to 1.24	Parodi et al. (2002)	Sd/Sm/Im/BCD
		0.34 to 1.24	Barazza et al. (2001)	Sm/Im/BCD
$(B-I)_0$ (mag)	1.85 ± 0.22			
$(V-R)_0$ (mag)	0.37 ± 0.20	0.10 to 0.71	Barazza et al. (2001)	Sm/Im/BCD
$(V-I)_0$ (mag)	0.83 ± 0.20			
$(R-I)_0$ (mag)	0.46 ± 0.20			

(1) Properties of ESO 215-G?009.
(2) Value we have derived for this property from our results.
(3) Typical range for this property in late-type dwarf galaxies as found in various literature sources.
(4) Reference for the column (3) value.
(5) Galaxy types within the sample from the column (4) reference.

[a]Quartile range.

of ~ 1 $\mathcal{M}_\odot/L_{\odot,B}$, we estimate a baryonic mass to total mass ratio of $\mathcal{M}_{bary}/\mathcal{M}_{tot} = 0.12$.

Fig. 6.6a shows that the H I envelope extends out much further than the main stellar component of the galaxy. For ESO 215-G?009 the H I gas can be traced out to $370'' \pm 20''$, while the Holmberg radius is only $57\farcs6 \pm 0\farcs6$ (at the extinction corrected surface brightness of 26.6 mag arcsec^{-2}). Therefore the gas extends to 6.4 ± 0.4 times the Holmberg radius, comparable to the extent of DDO 154 (Carignan & Purton, 1998).

The brightest part of the central stellar region (see Fig. 6.1) is slightly elongated in a direction aligned much closer to the rotational minor axis ($\sim 40°$). As the galaxy is seen at a low inclination this feature is potentially a weak central bar. The optical morphology of ESO 215-G?009 is otherwise rather smooth and featureless for a dwarf irregular, although its slightly mottled appearance in colour images,

the slowly rotating H I disk, and possible H II regions (see § 6.5.4) imply it is a late-type dwarf galaxy. The stellar distribution is located in the centre of the H I disk at the position of a shallow depression in the H I distribution.

6.5.2 The Importance of Accurate Multi-wavelength Measurements

To demonstrate the great uncertainties that can arise in determining H I mass-to-light ratios we will briefly discuss the Orion dwarf galaxy (H I 0542+05). In their initial study of H I envelopes around low luminosity galaxies, van Zee, Haynes, & Giovanelli (1995) included 33 galaxies mostly taken from the *Uppsala General Catalog* which they believed to have high $\mathcal{M}_{\rm HI}/L_{\rm B}$ ($> 5\ \mathcal{M}_{\odot}/L_{\odot,{\rm B}}$). One of these galaxies is the Orion dwarf, for which they derived an extreme $\mathcal{M}_{\rm HI}/L_{\rm B}$ of 84.1 $\mathcal{M}_{\odot}/L_{\odot,{\rm B}}$ using their measured Arecibo flux density of $F_{\rm HI} = 74.16$ Jy km s^{-1} and an extinction corrected B magnitude of 17.1 mag. They did not discuss this galaxy further. The optical magnitude for this galaxy, and for many others objects in their sample, had been obtained by eye. Unfortunately many were underestimates. Van Zee et al. (1997) state that "...the catalogued magnitudes of these systems were a severe underestimate of their true luminosity (by $\sim 1.5^m$); however, the revised values of $\mathcal{M}_H/L_B$ are still more than a factor of 2 higher than typical for dwarf galaxies". In later investigations (van Zee et al., 1996, 1997; van Zee, 2000, 2001) no galaxies with $\mathcal{M}_{\rm HI}/L_{\rm B} > 7\ \mathcal{M}_{\odot}/L_{\odot,{\rm B}}$ were found. In addition to this the Galactic extinction correction used for the Orion dwarf galaxy (~0.9 mag, Burstein & Heiles, 1978, although it is not clearly stated) is possibly also a severe underestimate as recent measurements give $A_{\rm B} = 3.17 \pm 0.51$ mag (SFD98), and Burstein & Heiles (1982) give 2.84 mag. They may have mistaken $A_{\rm B}$ for $EB-V$. Karachentsev & Musella (1996) performed the first CCD photometry on this galaxy getting a new $m_{\rm B}$ of 15.7 mag, and using an extinction of 2.7 mag they derived $\mathcal{M}_{\rm HI}/L_{\rm B} = 2.6\ \mathcal{M}_{\odot}/L_{\odot,{\rm B}}$. Barazza, Binggeli, & Prugniel (2001) found a similar B magnitude of 15.41 mag. Combined with the rise in the Galactic extinction, this galaxy appears approximately 5 magnitudes brighter than in van Zee et al. (1995), which means $\mathcal{M}_{\rm HI}/L_{\rm B}$ is overestimated by a factor of around 100. Using the Barazza et al. (2001) B magnitude, the SFD98 Galactic extinction, and the H I flux density from HIPASS ($F_{\rm HI} = 73 \pm 4$ Jy km s^{-1}), a more accurate H I mass-to-light ratio for the Orion dwarf (HIPASS J0545+05) is $0.9 \pm 0.5\ \mathcal{M}_{\odot}/L_{\odot,{\rm B}}$.

Problems can also arise with the H I observations. O'Neil, Bothun, & Schombert (2000) find four galaxies in the range $10\ \mathcal{M}_{\odot}/L_{\odot,{\rm B}} < \mathcal{M}_{\rm HI}/L_{\rm B} < 50\ \mathcal{M}_{\odot}/L_{\odot,{\rm B}}$ as part of an Arecibo follow-up of a group of low surface brightness galaxies, as well as six galaxies that deviated from the Tully & Fisher (1977) relationship. These were the first extragalactic observations taken after an upgrade at Arecibo. Later Chung et al. (2002) found that many of the galaxies observed by O'Neil et al. (2000) had been contaminated by other neighbouring objects within the sidelobes (see Heiles et al., 2001).

We conclude that to obtain accurate H I mass-to-light ratios it is vitally important that the H I flux density, the B band apparent magnitude and the Galactic extinction are well determined; error bars on all are essential and should always be quoted. Galaxies located near the Galactic Plane, where the extinction is high and uncertainty increases, are particularly difficult and should be treated with extra care.

6.5.3 Other Uncertainties to Consider

How well do we know the distance to ESO 215-G?009? While we have adopted the Hubble flow distance to ESO 215-G?009 of 4.2 Mpc using the Local Group velocity in this Thesis, the relative uncertainty in such a distance can be large for nearby galaxies. This is mostly due to peculiar motions and the difficulty in measuring the Hubble constant in the Local Universe. Alternatively, we can calculate a distance from the baryonic Tully & Fisher (1977) relationship (McGaugh et al., 2000) by first estimating a baryonic mass for ESO 215-G?009 from the relationship given the galaxy's rotation velocity of 51 ± 8 km s^{-1}. We estimate $\mathcal{M}_{\rm bary} = 2.1 \times 10^8\ \mathcal{M}_{\odot}$. Given the H I flux density and the B band apparent magnitude then ESO 215-G?009 would have to be at a distance of 2.6 Mpc to have this baryonic mass, almost half the Hubble flow distance. At the Hubble flow distance ESO 215-G?009 would lie above the baryonic Tully Fisher relationship. Table 6.4 gives examples of the effect of this uncertainty on the main distance dependent properties in this chapter. It shows the derived quantities at both distances, with the quoted uncertainty accounting for all other sources of error. Uncertainty in the estimated distance can have a large effect on properties such as B band luminosity and H I mass, both of which change by a factor of $\sim$2.5 between the two estimates. Baryonic Tully Fisher distances were not adopted in this Thesis as there is currently large uncertainty at the low-mass end of the relation.

Galactic dust extinction can strongly affect the final $\mathcal{M}_{\rm HI}/L_{\rm B}$ result, as we have seen in § 6.5.2. The relatively high Galactic extinction in the direction of ESO 215-G?009 and the large number of foreground stars may mean that we could ultimately miss some very faint components of the galaxy, and so underestimate the total apparent magnitude. There is also the question of whether the value of Galactic extinction we are using is completely wrong. The SFD98 Galactic extinction is measured over large scales, and there may be smaller scale variation. The redder colour of the galaxy may suggest stronger extinction than we are accounting for. To test this we looked at the extinction correction for galaxies in the surrounding field to see if there was a large extinction gradient in the area. We found that out to a radius of 1° the variation was between 0.8 and 1.1 mag, within the uncertainties of the extinction at ESO 215-G?009's position, and so we are confident that $A_{\rm B}$ is not too far from the SFD98 value. However we note that close to the Galactic Plane the dust distribution can be patchy, and it is entirely

Table 6.4. Comparison of Distance Dependent Properties for ESO 215-G?009 at Different Adopted Distances.

Property	Hubble Flow $D = 4.2$ Mpc	Baryonic Tully Fisher $D = 2.6$ Mpc
(1)	(2)	(3)
M_B (mag)	-12.9 ± 0.2	-11.9 ± 0.2
L_B ($\times 10^7$ $L_{\odot,B}$)	2.3 ± 0.4	0.9 ± 0.1
$\mathcal{M}_{HI}$ ($\times 10^8$ $\mathcal{M}_\odot$)	5.1 ± 0.2	1.95 ± 0.06
$\mathcal{M}_{tot}$ ($\times 10^9$ $\mathcal{M}_\odot$)	4.5 ± 1.6	2.8 ± 1.0
$\mathcal{M}_{HI}/\mathcal{M}_{tot}$	0.11 ± 0.04	0.07 ± 0.02
$\mathcal{M}_{tot}/L_B$ ($\mathcal{M}_\odot/L_{\odot,B}$)	200 ± 110	320 ± 150

(1) Property of ESO 215-G?009.
(2) Value for this property from our results using the Hubble flow distance.
(3) Value for this property from our results using the baryonic Tully Fisher distance.

possible that the extinction could be much higher at the position of ESO 215-G?009 than current measurements indicate.

Extinction from within ESO 215-G?009 itself must also be considered as that may reduce the total light we receive and redden the galaxy. It is not possible currently to estimate what the dust extinction could be in this galaxy as internal extinction is poorly understood in dwarf irregular galaxies, though it is often assumed to be low. The inclination of the galaxy is quite low as seen from the rotation curve analysis, and assuming that most of the galaxy's dust is in the plane of the H I, we find it unlikely that internal dust extinction has a large effect on the luminosity of ESO 215-G?009.

6.5.4 Stellar Population and Star Formation

The photometric colours (see end of Table 6.3) are all fairly red for a dwarf irregular galaxy, suggesting that ESO 215-G?009 contains a mainly old stellar population, which is uncommon in late-type galaxies. Parodi, Barazza, & Binggeli (2002) find the mean colour for late-type galaxies in their sample is $\langle B-R \rangle_{Late} = 0.90$, while for the small number of early-types in their sample it is $\langle B-R \rangle_{Early} = 1.21$. Their reddest late-type galaxy is ESO 006-G001 with $B-R = 1.24$, a galaxy they claim has an intermediate morphology (both late- and early-type). ESO 215-G?009's value of $(B-R)_0 = 1.39 \pm 0.22$ is closer to the colours of the dwarf ellipticals and the more extreme late-type dwarfs in the sample. The median $B-V$ colour for 210 Sm/Im galaxies in the Local Supercluster from Roberts & Haynes (1994) is 0.42. Again ESO 215-G?009 has a much redder colour, $(B-V)_0 = 1.02 \pm 0.21$. It should be noted that the uncertainties in these colours are quite high because of the position of the galaxy close to the Galactic Plane. Unfortunately these higher uncertainties due to Galactic extinction prevent us from performing a detailed analysis of the age and metallicity of the underlying stellar population.

Several of the colour profiles (Fig. 6.3) show slight gradients between the inner and outer regions of the galaxy. The $(B-I)_0$, $(V-I)_0$, and $(R-I)_0$ profiles all have shallow but distinct positive gradients going out from the galaxy center, meaning that the outer region of the galaxy is redder than the center. $(B-V)_0$, $(B-R)_0$, and $(V-R)_0$ had mostly flat trends, with the first two turning slightly to the blue at the outer edges. Parodi et al. (2002) also find that dwarf galaxies often have a positive colour gradient, with younger/bluer stars in the inner regions and the older/redder population in the outer regions. This is the opposite of larger spiral systems where spiral density waves drive star formation in the outer disk and the central region is dominated by an older red bulge. Of the late-type galaxies in the Parodi et al. (2002) sample only eight show a positive gradient in $B-R$, while a further eight showed a flat profile and a few showed negative profiles. In this colour ESO 215-G?009 also shows a mostly flat trend. It appears that there may be a slightly higher proportion of younger stars in the centre of ESO 215-G?009, but as we do not see it in all colours this trend is unlikely to be strong. van Zee (2001) find that colour gradients in dwarf irregular galaxies in a quiescent phase (non-starbursting) are generally not as pronounced as those of starburst galaxies (such as BCDs, where there is strong star formation confined to a small central region).

During the star subtraction of the optical images (Fig. 6.1) several bright slightly extended objects close to the galaxy which we believe are H II regions were not removed. The two most prominent can be seen best in the B image, on the outer north-eastern edge of the galaxy and close in on the north-western side. These regions appear to be rather blue compared with the rest of the galaxy. However they may be background galaxies or foreground features rather than H II regions associated with ESO 215-G?009. To try and confirm that these are indeed star forming regions we examined the SuperCOSMOS H-alpha Survey (SHS) image of the field around ESO 215-G?009 (Hambly et al., 2001, and references therein). The image can be seen in Fig. 6.11 with the contours from our 20 cm radio continuum observation of the field overlaid. The two regions mentioned show up distinctly as diffuse objects, while the main galaxy is barely visible at all. Two further diffuse regions are visible well beyond the optical galaxy and almost to the edge of the H I disk on the south eastern side. However, none of these diffuse regions in the Hα image correspond to any of the 20 cm continuum sources in the field. All of these objects could be H II regions in ESO 215-G?009, but this needs to be confirmed with follow up spectra and Hα imaging.

The upper limit for the star formation rate as derived from the 20 cm radio continuum flux density measurement within the optical galaxy region, $\sim 2.5 \times 10^{-3}\ \mathcal{M}_{\odot}\,\mathrm{yr}^{-1}$, is on the lower side even when compared with other quiescent dwarf irregular galaxies such as the sample of van Zee (2001). As is described in that paper, deriving a past star formation rate to compare with the present rate can be problematic for dwarf irregular galaxies. A rough estimate of the average

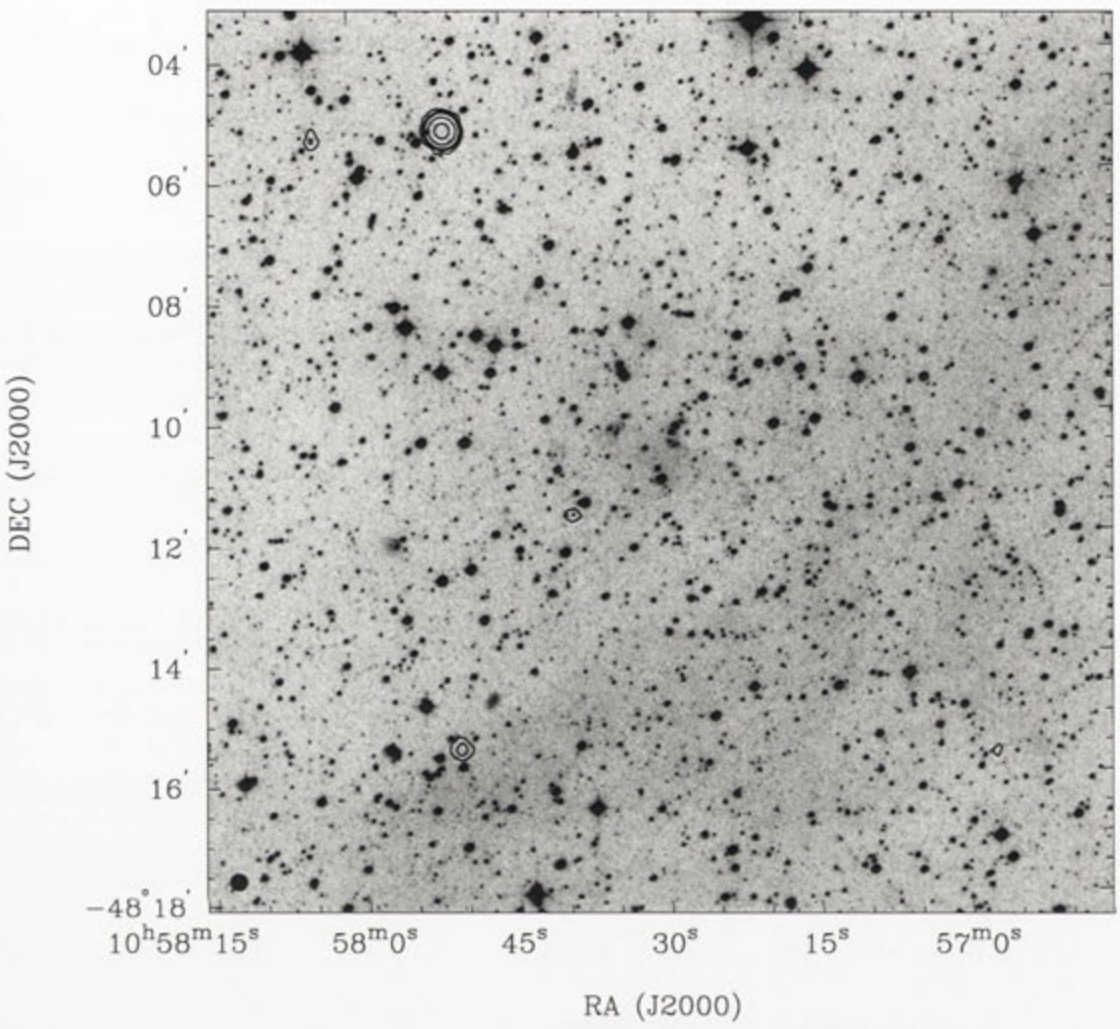

Fig. 6.11: The 20 cm radio continuum map overlaid on the SHS Hα image of the field around ESO 215-G?009.

past star formation rate for ESO 215-G?009 can be derived by dividing the total mass of stars formed by the length of time for which the galaxy has been forming stars, which can be expressed as (Tinsley, 1980):

$$\langle SFR \rangle_{past} = \frac{\Gamma_{\rm B} L_{\rm B}}{T_{sf}(1-R)} \ \mathcal{M}_{\odot}\,{\rm yr}^{-1}, \tag{6.3}$$

where $\Gamma_{\rm B}$ is the B band stellar mass-to-light ratio in $\mathcal{M}_{\odot}/L_{\odot,{\rm B}}$, T_{sf} is the time for which the galaxy has been forming stars in years, and R is the recycling fraction (essentially the proportion of the stars formed within the galaxy that are no longer visible).

$\Gamma_{\rm B}$ is poorly understood for dwarf irregular galaxies (see van Zee, 2001, and references therein), and as a conservative estimate we used $\Gamma_{\rm B} \sim 1\ \mathcal{M}_{\odot}/L_{\odot,{\rm B}}$ for ESO 215-G?009, although the actual value is probably higher given the seemingly older stellar population of the galaxy. For the other parameters in Eqn. 6.3 we

use the assumptions made in van Zee (2001) of $T_{sf} = 13$ Gyr and $R = 0.33$. Using $L_{\rm B} = (2.3 \pm 0.5) \times 10^7\ L_{\odot,{\rm B}}$ we derive $\langle SFR \rangle_{past} \sim 2.7 \times 10^{-3}\ \mathcal{M}_{\odot}\ {\rm yr}^{-1}$. Although this finding is uncertain, it is close to our upper limit for current star formation rate, suggesting either that star formation has been more or less constant throughout ESO 215-G?009's history or it may have been slightly higher in the past. It certainly implies that there have not been any major starburst events in ESO 215-G?009 during its history, consistent with the galaxy being spatially isolated and possibly never having interacted with another galaxy. The minimum gas depletion timescale for ESO 215-G?009 given the current star formation rate upper limit and using the same recycling fraction as above is ~ 300 Gyr.

6.5.5 *The Star Formation Threshold*

Kennicutt (1989, hereafter K89) and Martin & Kennicutt (2001, hereafter MK01) have found that gravitational instability may determine the star formation law for galactic disks, first proposed by Spitzer (1968) and Quirk (1972). K89 found that a modification to the simple thin-disk stability model proposed by Toomre (1964) could produce satisfactory star formation threshold gas surface densities in active star-forming galaxies. The model, the Toomre Q criterion, as a function of radius is given by (MK01):

$$Q(r) \equiv \frac{\sigma(r)\kappa(r)}{\pi G \mu_{gas}(r)}, \tag{6.4}$$

where $\sigma(r)$ is the gas dispersion velocity, $\kappa(r)$ is the epicyclic frequency, and $\mu_{gas}(r)$ is the surface density of the gas in the disk. When Q is less than 1 a thin galactic disk will be unstable to axisymmetric disturbances. This was used by K89 to derive a critical gas surface density $\mu_{crit}(r)$ above which large-scale star formation can occur, given by (MK01):

$$\mu_{crit}(r) = \alpha_Q \frac{\sigma(r)\kappa(r)}{\pi G}, \tag{6.5}$$

where α_Q is a constant close to unity which is included to account for a more realistic disk (i.e. thicker disk, embedded stellar population). $\alpha_Q = 1$ would return the model to the thin-disk approximation. If $\mu_{gas}(r)$ exceeds $\mu_{crit}(r)$ then the disk will be unstable (Q would be less than 1) and large-scale star formation can occur.

K89 examined the ratio $\mu_{gas}(r)/\mu_{crit}(r)$ (with a simplified model of $\mu_{crit}(r)$ and $\alpha_Q = 1$) as it approached $r_{\rm HII}$, the radius at the edge of the H II region disk, for a sample of active star forming galaxies (mostly Sb and Sc). He found that at this radius the ratio values were all remarkably well constrained between $\sim$0.5 and 0.85, and was able to determine a value of $\alpha_Q = \mu_{gas}(r_{\rm HII})/\mu_{crit}(r_{\rm HII}) = 0.63$[1]. MK01 reexamined these results with a larger sample and more detailed input parameters

[1] Adjusted as in MK01

(including measurements of the H_2 gas from CO observations). They confirmed the previous results for most spiral galaxies in the outer regions of galactic disks. They determined a median $\alpha_Q(r_{\rm HII}) = 0.69$, and found a weak trend for late-type galaxies to have higher $\alpha_Q(r_{\rm HII})$. They also found that the simple Toomre criterion breaks down in some circumstances, such as low shear rates and stellar bars.

We have examined the star-formation threshold throughout ESO 215-G?009 as a function of radius to determine if a subcritical gas density is preventing the galaxy from large-scale star formation. The gas velocity dispersion $\sigma(r)$ comes from our azimuthally averaged H I velocity dispersion radial profile. The epicyclic frequency $\kappa(r)$ can be determined from our H I rotation curve using (MK01):

$$\kappa^2(r) = 2\left(\frac{V^2}{R^2} + \frac{V}{R}\frac{dV}{dR}\right) \quad \mathrm{s}^{-2}, \tag{6.6}$$

where V is the rotation velocity in $\mathrm{km\,s^{-1}}$, and R is the radius in km. The derivative was determined with a forward difference method. We have assumed $\alpha_Q = 1$. Only the azimuthally averaged H I surface density, $\mu_{\rm HI}(r)$, was available for the gas surface density. We have made no estimate of the molecular hydrogen content (as was done in K89) for ESO 215-G?009 at this stage.

From these data we have estimated the ratio $\mu_{\rm HI}(r)/\mu_{crit}(r)$ as a function of radius, which can be seen in Fig. 6.12. Over all radii the ratio is less than the MK01 value of $\alpha_Q = 0.69$, strongly suggesting that the H I gas surface density of ESO 215-G?009 is not high enough to induce large-scale star formation within the disk. The profile is similar to the galaxies in both K89 and MK01 with low levels of star formation. However, the majority of those galaxies are early-type spiral galaxies (Sa to Sb), not dwarf galaxies. The exclusion of molecular gas from our estimate may have caused a significant underestimate of $\mu_{gas}(r)/\mu_{crit}(r)$, which may lead to part of the profile rising above the threshold. The estimate that K89 used ($\mu_{gas}(r) = 1.41\mu_{\rm HI}(r)$) may not be appropriate for ESO 215-G?009 or other dwarf irregular galaxies, so the only way to resolve this issue would be to obtain CO observations to estimate the H_2 content (which may be problematic for ESO 215-G?009 if the metalicity and excitation are low). It is important to note also that, as MK01 mention, using the azimuthally averaged H I surface density may not be appropriate for galaxies like ESO 215-G?009 where the variation in density at a particular radius can be large. Several regions of the galaxy have H I densities much higher than the azimuthal average at their location (such as the region to the north of the galaxy center) and local densities may approach or exceed the threshold density.

6.5.6 Possible Causes of a High $\mathcal{M}_{\rm HI}/L_{\rm B}$

Table 6.3 gives a summary of the major properties of ESO 215-G?009, and how they compare with literature values for "typical" late-type dwarf galaxies. Column

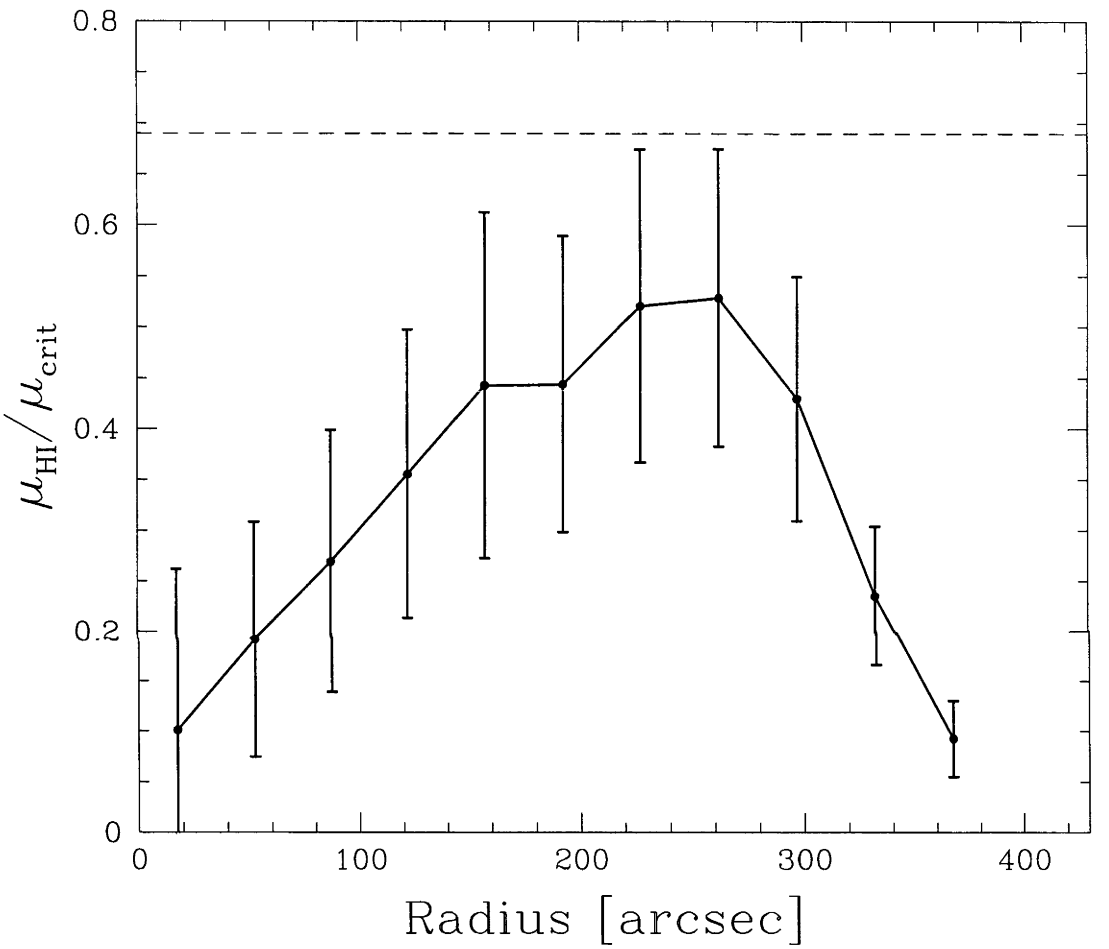

Fig. 6.12: The ratio of H I surface density to the critical surface density (as predicted from the Toomre (1964) thin-disk gravitational stability Q criterion for thin-disks) as a function of radius for ESO 215-G?009. The dashed line shows $\alpha_Q = 0.69$, the median value from Martin & Kennicutt (2001) above which the gas density is high enough for large-scale star formation (see § 6.5.5). Error bars reflect the uncertainties in the H I radial profile, H I velocity dispersion profile and rotation curve.

(1) gives the property. Column (2) gives the value we have derived for ESO 215-G?009. Column (3) gives the typical range for this property in late-type dwarf galaxies as found in various literature sources. Column (4) gives the reference for the column (3) value, and column (5) gives the galaxy types within the sample from that reference. The results from Roberts & Haynes (1994) are given as the inter-quartile range for Sm and Im galaxies, while other results cover the full range of the sample given in the reference. When compared with the Roberts & Haynes (1994) sample, the total mass of ESO 215-G?009 is at the low end of the quartile range, and we can use this as an anchor point for comparing the other parameters. We see that the H I mass is also at the low end of the quartile range (along with other parameters not dependent on the luminosity), and in general is consistent with the literature values for late-type galaxies. However, along with ESO 215-G?009's $\mathcal{M}_{\rm HI}/L_{\rm B}$, parameters such as luminosity (and therefore absolute magnitude) and total mass-to-light ratio can differ from the typical dwarfs by an order of magnitude or more. Galaxies with such low luminosities/absolute magnitudes are still in other dwarf irregular samples (see Lee et al., 2003; Stil & Israel, 2002a) but are generally among the outliers. This suggests that ESO 215-G?009 has a normal H I content for its type, but is underluminous.

ESO 215-G?009 shows no signs that it has been perturbed by a neighbour. No nearby galaxies were found within the H I data cube. We searched the field around the galaxy in LEDA out to approximately 13.°6 (1 Mpc at our assumed distance of 4.2 Mpc) within the velocity range 200 km s^{-1} < v_{sys} < 1300 km s^{-1}. We found nine galaxies, all with $M_{\rm B}$ < -17.5 mag, all but one being a late-type spiral or irregular. Only one galaxy, ESO 264-G035, had a systemic velocity close to ESO 215-G?009's of v_{sys} = 770 km s^{-1}, which is still much higher than ESO 215-G?009's velocity. Karachentsev et al. (2002) include ESO 215-G?009 (KKs 40) in their list of galaxies around the Centaurus A group (26.°16 away). While this is the nearest group, assuming that they are the same distance from us (the Cen A group is $\sim$ 4 Mpc away, Jerjen, Freeman, & Binggeli, 2000) then ESO 215-G?009 is well outside the group at a projected distance of 1.9 Mpc from the centre. The nearest galaxy in this group to ESO 215-G?009 appears to be the large spiral NGC 4945, but it is still at a projected distance of $\sim$1.7 Mpc. So from our current knowledge of the field around it ESO 215-G?009 is a very isolated system.

If ESO 215-G?009 were still in its first episode of collapse that may explain why it has been able to hold onto its H I. For the rotational velocity at the outer edge of the H I disk (see § 6.4.2) the dynamical timescale of ESO 215-G?009 is 9.1×10^8 years. This is a much shorter timescale than a Hubble time and is similar to that which van Zee et al. (1996) found for UGCA 020 ($\sim 8 \times 10^8$ years). For most of the galaxies in van Zee et al. (1995) the free fall timescale was less than $\sim 7 \times 10^8$ years. In contrast, Giovanelli, Williams, & Haynes (1991) investigated the dynamically young "evolving" system H I 1225+01 and found the free-fall timescale to be on the order of 5×10^9 years, and the dynamical timescale to be even longer

($\sim 1 \times 10^{10}$ years). This suggests that ESO 215-G?009 is not currently in the process of collapsing for the first time. Instead, van Zee et al. (1996) suggest that this indicates the evolution process has been inhibited in some way.

This possibility is supported by the stellar population, which suggests that while some star formation is continuing today the majority of stars in ESO 215-G?009 are from past star formation events. It certainly is not undergoing any vigorous star formation activity currently, and the past star formation rate suggests that it may never have undergone such a phase. The stellar population and star formation rate (present and past) are consistent with the galaxy having a low, more or less constant star formation rate since its formation. As the galaxy shows no sign of disturbance, a slow, constant star formation rate is also consistent with the isolation of the galaxy. Finally, the analysis of H I gas surface density compared with the star formation threshold density derived from the Toomre stability criterion shows that gas density is probably too low for efficient star formation, although further analysis of ESO 215-G?009's molecular gas content and of the validity of this criterion in dwarf irregulars is required. Verde, Oh, & Jimenez (2002) propose that, if angular momentum is conserved during gas contraction, low mass dark matter halos may form Toomre stable discs and therefore remain "dark" galaxies with little star formation. ESO 215-G?009 is potentially such a galaxy, and if these dark galaxies do exist in sufficient numbers it could go some way to explain the current discrepancy between observed galaxy counts and the predictions from theoretical models such as ΛCDM. This is an idea we will discuss in more detail in the following chapter.

7. ON THE NUMBER FREQUENCY OF DARK GALAXIES IN THE LOCAL UNIVERSE: A STUDY OF NINE SAMPLE GALAXIES

In Chapter 1 we looked at the disagreement between the number of low mass dark matter halos predicted by ΛCDM cosmological models and the number of faint galaxies that have been observed. The existence of many high $\mathcal{M}_{\rm HI}/L_{\rm B}$ galaxies are one of the possible scenarios which could correct the observational results. If we could find more of galaxies similar to ESO 215-G?009 it may go some way to explaining the discrepancy between the dark matter halo mass function and the observed galaxy luminosity function. In this chapter, to be published shorlty as Warren, Jerjen, & Koribalski (2005a), to continue our study of the physical properties of galaxies with high $\mathcal{M}_{\rm HI}/L_{\rm B}$ we have selected nine candidates (including ESO 215-G?009) from our sample that appear to have high ratios, ranging from above average ratios of $\sim 3\ \mathcal{M}_{\odot}/L_{\odot,\rm B}$ up to what might be considered extreme ratios of $\sim 27\ \mathcal{M}_{\odot}/L_{\odot,\rm B}$. These include the galaxies with the highest ratios in our sample, and also some chosen for reasons of unusual morphology or after initial ATCA follow up observations produced unexpected results (see § 7.2.1). From these results we will look at whether there exist sufficent numbers of high $\mathcal{M}_{\rm HI}/L_{\rm B}$ galaxies to correct observed luminosity functions, and the implications of the existance of galaxies like ESO 215-G?009

7.1 The Nine Galaxies Selected

Table 7.1 summarises some of the previously measured properties of the nine galaxies which we have chosen for examination here (see Chapter 3 for full details). The sample includes the four galaxies with multiple deep east-west array H I observations on the ATCA (ESO 121-G020, ESO 428-G033, ESO 215-G?009, and ESO 348-G009) for which we have been able to obtain rotation curves (see below). It also includes the three galaxies where we have deep observations on the hybrid arrays (MCG–04-02-003, ESO 505-G007, and IC 4212), which have much poorer resolution. The remaining two only had H I snapshots (both on hybrid arrays). 2.3m B and R band photometry was available for all nine galaxies, while V and I photometry was obtained for most. See Chapter 4 for the full observing details.

Table 7.1. Summary of BGC and LEDA Properties of the Nine Galaxies Selected from Our Sample.

Name HIPASS Name (1)	Center α(J2000.0) δ(J2000.0) (2)	Galactic l b (3)	BGC v_{sys} (km s^{-1}) (4)	BGC D (Mpc) (5)	BGC F_{HI} (Jy km s^{-1}) (6)	LEDA m_B (mag) (7)	SFD98 A_B (mag) (8)	M_B (mag) (9)	$\mathcal{M}_{HI}/L_B$ ($\mathcal{M}_\odot/L_{\odot,B}$) (10)
MCG–04-02-003	$00^h\,19^m\,11^s$	62°.6	669 ± 3	9.5	16.0 ± 2.5	15.8 ± 0.2	0.08 ± 0.01	-14.1 ± 0.2	4.8 ± 1.6
HIPASS J0019–22	$-22°\,40'\,14''$	−81°.4							
ESO 473-G024	$00^h\,31^m\,23^s$	75°.7	540 ± 4	7.6	7.2 ± 1.8	16.2 ± 0.2	0.08 ± 0.01	-13.3 ± 0.2	3.0 ± 1.3
HIPASS J0031–22	$-22°\,46'\,02''$	−83°.7							
ESO 121-G020	$06^h\,15^m\,53^s$	266°.5	577 ± 5	4.1	14.1 ± 2.9	17.0 ± 0.4	0.17 ± 0.03	-11.3 ± 0.4	11 ± 6
HIPASS J0615–57	$-57°\,43'\,24''$	−27°.3							
ESO 428-G033	$07^h\,25^m\,49^s$	244°.2	1727 ± 4	19.5	12.8 ± 2.7	17.9 ± 0.5	1.10 ± 0.18	-14.7 ± 0.5	10 ± 7
HIPASS J0725–30B	$-30°\,55'\,05''$	−6°.9							
ESO 215-G?009	$10^h\,57^m\,30^s$	284°.1	598 ± 2	4.2	104.4 ± 11.5	16.4 ± 0.4	0.95 ± 0.15	-12.6 ± 0.4	24 ± 12
HIPASS J1057–48	$-48°\,11'\,02''$	10°.5							
ESO 572-G009	$11^h\,53^m\,23^s$	284°.1	1745 ± 3	20.4	8.5 ± 1.9	17.4 ± 0.2	0.16 ± 0.03	-14.3 ± 0.2	10 ± 4
HIPASS J1153–18	$-18°\,09'\,59''$	42°.6							
ESO 505-G007	$12^h\,03^m\,30^s$	289°.5	1785 ± 4	20.8	20.5 ± 3.2	17.7 ± 0.2	0.36 ± 0.06	-14.2 ± 0.2	27 ± 9
HIPASS J1203–25	$-25°\,28'\,22''$	36°.1							
IC 4212	$13^h\,12^m\,09^s$	312°.0	1484 ± 2	18.1	47.5 ± 4.6	16.4 ± 1.1	0.19 ± 0.03	-15.0 ± 1.1	~ 23[a]
HIPASS J1311–06	$-06°\,58'\,31''$	55°.5							
ESO 348-G009	$23^h\,49^m\,23^s$	349°.8	648 ± 4	8.4	13.4 ± 2.2	16.7 ± 0.7	0.06 ± 0.01	-13.0 ± 0.7	9 ± 7
HIPASS J2349–37	$-37°\,46'\,23''$	−73°.2							

(1) Optical and HIPASS name of the galaxy.
(2) J2000.0 right ascension and declination from the RC3 (de Vaucouleurs et al., 1991).
(3) Galactic longitude and latitude.
(4) Systemic velocity taken from the BGC.
(5) Approximate distance derived from the BGC Local Group velocity.
(6) BGC total integrated H I flux density.
(7) Apparent B band magnitude as it appears in LEDA.
(8) SFD98 Galactic dust extinction value in the B band.
(9) Absolute B band magnitude calculated as in eqn. 3.4 using the LEDA magnitude and SFD98 extinction.
(10) Preliminary estimate of the H I mass-to-light ratio calculated as in eqn. 3.3 from the LEDA, BGC and SFD98 data.

[a]Uncertainty in LEDA apparent magnitude gives unrealistic uncertainty in $\mathcal{M}_{HI}/L_B$. Uncertainty not expressed.

7.2 Radio Properties

7.2.1 H I Structure

The integrated H I distribution for all nine galaxies overlaid on Digitized Sky Survey (DSS) II red optical images are shown in Appendix A with the maps for the other galaxies. The beam sizes differ a lot between the four galaxies observed on the longer east-west configurations and the five that used only the compact hybrid arrays. Of the hybrid observations, four galaxies (ESO 473-G024, ESO 572-G009, ESO 505-G007, and IC 4212) had beams too large to resolve anything of the H I structure of the galaxy (although in the case of IC 4212 the size of the source indicates it may be extended, and ESO 505-G007 has a neighbour). Only for MCG–04-02-003 is the beam sufficiently small that we can see that the H I distribution is extended significantly North-South (although little other structure is distinguishable). In contrast we have very high resolution in the H I distribution maps for the fields of ESO 121-G020, ESO 428-G033, ESO 215-G?009, and ESO 348-G009, all observed with multiple arrays of various lengths. In all of these images we can see detailed structure within the H I disks of the galaxies, and in the case of ESO 121-G020 a previously uncatalogued companion (see below). Due to the resolution differences the galaxies have been plotted on different scales.

The H I spectra of the galaxies are also shown in Appendix A. Five galaxies (MCG–04-02-003, ESO 428-G033, ESO 215-G?009, IC 4212, and ESO 348-G009) appear to have shapes similar to the classic double horn profile of a rotating disk galaxy, with those for MCG–04-02-003, ESO 428-G033, and IC 4212 being especially prominent. As IC 4212 appears close to face on in optical images, the broad double horn profile ($w_{50} = 158 \pm 2$ km s^{-1}) suggests that the galaxy is rotating very fast. The spectra for ESO 473-G024 and ESO 572-G009 on the other hand are narrow lines, which suggests that they might be seen from face on.

As well as confirming the BGC identification of the optical counterpart for the H I source, looking at detail of the structure, and possibly obtaining rotation curves, one of the most important reasons for ATCA follow-up of the HIPASS detections is shown by the high resolution H I distribution map of ESO 121-G020 (see page 175). The map reveals that while most of the H I emission in this field comes from the optically identified low surface brightness irregular galaxy ESO 121-G020, there is a previously uncatalogued companion galaxy only 2′57″ away that also has a significant quantity of H I emission. We will refer to this new galaxy as ATCA J061608–574552 according to its measured H I centre position. The spectra of the individual galaxies as well as the total spectrum for the system is shown in Fig. 7.1 (the ATCA spectrum in Appendix A, Fig. A.40 is the overall system spectrum).

The two objects are well resolved spatially in our observations, and any bridge that might exist between them or tails caused by tidal interaction are below our

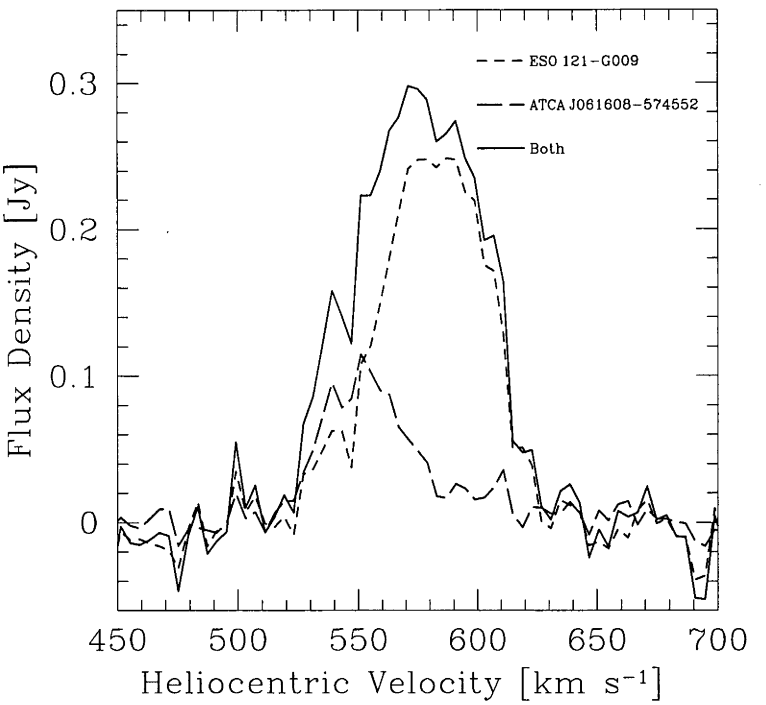

Fig. 7.1: H I spectra of ESO 121-G020 and ATCA J061608–574552 as obtained from the ATCA, showing the spectra for both galaxies (dashed lines) and for the total system (solid line, as shown in Fig. A.40).

detection limits. The systemic velocity difference between these two galaxies is only 21 ± 6 km s^{-1}, much less than the 50% velocity width of both galaxies. The two galaxies are unresolved in the HIPASS data, so the BGC flux density includes all the H I from both objects but the LEDA data we used to calculate $\mathcal{M}_{\rm HI}/L_{\rm B}$ only includes light from ESO 121-G020. ATCA J061608–574552 has no known optical measurements so we included it in our optical observations (see § 7.3). The inclusion of ATCA J061608–574552 in calculations of $\mathcal{M}_{\rm HI}/L_{\rm B}$ (or alternatively the exclusion of the H I belonging to it) will alter the ratio for the ESO 121-G020 system depending on the optical results. From here on the results for these two galaxies are presented separately.

Another interesting result from the H I observations is that for ESO 505-G007. Here we find H I from a catalogued neighbour $\sim 7'$ away, ESO 505-G008, within the data cube of the observations. The beam for these observations is still very large as we used the short hybrid arrays, so unlike the case of ESO 121-G020 and ATCA J061608–574552 the two objects are not entirely spatially resolved. This would not be such a problem if they were spectrally resolved. ESO 505-G007 appears to be close to face on and its H I line is a strong, sharp, narrow line. But ESO 505-G008 looks like an edge on disk galaxy in the optical, and its H I line is very broad with a low peak not much above the 20cm radio continuum level. As a

result it looks like an extended tail to the high velocity side of the ESO 505-G007 line (see Fig. A.106), which can also be seen in the BGC spectrum.

It is very difficult to separate the H I flux density of these two objects as a result in both HIPASS and our observations. Even using robust weighting for our H I maps fails to completely resolve the two, mainly because most of the observations for this field were done on the shortest possible ATCA array configuration, H75B. It is likely that in the BGC reduction most of the flux density from ESO 505-G008 was subtracted as continuum, but it will have contaminated ESO 505-G007's total H I flux density by some amount, which will have affected the $\mathcal{M}_{\rm HI}/L_{\rm B}$. This is a much more difficult problem to resolve than the previous case as not only do we have trouble separating the two galaxies in H I with the current observations, but we also do not currently have optical results for the contaminating galaxy. To limit this effect in our own results we calculated the flux density from a short velocity range (cutting off just after ESO 505-G007's line appears to finish, at 1836 $\mathrm{km\,s^{-1}}$) and spatially restricted to the area of ESO 505-G007. However, there is still ESO 505-G008 contamination, so the H I flux density for this galaxy expressed below should therefore be considered an upper limit.

The ATCA maps of the other seven sources show that none of their BGC results are affected by other galaxies within the beam of the Parkes observations, and all H I sources matched the optical counterpart identified in the BGC. Therefore the BGC results can be considered an accurate measurements of the H I associated with the optical galaxies for those seven. We would expect that the flux density measured with an interferometer like the ATCA is generally equal or lower than for a single dish telescope. As we mentioned in Chapter 6, this is not the case for ESO 215-G?009 where our ATCA measurement was higher than the BGC value. The HIPASS BGC flux density may be underestimated in this case due to the large extent and high peak flux density of the source (see Barnes et al., 2001). For all other galaxies the H I flux density measurements from the ATCA were in agreement with the BGC (including the combined ESO 121-G020/ATCA J061608–574552 system, and the contaminated measurement of ESO 505-G007). Most of the systemic velocities are consistent with the BGC also, an obvious exception being the ESO 121-G020 and ATCA J061608–574552 whose velocities were either side of the BGC value. Table 7.2 lists the results of the radio observations for the nine galaxies.

7.2.2 H I Gas Dynamics

Fig. 7.2 shows the H I velocity fields (1st moment maps) for the galaxies where we have the best resolution, ESO 121-G020/ATCA J061608–574552, ESO 428-G033, ESO 215-G?009 (see description in Chapter 6), and ESO 348-G009. All galaxies (including the small companion to ESO 121-G020, ATCA J061608–574552) show clear signs of rotation. ESO 428-G033 appears to have a velocity field similar

Table 7.2. ATCA Radio Results for each Galaxy.

Name (1)	Beam (H I) (arcsec) (2)	S_{peak} (Jy) (3)	F_{HI} (Jy km s^{-1}) (4)	v_{sys} (km s^{-1}) (5)	w_{50} (km s^{-1}) (6)	w_{20} (km s^{-1}) (7)
MCG–04-02-003	193 × 129	0.232 ± 0.009	16.2 ± 0.6	670 ± 2	112 ± 2	126 ± 2
ESO 473-G024	359 × 205	0.17 ± 0.02	5.7 ± 0.9	542 ± 3	37 ± 2	50 ± 3
ESO 121-G020	32 × 30	0.248 ± 0.006	8.8 ± 0.3	588 ± 2	56 ± 2	78 ± 7
ATCA J061608–574552	32 × 30	0.115 ± 0.006	2.5 ± 0.2	567 ± 4	38 ± 3	72 ± 16
ESO 428-G033	45 × 30	0.292 ± 0.005	14.6 ± 0.3	1720 ± 3	91 ± 2	115 ± 5
ESO 215-G?009	38 × 35	2.128 ± 0.005	122 ± 4	597 ± 1	64 ± 2	90 ± 4
ESO 572-G009	477 × 327	0.25 ± 0.03	7.2 ± 1.3	1740 ± 4	36 ± 2	49 ± 2
ESO 505-G007	413 × 304	0.347 ± 0.009	22.9 ± 0.6	1776 ± 2	69 ± 3	88 ± 5
IC 4212	444 × 357	0.342 ± 0.009	46.0 ± 1.0	1476 ± 1	158 ± 2	172 ± 2
ESO 348-G009	44 × 27	0.271 ± 0.005	15.7 ± 0.3	645 ± 1	97 ± 2	109 ± 4

(1) Galaxy name (with ATCA J061608–574552 included).
(2) Beam size of the H I observations (major and minor axes).
(3) H I peak flux density.
(4) Total integrated H I flux density.
(5) Systemic velocity from the H I line.
(6) Velocity width of the H I line at 50% of the peak flux density.
(7) Velocity width of the H I line at 20% of the peak flux density.

to that of ESO 215-G?009, with fairly regular undisturbed velocity contour lines. Unlike ESO 215-G?009, the last velocity contours on both the approaching and receding sides close, suggesting that the rotation curves on both sides may turn down (only the approaching side did this for ESO 215-G?009). The direction that the rotation is aligned appears to line up to what appears in the optical to be an edge on disk. Likewise, the rotation for ESO 348-G009 appears to align well with the optical disk of the galaxy (see §§ 7.3 and 7.4.1 for more on the optical details of the galaxies).

The H I beam sizes for ESO 121-G020, ESO 428-G033, ESO 215-G?009, and ESO 348-G009 were sufficiently small that rotation curve analysis could be performed. Unfortunately the companion galaxy ATCA J061608–574552 was not sufficiently resolved to produce a good fit. The analysis of the rotation curve for ESO 215-G?009 using ROCUR in *AIPS* was presented in Chapter 6. For the other three galaxies we instead used the very similar procedure ROTCUR in GIPSY (both use the tilted ring algorithm described by Begeman, 1989). We used the standard procedure of narrowing the free parameters (centre position, v_{sys}, position angle, and inclination) down one at a time until the best fit to all parameters was obtained and a rotation curve could be produced. All three fits were done with 10″ rings

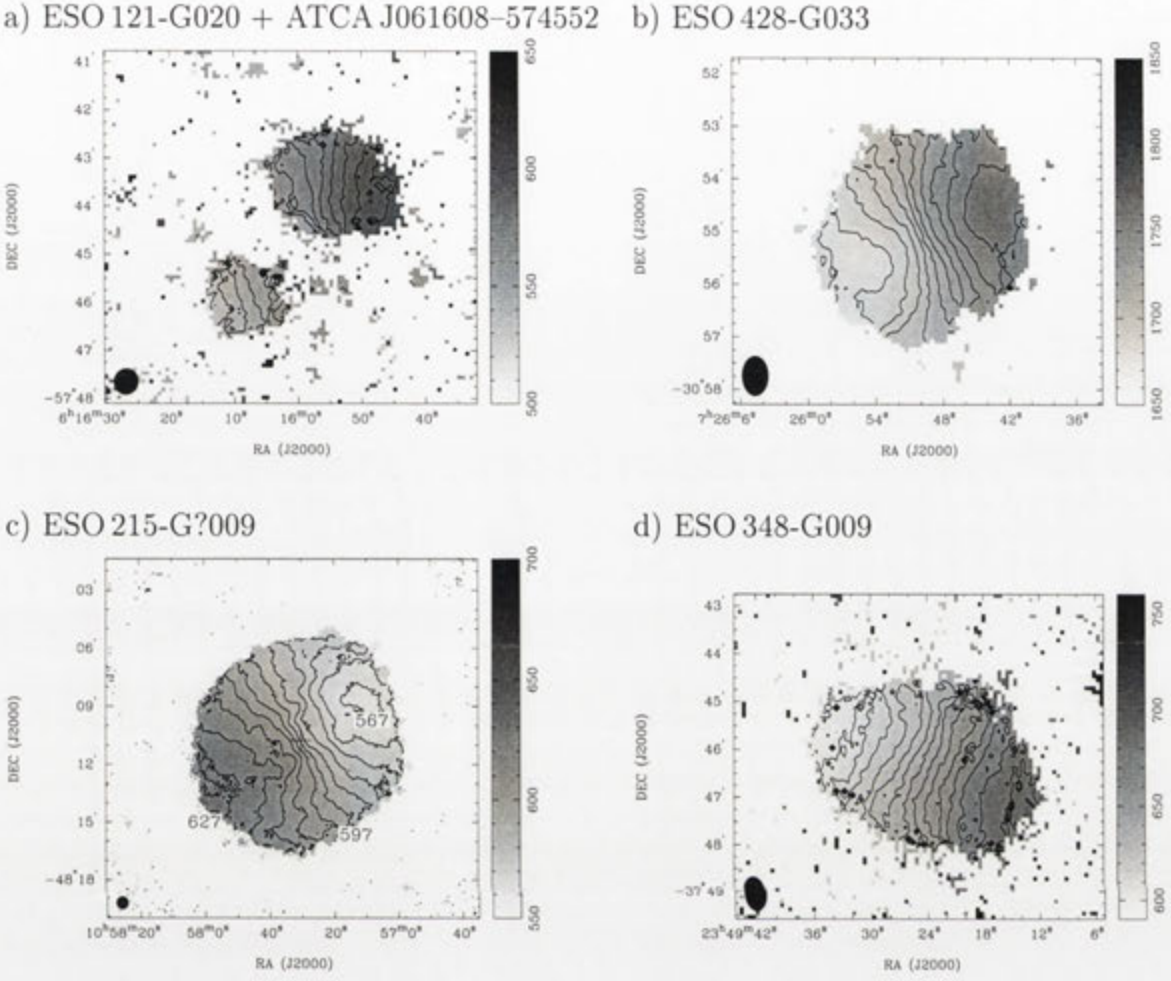

Fig. 7.2: The H I velocity fields (moment 1 maps) for the four galaxy fields with the best resolution. Velocity contours are 6 km s^{-1} apart in all images, except for ESO 428-G033 where they are 8 km s^{-1} apart.

(the ESO 215-G?009 fit used 12″ rings). After an initial fit which included both sides of the galaxy, the fit was done individually for the approaching and receding sides of the galaxy to check for any asymmetry. Of the three new fits, the only galaxy which had significant differences between the two sides was ESO 428-G033, where the inclination fit was lower on the approaching side, which may have been a result of the very low inclination (this was included in the uncertainties below).

Table 7.3 lists the results of fitting rotation curves to the H I velocity fields of these four galaxies. The final rotation curves are shown in Fig. 7.3. The very low inclination of ESO 428-G033 produced a high uncertainty in the rotation velocity values as shown by the curves plotted. In the case of ESO 348-G009 the curve appears to still be rising at the last points of the rotation curve, suggesting that we are not tracing the H I in this galaxy out to the radius at which the maximum rotation velocity is reached (so $v_{\rm max}$ should be considered a lower limit in this case). Similarly for ESO 121-G020, where we may just be reaching the point where the

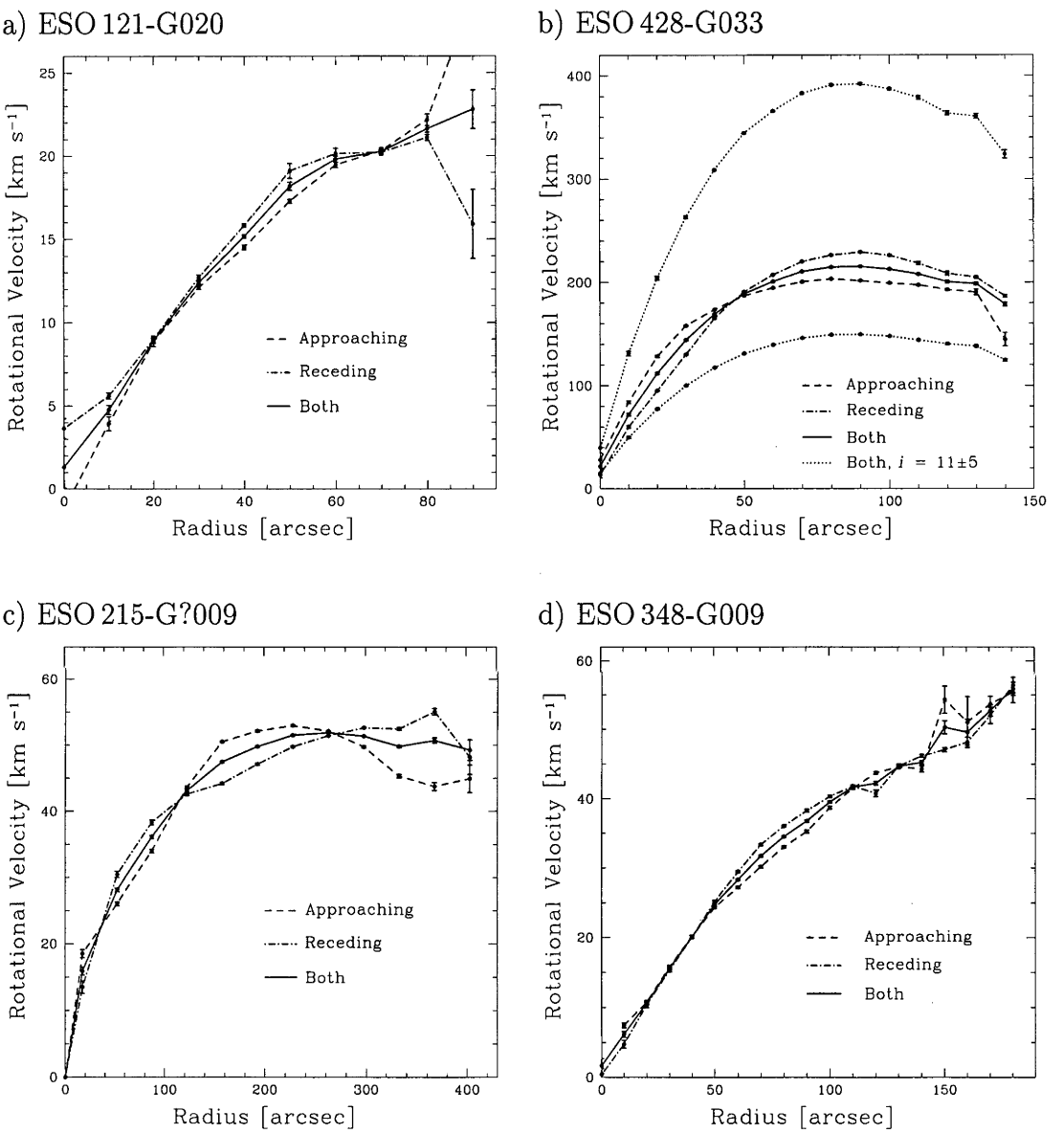

Fig. 7.3: The H I rotation curves as derived from the mean H I velocity field for the four galaxies to which they were fit. The three curves which are in all panels correspond to the approaching side (dashed line), receding side (dot-dashed line), and both sides (solid line). The dotted curves in the ESO 428-G033 panel show the difference which the inclination uncertainty makes for that galaxy.

Table 7.3. Rotation Curve Fit for Galaxies with Sufficient H I Data.

Name	v_{sys}	PA	i	v_{max}	r_{max}
	($km\,s^{-1}$)	(degrees)	(degrees)	($km\,s^{-1}$)	(arcsec)
(1)	(2)	(3)	(4)	(5)	(6)
ESO 121-G020	584.5 ± 1.0	262 ± 2	78 ± 5	21 ± 2	80 ± 10
ESO 428-G033	1717 ± 3	295 ± 5	11 ± 5	200^{+160}_{-60}	130 ± 5
ESO 215-G?009	597 ± 1	119 ± 2	36 ± 10	51 ± 8	370 ± 20
ESO 348-G009	646 ± 2	245 ± 3	80 ± 5	50 ± 5	160 ± 15

(1) Galaxy name.
(2) Systemic velocity calculated by the fit.
(3) Position angle of the galaxy's receding side.
(4) Galaxy inclination calculated from the fit.
(5) Maximum rotation velocity calculated from the fit.
(6) Radius out to which we trace the rotation curve.

curve flattens out. In the other two galaxies we appear to have reached the flat part of the curve.

7.3 *Optical Properties*

The *B* images taken on the 2.3m Telescope of all nine galaxies before and after foreground star subtraction are shown in Appendix A. Star contamination is obviously a problem for ESO 215-G?009 and especially ESO 428-G033, both of which are close to the Galactic Plane, so special care was taken with these images. Some of the galaxies (notably MCG–04-02-003, ESO 215-G?009, ESO 505-G007 and ESO 348-G009) were affected by moderately bright foreground stars sitting on top of the galaxy that had to be removed with care. As mentioned in § 7.2, a companion galaxy to ESO 121-G020 was found in the H I imaging. The optical image for ESO 121-G020 also includes ATCA J061608–574552, and the photometry for that galaxy is included with the other results here. For each galaxy a growth curve was measured on the star-subtracted images from the luminosity weighted center in 2 pixel ($\sim$1.″2) circular aperture rings to obtain the total intensity. Table 7.4 lists the results of the optical *BVRI* photometry taken on the 2.3m Telescope for the nine galaxies. No Galactic extinction correction was applied to the apparent magnitude and surface brightness.

Table 7.4. 2.3m Telescope Optical Results for each Galaxy.

Name	Band	m_T[a] (mag)	μ_0[a] (mag arcsec^{-2})	$\langle\mu\rangle_{\rm eff}$[a] (mag arcsec^{-2})	$r_{\rm eff}$ (arcsec)	$r_{\rm H,0}$ (arcsec)	$A_{\rm G}$ (mag)
(1)	(2)	(3)	(4)	(5)	(6)	(7)	(8)
MCG–04-02-003	*B*	15.32 ± 0.06	22.34 ± 0.02	23.77 ± 0.04	19.6 ± 0.7	51.0 ± 2.0	0.08 ± 0.01
	V	14.91 ± 0.05	21.89 ± 0.01	22.98 ± 0.04	16.4 ± 0.6	–	0.06 ± 0.01
	R	14.40 ± 0.05	21.60 ± 0.01	22.68 ± 0.05	18.1 ± 0.7	–	0.05 ± 0.01
	I	13.60 ± 0.06	21.17 ± 0.01	22.76 ± 0.05	27.1 ± 1.0	–	0.04 ± 0.01
ESO 473-G024	*B*	16.38 ± 0.06	24.63 ± 0.04	25.30 ± 0.04	24.3 ± 0.8	32.4 ± 0.8	0.08 ± 0.01
	V	15.44 ± 0.07	23.73 ± 0.03	24.46 ± 0.03	25.4 ± 0.7	–	0.06 ± 0.01
	R	15.19 ± 0.03	23.51 ± 0.03	24.18 ± 0.02	25.1 ± 0.4	–	0.05 ± 0.01
	I	14.76 ± 0.07	23.42 ± 0.08	24.35 ± 0.02	33.0 ± 0.9	–	0.04 ± 0.01
ESO 121-G020	*B*	15.27 ± 0.05	23.36 ± 0.03	23.95 ± 0.02	21.7 ± 0.4	47.0 ± 2.0	0.17 ± 0.03
	R	14.62 ± 0.04	22.71 ± 0.03	23.29 ± 0.02	21.6 ± 0.5	–	0.11 ± 0.02
ATCA J061608–574552	*B*	17.01 ± 0.06	22.81 ± 0.04	23.34 ± 0.02	7.4 ± 0.3	18.6 ± 0.6	0.17 ± 0.03
	R	16.36 ± 0.06	22.07 ± 0.02	22.72 ± 0.02	7.5 ± 0.2	–	0.11 ± 0.02
ESO 428-G033	*B*	16.90 ± 0.10	23.33 ± 0.11	24.69 ± 0.02	14.4 ± 0.5	37.2 ± 1.2	1.10 ± 0.18
	V	16.13 ± 0.10	23.12 ± 0.02	24.23 ± 0.05	16.7 ± 0.8	–	0.85 ± 0.14
	R	15.61 ± 0.08	22.56 ± 0.02	23.48 ± 0.05	15.0 ± 0.9	–	0.68 ± 0.11
	I	15.04 ± 0.09	22.01 ± 0.03	22.95 ± 0.04	15.2 ± 0.7	–	0.50 ± 0.08
ESO 215-G?009	*B*	16.13 ± 0.07	24.97 ± 0.03	25.48 ± 0.02	29.7 ± 0.6	57.6 ± 0.6	0.95 ± 0.15
	V	14.89 ± 0.06	23.65 ± 0.03	24.14 ± 0.02	28.3 ± 0.7	–	0.73 ± 0.12
	R	14.38 ± 0.05	23.16 ± 0.02	23.64 ± 0.03	28.4 ± 0.5	–	0.59 ± 0.09
	I	13.76 ± 0.06	22.91 ± 0.04	23.40 ± 0.03	33.9 ± 0.8	–	0.43 ± 0.07
ESO 572-G009	*B*	16.79 ± 0.05	24.96 ± 0.05	26.03 ± 0.02	28.1 ± 0.7	30.6 ± 1.2	0.16 ± 0.03
	V	15.65 ± 0.07	23.69 ± 0.02	25.12 ± 0.02	31.1 ± 0.8	–	0.12 ± 0.02
	R	15.40 ± 0.04	23.42 ± 0.03	24.75 ± 0.01	29.6 ± 0.5	–	0.10 ± 0.02
ESO 505-G007	*B*	14.20 ± 0.06	23.99 ± 0.04	24.00 ± 0.01	36.4 ± 0.7	82.8 ± 1.2	0.36 ± 0.06
	V	14.48 ± 0.05	23.89 ± 0.04	23.96 ± 0.01	31.3 ± 0.6	–	0.28 ± 0.04
	R	13.97 ± 0.04	23.46 ± 0.04	23.66 ± 0.02	34.6 ± 0.5	–	0.22 ± 0.04
IC 4212	*B*	14.11 ± 0.04	22.38 ± 0.02	24.42 ± 0.02	46.0 ± 1.0	98.4 ± 0.6	0.19 ± 0.03

Table 7.4 (cont'd)

Name	Band	m_T[a] (mag)	μ_0[a] (mag arcsec^{-2})	$\langle\mu\rangle_{\rm eff}$[a] (mag arcsec^{-2})	$r_{\rm eff}$ (arcsec)	$r_{\rm H,0}$ (arcsec)	$A_{\rm G}$ (mag)
(1)	(2)	(3)	(4)	(5)	(6)	(7)	(8)
	V	13.69 ± 0.05	22.00 ± 0.03	23.98 ± 0.01	45.7 ± 0.9	–	0.14 ± 0.02
	R	13.29 ± 0.06	21.53 ± 0.02	23.53 ± 0.02	44.5 ± 0.9	–	0.12 ± 0.02
ESO 348-G009	B	14.81 ± 0.07	23.78 ± 0.04	24.79 ± 0.03	39.5 ± 0.9	72.0 ± 0.6	0.06 ± 0.01
	V	14.68 ± 0.06	23.42 ± 0.03	24.40 ± 0.03	35.1 ± 1.0	–	0.04 ± 0.01
	R	14.48 ± 0.05	23.13 ± 0.03	24.03 ± 0.03	32.4 ± 0.8	–	0.04 ± 0.01
	I	13.75 ± 0.10	22.75 ± 0.03	23.72 ± 0.02	39.3 ± 1.1	–	0.03 ± 0.01

(1) Galaxy name.
(2) Broad band filter used for the observation (Cousins filters).
(3) Total apparent magnitude.
(4) Central surface brightness.
(5) Effective surface brightness, the average surface brightness out to the half light radius.
(6) Half light (effective) radius.
(7) Radii out to $\mu = 26.6$ mag arcsec^{-2} (which is the Holmberg radius in the B band, extinction corrected).
(8) Galactic extinction from SFD98.

[a]Correction for Galactic extinction not applied.

The surface brightness profiles for the nine galaxies in each of the observed bands are in Appendix A. All profiles have been corrected for Galactic extinction, but no attempt to correct for inclination was made as it is difficult to calculate given the morphology of many galaxies, and as the correction for edge on galaxies (such as ESO 348-G009) would be unrealistic without correction for the thickness of the stellar disk. The profiles for several galaxies show some of the underlying morphology. MCG–04-02-003's profiles (Fig. A.7) show two distinct components, an inner bright bulge region which is prominent in the optical image, and a surrounding low surface brightness disk (almost 4 mag fainter in surface brightness). The profiles of IC 4212 (Fig. A.129) shows a small central bulge and bumps caused by the arms of this face on spiral. ESO 572-G009 (Fig. A.101) also seems to have a slight central bulge, which is seen in the image (Fig. A.99). ESO 348-G009 and ESO 428-G033 (Figs. A.155 and A.69) look like exponential disks, while ESO 473-G024 (Fig. A.11) is similar but with a slightly flatter central region.

The profiles of ESO 505-G007 (Fig. A.105) are very flat in the central region as the luminosity weighted centre of this galaxy is a faint region between many brighter patches that are probably star formation regions. The optical structure of this galaxy (see Fig. A.103) possibly reflects a highly disturbed galaxy with increased star formation due to interaction with the galaxy ESO 505-G008 (the source which contaminates its H I spectrum). The companion to ESO 121-G020, ATCA J061608–574552, notably has a much steeper exponential profile than its neighbour, as well as a higher central surface brightness. This denser structure may be the result of recent star formation (there is a bright patch in the centre of the galaxy which could be a star formation site), and may have lead to it previously being missed in optical surveys if it were mistaken for a star (Monet et al., 2003, it is included as a star in the USNO star catalogue).

For only two galaxies, ESO 473-G024 and ESO 215-G?009, did we get B band apparent magnitudes that agreed with the values quoted in LEDA (even within their sometimes large error bars). In the case of all seven other galaxies our value of $m_{\rm B}$ was brighter than LEDA's, in some cases by several magnitudes. This will bring most of the H I mass-to-light ratios in our sample down, a trend we will discuss in the following section.

7.4 Discussion

7.4.1 Comparing Optical and H I Properties

Now that we have new optical and H I measurements we can recalculate many of the physical properties of the galaxies, including $\mathcal{M}_{\rm HI}/L_{\rm B}$. Table 7.5 summarises the main derived results from our observations of the nine galaxies. The last three values ($\mathcal{M}_{\rm tot}$, $\mathcal{M}_{\rm HI}/\mathcal{M}_{\rm tot}$, and $\mathcal{M}_{\rm tot}/L_{\rm B}$) are only available for the four galaxies with rotation curve fits.

Table 7.5. Summary of Derived Results for each Galaxy from ATCA and 2.3m Data.

Name	M_B (mag)	L_B ($\times 10^7\ L_{\odot,B}$)	$\mathcal{M}_{HI}$ ($\times 10^7\ \mathcal{M}_\odot$)	$\mathcal{M}_{HI}/L_B$ ($\mathcal{M}_\odot/L_{\odot,B}$)	$\mathcal{M}_{tot}$ ($\times 10^9\ \mathcal{M}_\odot$)	$\mathcal{M}_{HI}/\mathcal{M}_{tot}$	$\mathcal{M}_{tot}/L_B$ ($\mathcal{M}_\odot/L_{\odot,B}$)
(1)	(2)	(3)	(4)	(5)	(6)	(7)	(8)
MCG–04-02-003	-14.65 ± 0.06	11.3 ± 0.6	34.5 ± 1.3	3.0 ± 0.3			
ESO 473-G024	-13.10 ± 0.06	2.7 ± 0.1	7.8 ± 1.2	2.8 ± 0.6			
ESO 121-G020	-12.97 ± 0.06	2.39 ± 0.13	3.49 ± 0.12	1.44 ± 0.13	0.16 ± 0.05	0.22 ± 0.11	7 ± 4
ATCA J061608–574552	-11.23 ± 0.07	0.48 ± 0.03	0.99 ± 0.08	2.0 ± 0.3			
ESO 428-G033	-16.7 ± 0.2	28 ± 5	131 ± 3	4.6 ± 0.9	110^{+190}_{-70}	$0.012^{+0.020}_{-0.008}$	~ 380
ESO 215-G?009	-12.9 ± 0.2	2.3 ± 0.4	50.8 ± 1.7	22 ± 4	4.5 ± 1.6	0.11 ± 0.04	200 ± 110
ESO 572-G009	-14.92 ± 0.06	14.5 ± 0.8	71 ± 13	4.8 ± 1.1			
ESO 505-G007	-17.75 ± 0.08	196 ± 14	234 ± 6	1.18 ± 0.12			
IC 4212	-17.36 ± 0.05	137 ± 6	356 ± 8	2.55 ± 0.17			
ESO 348-G009	-14.87 ± 0.07	13.8 ± 0.9	26.1 ± 0.5	1.87 ± 0.16	3.8 ± 1.1	0.07 ± 0.02	27 ± 10

(1) Galaxy name.
(2) B band absolute magnitude.
(3) B band luminosity.
(4) H I mass.
(5) H I mass-to-B band luminosity ratio ($\mathcal{M}_{HI}/L_B$).
(6) Total mass (dynamical mass, derived from the maximum velocity of H I rotation curve).
(7) H I mass-to-total mass ratio.
(8) Total mass-to-B band luminosity ratio.

MCG–04-02-003 (see also page 149)

Our B band apparent magnitude for this galaxy is between 0.2 mag and 0.7 mag brighter than that expressed in LEDA, which is based on the APM plate scan results of Maddox et al. (1990). The galaxy has a distinctive optical morphology. A quick look at its image shows only a small, bright, centrally concentrated circular region like BCD. Closer inspection shows that there is in fact a second very low surface brightness disk component extending well beyond this central bulge, which is clearly shown in our surface brightness profile for this galaxy (Fig. A.7). This outer low surface brightness disk could be easily missed or underestimated, and it is likely that this causes the disagreement between the two apparent magnitude measurements. The disk actually contains a large proportion of the luminosity from the galaxy (the half light radius of the galaxy, $19\farcs6 \pm 0\farcs7$, is in the transition region between the bulge and disk), so it is unlikely that the previous measurement missed it entirely. The H I flux density result on the other had is in excellent agreement with the BGC, suggesting we have recovered almost all the Parkes flux density (this is probably due to the short spacing of the array configurations used, which are not much longer than the diameter of the Parkes dish). The result of our combined H I and optical values is that the H I mass-to-light ratio drops moderately to $3.0 \pm 0.3\ \mathcal{M}_{\odot}/L_{\odot,\mathrm{B}}$, which is still higher than 'typical' late-type galaxies but not unusually so.

The MCG–04-02-003 has low foreground star contamination and very low Galactic extinction. There is one relatively bright star superimposed on the central bulge, which is potentially a star formation region. However, it was removed during the foreground star subtraction as it appeared to have the profile of a point source, it has only a small effect on the total magnitude, and was still bright in the redder bands. In H I, the other four sample galaxies observed on hybrid arrays had beam sizes that were still too large to resolve any details of their structure. However, despite the large beam for MCG–04-02-003, we can clearly see the H I envelope is extended in a north-south direction. This is in the same direction as the outer low surface brightness optical disk, and the two correlate quite well in both shape and extent.

Given the velocity and sky position it appears to be located at the far end of the Sculptor group (when compared to the sample of Côté et al., 1997). The Hubble flow distance quoted here puts it well beyond this group, however, as Jerjen, Freeman, & Binggeli (1998) discuss the local distance-velocity relation in the Sculptor group appears to have a steeper slope due to the probable gravitational influence of the more massive Local Group, so MCG–04-02-003 may be much closer than estimated from employing a global Hubble law.

ESO 473-G024 (see also page 153)

Of the nine galaxies here, ESO 473-G024 had the best agreement with the B band apparent magnitude quoted in LEDA, also agreeing with the results in Lauberts & Valentijn (1989) and Maddox et al. (1990). As a result $\mathcal{M}_{\rm HI}/L_{\rm B}$ remained at a moderate ratio of 2.8 ± 0.6 $\mathcal{M}_{\odot}/L_{\odot,{\rm B}}$, and with the many of the other galaxies having much lower ratios than before it has gone from the lowest to one of the higher ratio of this sample. The relatively large beam created by the short hybrid ATCA configurations and the low signal-to-noise of the snapshot observing mode mean that in H I for this galaxy we can do little more spatially than confirm the position of HIPASS source, its flux density, and that there are no other galaxies contributing to the HIPASS data. In the optical, it has the appearance of a low surface brightness dwarf irregular galaxy, and is slightly extended in the north-south direction. The galaxy has a slightly mottled appearence and there are a number of potential star formation sites dotted around it. It is a member of the Sculptor group (confirmed by Côté et al., 1997), and as in the case of MCG–04-02-003 the distance derived from the Local Group velocity may be an overestimate.

ESO 121-G020 and ATCA J061608–574552 (see also page 175)

The discovery of the companion galaxy ATCA J061608–574552 to the south east of ESO 121-G020 obviously affects the $\mathcal{M}_{\rm HI}/L_{\rm B}$ calculations for this galaxy. The new galaxy is within the beam of the HIPASS observations, and so the BGC H I flux density measurement for HIPASS J0615–57 includes the total H I from both galaxies. The preliminary $\mathcal{M}_{\rm HI}/L_{\rm B}$ for the ESO 121-G020/ATCA J061608–574552 system is therefore an overestimate of the true ratio as the optical component of ATCA J061608–574552 was not included (alternatively, it is an overestimate for ESO 121-G020 alone as the H I of the other galaxy was not excluded). However, like many of the other galaxies it is the underestimated optical luminosity which drags the ratio down to levels more typical of dwarf galaxies. The new ratio for the combined system is 1.55 ± 0.18 $\mathcal{M}_{\odot}/L_{\odot,{\rm B}}$, and for the individual galaxies it is 1.44 ± 0.13 $\mathcal{M}_{\odot}/L_{\odot,{\rm B}}$ for ESO 121-G020 and 2.0 ± 0.3 $\mathcal{M}_{\odot}/L_{\odot,{\rm B}}$ for ATCA J061608–574552. There does not appear to be an H I or stellar bridge between the two galaxies, at least down to the sensitivities we are measuring.

ESO 428-G033 (see also page 195)

At only 6°.9 from the Galactic Plane, ESO 428-G033 suffers from relatively high Galactic extinction and foreground star contamination. Our B band measurement is about a magnitude brighter than the LEDA value, but agrees with the Lauberts & Valentijn (1989) measurement (16.83 ± 0.09 mag). The LEDA value has a suspiciously high uncertainty of around half a magnitude, leading to a very high uncertainty in the initial estimate of $\mathcal{M}_{\rm HI}/L_{\rm B}$. Despite all this, with our new data

the galaxy still has a moderately high H I mass-to-light ratio of $4.6\pm0.9\ \mathcal{M}_{\odot}/L_{\odot,\mathrm{B}}$. However, the foreground star contamination makes it very difficult to properly clean the field of the optical image without affecting the galaxy brightness. On top of this the galaxy suffers from the highest Galactic extinction of the galaxies here, although this can be taken into account (see § 7.4.3). For these reasons it may have a slightly lower H I mass-to-light ratio than we calculate.

The optical morphology of the galaxy appears to be that of an edge on disk galaxy with a slight bulge, though the star contamination makes any particular features difficult to distinguish. In H I we have very good resolution due to the multiple observing runs on longer arrays. The H I appears extended along the disk-like feature of the optical component, with the velocity field indicating that the rotation is aligned with this disk. But the rotation curve fit shows that rather than being an edge on disk, ESO 428-G033 is close to face on. This feature may instead be a central bar which happens to be at the right angle to us.

ESO 215-G?009 (see also page 207)

This low surface brightness dwarf irregular galaxy was discussed in detail in Chapter 6, where we confirmed that it did have the unusually high $\mathcal{M}_{\mathrm{HI}}/L_{\mathrm{B}}$ suggested by the combined BGC and LEDA results. It is included here for comparison with the other galaxies and we refer the reader to the previous work for more details on it. After obtaining new estimates of m_{B} and F_{HI} for all our sample galaxies, ESO 215-G?009 remains as the stand out galaxy with $\mathcal{M}_{\mathrm{HI}}/L_{\mathrm{B}} = 22\pm4\ \mathcal{M}_{\odot}/L_{\odot,\mathrm{B}}$. To our knowledge it has one of the highest (if not the highest) $\mathcal{M}_{\mathrm{HI}}/L_{\mathrm{B}}$ that has been confirmed by accurate measurement to date for any galaxy system, being approximately double the ratio of DDO 154 (the most promising high $\mathcal{M}_{\mathrm{HI}}/L_{\mathrm{B}}$ candidate in the literature, see Hoffman et al., 1993), and about four times the ratio of our nearest sample objects (ESO 572-G009 and ESO 428-G033). Although the Galactic extinction for this galaxy is relatively high and it has some foreground star contamination, this is less of a problem than it was for ESO 428-G033, and it is unlikely to suffer from strong internal extinction. The nearest neighbour we can identify is approximately 1.9 Mpc away in the Centaurus A Group, making it a very isolated galaxy.

ESO 572-G009 (see also page 219)

Although the $\mathcal{M}_{\mathrm{HI}}/L_{\mathrm{B}}$ of this galaxy dropped significantly due to a half magnitude rise in m_{B}, it is still one of the few galaxies to retain a reasonably high ratio at $4.8 \pm 1.1\ \mathcal{M}_{\odot}/L_{\odot,\mathrm{B}}$ (the equal second highest in this sample, although along way behind ESO 215-G?009). Morphologically it is a faint low surface brightness galaxy and appears to have two components, a brighter cigar shaped central region (likely to be a central bar) surrounded by a fainter disk that extends only a short distance. The H I observations for this galaxy were done on a short hybrid array

in snapshot mode, and had the least time on source of the nine galaxies, ~1.0 hours observations over ~6 hours, which still gives relatively even but sparse U-V coverage on the hybrid array, and low signal-to-noise.

ESO 505-G007 (see also page 222)

A previous measurement of the integrated H I flux density by Huchtmeier & Richter (1989, 19.3 ± 2.2 Jy km s^{-1}) agrees with both the BGC's and our results within uncertainties. But literature m_B measurements vary wildly (both 17.64 ± 0.09 and 15.95 ± 0.09 from Lauberts & Valentijn, 1989, dependent on the isophotal level it is measured to), suggesting that the LEDA magnitude could be suspect. Our measurement is ~3.5 mag brighter, about 25 times more emission. The severe underestimate of the value of the B band apparent magnitude for this galaxy in LEDA ($\sim$ 3.5 mag fainter than our result) has a dramatic effect on the H I mass-to-light ratio. From the highest ratio of the 789 BGC galaxies with LEDA B magnitudes, $\mathcal{M}_{HI}/L_B$ for ESO 505-G007 has dropped down to a fairly typical value of 1.18 ± 0.12 $\mathcal{M}_\odot/L_{\odot,B}$, which is now the lowest of the nine galaxies examined here.

In addition, as we mentioned earlier the low resolution from the hybrid ATCA configurations causes other problems. It is difficult to separate the flux density measurement for ESO 505-G007 from its neighbour ESO 505-G008, which has a very wide velocity dispersion owing to its edge on appearance. So the large beam that does not give full spatial separation of the two galaxies means that ESO 505-G008 is probably contributing to the flux density measurements for our results, and certainly for the BGC result due to the lower resolution. The beam also makes it difficult to make any comparison between the physical sizes of the optical and H I components of ESO 505-G007, and impossible to make structural comparisons. Optically, ESO 505-G007 has an unusual irregular morphology, with several large clumpy structures and some ragged spiral arm-like features, which could suggest that the galaxy has been disturbed by interaction with ESO 505-G008.

IC 4212 (see also page 240)

IC 4212 was always an unusual galaxy to be in a sample of faint high $\mathcal{M}_{HI}/L_B$ galaxies since its optical morphology is that of a face on spiral with two bright, loosely wound arms, several fainter arms and a small bright central bar. The uncertainty in the LEDA apparent magnitude, ± 1.1 mag, seems excessively large (this covers nearly an order of magnitude range in luminosity). So it is hardly surprising that our optical measurements show that it is a much brighter object than the LEDA m_B value suggests, and that the $\mathcal{M}_{HI}/L_B$ is much lower. Still, while it is not as extreme a galaxy as suggested by its initial $\mathcal{M}_{HI}/L_B$, IC 4212 still retains at a relatively high $\mathcal{M}_{HI}/L_B$ of 2.55 ± 0.17 $\mathcal{M}_\odot/L_{\odot,B}$, especially for such a spiral galaxy. This is the most northern of the galaxies and so needed to

be observed on the short hybrid arrays, meaning that the beam size is very large (several times the optical extent). So again we have little basis to compare the spatial properties of the optical and H I components. However, the great extent of the galaxy in the H I image is much larger than the beam, which suggests that the H I disk may extend far beyond the optical galaxy if we had better resolution.

ESO 348-G009 (see also page 258)

The apparent B magnitude we measured for ESO 348-G009 was, like for many of the other galaxies here, significantly brighter than the value in LEDA, while the H I flux density is consistent with the BGC result. This means we end up with an H I mass-to-light ratio of $1.87 \pm 0.16\ \mathcal{M}_{\odot}/L_{\odot,\mathrm{B}}$, much lower than suggested by the preliminary value of $9 \pm 7\ \mathcal{M}_{\odot}/L_{\odot,\mathrm{B}}$ (although still within the error bars due to the LEDA uncertainty in the B apparent magnitude of ± 0.7 mag). The optical image shows an edge on disk galaxy extending East-West, with some clumpy structures visible along the length of the disk. The H I map shows that the gas is also extended along the stellar disk, and the rotation follows it too. Côté et al. (1997) identify ESO 348-G009 as another Sculptor group member, the third in this sample. Once again, the distance for this galaxy may be lower than the Local Group velocity predicts (Jerjen et al., 1998).

7.4.2 The Tendency for the $\mathcal{M}_{\mathrm{HI}}/L_{\mathrm{B}}$ to Fall

Fig. 7.4 shows the same plot as Fig. 1.1 with the new positions of the galaxies with our observations marked. The dots mark the BGC and LEDA results as in Fig. 1.1, with the open circles marking the original positions of the nine galaxies examined here. The filled circles mark the new results, with the lines connecting them to the old measurements. All of the galaxies drop in $\mathcal{M}_{\mathrm{HI}}/L_{\mathrm{B}}$, and although most stay within the large uncertainties of the original values, if we ignore those error bars some are large shifts from the original estimates.

In all but one case (ESO 473-G024) the changes are mostly due to underestimates of the optical B band apparent magnitudes in LEDA (with major changes in F_{HI} only occurring where there were companions or problems with the HIPASS data). In a way this is hardly surprising as we have selected some of the most extreme galaxies in a sample with large uncertainties in individual optical results, so we are more likely to have selected the galaxies where the optical magnitude was underestimated. The various parameters that LEDA provided were the weighted mean values of all available measurements (regardless of the source, which in a few cases included results which do not represent total B band apparent magnitude such as B_{25}). The weighting for B band apparent magnitude was from the inverse square of the mean standard deviation. This has the disadvantage that if there is a spread of results then any outliers will have a sometimes significant effect on the value that they quoted. In the case of many of our galaxies there are existing

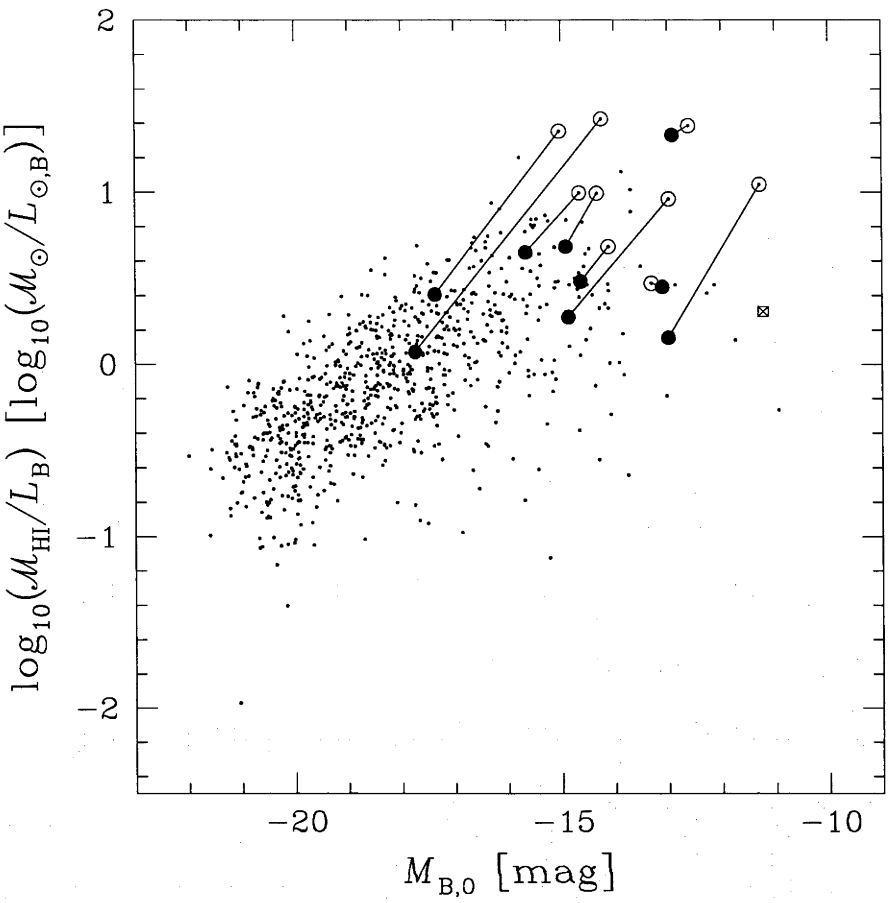

Fig. 7.4: H I mass-to-light ratio versus absolute B magnitude, with the 789 galaxies in Fig. 1.1 marked with small dots. The open circles mark the positions of the nine galaxies in this paper from the combination of the BGC and LEDA, while the filled circles mark the positions of the galaxies using the observations presented here.

optical results that agree with our results or are closer to them than LEDA (such as the total B magnitude values from Lauberts & Valentijn, 1989).

While we started with seven of our nine galaxies having $\mathcal{M}_{\rm HI}/L_{\rm B}$ that might be considered very high (ratios of ~9-10 $\mathcal{M}_{\odot}/L_{\odot,\rm B}$ or higher), we are now left with only one, ESO 215-G?009. The other galaxies we initially considered may have high H I mass-to-light ratios turned out to have much lower ratios in the range ~1-5 $\mathcal{M}_{\odot}/L_{\odot,\rm B}$. This is by no means uncommon among claims of such galaxies, as we discussed in § 6.5.2 of Chapter 6, and as seen in van Zee et al. (1997) and Chung et al. (2002). The faint luminosity of these galaxies and the problems in getting high quality data in both the optical and radio make examples of this class of galaxy difficult to find. We have not been able to find here any galaxies to bridge the gap between the moderately high H I mass-to-light ratio galaxies that remain and the seemingly extreme ratio of ESO 215-G?009. How significant the position of ESO 215-G?009 relative to other galaxies is, and what implications this may

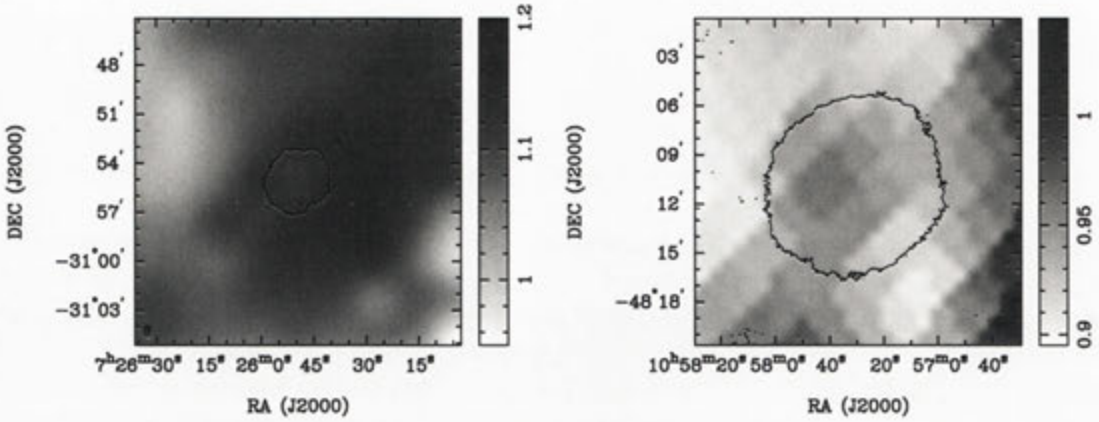

Fig. 7.5: The Schlegel et al. (1998) Galactic extinction maps for ESO 428-G033 (left) and ESO 215-G?009 (right) in A_B (units of magnitudes). The contours marked on each image indicate the lowest H I contours for each galaxy as shown in Appendix A.

have for cosmological predictions of low mass galaxy dark matter halo numbers or setting limitations on initial mass functions for galaxy modeling we will discuss in § 7.4.5. But first we must look at some other aspects of the results.

7.4.3 Dust Extinction and Distance Uncertainties

As well as the accuracy of the optical photometry and H I line observations it is also important to consider the one contributor to $\mathcal{M}_{HI}/L_B$ that is beyond the scope of our observations, the dust extinction due to both our Galaxy and the host galaxy ("internal" extinction). As we discussed in Chapter 6 Galactic extinction is particularly important for ESO 215-G?009 due to its sky position only 10.°5 away from the Galactic Plane. Of the other eight galaxies here, ESO 428-G033 at b = -6.°9 is the only other that is subject to significantly high Galactic extinction (A_B = 1.10 ± 0.18 mag, SFD98), with many of the others having very low extinction (especially the three associated with the Sculptor group, which is close to the Southern Galactic Pole).

The uncertainties in the SFD98 Galactic extinction grow proportionally to the value. It is only for ESO 215-G?009 and ESO 428-G033 where this uncertainty is a large fraction of the total error. Also, close to the Galactic Plane the dust distribution can be patchy. The SFD98 dust maps, which cover large scales, could miss small scale variations. Willick (1999b, see § 1.4) propose that observers also use the older Burstein & Heiles (1982) Galactic extinction maps, but we have chosen to use only the SFD98 values for Galactic extinction to remain consistent with recent publications that favour these newer maps.

Fig. 7.5 shows the SFD98 dust extinction maps in terms of A_B for the regions around ESO 428-G033 and ESO 215-G?009, the only two galaxies suffering from significant dust extinction. The maps are the same scale as the H I distribution

maps ($20' \times 20'$) and show the last H I contour from those maps for reference. Both maps show relatively low variation in the amount of extinction over the field around the galaxy, less than the uncertainty in A_B in both cases, and there appears to be no strong gradients. Both galaxies seem to be in a relatively flat area of the Galactic dust distribution. This suggests that the SFD98 value at the position of both galaxies is an accurate representation of the true extinction. ESO 428-G033 was studied by Kraan-Korteweg & Huchtmeier (1992) as part of an H I investigation of galaxies in the Puppis region of the Galactic Plane, an area of the Plane where there is reduced dust extinction. Their results are in agreement with our measurements for this galaxy (including for $\mathcal{M}_{HI}/L_B$), and in general they found that the properties of their sample objects were typical of other samples of nearby galaxies despite the relatively high extinction. It is worth noting that even if there where much higher Galactic extinction at the position of ESO 215-G?009, say 0.5 mag that might still be realistic (though unlikely), then that galaxy would still have a very high $\mathcal{M}_{HI}/L_B$ of $14 \pm 4\ \mathcal{M}_\odot/L_{\odot,B}$.

While we can at the very least get a reasonably accurate estimate of extinction caused by the Milky Way at the position of a galaxy, dust extinction internal to the host galaxy itself is much harder to quantify. Dust extinction in late-type galaxies is poorly understood but thought to be lower than in early-type spirals, although we can expect that a disk galaxy may have significant extinction when viewed through the galaxy's plane where the dust is generally concentrated. We discussed this in Chapter 6 with regards to ESO 215-G?009, concluding that it was unlikely to have strong internal extinction as we are viewing the galaxy close to face on. The low rate of star formation in this galaxy also suggests that it has a low metalicity, and therefore less dust.

Of the other galaxies, ESO 473-G024 and ESO 505-G007 are likely to have low internal extinction as the optical images and H I spectra indicate they are orientated close to face on to us (so we are probably not looking through the disk), and are of late-type morphology. IC 4212 may have large amounts of dust in its disk but as we are viewing close to face on it is likely to have only a minor extinction effect. Similarly for the very faint near face on disk of MCG–04-02-003. It is difficult to tell what the inclination of ESO 572-G009 from either the low resolution H I snapshot image or the optical observations (which could suggest a face on bar or an edge on disk), but the H I line is narrow suggesting it is face on, so dust extinction is probably not a factor.

However, the fitting of rotation curves to some of the other galaxies has shown that appearances can be deceptive when it comes to inclination. The optical image of ESO 428-G033, although strongly affected by foreground stars, appears to be that of an edge on disk, and the double horn profile of the H I line suggests the galaxy is inclined to a reasonable degree at least. But the rotation curve fit produced a very low nearly face on inclination of $11° \pm 5°$, so internal extinction is less likely to be a factor. Meanwhile for ESO 121-G020 we get a high inclination of

78°±5°, which is not apparent from the fuzzy blob in the optical image, and may actually have a moderate amount of internal extinction. ESO 348-G009 is likely to be the most affected by internal dust extinction as it is an edge on disk galaxies as shown by both the optical image and the rotation curve fit ($i = 80°\pm5°$). The optical image of ESO 348-G009 seems to suggest some dust extinction with clumpy patches along the disk (although these could be H II regions also).

As was discussed in Chapter 6, the use of distances calculated from Local Group velocities for galaxies in the nearby Universe can be problematic. As all the redshift velocities for our galaxies are very low peculiar velocities can contribute a significant proportion to the systemic velocity especially for galaxies associated with groupings, and so the uncertainty in the distance calculated by this method can be high. In addition there is an uncertainty in using the Hubble constant in the Local Universe as it may be different from further out where it is calculated (our adopted value of $H_0 = 75\ \mathrm{km\,s^{-1}\,Mpc^{-1}}$ is only following the HIPASS convention and not any particular observational result). However there is no easily available method currently for finding an accurate distance to all of these galaxies, and even where there is it requires considerable investment of resources even for the closest galaxies (such as time on HST for tip of the red giant branch distances), so the Hubble flow distances remain the most reliable for now.

Evidence from studies on the Sculptor group of galaxies (Jerjen et al., 1998) suggests that the Hubble relationship is much steeper in this group than for galaxies further out due to the probable gravitational influence of the Local Group. So for the three galaxies in our sample that appear to be members of Sculptor our distance values are likely to be overestimates. If we use the Sculptor Hubble constant of Jerjen et al. (1998, $H_0 = 119\ \mathrm{km\,s^{-1}\,Mpc^{-1}}$) then the Local Group velocity distances to these galaxies would be 6.0 Mpc for MCG–04-02-003, 4.8 Mpc for ESO 473-G024, and 5.3 Mpc for ESO 348-G009. This would put all three on the far side of the Sculptor group (Côté et al., 1997), and would mean that the distance dependent properties in Table 7.5 for these galaxies (everything except $\mathcal{M}_{\mathrm{HI}}/L_{\mathrm{B}}$) would be significantly different.

7.4.4 Finding High $\mathcal{M}_{\mathrm{HI}}/L_{\mathrm{B}}$ Galaxies

We have seen that ultimately only one of our galaxies has proved to have an extreme H I mass-to-light ratio, the subject of Chapter 6 ESO 215-G?009. The position of this galaxy in Fig. 7.4 shows that it is significantly separated from the other galaxies examined here. It is also likely that many of the remaining candidates from the BGC with high ratios will fall to lower $\mathcal{M}_{\mathrm{HI}}/L_{\mathrm{B}}$ values if we had also observed them. So the questions now are how significant is the position of ESO 215-G?009, and can we find a way to effectively find more of these very high to extreme $\mathcal{M}_{\mathrm{HI}}/L_{\mathrm{B}}$ galaxies if they exist?

Firstly, we must be very careful here of small number statistics, after all we

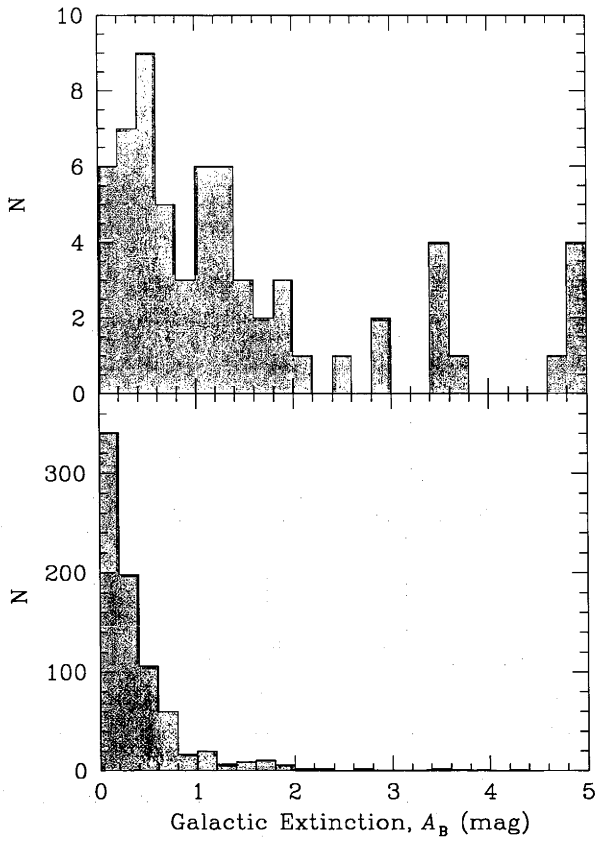

Fig. 7.6: Histogram of B band Galactic extinction for the 64 galaxies in the BGC with clear optical identifications but no B band apparent magnitude in LEDA (top). For comparison the histogram for the 789 BGC galaxies with LEDA magnitudes is included (bottom). The last bin in both includes all galaxies with $A_B > 5$ mag.

have only examined nine galaxies out of the 1000 in the BGC. It is possible that there are some other galaxies in the BGC that the B magnitudes LEDA provided were more accurate reflections of the true values, or that were overestimates that would increase the ratio. Also, there may be other candidates in the 211 BGC galaxies for which we do not have B magnitudes from LEDA. Of these objects, 64 were identified in LEDA but had no B magnitude measurement. 91 were classified as "new" in the BGC, having no previously known optical counterpart in the databases. All but one of the remaining objects was identified as a group or pair of galaxies that could not be separated in the HIPASS observations (the other object, ESO 174-G?001, was not available in LEDA due to name confusion, see Chapter 6). Among the galaxies with no B band data or the new galaxies there could potentially be more examples of high $\mathcal{M}_{HI}/L_B$ dwarfs, or even object with H I emission but no stars.

Fig. 7.6 shows a histogram of the SFD98 Galactic extinction (A_B) for the 64

objects that were in LEDA but had no B band measurement (top panel). Beneath is the histogram for the 789 galaxies with B band data. While the vast majority of the latter galaxies have low Galactic extinction, less than 9% having $A_B > 1$ mag, just over half of the objects without B measurements (34 galaxies) have extinctions higher than 1 mag. It is clear that most of these object have no measurements as they are located in the Galactic Plane where such measurements are more difficult due to high extinction and foreground stars. Likewise, when Ryan-Weber et al. (2002) studied the newly cataloged galaxies in the BGC, they found the majority were close to the Galactic Plane ($|b| < 10°$), and were able to find optical counterparts to all but one of the 87 they examined (the remaining galaxy being behind the LMC).

The greatest difficulty in finding more extreme $\mathcal{M}_{HI}/L_B$ candidates is collecting together a large enough sample of galaxies for which we have accurate (and hopefully homogeneous) data in both the optical and radio. Many modern surveys with large numbers of galaxies now exist in both optical and H I, but they only have small overlaps. While HIPASS covers a large sky area to low redshifts, surveys like SDSS[1] cover smaller sky regions out to very high redshifts. Online databases such as LEDA are another option, but their natural inhomogeneity presents a problem. As we mentioned earlier (§ 7.4.2) we preferentially select galaxies that are more likely to have underestimated B band magnitudes in LEDA. The decision to use LEDA to obtain the optical data for the galaxies in the BGC was motivated by the fact that the database can handle large galaxy samples easily and the large variety of parameters available. LEDA has since merged with a Galactic database (Hypercat) to become HyperLEDA[2], but the data still exists in the same form.

Another online extragalactic database, the NASA/IPAC Extragalactic Database (NED[3]), prefer to list the results that they believe are the most accurate up front, and then list other available results separately with references. NED's strength lies in its presentation of individual galaxies and searches around a position, but it does not handle large batch jobs well. The use of both databases in tandem to obtain optical data for initial estimates appears to be the best database centred approach, but individual results need to be examined and/or followed up. The data would be more consistent if they came from a single source, such as the ESO-LV (Lauberts & Valentijn, 1989, whose results mostly agree with our B apparent magnitudes), although this would limit the size of the sample for comparisons. Ultimately we would like CCD photometry follow ups of all the HIPASS galaxies, although this is a large undertaking. As a start, the 6dF Galaxy Survey[4] is currently following up galaxy redshifts for many of the galaxies in HICAT (Meyer et al., 2004; Zwaan et al., 2004), the catalogue of all 4315 galaxies detected

[1] http://www.sdss.org/
[2] http://www-obs.univ-lyon1.fr/hypercat/
[3] http://nedwww.ipac.caltech.edu/
[4] http://www.aao.gov.au/local/www/6df/

by HIPASS. An alternative approach for finding "dark" galaxies in general might be to follow a more targeted stratergy as suggested by Trentham et al. (2001), by searching around isolated dwarf galaxies which are undergoing starbursts, like BCDs, for other galaxies which might be disturbers.

7.4.5 The Implications for Cosmology and Modeling

Although we have successfully found one galaxy that approaches the description of a "dark" galaxy (although as it still has optical emission it might more aptly be described as "dim"), it appears to be a rare example at this stage. This galaxy alone does not support the existence of sufficient numbers of optically elusive galaxies in the Universe to steepen observational luminosity functions to match the predicted frequency of low mass dark matter halos from ΛCDM cosmology. As for dark galaxies themselves, many of the studies of the BGC sample (such as Ryan-Weber et al., 2002) have not found any H I sources which are not associated with an optical source (either directly or in the immediate vicinity of the optical galaxy). Further studies of the optical properties of the complete HICAT sample of 4315 galaxies (Doyle et al., 2005, in preparation) have not found any galaxies which would potentially be good dark galaxy candidates.

The implication of this is that dim galaxies like ESO 215-G?009 and dark galaxies are at best only a small part of the solution to the low mass galaxy discrepancy. If there is an observational solution to this problem then it would appear lie with the "empty" dark matter halos, although the existence of such objects is still highly speculative. However, until we have a sufficiently large and complete sample of galaxies with accurate optical and H I data then there is the possibility that we are missing some galaxies with extreme $\mathcal{M}_{\rm HI}/L_{\rm B}$'s.

Even if they cannot account for the discrepancy between cosmological models and observations, the existence of even a few galaxies like ESO 215-G?009 has important implications for galaxy modeling. As seen in Figs. 1.1, 3.1 and 7.4 and mentioned in Chapter 3, there appears to be an upper limit for the H I mass-to-light ratio as a function of luminosity, with low luminosity galaxies able to have higher ratios. ESO 215-G?009 appears at or close to this limit. If this is so and we can restrain this limit a bit more, then we can place an upper limit on the amount of H I that a galaxy can retain for a given initial mass. This can help to further restrain semi-analytical galaxy models (Somerville & Primack, 1999).

Fig. 7.7 shows $\mathcal{M}_{\rm HI}/L_{\rm B}$ versus the B band effective surface brightness, $\langle\mu\rangle_{\rm eff}$, for the 596 galaxies in the BGC for which $\langle\mu\rangle_{\rm eff}$ exists, with the results of the nine galaxies from this study plotted on top. The symbols are as in Fig. 7.4. Despite the high uncertainties for the LEDA values, there appears to be a strong trend here for galaxies with lower effective surface brightness (i.e. lower star density) to have high H I mass-to-light ratios. The results for our galaxies follow this trend. A low $\langle\mu\rangle_{\rm eff}$ indicates that the dark matter potential of the galaxy is shallow (as

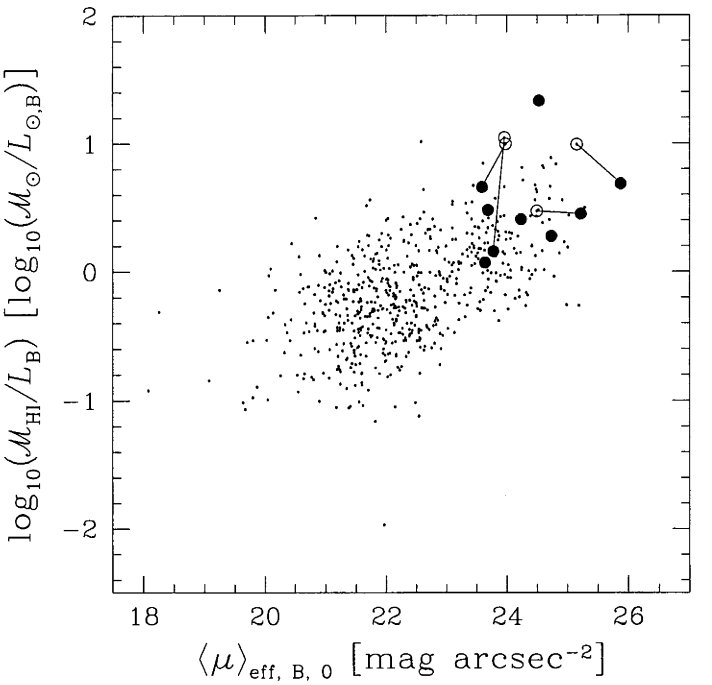

Fig. 7.7: H I mass-to-light ratio versus B band effective surface brightness for 596 galaxies from the BGC, with the results of our nine galaxies over plotted. Symbols are as in Fig. 7.4.

seen in the simulations of Mo, Mao, & White, 1998). As with the stars, we would expect that in a shallow potential the gas component would also be at a lower density. In this situation a Toomre stable gas disk may be formed as described in Verde et al. (2002), and as seen in the case of ESO 215-G?009 in Chapter 6. We will explore this idea further in the following chapter using our full sample of galaxies.

8. PROPERTIES OF A GALAXY SAMPLE BASED ON H I MASS-TO-LIGHT RATIO

We will now investigate the statistical properties of our entire sample of galaxies (41 in total) taking advantage of our more accurate values of H I mass-to-light ratio. By comparing other galaxy quantities that correlate (or do not correlate) with $\mathcal{M}_{\rm HI}/L_{\rm B}$ we may be able to determine what causes the spread in this ratio for dwarf galaxies, and why galaxies like ESO 215-G?009 can retain such a high proportion of neutral hydrogen gas. These results will be published later this year as Warren, Jerjen, & Koribalski (2005b)

8.1 The New H I Mass-to-Light Ratios

As with the nine galaxies in Chapter 7, we can now plot our new H I mass-to-light ratios, using the ATCA and 2.3m results, against the B band absolute magnitude to compare to our original plots based on LEDA magnitudes (Figs. 1.1 and 3.1). Table 8.1 summarises the main derived parameters from our observations of the entire sample (41 galaxies), including $\mathcal{M}_{\rm HI}/L_{\rm B}$ and $M_{\rm B}$. Fig. 8.1 shows the comparison of these two values, with the same markings as Fig. 7.4. As we have seen in Chapter 5 (Fig. 5.1 and 5.2) while most of the ATCA H I flux densities are in good agreement with the BGC many of the galaxies have 2.3m B band apparent magnitudes which are brighter than the values expressed in LEDA. This means that most of the $\mathcal{M}_{\rm HI}/L_{\rm B}$'s from our data are in fact significantly lower than the initial estimates. Most of our original high $\mathcal{M}_{\rm HI}/L_{\rm B}$ sample has slid down into the control sample region in Fig. 8.1, with some of the galaxies (such as IC 4212 and ESO 505-G007) proving to be brighter than our $M_{\rm B}$ limit for dwarf galaxies (> -16.5 mag). We are left with three galaxies (ESO 215-G?009, ESO 428-G033, and ESO 572-G009) with $\mathcal{M}_{\rm HI}/L_{\rm B}$ above 3 $\mathcal{M}_{\odot}/L_{\odot,{\rm B}}$, and four or five others at or around this value.

As we discussed in Chapter 7, §§ 7.4.2 and 7.4.4, this appears to be due to the fact we have selected some of the most extreme galaxies from the sample. We have therefore preferentially select many galaxies where the LEDA B band data, as a mean of numerous measurements, was affected by outlying measurements, and this trend continues throughout most of the sample. In general, the more extreme galaxies in the high $\mathcal{M}_{\rm HI}/L_{\rm B}$ are more likely to be significantly brighter than in LEDA ($\langle \Delta m_{\rm B} \rangle_{high} = 1.47$ mag brighter), while those in the control sample are

Table 8.1. Summary of Derived Parameters for each Galaxy from ATCA and 2.3m Data.

Name	M_B (mag)	L_B (10^7 $L_{\odot,B}$)	$\mathcal{M}_{HI}$ (10^7 $\mathcal{M}_\odot$)	$\mathcal{M}_{HI}/L_B$ ($\mathcal{M}_\odot/L_{\odot,B}$)
(1)	(2)	(3)	(4)	(5)
ESO 349-G031	-11.58 ± 0.06	0.67 ± 0.04	0.80 ± 0.15	1.2 ± 0.3
MCG-04-02-003	-14.65 ± 0.06	11.3 ± 0.6	34.5 ± 1.3	3.0 ± 0.3
ESO 473-G024	-13.11 ± 0.06	2.7 ± 0.2	7.8 ± 1.2	2.8 ± 0.6
IC 1574	-13.75 ± 0.03	4.90 ± 0.14	3.2 ± 0.6	0.64 ± 0.13
UGCA 015	-12.94 ± 0.05	2.33 ± 0.11	1.1 ± 0.3	0.48 ± 0.13
ESO 085-G047	-16.99 ± 0.04	97 ± 4	92 ± 7	0.94 ± 0.11
ESO 120-G021	-15.97 ± 0.06	37 ± 2	49 ± 6	1.3 ± 0.2
ESO 425-G001	-16.07 ± 0.06	42 ± 2	35 ± 9	0.8 ± 0.3
UGCA 120	-17.03 ± 0.07	101 ± 6	58 ± 2	0.57 ± 0.06
ESO 121-G020	-12.97 ± 0.06	2.39 ± 0.13	3.49 ± 0.12	1.44 ± 0.13
ATCA J061608-574552	-11.23 ± 0.07	0.48 ± 0.03	0.99 ± 0.08	2.0 ± 0.3
WHI B0619-07	-17.3 ± 0.4	130 ± 50	73 ± 4	0.5 ± 0.2
ESO 490-G017	-15.08 ± 0.07	16.7 ± 1.0	2.2 ± 0.3	0.13 ± 0.03
CGMW 1-0260			14.3 ± 1.8	
ESO 255-G019	-16.32 ± 0.08	53 ± 4	73 ± 5	1.37 ± 0.19
CGMW 1-0381			25.3 ± 1.9	
ESO 207-G007	-16.77 ± 0.06	80 ± 5	44 ± 5	0.55 ± 0.09
ESO 207-G022	-16.14 ± 0.11	45 ± 5	14 ± 3	0.31 ± 0.10
ESO 428-G033	-16.7 ± 0.2	28 ± 5	131 ± 3	4.6 ± 0.9
ESO 257-G?017	-14.75 ± 0.14	12.3 ± 1.6	34 ± 4	2.7 ± 0.7
ESO 368-G004	-16.7 ± 0.3	80 ± 20	76 ± 8	1.0 ± 0.4
PGC 023156	-16.2 ± 0.3	45 ± 12	111 ± 17	2.4 ± 1.0
ESO 164-G?010	-17.7 ± 0.3	180 ± 40	27 ± 4	0.15 ± 0.06
ESO 215-G?009	-12.9 ± 0.2	2.3 ± 0.4	50.8 ± 1.7	22 ± 4
CGCG 012-022	-16.45 ± 0.03	61.3 ± 1.7	112 ± 17	1.8 ± 0.3
UGC 06780	-17.78 ± 0.08	201 ± 15	220 ± 30	1.1 ± 0.2
ESO 572-G009	-14.92 ± 0.06	14.5 ± 0.8	71 ± 13	4.8 ± 1.1
ESO 505-G007	-17.75 ± 0.08	196 ± 14	234 ± 6	1.18 ± 0.12
ESO 572-G052	-15.96 ± 0.07	38 ± 3	62 ± 14	1.6 ± 0.5
UGCA 289	-16.51 ± 0.04	63 ± 2	66 ± 5	1.04 ± 0.11
UGCA 307	-15.39 ± 0.05	22.2 ± 1.0	43 ± 2	1.90 ± 0.19
UGCA 312	-15.95 ± 0.03	37.4 ± 1.2	72 ± 7	1.9 ± 0.2
UGCA 322	-18.01 ± 0.04	249 ± 8	247 ± 13	0.98 ± 0.08
IC 4212	-17.37 ± 0.05	138 ± 6	356 ± 8	2.56 ± 0.17
IC 4824	-15.98 ± 0.11	38 ± 4	52 ± 3	1.4 ± 0.2
ESO 141-G042	-16.65 ± 0.10	71 ± 6	28 ± 3	0.39 ± 0.08
IC 4870	-15.70 ± 0.10	30 ± 3	47 ± 3	1.6 ± 0.2
IC 4951	-15.95 ± 0.03	37.2 ± 1.2	44 ± 4	1.17 ± 0.15
ESO 347-G017			17 ± 2	
UGCA 442			18.3 ± 0.5	
ESO 348-G009	-14.86 ± 0.07	13.6 ± 0.9	26.1 ± 0.5	1.89 ± 0.16
ESO 149-G003	-14.33 ± 0.03	8.4 ± 0.2	5.6 ± 0.8	0.66 ± 0.11

(1) Galaxy name (as in Table 3.1 and other previous tables).
(2) B band absolute magnitude (from Eqn. 3.4).
(3) B band luminosity (from Eqn. 3.2).
(4) H I mass (from Eqn. 3.1).
(5) H I mass-to-B band luminosity ratio ($\mathcal{M}_{HI}/L_B$, from Eqn. 3.3).

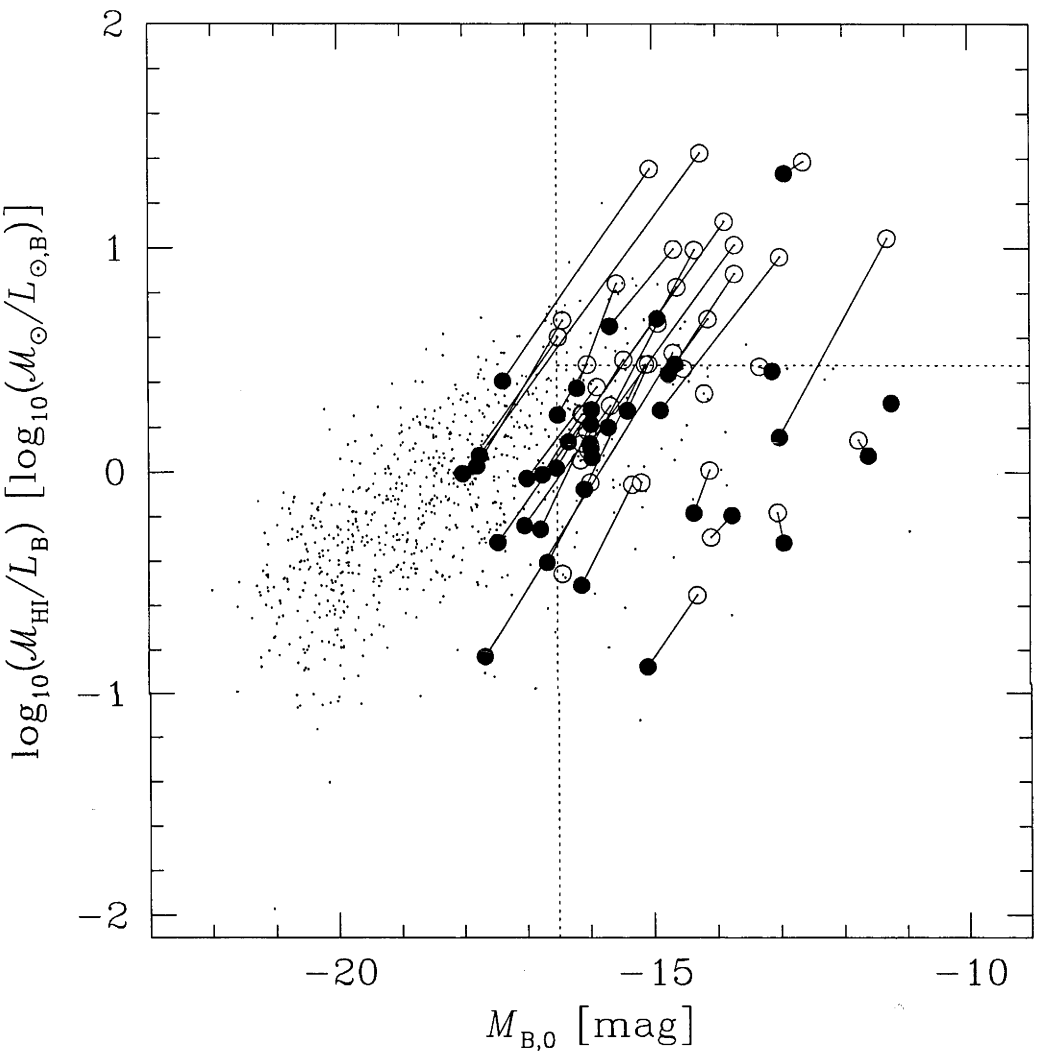

Fig. 8.1: H I mass-to-light ratio versus absolute B magnitude showing our recalculated values. The open circles mark the positions of our 41 sample galaxies from the combination of the BGC and LEDA data, while the filled circles mark the positions using our new data for the 37 sample galaxies (plus ATCA J061608–574552) for which we have CCD photometry. The solid lines join the new results to the BGC and LEDA data. The filled circle without a joining line is ATCA J061608–574552. The 789 BGC galaxies in Fig. 1.1 are marked with the small dots. The dotted sectioning lines for dwarfs and high $\mathcal{M}_{\rm HI}/L_{\rm B}$ galaxies are as in Fig. 3.1.

Table 8.2. Data for Other Galaxies Known to have High H I Mass-to-Light Ratios.

Name	M_B (mag)	L_B ($\times 10^7$ $L_{\odot,B}$)	$\mathcal{M}_{HI}$ ($\times 10^7$ $\mathcal{M}_\odot$)	$\mathcal{M}_{HI}/L_B$ ($\mathcal{M}_\odot/L_{\odot,B}$)	References
(1)	(2)	(3)	(4)	(5)	(6)
DDO 154	−13.8	5.2	49.0	9.4	Carignan & Beaulieu (1989) Hoffman et al. (1993)
NGC 3741	−13.1	2.8	16.0	5.8	Begum et al. (2005)
NGC 2915	−15.9	35.5	95.8	2.7	Meurer et al. (1994, 1996)
UGCA 292	−11.7	0.72	5.1	7.0	Young et al. (2003)

(1) Galaxy name.
(2) *B* band absolute magnitude.
(3) *B* band luminosity.
(4) H I mass.
(5) H I mass-to-light ratio.
(6) Reference/s where we obtained the information on the galaxies.

more likely to have accurate LEDA values or be slightly brighter ($\langle \Delta m_B \rangle_{control}$ = 0.30 mag brighter). There is a clue to this from our initial look at the sample back in Chapter 3 in the morphological types listed by LEDA. We can see from Fig. 3.3 that while the control sample galaxies are almost all irregulars and Sm types, the high $\mathcal{M}_{HI}/L_B$ sample had a larger spread of morphologies, up to moderately large spiral galaxies. Indeed we see that several of these stellar systems (such as IC 4212, UGCA 322, and UGC 06780) are among the galaxies that we now find, somehow not surprisingly, are brighter than our dwarf magnitude limit.

Fig. 8.2 again shows $\mathcal{M}_{HI}/L_B$ versus M_B, but only for the 37 galaxies with our recalculated values and ATCA J061608–574552, including error bars. We have included the upper envelope line which we empirically determined in Fig. 1.1, and is given by Eqn. 1.3. At a given absolute magnitude we would not expect the $\mathcal{M}_{HI}/L_B$ to exceed the value defined by this envelope if the trend seen in the BGC and LEDA results can be followed to the dwarf regime. All our sample objects remain within this envelope, and the more extreme objects appear to trace the envelope line well. This indicates that this upper envelope may reflect a true physical limitation on the H I mass-to-light ratio for a galaxy of a certain initial mass. As we discussed in § 7.4.5 of the previous chapter, this could be used to constrain galaxy modeling programs, although we would need more galaxies near the envelope line at the faint end and accurate optical results at the bright end to better determine the limit.

With few galaxies remaining in our sample with $\mathcal{M}_{HI}/L_B$ greater than our original cut off value of 3 $\mathcal{M}_\odot/L_{\odot,B}$ we would like to include other galaxies known to have unusual H I properties for comparison. Tables 8.2 and 8.3 summarise the properties of four galaxies from the literature known for their H I extent and/or $\mathcal{M}_{HI}/L_B$, DDO 154 (Carignan & Freeman, 1988; Carignan & Beaulieu,

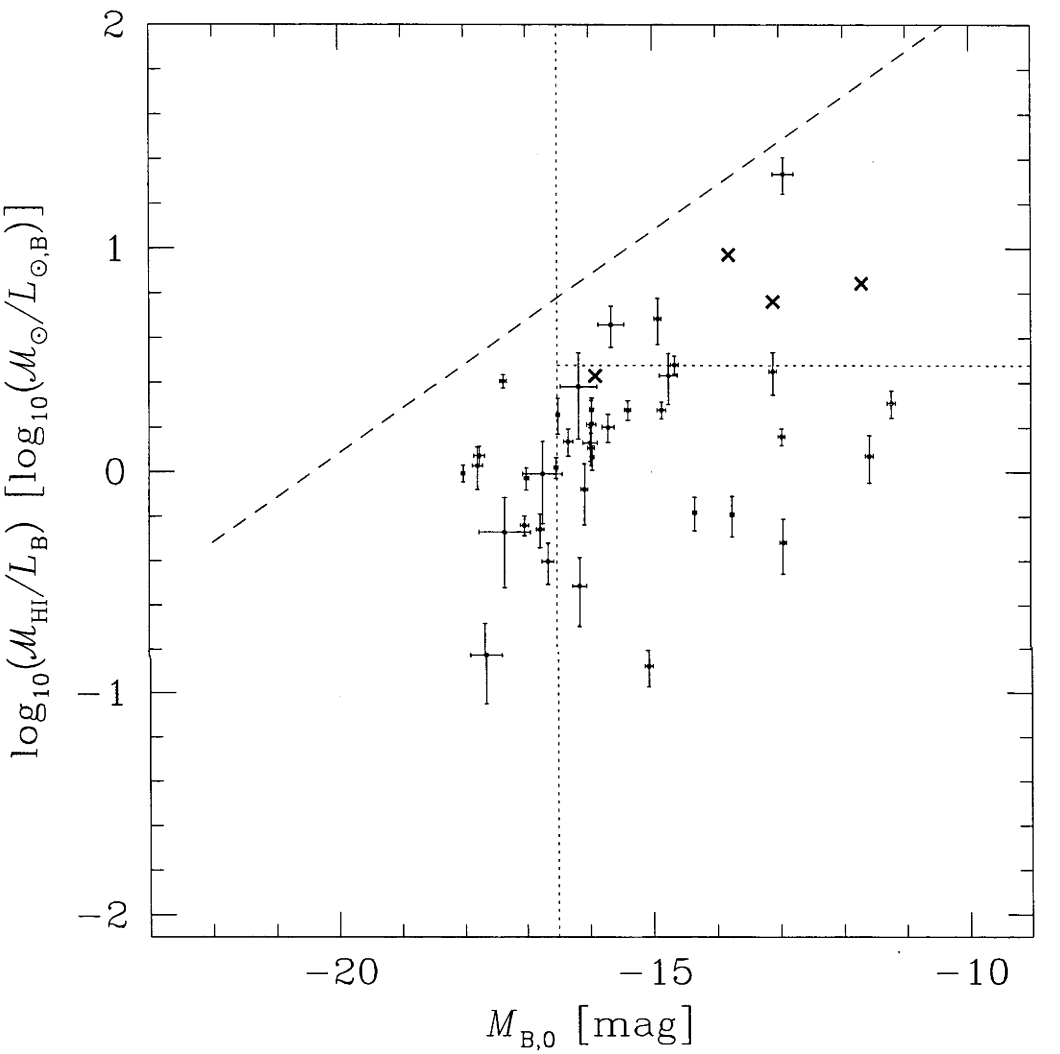

Fig. 8.2: H I mass-to-light ratio versus absolute B magnitude using our new data for the 37 sample galaxies (plus ATCA J061608–574552) for which we have CCD photometry, including uncertainties (small dots with error bars). The crosses mark the position of the four galaxies from other literature sources (see text). The upper envelope line from Fig. 1.1 is shown as the dashed line. The dotted sectioning lines for dwarfs and high $\mathcal{M}_{\rm HI}/L_{\rm B}$ galaxies are as in Fig. 3.1.

Table 8.3. Further Data for Other Galaxies Known to have High H I Mass-to-Light Ratios.

Name	A_B, SFD98 (mag)	$r_{25,B}$ (arcsec)	D (Mpc)	$w_{20}/\sin i$ ($km\,s^{-1}$)	References
(1)	(2)	(3)	(4)	(5)	(6)
DDO 154	0.04 ± 0.01	144	5.0	156	Krumm & Burstein (1984)
NGC 3741	0.11 ± 0.02	81	3.7	119	LEDA
NGC 2915	1.19 ± 0.19	120	2.7	188	Meurer et al. (1996)
UGCA 292	0.07 ± 0.01	104	4.3	66	LEDA

(1) Galaxy name (as in Table 8.3).
(2) SFD98 *B* band Galactic extinction value (A_B).
(3) Galaxy radius to the 25th mag arcsec^2 isophot in the *B* band, from LEDA.
(4) Approximate distance derived from the Local Group velocity (using NED systemic velocity).
(5) Velocity width of the H I line at 20% of peak flux density corrected for inclination.
(6) Reference where we obtained the velocity width and inclination correction for column (5).

1989), NGC 3741 (Begum et al., 2005), NGC 2915 (Meurer et al., 1994, 1996), and UGCA 292 (Young et al., 2003). These galaxies are marked with crosses in Fig. 8.2 for comparison with our sample. Three of these galaxies (DDO 154, NGC 3741, and UGCA 292) fit nicely into the gap between ESO 215-G?009 and the rest of our sample, while NGC 2915 is comparable to the mid-range $\mathcal{M}_{HI}/L_B$ galaxies in our control sample (this galaxy is also in the BGC, but we do not used those results here). Tables 8.2 and 8.3 summarise the properties of these four galaxies

While we have far fewer high H I mass-to-light ratio galaxies than was suggested by the combination of the BGC and LEDA data, we still have a good range in both $\mathcal{M}_{HI}/L_B$ (between about 0.15 and 20 $\mathcal{M}_\odot/L_{\odot,B}$) and luminosity ($M_B$ between about -11.2 and -18.0, most galaxies still being dwarfs). Importantly, we have a range in $\mathcal{M}_{HI}/L_B$ for galaxies at similar luminosities over most of the luminosity range. With the addition of the four literature galaxies this gives us a good basis for the comparison of sample properties based on $\mathcal{M}_{HI}/L_B$. And once again one of the first things we must look at is Galactic extinction.

8.2 Could Galactic Extinction be Affecting $\mathcal{M}_{HI}/L_B$?

Galactic dust extinction is a subject which we have visited many times in this thesis. As we saw in § 6.5.2 this can have a very strong effect on the H I mass-to-light ratio of of a galaxy when it is not treated properly. The SFD98 Galactic extinction correction values that we are using are measured over relatively large scales compared to the optical images, and there may be smaller scale variations especially in around the Galactic Plane (see § 7.4.3). It is possible that small dust clouds in the plane of the Milky Way could produce "fake" high H I mass-to-light ratio galaxies by blocking light or hiding parts of the optical galaxy. If we were to see a trend for high $\mathcal{M}_{HI}/L_B$ galaxies to be located close to the Galactic Plane

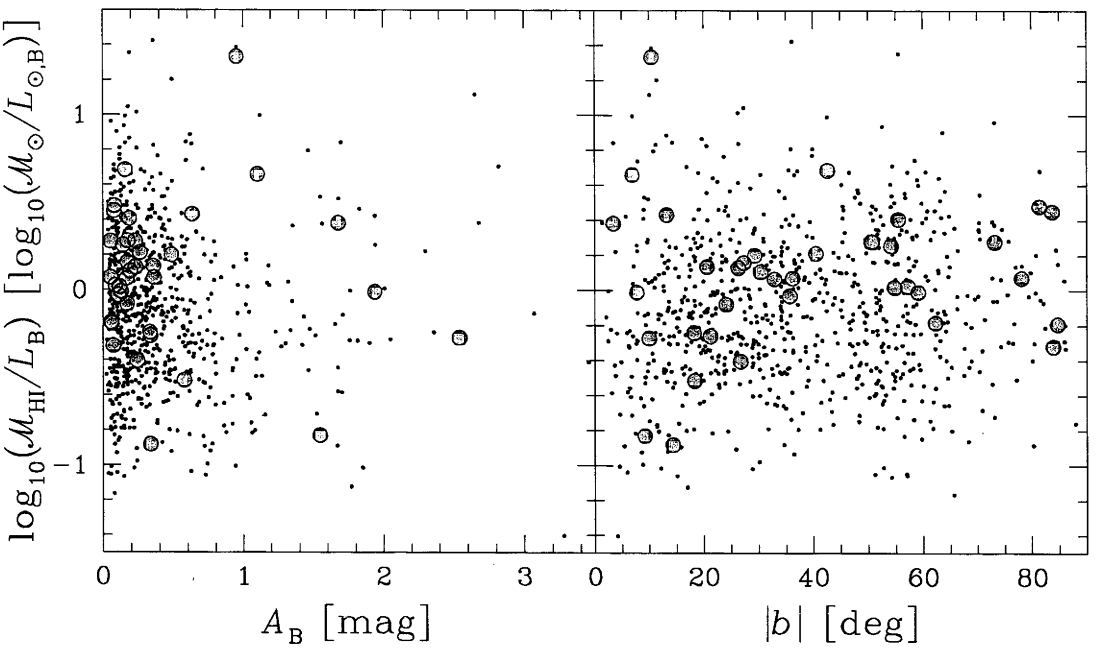

Fig. 8.3: H I mass-to-light ratio versus the SFD98 B band Galactic extinction (left) and versus the absolute Galactic Latitude (right). In both plots, the large solid points mark our new values for the 37 sample galaxies (plus ATCA J061608–574552) for which we have CCD photometry, while the small points mark the 789 BGC galaxies (including the previous positions of our sample objects).

or surrounding sky areas with relatively high dust extinction it could call into question many of the $\mathcal{M}_{\rm HI}/L_{\rm B}$ values we have calculated.

Fig. 8.3 shows $\mathcal{M}_{\rm HI}/L_{\rm B}$ versus both the SFD98 Galactic extinction ($A_{\rm B}$) and Galactic latitude (b), with both our new results and the BGC/LEDA galaxies. There is no significant trend in either plot to indicate that we are only getting high $\mathcal{M}_{\rm HI}/L_{\rm B}$ galaxies close to the Galactic Plane. Therefore we can be confident that our ratios are not affected by Galactic dust or star contamination beyond the stated uncertainties (except in the cases we have already noted). Of the four literature galaxies only NGC 2915, the galaxy with the lowest $\mathcal{M}_{\rm HI}/L_{\rm B}$, is close to the Galactic Plane and has a significant level of Galactic extinction.

Kraan-Korteweg & Huchtmeier (1992) investigated galaxies in the Puppis region of the Plane of the Milky Way, an area lower dust density than much of the rest of the plane at similar Galactic latitudes (although the extinction is still significant). They found that for their sample of galaxies in this region the global properties, including $\mathcal{M}_{\rm HI}/L_{\rm B}$, were similar to those of typical disk galaxies in the Local Universe, suggesting that in general that the effect of Galactic dust is not causing problems with "fake" high $\mathcal{M}_{\rm HI}/L_{\rm B}$ objects.

The ability of H I observations to see through the Galactic plane (the only interference being H I emission and absorption from the Milky Way itself at low

velocities) is an increasingly important asset for those who wish to look at the structure of the Local Universe over the whole sky. Surveys like HIPASS (see the BGC) as well as those targeted directly at the Galactic plane, such as the Dwingeloo Obscured Galaxy Survey (Henning et al., 1998) and the HIPASS Zone of Avoidance (ZOA) Survey (going deeper than the rest of HIPASS, Henning et al., 2000; Donley et al., 2005), show filaments, groups and other features not previously seen due to their obscuration in the optical. However, as we require accurate optical observations to confirm a high $\mathcal{M}_{\rm HI}/L_{\rm B}$ we cannot venture too far into the Galactic Plane to search for more galaxies of this type. In the future it would be advantageous to use redder optical bands or near-infrared observations rather than B band as we would be able to observe galaxies deeper in the Galactic Plane, as well as reduce any internal extinction effects.

8.3 The Tully Fisher Relationship

In Chapter 2, § 2.3, we looked at the Tully & Fisher (1977) relationship produced by the sample of BGC objects, using both the stellar and the baryonic masses of the galaxies (Fig. 2.10). Fig. 8.4 shows these same relations with our final sample of 38 galaxies (the large points) and the four literature galaxies (crosses) for both the classical and baryonic cases. For our sample galaxies the rotation was estimated from our new w_{20} values corrected by the LEDA inclination values (as we only have inclination for a few galaxies from the rotation curve fit), the stellar mass was estimated using the B band magnitudes (see § 2.3), and we have not limited the galaxies plotted as we did for Fig. 2.10. As in the original plot, the baryonic version of this empirical relation is much tighter than the classical (stellar mass only) version, and the relation appears to hold down into the dwarf regime. Unlike McGaugh et al. (2000, who used I band data for the stellar mass) we do not see a distinct drop off in mass at the dwarf regime end in the stellar mass version of the relation, merely a larger range in mass than is seen in the baryonic plot. The McGaugh et al. (2000) results contained a systematic error in their calculation of I band magnitudes which is described by Gurovich et al. (2004).

The dashed line going through the baryonic Tully & Fisher plot (lower panel) is the recently derived least squares fit to the baryonic relationship derived by (Pfenniger & Revaz, 2005). They used the same sample which (McGaugh et al., 2000) used for their baryonic Tully & Fisher relationship, and included a correction factor c to the H I mass to account for other baryonic matter within the galaxy (such as H_2), which was optimised to produce the lowest scatter in their relationship ($c = 2.98$). We have *not* used this factor to correct our calculation of the baryonic mass (the scatter in our results reduces its effectiveness), but almost all our sample still follow this trend very closely, as do the four literature galaxies.

The blue points in both panels of Fig. 8.4 show the galaxies in our sample with H I mass-to-light ratios greater than 2 $\mathcal{M}_{\odot}/L_{\odot,\rm B}$. One of these galaxies,

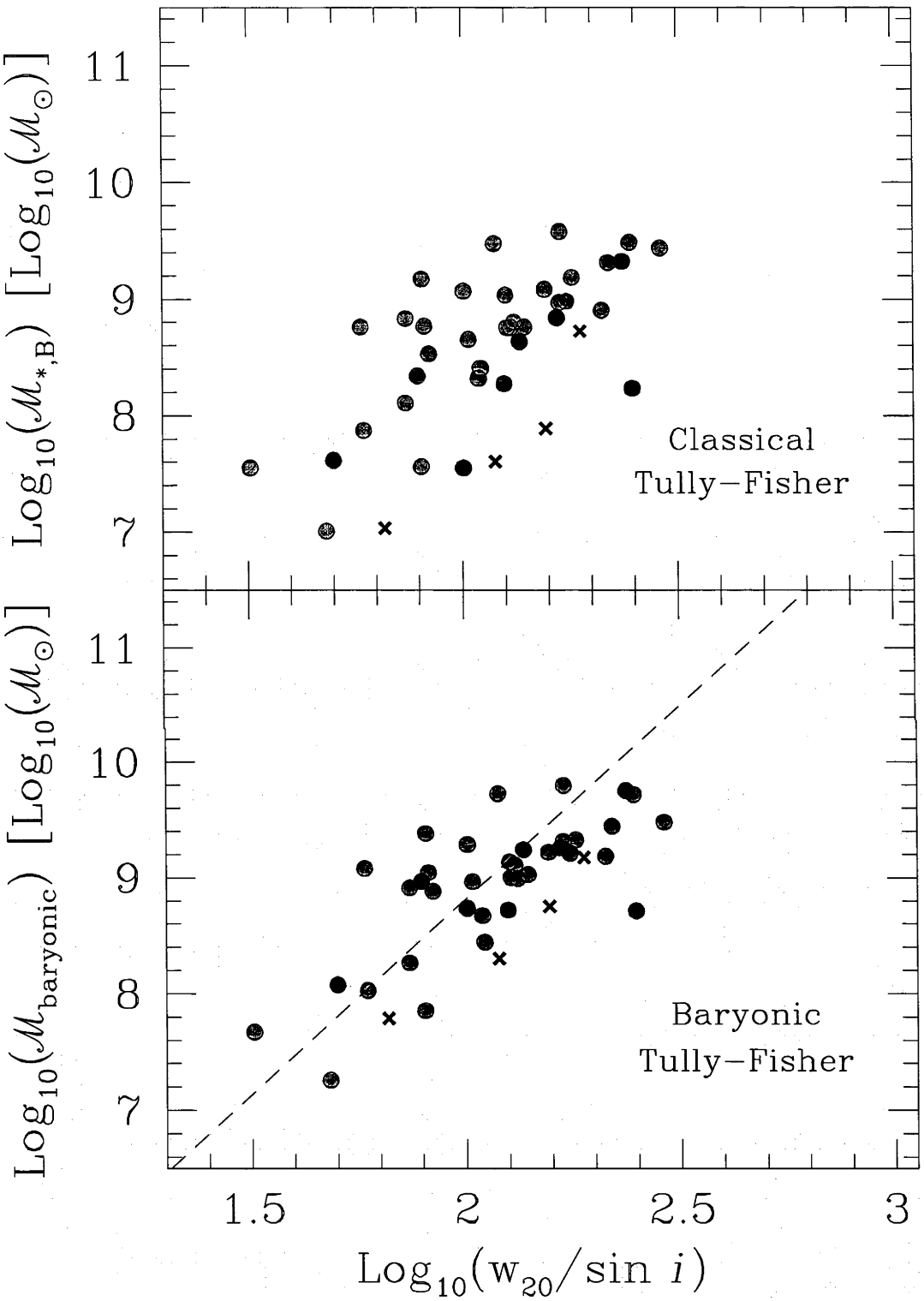

Fig. 8.4: The classical (stellar, top) and baryonic (bottom) Tully Fisher relations (Tully & Fisher, 1977), showing our 37 sample objects (large grey and blue points), and the four literature galaxies (crosses). Stellar mass is calculated from the B band magnitude (see § 2.3). The blue points are the galaxies in our sample with $\mathcal{M}_{\rm HI}/L_{\rm B} > 2\ \mathcal{M}_{\odot}/L_{\odot,{\rm B}}$. The dashed line in the bottom panel marks the baryonic Tully Fisher relation derived by (Pfenniger & Revaz, 2005). The scale is the same as Fig. 2.10 for comparison.

MCG–04-02-003, is the object which falls below the trend in both plots. This appears to be due to the inclination correction we used for this galaxy (30° from LEDA) which may have been estimated from the central region of the galaxy only (see § 7.4.1), while a higher inclination (consistent with the outer disk and the H I distribution) would bring it back into the main trend. All the other higher $\mathcal{M}_{\rm HI}/L_{\rm B}$ galaxies, as well as the four literature galaxies, appear to sit slightly below the trend of the other galaxies in the classical Tully & Fisher plot, but are in line with the others in the baryonic Tully & Fisher plot. This reinforces the results of the study of ESO 215-G?009, that high H I mass-to-light ratio galaxies appear to have normal quantities of baryonic matter in them, but are deficient in luminous matter (possibly due to inefficent star formation).

8.4 Stellar Density

Fig. 8.5 shows $\mathcal{M}_{\rm HI}/L_{\rm B}$ versus the B band effective surface brightness ($\langle\mu\rangle_{\rm eff,B}$), with both our new results and those from the BGC and LEDA (this parameter was only available for one of the literature galaxies, so they are not plotted). Importantly, both quantities are distance independent, especially as we only have Local Group velocity distances for these galaxies. There appears to be a strong trend between these two values, with low surface brightness (LSB) galaxies (i.e. galaxies with low stellar densities) having higher $\mathcal{M}_{\rm HI}/L_{\rm B}$'s, but it is important to understand the selection effects which may be at work here. Low H I mass-to-light ratio LSB galaxies are unlikely to be in the sample or the BGC optical properties list as they are both less likely to make the BGC or to have been catalogued in the optical, so this region of the plot is unpopulated although we know such galaxies exist (dwarf ellipticals and other gas poor dwarfs).

Very compact galaxies which resemble stars, and therefore have very high surface brightness (HSB), are also unlikely to be catalogued, as we saw with the case of ATCA J061608–574552. Whether these galaxies might also have high H I mass-to-light ratios, and thus fall above the trend seen in Fig. 8.5 is a matter of speculation. These galaxies with high stellar densities are likely to be experiencing a strong burst of star formation, which could mean they have consumed much of their gas, or at least become bright enough to reduce $\mathcal{M}_{\rm HI}/L_{\rm B}$ to typical levels.

If this was true, and compact high $\mathcal{M}_{\rm HI}/L_{\rm B}$ galaxies are not present, then the trend seen in Fig. 8.5 represents a limit to the H I mass-to-light ratios for galaxies with a given stellar density, with only low density systems able to reach high $\mathcal{M}_{\rm HI}/L_{\rm B}$'s. The surface brightness is an indicator of the depth of the dark matter potential of the galaxy (Mo et al., 1998), with higher surface brightness galaxies having deeper potentials. Therefore for a galaxy to end up with a very a high $\mathcal{M}_{\rm HI}/L_{\rm B}$ today it would need to initially have a shallow dark matter potential.

This fits with the results of de Blok, McGaugh, & van der Hulst (1996), who looked a sample of LSB galaxies in H I drawn from the sample of Schombert et al.

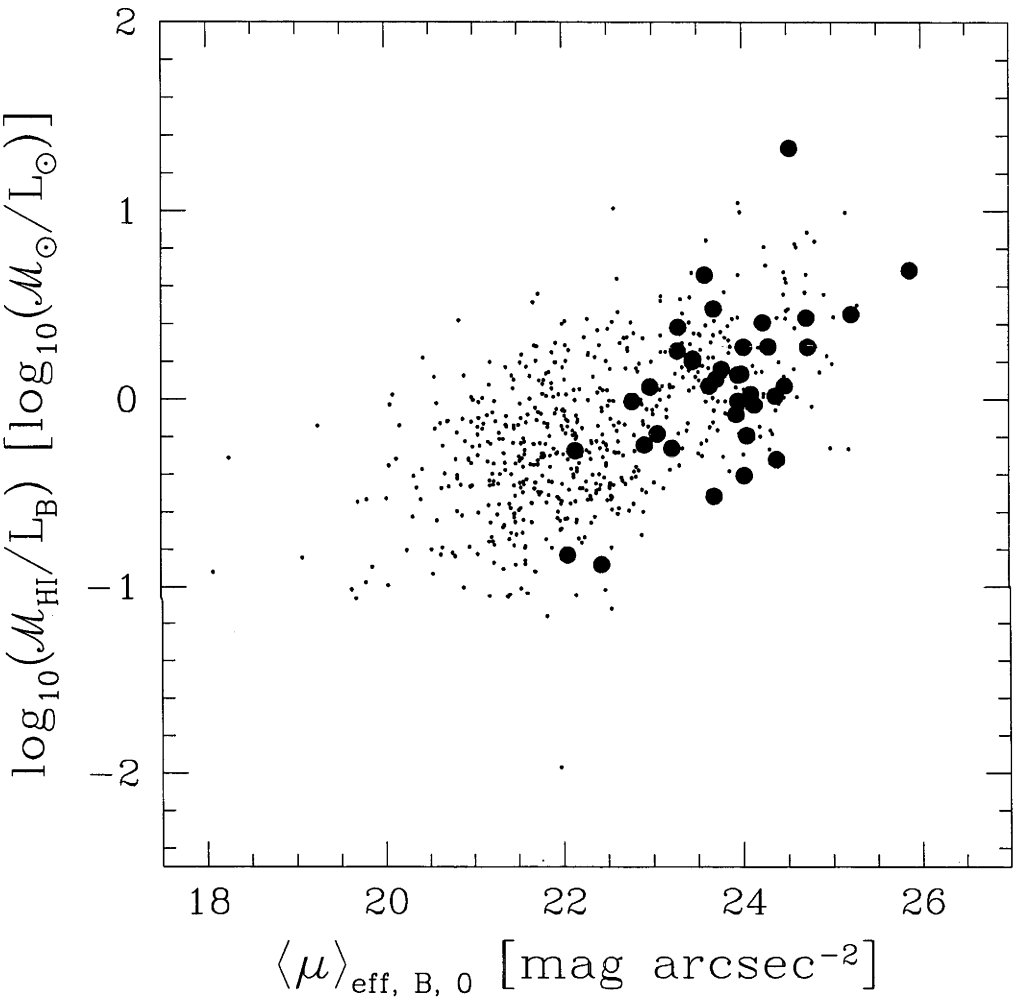

Fig. 8.5: H I mass-to-light ratio versus the B band effective surface brightness. The large solid points mark our new values for the 37 sample galaxies (plus ATCA J061608–574552) for which we have CCD photometry, while the small points mark the 594 BGC galaxies (including the previous positions of our sample objects).

(1992). They found that their sample galaxies had higher H I gas mass fractions than a sample of HSB galaxies for the same luminosity, which is present regardless of the band in which the luminosity was measured. When they looked at the relation between central surface brightness ($\mu_{0,B}$) and $\mathcal{M}_{HI}/L_B$ they found the same trend as we do for $\langle\mu\rangle_{eff,B}$, with lower surface brightness galaxies having higher ratios. We have chosen $\langle\mu\rangle_{eff,B}$ over $\mu_{0,B}$ for our analysis as it is more representative of the overall stellar density of the galaxies given the difficulty in determining the centre of dwarf irregular galaxies. These galaxies often have multiple H II regions located close to their isophotal centre (see for example the surface brightness profile of ESO 505-G007, Fig. A.105).

De Blok et al.(1996) also found a trend for LSB galaxies to have low H I gas surface densities in comparison to their HSB counterparts. This is consistent with the low gas surface density we have found for ESO 215-G?009, a LSB galaxy itself. If the dark matter potentials of these galaxies are shallow as suggested by their low stellar and gas densities then they may form into the Toomre stable disks as suggested by Verde et al. (2002). This would cause the galaxy to have inefficent star formation (see § 6.5.5) and ultimately lead to the galaxy having a high H I mass-to-light ratio, provided there were no other processes which disturbed the galaxy into more efficient star formation.

8.5 Galaxy Extent

Fig. 8.6 shows $\mathcal{M}_{HI}/L_B$ versus the optical radius ($r_{25,B}$ in kpc) from LEDA for all the galaxies in the BGC for which we had initial $\mathcal{M}_{HI}/L_B$ estimates. Overall, the trend is for more extended galaxies to have a much narrower range in $\mathcal{M}_{HI}/L_B$, converging towards a relatively low ratio of $\sim$ 0.5 $\mathcal{M}_\odot/L_{\odot,B}$ for large galaxies (presumably these are large spiral galaxies). The dwarf galaxies in the BGC ($M_B >$ -16.5 mag) are marked in grey. These galaxies also show a tendency to converge to a narrow range in $\mathcal{M}_{HI}/L_B$ with larger radii, although they converge to a higher ratio at smaller radii. This reflects both the tendency for dwarfs to have higher $\mathcal{M}_{HI}/L_B$'s in general (as seen in Roberts & Haynes, 1994), their smaller size, and the selection effects at work for dwarf galaxies in the BGC (see § 3.1) which means we are less likely to have extended LSB galaxies with low $\mathcal{M}_{HI}/L_B$ in the BGC sample.

Fig. 8.7 shows $\mathcal{M}_{HI}/L_B$ versus the effective optical radius ("half light" radius, $r_{eff,B}$ in kpc) for our sample galaxies using our recalculated values. Once again we see the narrowing of the $\mathcal{M}_{HI}/L_B$ range with increasing radius, confirming that the trend seen in Fig. 8.6 remains after the ratios are recalculated (although we are comparing different radii measurements). Both of these comparisons suggest that galaxies with large optical extent, such as spiral galaxies, are unable to retain large proportions of H I gas as smaller galaxies are, reflecting the limitations seen in our $\mathcal{M}_{HI}/L_B$ versus M_B plots (such as Fig. 8.1). It has been seen that very high

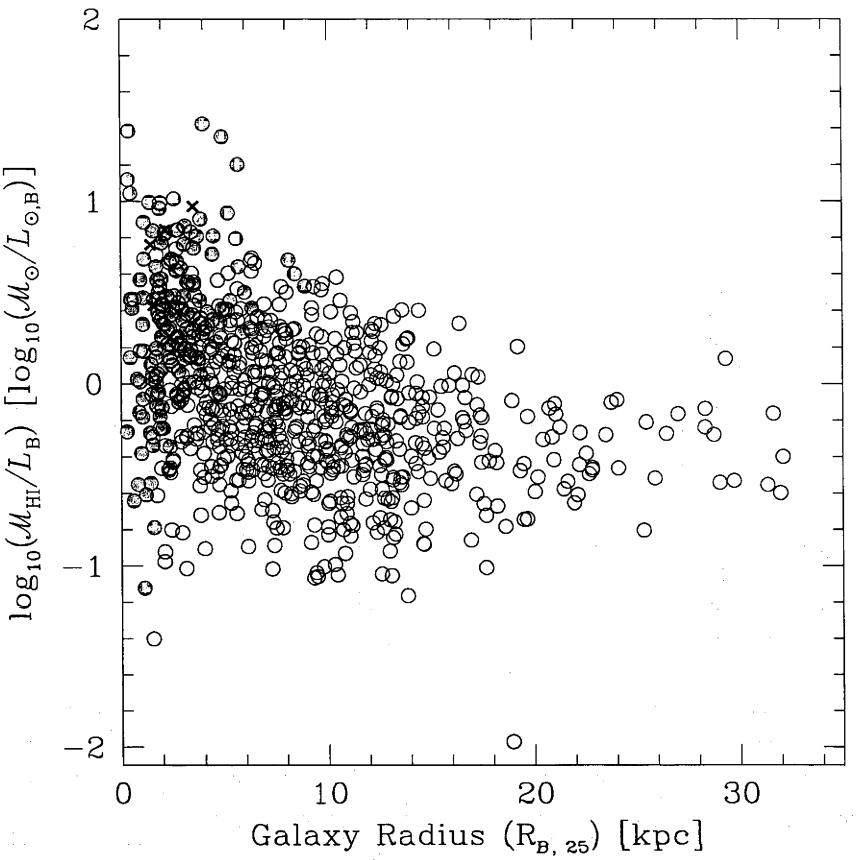

Fig. 8.6: H I mass-to-light ratio versus $r_{25,B}$, the B band optical radius of the galaxy out to the 25 mag isophot from LEDA (converted to kpc using our estimated distances), for the 787 BGC galaxies which have blue apparent magnitudes and $r_{25,B}$ in LEDA. The grey points mark the 148 galaxies which we classified as dwarfs ($M_B > -16.5$ mag) in § 3.2.

$\mathcal{M}_{HI}/L_B$ galaxies like ESO 215-G?009 (Chapter 6), DDO 154 (Krumm & Burstein, 1984), and NGC 3741 (Begum et al., 2005) have very extended H I distributions compared to their optical extent. As the beam of our ATCA H I observations comparable to the size of the H I distribution for all but a few of our galaxies we are unable to make this comparison for all our sample as we have done for ESO 215-G?009 currently. Certainly if the arguments of § 8.4 hold we might expect that there is a strong relationship between $\mathcal{M}_{HI}/L_B$ and the H I extent scaled to the optical size.

The question should be asked here what the best method to measure the extent of a galaxy in both the optical and H I. There are many values used in the literature, including the radius at a specific isophotal/isodensity level (as in the case of $r_{25,B}$ and the Holmberg radius), the half light (effective) radius (as in Fig. 8.7 above), and the radius at the detection limit of the observations (often the case for H I observations, as we have done for the H I of ESO 215-G?009). All of these

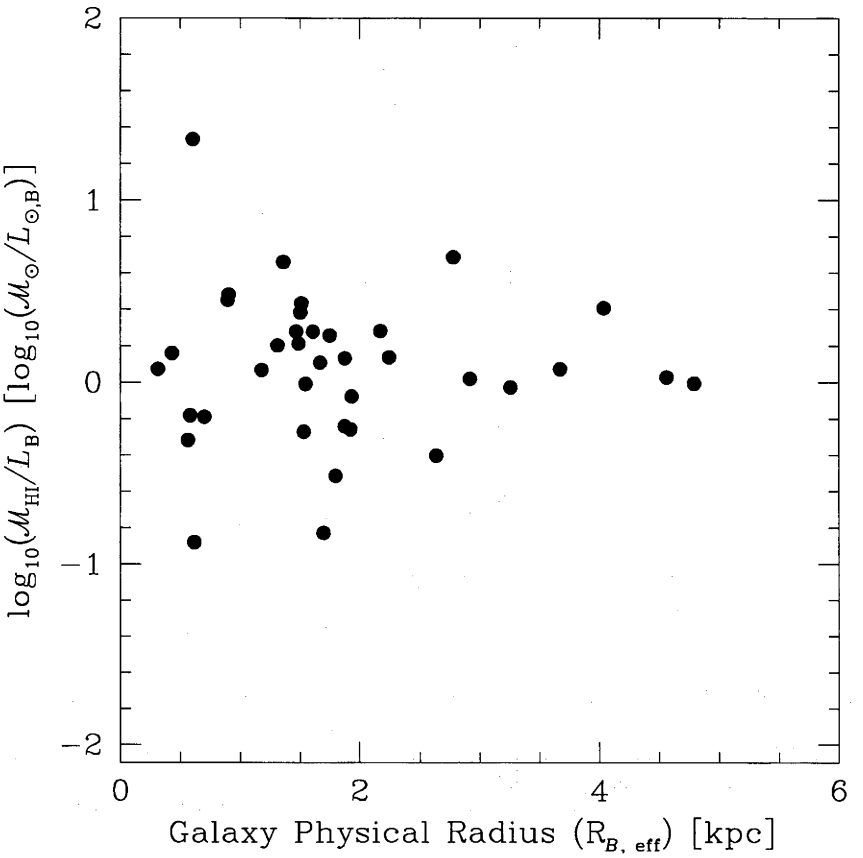

Fig. 8.7: H I mass-to-light ratio versus the B band effective radius using our new values for the 37 sample galaxies (plus ATCA J061608–574552) for which we have CCD photometry.

methods have limitations. LSB galaxies might have central surface brightness' close to or below any isophotal level chosen, which could make the first method meaningless for those galaxies. The second method can be affected by the radial structure of the galaxy, as seen in the case of MCG–04-02-003 (see the surface brightness profile in Fig. A.7) with the effective radius sitting at the transition between the compact central region and the extended disk surrounding it. And the third method is dependent on the sensibility of the observations, which is not ideal when the galaxies are not all observed to the same depth. It is important to reconcile these problems and have a standard method of measuring both the optical and H I extent of a galaxy so that observers are comparing the same quantity.

8.6 The Effect of the Environment

The variation in the properties of galaxies with the environment which they exist in has been noted since the early years of extragalactic astronomy, with studies such as Hubble & Humason (1931) showing that early type galaxies such as giant

ellipticals are more common in rich cluster environments. The morphology-density relationship is now a well know correlation, generally characterised by a transition from greater numbers of spiral galaxies in low density environments to greater numbers of ellipticals in dense environments (Oemler, 1974; Dressler, 1980). It is particularly prominent in and around galaxy clusters, but has been seen to extend out several orders lower in space density (Dressler, 1984), into groups (Postman & Geller, 1984) and the field (Binggeli et al., 1990) where we find most of the galaxies we have looked at in our sample. Many of these early morphology-density relationship analyses were done using projected distances between the galaxies only (i.e. the line of sight separation was not taken into account).

As well as morphology, the H I content of galaxies has been seen to correlate with environment (Dressler, 1984; Karachentsev et al., 2004). We have already seen in Chapter 6, § 6.5.6 that ESO 215-G?009 is a very isolated galaxy, being about 1.9 Mpc from the centre of the nearest group, the Centaurus A group, and ~1.7 Mpc from NGC 4945, which appears to be the nearest neighbour galaxy. If there were a trend in our sample for the higher $\mathcal{M}_{\rm HI}/L_{\rm B}$ dwarf galaxies to be generally more isolated than their low $\mathcal{M}_{\rm HI}/L_{\rm B}$ counterparts this could suggest that the quantity of H I a low mass galaxy can retain, or in other words the effectivness of star formation in the galaxy, partially depends on the gravitational influence of neighbouring galaxies even for the most isolated systems.

Karachentsev et al. (2004) used a tidal index, Θ defined by Karachentsev & Makarov (1999), to quantify the tidal influence of neighbouring galaxies on a large sample of galaxies (451) within 10 Mpc of the Milky Way (including most of our sample objects within this radius). The index for a galaxy is based on the mass of the "main disturber" (the galaxy which appears to exert the largest tidal influence) divided by the cube of the distance between the two, and is scaled such that objects with $\Theta < 0$ can be considered isolated. Begum et al. (2005) have noted that the Θ given by Karachentsev et al. (2004) for NGC 3741, DDO 154, and ESO 215-G?009 are all negative and all around $\Theta \sim -1$, suggesting a strong connection between high $\mathcal{M}_{\rm HI}/L_{\rm B}$ galaxies and low density environments. Indeed, the other two galaxies we have chosen from the literature have negative indexes as well.

In order to investigate how the environment of a galaxies could affect the H I mass-to-light ratio we have looked at the neighbours of our sample galaxies and what influence they might have. NED has an option to search in a radius around a position (or a galaxy) for other objects in the database (this was used by Koribalski et al., 2004, to find the optical counterparts for the BGC galaxies, see § 2.1). We used this search to find neighbouring galaxies to the sample objects and extract some basic details on the neighbour, finding the galaxy with the smallest separation from each sample object (the "nearest" neighbour) using a rough estimate of the distance between the two based on the sky separation and the redshift velocity difference. In this way we are producing a three dimentional $\mathcal{M}_{\rm HI}/L_{\rm B}$-density

relation.

The NED search is limited to a maximum of 5° around the position chosen, which can restrict the search volume in the direction perpendicular to the line of sight for nearby galaxies quite severely. For example, at 4.2 Mpc the NED search radius around ESO 215-G?009 for an object at the same distance from us is limited to $\sim$ 370 kpc. For several galaxies, including ESO 215-G?009, this radius was inadequate to find the nearest neighbour, all objects within 5° having redshifts well beyond the galaxy. In these cases we had to resort to other search methods, such as searching at different positions around this radius or neighbours mentioned in literature sources (several come from the analysis of Karachentsev et al., 2004). Finding neighbours for objects close to the Galactic Plane is also a problem as such galaxies could easily have been missed by the optical surveys which NED draws most heavily on. This is becoming less of a problem though as surveys at other wavelengths such as H I become more extensive around the Galactic Plane (see § 8.2). However, for ESO 368-G004, which is deep in the Galactic Plane, we were unable to identify a galaxy which was appropriate, so we have excluded it from this analysis.

The velocity separation is also a problem as both the sample galaxy and its neighbour could be affected by motions not related to the Hubble flow, especially in areas where they are subject to strong gravitational effects from clusters, groups, or even each other. It is possible that ESO 505-G007 is such a case, with the galaxy that contaminates its H I measurements, ESO 505-G008 (see § 7.2.1), potentially a close neighbour except for the large velocity difference which puts it much further away than other nearby objects. Therefore, the galaxy found to be the nearest, and its estimated separation, only give an indication of the true environment of the sample galaxies as we may not have accurate distances between the galaxies.

As well as looking at which galaxy is closest, we have also looked at which neighbour potentially has the greatest tidal influence on the galaxy. Using the previously mentioned Karachentsev & Makarov (1999) tidal index as a basis we determined the galaxy which is the main disturber, using the disturber's approximate luminosity as an rough indicator of mass (from the data available in NED) divided by the cube of the separation between the galaxy and the disturber. In many cases the main disturbers were the same galaxies as the nearest neighbours, especially where those galaxies were very close. Table 8.4 gives the details of both the nearest neighbours and the main disturber galaxies that we identified in NED for the 37 galaxies in our sample with new $\mathcal{M}_{\rm HI}/L_{\rm B}$ values and the four literature galaxies.

Table 8.4. The Nearest Neighbours and Main Disturbers taken from NED for our Sample Galaxies and the Four Additional High $\mathcal{M}_{\rm HI}/L_{\rm B}$ Galaxies.

Name	Nearest Neighbour		Main Disturber Galaxy		
	Name	Separation (Mpc)	Name	Separation (Mpc)	$\sim \log_{10}(L_{\rm B,MD})$ $(\log_{10}(L_{\odot,\rm B}))$
(1)	(2)	(3)	(4)	(5)	(6)
ESO 349-G031	NGC 7793	0.34	NGC 7793	0.34	9.28
MCG–04-02-003	NGC 0024	1.62	NGC 0024	1.62	9.35
ESO 473-G024	NGC 0045	1.07	NGC 0045	1.07	9.47
IC 1574	UGCA 015	0.91	NGC 0253	1.63	10.38
UGCA 015	NGC 0253	0.79	NGC 0253	0.79	10.22
ESO 085-G047	ESO 085-G014	0.86	NGC 1703	1.15	9.91
ESO 120-G021	ESO 120-G012	0.74	ESO 120-G006	1.34	10.37
ESO 425-G001	UGCA 117	0.87	UGCA 117	0.87	8.98
UGCA 120	ESO 555-G028	0.48	ESO 555-G028	0.48	7.36
ESO 121-G020	ATCA J061608–574552	0.28	ATCA J061608–574552	0.28	6.70
ATCA J061608–574552	ESO 121-G020	0.28	ESO 121-G020	0.28	7.38
WHI B0619–07	UGCA 127	0.28	UGCA 127	0.28	9.31
ESO 490-G017	ESO 489-G?056	0.23	ESO 489-G?056	0.23	7.18
ESO 255-G019	ESO 256-G013	0.71	ESO 207-G007	0.91	8.91
ESO 207-G007	ESO 207-G022	0.64	ESO 207-G022	0.64	8.59
ESO 207-G022	ESO 207-G007	0.64	ESO 208-G021	0.79	9.67
ESO 428-G033	NGC 2380	1.38	NGC 2380	1.38	10.30
ESO 257-G?017	NGC 2427	0.63	NGC 2427	0.63	9.63
ESO 368-G004					
PGC 023156	ESO 431-G001	0.66	UGCA 137	0.72	10.59
ESO 164-G?010	NGC 2640	0.35	NGC 2640	0.35	9.87
ESO 215-G?009	NGC 4945	1.70	NGC 4945	1.70	10.11
CGCG 012-022	CGCG 012-003	0.35	CGCG 012-003	0.35	8.90
UGC 06780	CGCG 012-105	0.67	NGC 3818	1.67	9.80
ESO 572-G009	ESO 572-G006	0.15	ESO 572-G006	0.15	8.32
ESO 505-G007	UGCA 263	0.53	UGCA 263	0.53	9.34
ESO 572-G052	UGCA 257	0.80	UGCA 257	0.80	9.51
UGCA 289	NGC 4504	0.24	M 104	0.88	10.75
UGCA 307	NGC 4757	0.42	NGC 4757	0.42	8.19
UGCA 312	NGC 4920	0.47	NGC 4781	0.85	9.97
UGCA 322	LCRS B130157.2–024313	0.88	UGC 08041	1.27	9.65
IC 4212	NGC 4948A	1.12	NGC 4948A	1.12	8.99
IC 4824	AM 1909–615	0.10	ESO 141-G042	0.26	8.90

Table 8.4 (cont'd)

Name	Nearest Neighbour		Main Disturber Galaxy		
	Name	Separation (Mpc)	Name	Separation (Mpc)	$\sim \log_{10}(L_{B,MD})$ $(\log_{10}(L_{\odot,B}))$
(1)	(2)	(3)	(4)	(5)	(6)
ESO 141-G042	AM 1909–615	0.18	IC 4824	0.26	8.54
IC 4870	NGC 6744	0.80	NGC 6744	0.80	10.75
IC 4951	ESO 141-G042	1.95	ESO 141-G042	1.95	8.73
ESO 348-G009	NGC 7713	0.57	NGC 7713	0.57	8.59
ESO 149-G003	ESO 348-G009	1.97	ESO 348-G009	1.97	7.93
DDO 154	NGC 4736	1.53	NGC 4736	1.53	10.13
NGC 3741	LEDA 166115	0.28	UGC 06541	0.38	7.57
NGC 2915	HIPASS J0851–75	0.22	Circinus	1.35	10.15
UGCA 292	NGC4395	0.26	NGC4395	0.26	9.25

(1) Galaxy name.
(2) Name of the galaxy identified as the nearest neighbour.
(3) Approximate separation between the sample galaxy and the nearest neighbour in Mpc.
(4) Name of the galaxy identified as the main disturber.
(5) Approximate separation between the sample galaxy and the main disturber in Mpc.
(6) Approximate luminosity of the main disturber galaxy.

Figure 8.8 shows the H I mass-to-light ratio versus the approximate distance to the most likely nearest neighbouring galaxy for the 37 sample galaxies for which we were able to find a nearby neighbour, with the addition of the four literature galaxies. Although there is a large scatter (as we might expect given the way in which the distances were calculated) there is a slight trend for $\mathcal{M}_{\rm HI}/L_{\rm B}$ to increase as the galaxies become more isolated. ESO 215-G?009 stands out at the top right, both isolated and with a high $\mathcal{M}_{\rm HI}/L_{\rm B}$, with DDO 154 between it and the other galaxies. The majority of the sample have a neighbour within 1 Mpc, and almost all of these objects have low $\mathcal{M}_{\rm HI}/L_{\rm B}$, all but one having a ratio less than 3 $\mathcal{M}_{\odot}/L_{\odot,{\rm B}}$. For the few more isolated galaxies there appears to be a greater spread of $\mathcal{M}_{\rm HI}/L_{\rm B}$, but in general they have higher ratios.

Figure 8.9 shows the same sort of plot but this time with the distances to the main disturber galaxies plotted for both our sample and the four literature galaxies. The points and crosses are also colour and size coded to indicate the approximate tidal effect of the disturber based on the Karachentsev & Makarov (1999) tidal index, by dividing the approximate luminosity of the disturber by the cube of the separation between the galaxies. Large red points indicate a strong effect ($\log_{10}(L_{\rm B,MD}/D^3_{\rm MD}) > 11$), yellow moderate ($11 > \log_{10}(L_{\rm B,MD}/D^3_{\rm MD}) > 10$), green low ($10 > \log_{10}(L_{\rm B,MD}/D^3_{\rm MD}) > 9$), and the small blue points showing those least affected by neighbours ($9 > \log_{10}(L_{\rm B,MD}/D^3_{\rm MD})$). Again we see that there is a trend for more isolated galaxies to have higher $\mathcal{M}_{\rm HI}/L_{\rm B}$ than galaxies with close main disturbers. There is also a slight trend for the galaxies which appear to be more strongly affected by tidal forces from their main disturber to have lower ratios. Of the four literature galaxies only UGCA 292 appears to have a neighbour with a strong tidal influence.

The uncertainty in the separation values creates a large scatter for both plots. The latter plot naturally has larger uncertainty since in addition to the separation uncertainty we introduce errors from the determination of the luminosity of the disturber, as well as the possibility that another galaxy could in fact be the disturber with more accurate measurements. However, both of these two plots strongly suggest that spatial isolation is a crutial factor in the evolution of a dwarf galaxy. The more isolated the galaxy the lower the star formation rate, the lower the efficiency to convert H I into stars. Therefore, in order to find more high $\mathcal{M}_{\rm HI}/L_{\rm B}$ galaxies, or even any true "dark" galaxies which may exist, we need to look at the low galaxy density regions of the Local Universe where according to our three dimentional $\mathcal{M}_{\rm HI}/L_{\rm B}$-density relation they are most likely to form.

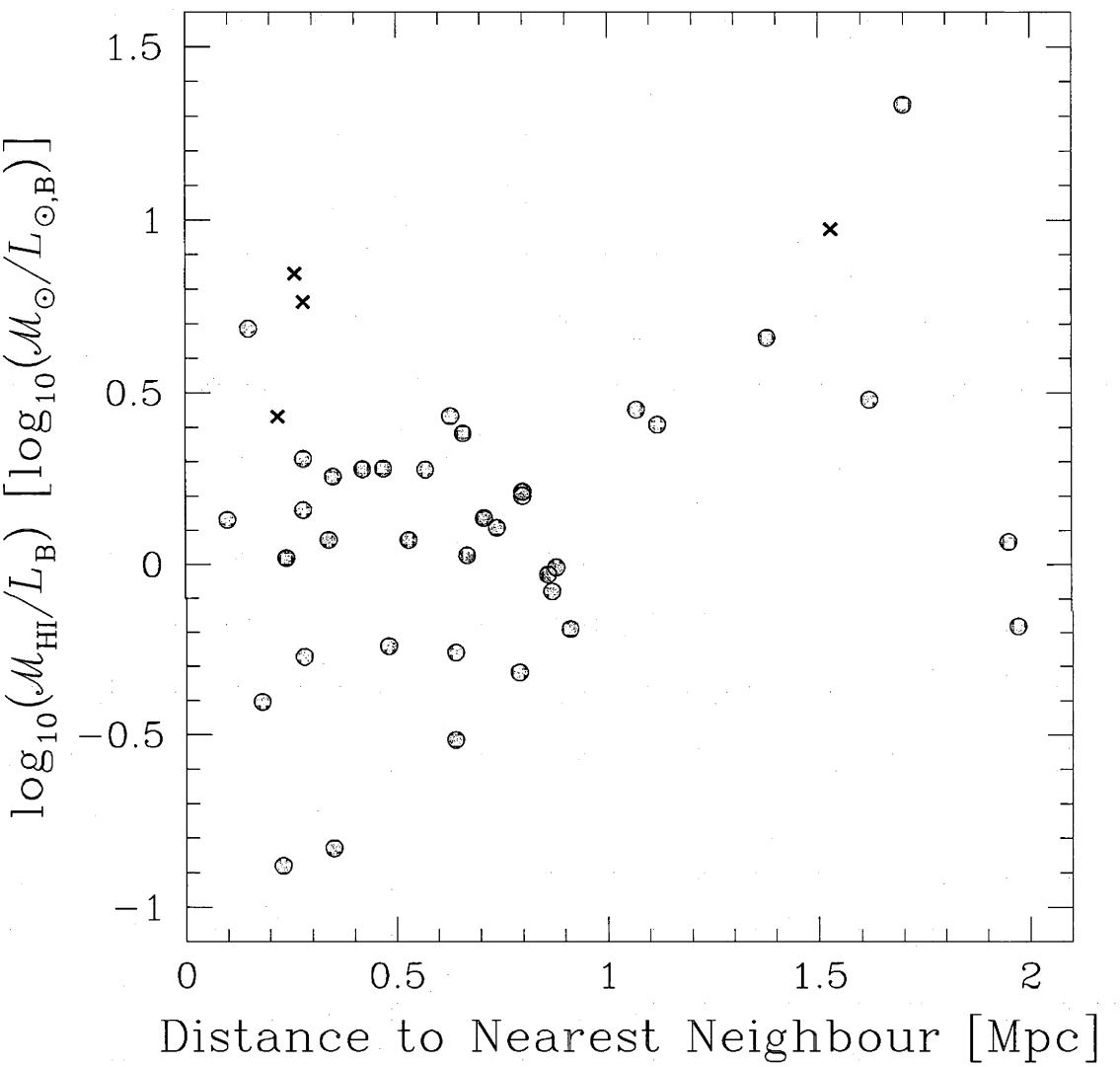

Fig. 8.8: H I mass-to-light ratio versus the distance to the nearest neighbouring galaxy for the 37 galaxies where we have both values (grey points). The crosses mark the positions of the four galaxies we have taken from the literature sources.

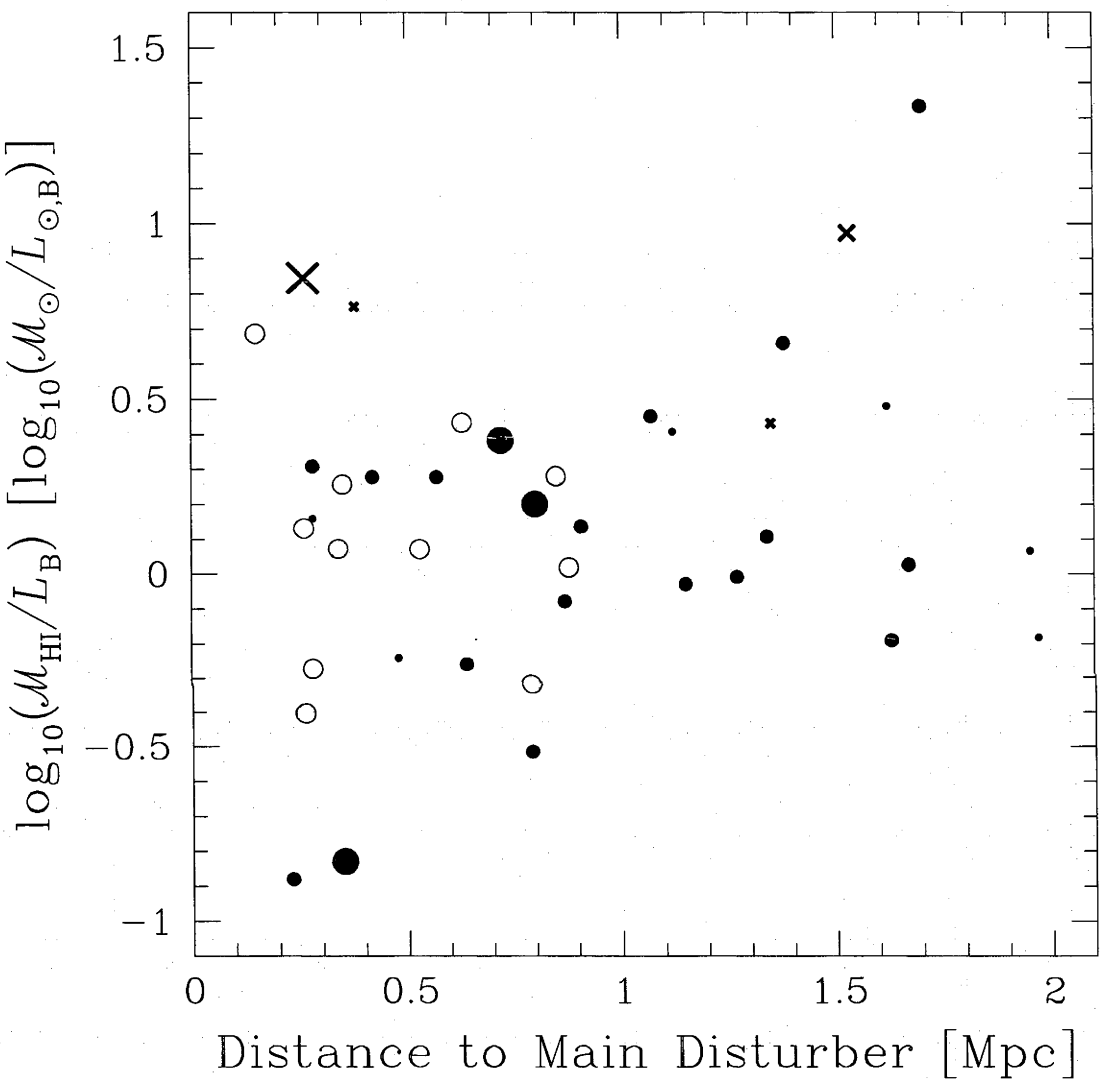

Fig. 8.9: H I mass-to-light ratio versus the distance to the main disturber galaxy for the 37 galaxies where we have both values. The sizes and colours indicate the approximate tidal effect of the disturber based on the Karachentsev & Makarov (1999) tidal index, with the large red indicating a strong effect, yellow moderate, green low, and the small blue points showing those least affected by neighbours. The crosses mark the positions of the four galaxies we have taken from the literature sources, with the colours as for the other objects.

9. CONCLUSIONS AND FURTHER WORK

The first dwarf galaxy discovered to have an extraordinary quantity of H I in comparison to its stellar component, DDO 154 (also known as NGC 4789A), has been studied for over two decades at the time of this thesis (Krumm & Burstein, 1984; Carignan & Freeman, 1988; Carignan & Beaulieu, 1989; Hoffman et al., 1993; Carignan & Purton, 1998, and others). It was first examined in detail by Krumm & Burstein (1984) after they fortuitously discovered it had an extended H I distribution using the Arecibo 305-m telescope (it was to be used as a calibration source until then), following up observations of Allen & Shostak (1979, who also note that it could be extended). Since that time very few galaxies similar to it have been found despite technological advances, wider and more extensive galaxy surveys (both blind and targeted), and a great increase in our knowledge of galaxies in general. It is only in recent years that several galaxies with similar extreme H I properties have been confirmed, such as UGCA 292 (van Zee, 2001; Young et al., 2003), NGC 3741 (Begum et al., 2005), and our own ESO 215-G?009 (Warren et al., 2004, and this thesis).

So why are there still so few very high $\mathcal{M}_{\rm HI}/L_{\rm B}$ galaxies known? We have seen that these galaxies can be difficult to find due to their faint optical emission, and as many past investigations have targeted optically detected galaxies we have missed these unique objects. This situation has improved of late as H I observations have become even more extensive and the usefulness of multiwavelenght astronomy has been realised by more observers. Optical faintness also makes them difficult to detect beyond the Local Universe. We have also seen that it is easy for errors in calculating $\mathcal{M}_{\rm HI}/L_{\rm B}$ to produce false high ratios (see §§ 6.5.2 and 8.1), which could mean the false high ratio galaxies are investigated preferentially over ones which might be more accurate. But it is also the apparent rarity of these galaxies which has restricted our knowledge of them until recently. By why do these galaxies exist in the first place, and what do they tell us about how galaxies might form? To conclude this thesis we will summarise our findings and look at how further studies can proceed to extend our knowledge of high H I mass-to-light ratio galaxies.

9.1 ESO 215-G?009

ESO 215-G?009 (Chapter 6) is by far the most unique galaxy in our sample, with a confirmed high $\mathcal{M}_{\rm HI}/L_{\rm B}$ of $22 \pm 4\ \mathcal{M}_{\odot}/L_{\odot,{\rm B}}$. To our knowledge this is the

highest $\mathcal{M}_{\rm HI}/L_{\rm B}$ for a stellar system to be confirmed by accurate measurement to date, being approximately double the next nearest reliable galaxy, DDO 154. It has an extended regularly rotating H I disk that can be traced out well beyond the stellar distribution, to 6.4 ± 0.4 times the Holmberg radius ($r_{26.6}$ in the B band) at a column density of $\sim 5.0 \times 10^{19}$ atoms cm^{-2}, making it one of the most extended H I envelopes relative to its optical extent. This is comparable to galaxies such as DDO 154 (Carignan & Beaulieu, 1989) and NGC 3741 (Begum et al., 2005). The galaxy is very isolated, with the nearest identified neighbour $\sim$1.7 Mpc away. This means it has a low tidal influence from neighbouring galaxies, another property it shares with DDO 154 and NGC 3741.

Optical colours for ESO 215-G?009 suggest that the stellar population is older than is usually found in dwarf irregular galaxies. Some shallow positive colour gradients are observed between the inner and outer parts of the optical galaxy, suggesting that there are slightly more younger stars in the center of the galaxy. However the large uncertainty caused by the high Galactic extinction prevents further analysis of the underlying stellar population.

ESO 215-G?009 has a relatively normal H I content for a late-type dwarf galaxy with its total mass. However it is less luminous than galaxies with similar total masses, suggesting that it is star poor rather than gas rich. The current star formation rate within the galaxy is very low from 20 cm radio continuum observations, and may have remained relatively constant throughout the galaxies existence given the small amount of luminous matter present. From an analysis of the critical gas surface density of ESO 215-G?009 as outlined by K89 and MK01 we find that the H I gas surface density may be too low for the galaxy to efficiently form stars if the Toomre stability criterion determines the star formation threshold.

9.2 The Scarcity of "Dark" Galaxies

As we saw in Chapter 7 and § 8.1, many of the galaxies initially chosen for our sample because of their high $\mathcal{M}_{\rm HI}/L_{\rm B}$ from the combination of BGC H I and LEDA optical data were not in fact high ratio galaxies due to underestimates of their luminosities in LEDA (which our selection criteria preferentially choose). Hence there appear to be very few galaxies with very high ratios in the BGC, any remaining objects that were not studied having few opportunities to hide in the catalogue (see § 7.4.4). We are left with one "dim" galaxy (ESO 215-G?009) in our sample and the Local Universe with only a handfull of high $\mathcal{M}_{\rm HI}/L_{\rm B}$ galaxies, which on its own cannot support the existence of sufficient numbers of "dark" galaxies in the Universe to steepen observational luminosity functions and match the predicted frequency of low mass dark matter halos from ΛCDM cosmology, as outlined in § 1.1. Other studies of the HIPASS data set have produced similar results, with no potential completely "dark" galaxy candidates emerging from the survey (Ryan-Weber et al., 2002; Doyle et al. 2005, in preparation). The star formation process

in galaxies appears to be efficent enough to at least produce a small population of stars in any dark matter halo containing an appreciable quantity of primordial H I gas, making the galaxies optically visible today.

When discussing DDO 154 Carignan & Freeman (1988) suggested that many other such objects may exist but remain unseen due to their low luminosity (or even optical invisibility), noting that further studies of similar galaxies are required. But since that discovery we are yet to find a large enough sample of other similar objects which could suggest there is an undiscovered population of dwarf galaxies with low to undetectable optical emission. It appears that objects like DDO 154 and ESO 215-G?009 are rare compared to other galaxy types, and may define an upper envelope for $\mathcal{M}_{\rm HI}/L_{\rm B}$ at a given luminosity/mass. If this is true then we may be able to use these extreme objects to constrain galaxy models by fixing the maximum H I mass fraction they can have for a given initial mass.

9.3 Can We Explain Why Some Galaxies Have High $\mathcal{M}_{\rm HI}/L_{\rm B}$?

Our comparison of the full sample of galaxies in Chapter 8 suggest several possibilities for why a galaxy could form into a high $\mathcal{M}_{\rm HI}/L_{\rm B}$ object and retain that ratio. In general these galaxies are small low mass systems, and their lack of stars means they are both faint and have small radii in the optical (§§ 8.1 and 8.5). The classical (stellar mass) and baryonic Tully & Fisher (1977) relationship analysis (§ 8.3) and the comparison of the properties of ESO 215-G?009 to "typical" dwarf galaxies (§ 6.5.6) both suggest that high $\mathcal{M}_{\rm HI}/L_{\rm B}$ galaxies have normal quantities of baryonic mass in comparison to other galaxies with similar dynamical mass, but they have less luminous matter than these galaxies. It is a lack of stars, not an excess of gas, which define these galaxies

There appear to be at least two factors which correlate well with H I mass-to-light ratio and suggest possible reasons why these galaxies are so star deficient. The stellar density of the high $\mathcal{M}_{\rm HI}/L_{\rm B}$ galaxies is lower than other system (§ 8.4), which implies that the dark matter potentials of these galaxies are shallow, making it more likely that the gas will not collapse to densities high enough for efficient star formation. The highest ratio galaxies also appear to be in isolation (§ 8.6), suggesting that tidal interactions can affect the gas content of the galaxies.

It appears that only a combination of conditions can produce galaxies with very high H I mass-to-light ratio. The galaxy needs to have a low initial mass and a shallow dark matter potential so that it can collapse into a Toomre stable disk. But in most cases it will only remain this way if it continues in relative isolation.

9.4 Further Investigations

This study provides a basis for further investigation of high H I mass-to-light ratio objects, from further examination of objects in our sample to finding any more

high $\mathcal{M}_{\rm HI}/L_{\rm B}$ objects which we are yet to discover. We have seen that high $\mathcal{M}_{\rm HI}/L_{\rm B}$ galaxies can be found in both blind surveys like HIPASS (as ESO 215-G?009 was) and investigations targeted at galaxies based on optical properties like van Zee et al. have done. As a first step, the optical properties of the full HIPASS catalogue (HICAT Meyer et al., 2004; Zwaan et al., 2004) should be examined, the beginning of which is an optical catalogue (Doyle et al., 2005, in preparation). Optical follow up of the uncatalogued/unobserved galaxies in both the BGC and HICAT may also produce some interesting galaxies, although many of these are likely to have problems in the optical due to Galactic extinction or foreground star contamination (Ryan-Weber et al., 2002). Targeted H I observations of optically discovered objects should look towards the isolated late-type low surface brightness dwarf galaxies.

We have seen that it is very important to have reliable observations for these galaxies in order to confirm the high ratios (§ 6.5.2), with accurate values for both optical and H I values essential. It is also necessary to accurately take Galactic extinction into account, which seems to be accounted for well by the use of the SFD98 maps unless the galaxy is deep in the Galactic Plane. Internal extinction, which we currently have not been able to account for, would be a useful future addition to the calculation of $\mathcal{M}_{\rm HI}/L_{\rm B}$. Shifting away from the B band in the optical to redder optical bands, or into the near infrared, would also be an improvement in the analysis of these objects as these bands are both less affected by dust extinction and are more representative of the stellar mass of the systems (being less affected by high current star formation rates).

Some of the analysis techniques we used, especially those done for ESO 215-G?009, could be extended further. For example, the K89 star formation threshold analysis could be extended to a two dimensional analysis to look for specific sites within the galaxy where the H I gas surface density exceeds the critical surface density for the Toomre (1964) criteria to apply. Additional observations of the Hα line and 20cm radio continuum observations can give us an accurate measure of the current star formation rate that can be compared to the critical gas surface density, and may also give us further indication of the effect of dust extinction. We could also gain greater insight into these objects by going beyond the current optical and H I line observations into other wavelengths, such as millimetre observations to look at the molecular line CO, an indicator of the quantity of molecular hydrogen gas (H_2) in the galaxy.

Ultimately, we need to extend the sample of high H I mass-to-light ratio galaxies, and to improve the observations for those galaxies we have already found, to determine exactly how these galaxies form. But it seems clear that high $\mathcal{M}_{\rm HI}/L_{\rm B}$ dwarf galaxies are an evolutionary extreme that are an important piece of the galaxy formation and evolution puzzle.

APPENDIX

A. OPTICAL IMAGES AND PROFILES, H I MAPS AND SPECTRA

ESO 349-G031

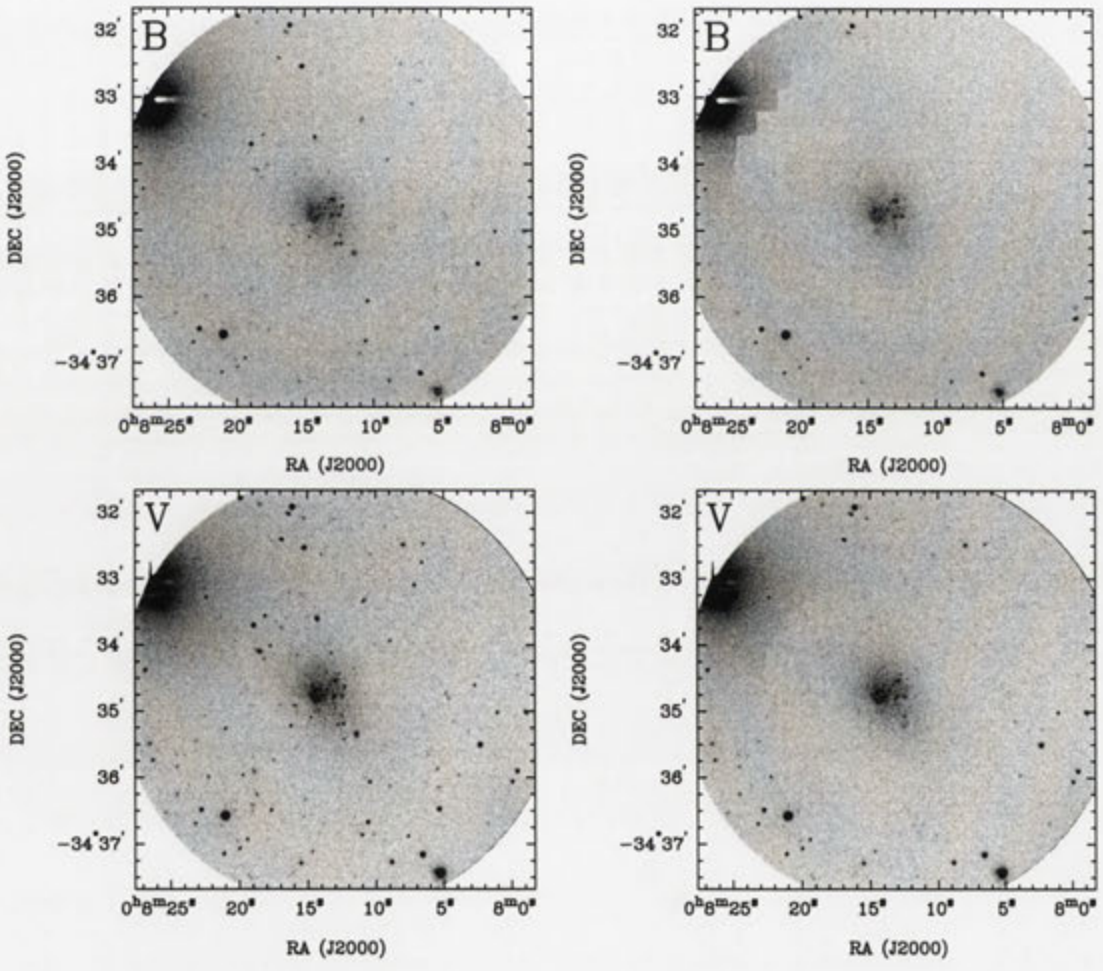

Fig. A.1: Deep *BVRI* images of ESO 349-G031 before and after subtraction of the foreground stars.

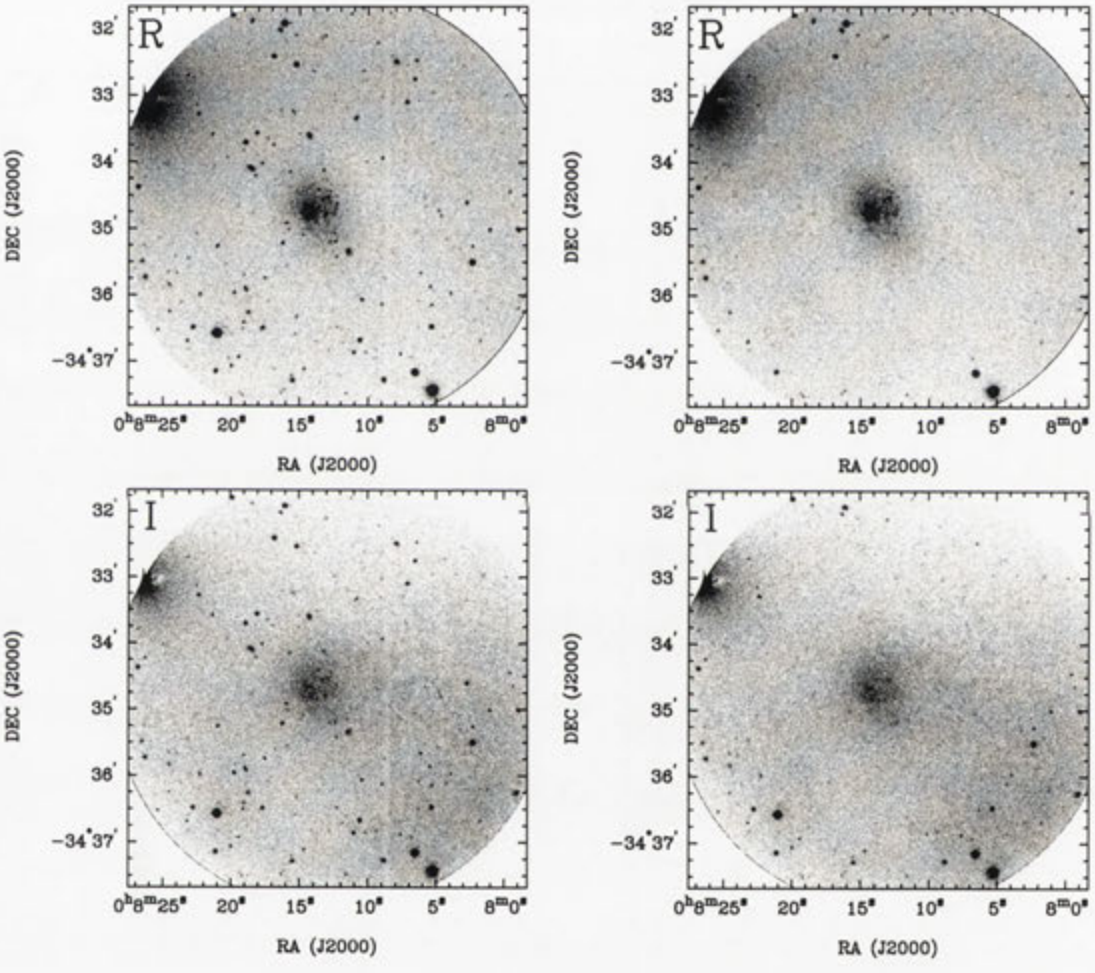

Fig. A.1: continued

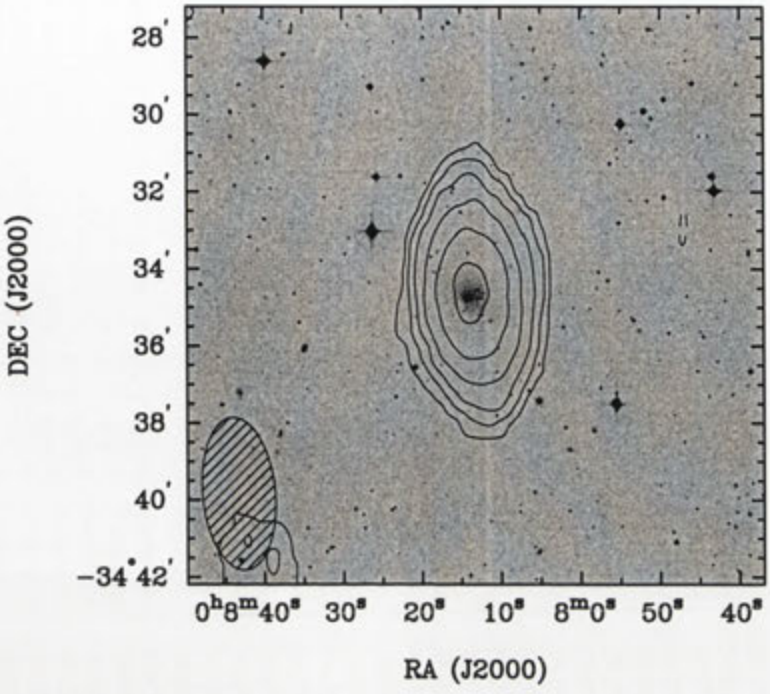

Fig. A.2: Integrated H I intensity distribution of ESO 349-G031 overlaid onto an optical DSS II R band image. The synthesised beam is displayed in the bottom left corner.

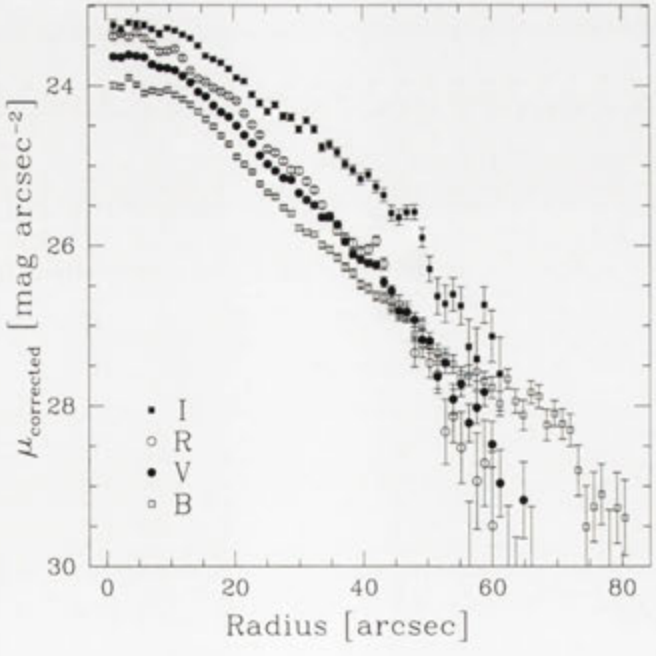

Fig. A.3: *BVRI* surface brightness profiles of ESO 349-G031, corrected for Galactic extinction.

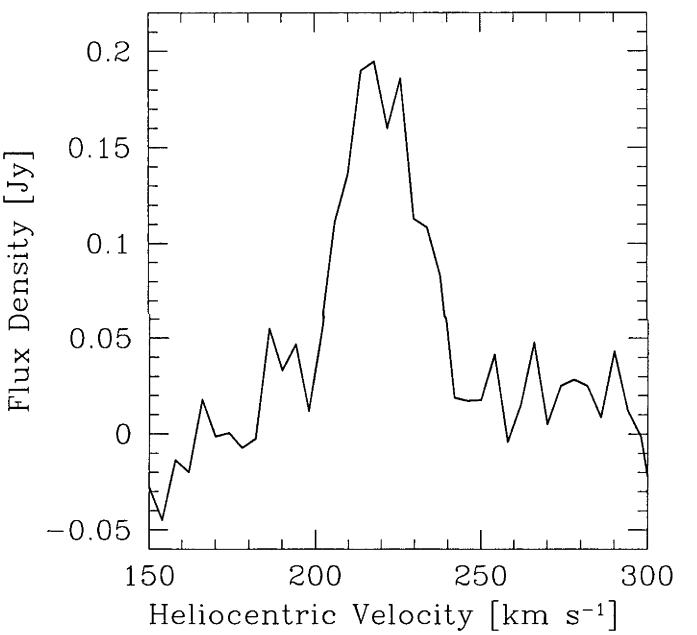

Fig. A.4: Global H I spectra of ESO 349-G031 as obtained from the ATCA.

MCG–04-02-003

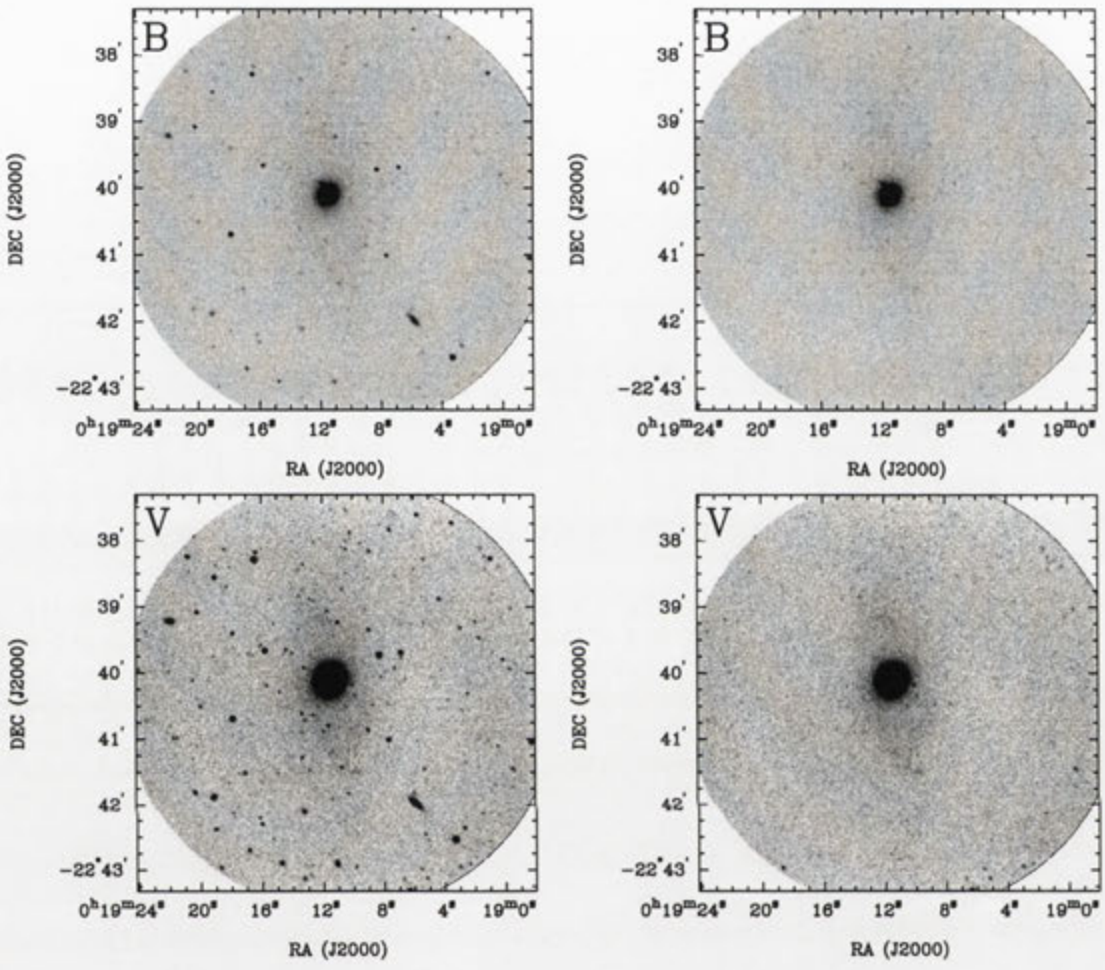

Fig. A.5: Deep *BVRI* images of MCG–04-02-003 before and after subtraction of the foreground stars.

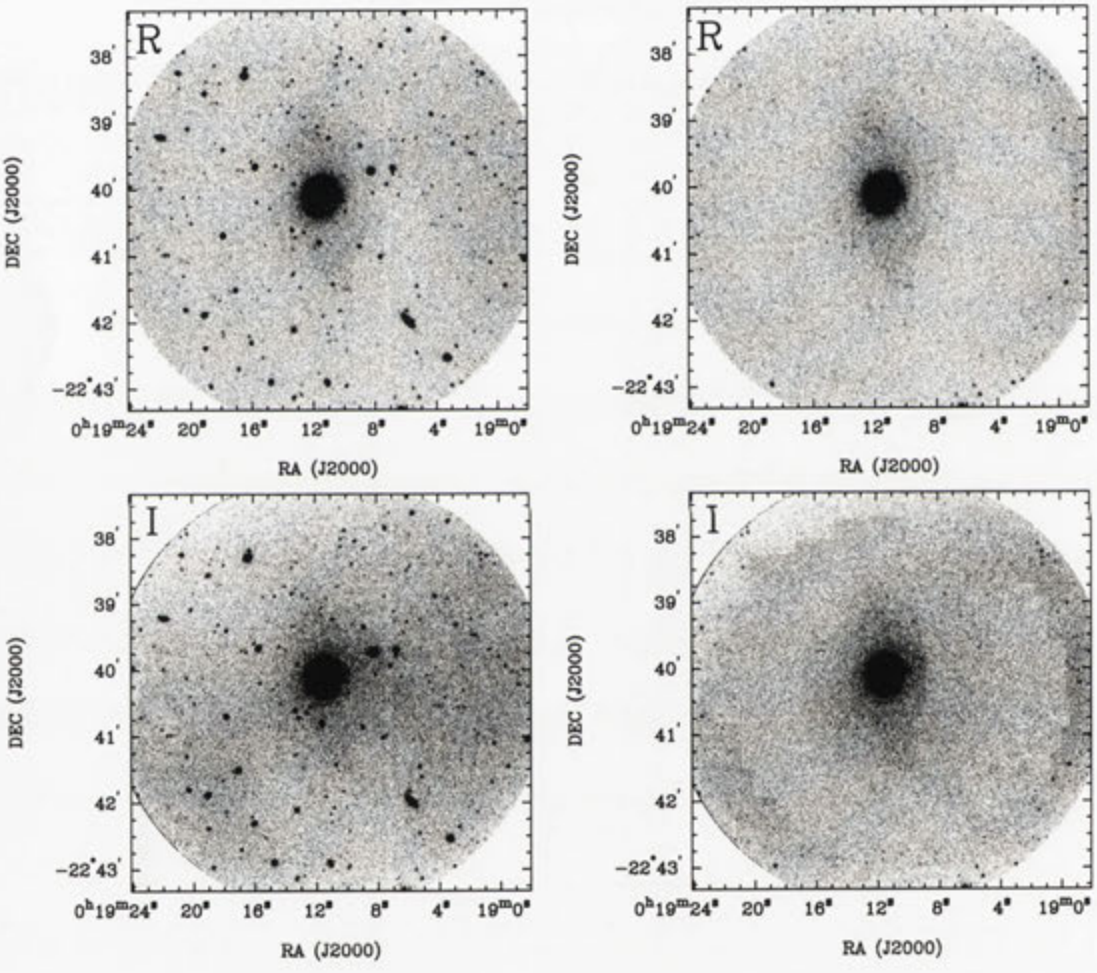

Fig. A.5: continued

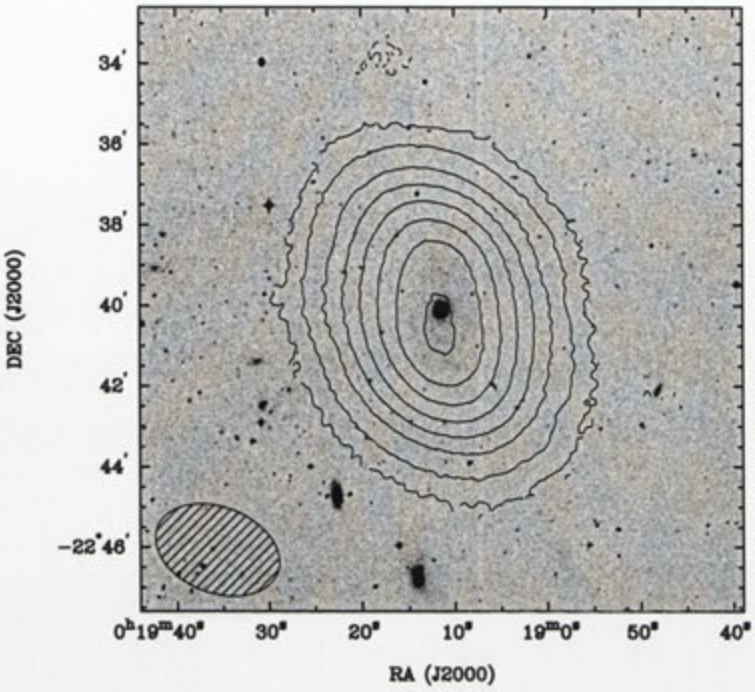

Fig. A.6: Integrated H I intensity distribution of MCG–04-02-003 overlaid onto an optical DSS II R band image. The synthesised beam is displayed in the bottom left corner.

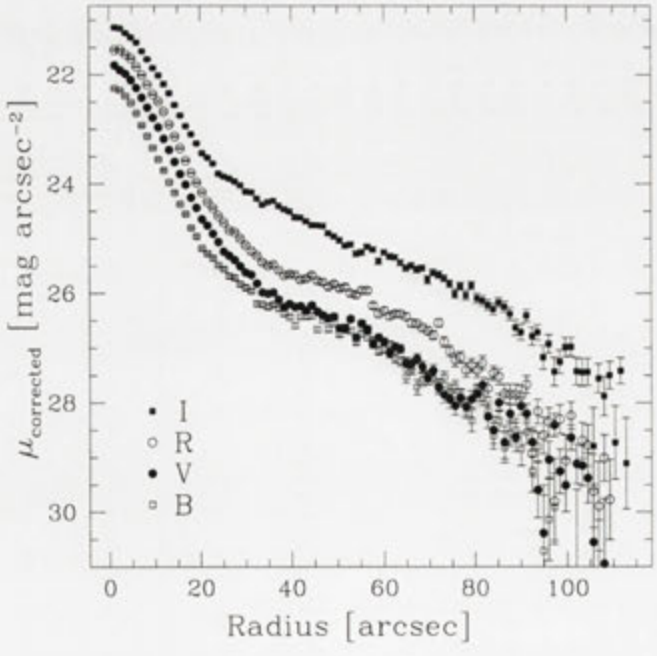

Fig. A.7: *BVRI* surface brightness profiles of MCG–04-02-003, corrected for Galactic extinction.

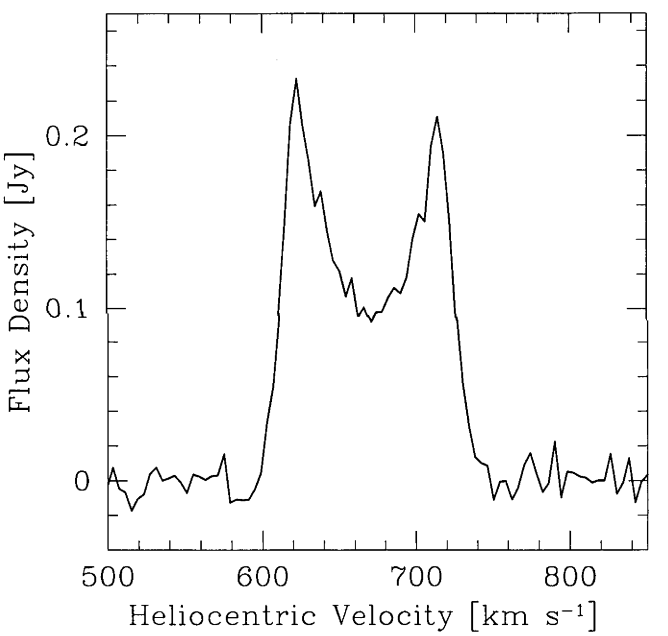

Fig. A.8: Global H I spectra of MCG–04-02-003 as obtained from the ATCA.

ESO 473-G024

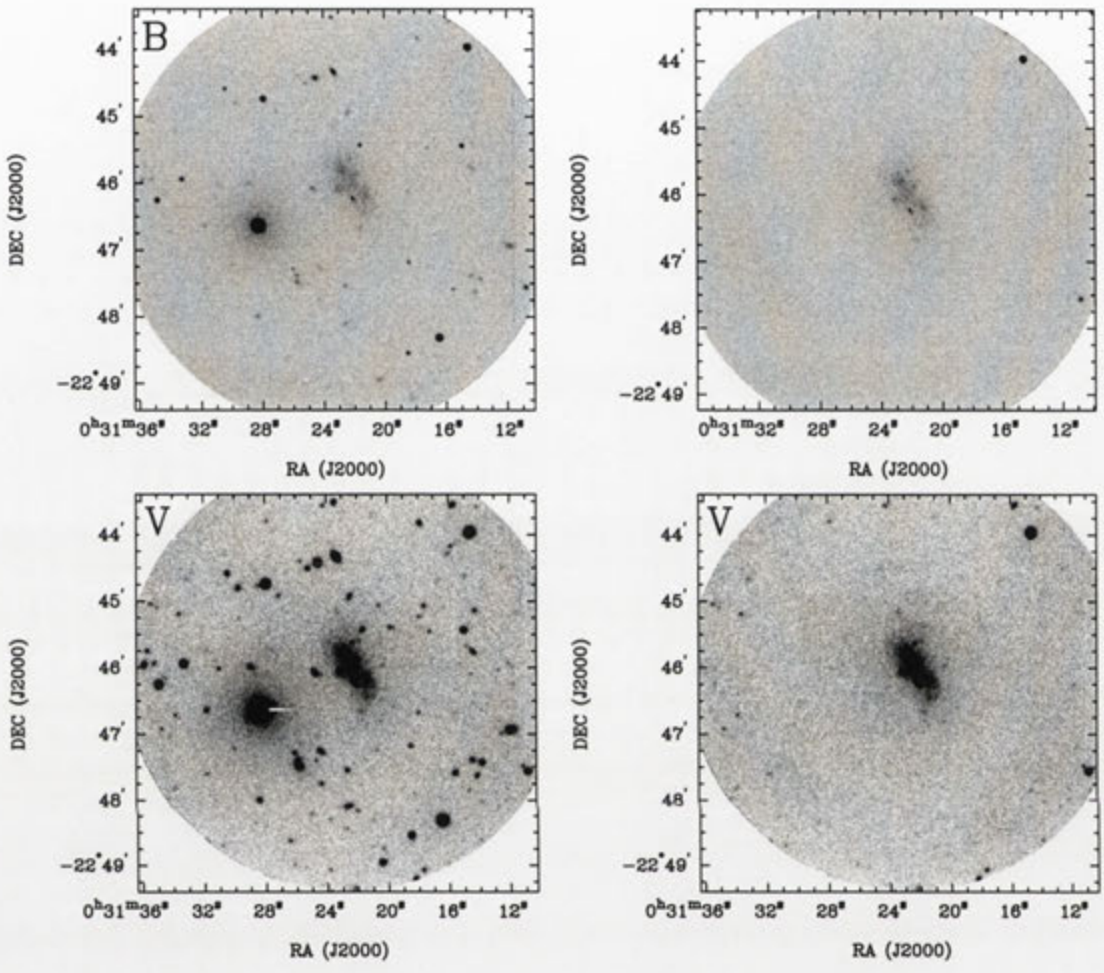

Fig. A.9: Deep *BVRI* images of ESO 473-G024 before and after subtraction of the foreground stars.

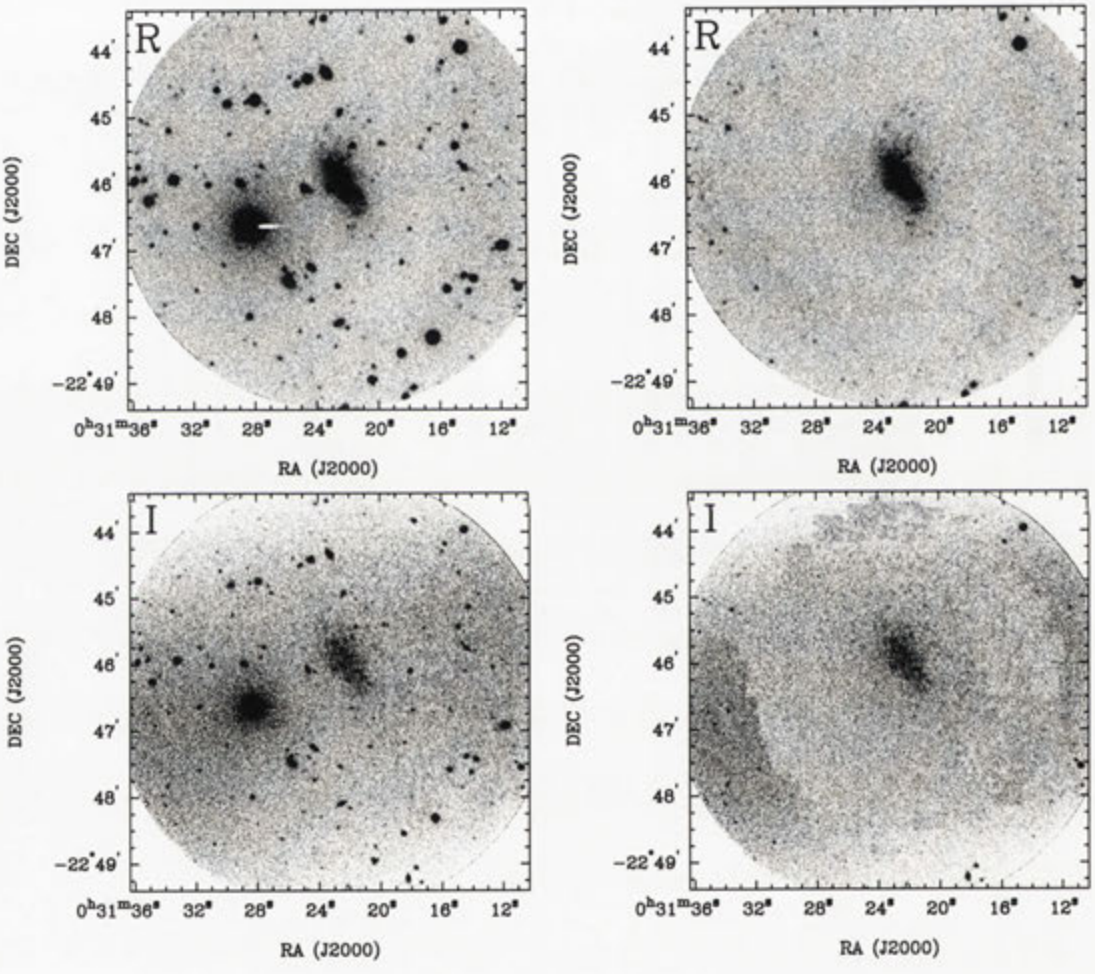

Fig. A.9: continued

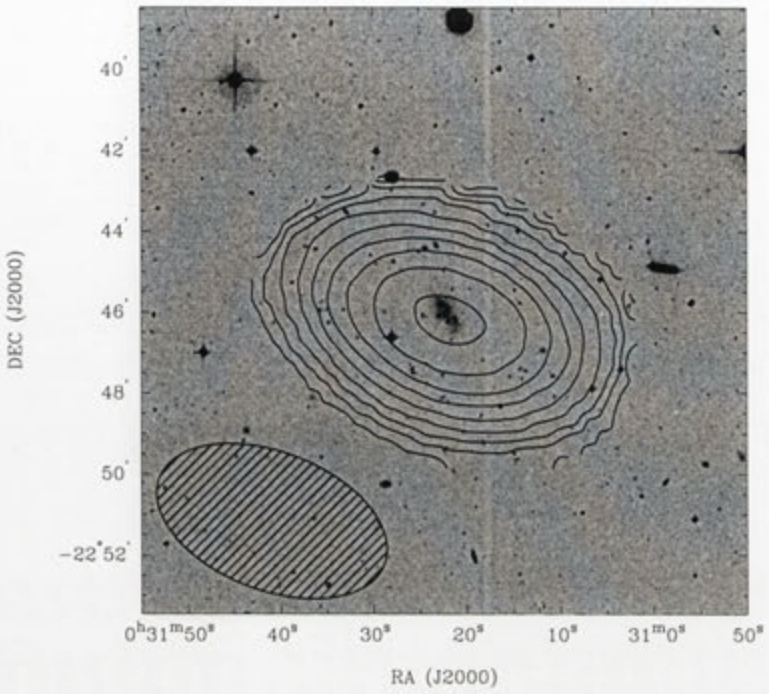

Fig. A.10: Integrated H I intensity distribution of ESO 473-G024 overlaid onto an optical DSS II *R* band image. The synthesised beam is displayed in the bottom left corner of both panels.

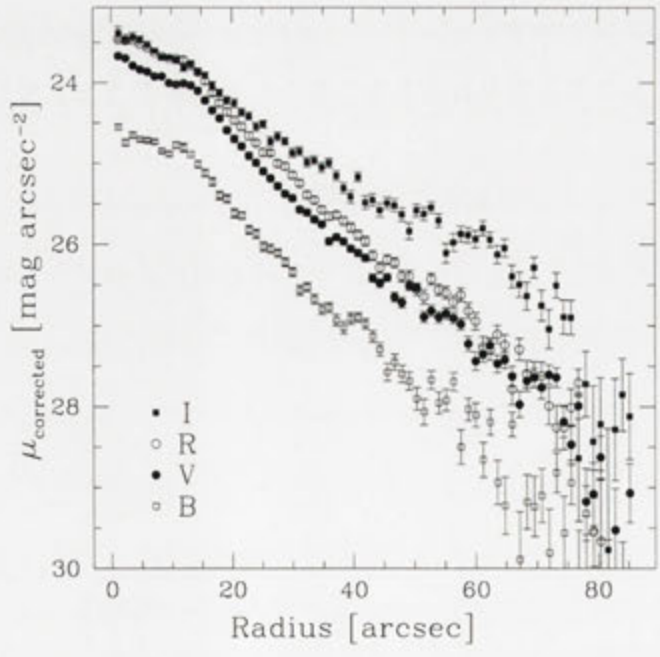

Fig. A.11: *BVRI* surface brightness profiles of ESO 473-G024, corrected for Galactic extinction.

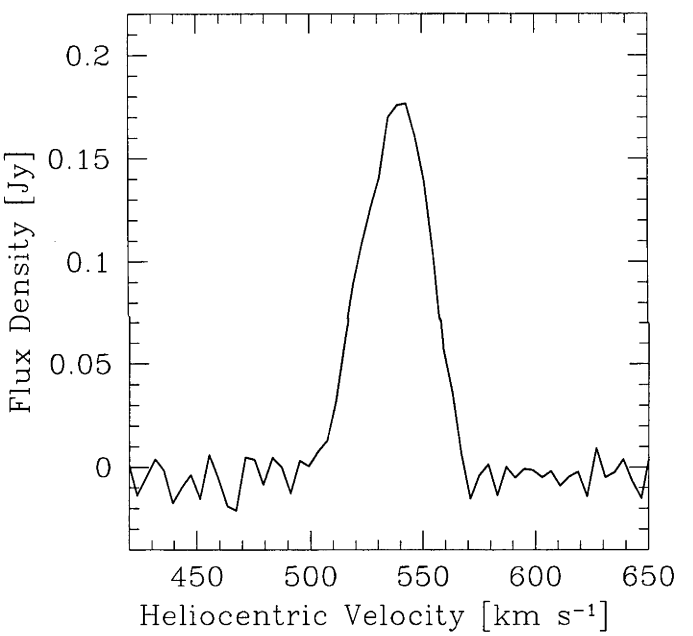

Fig. A.12: Global H I spectra of ESO 473-G024 as obtained from the ATCA.

IC 1574

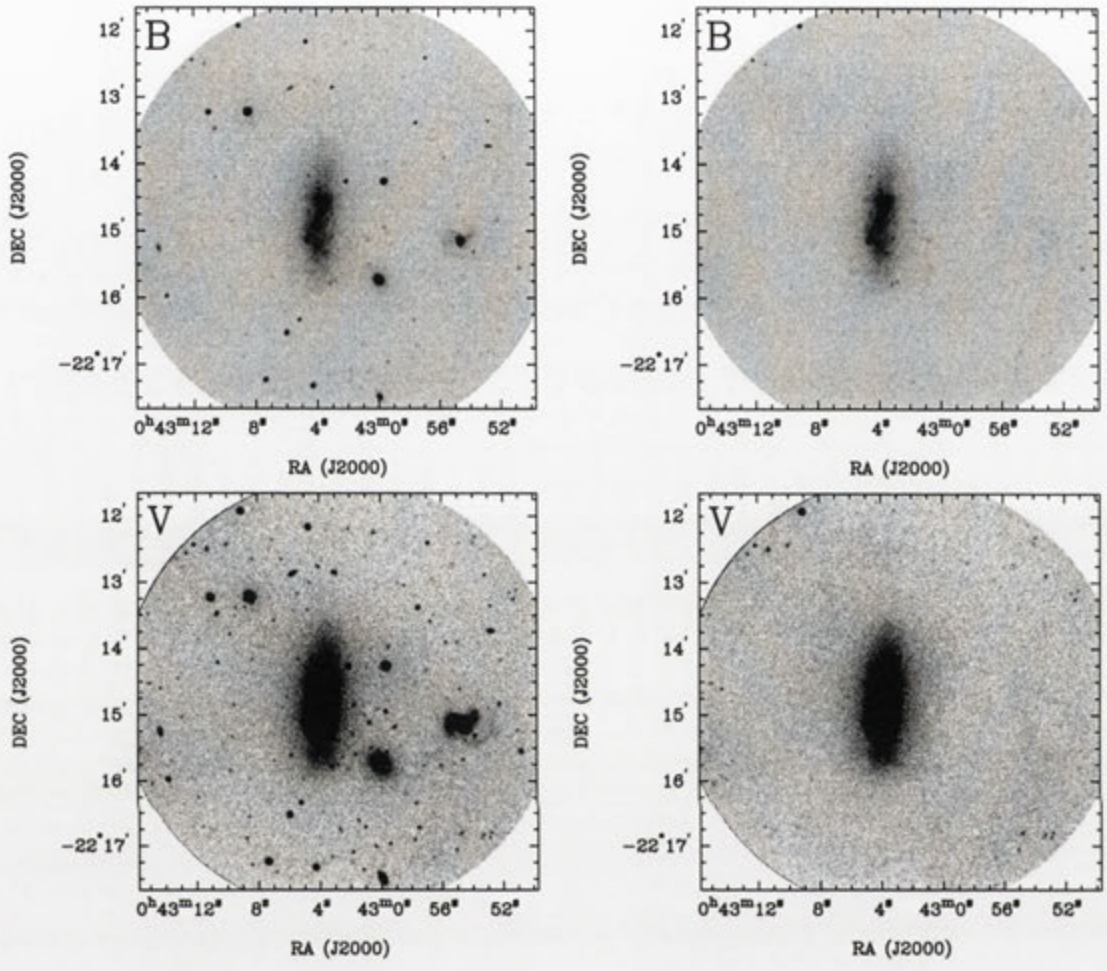

Fig. A.13: Deep *BVRI* images of IC 1574 before and after subtraction of the foreground stars.

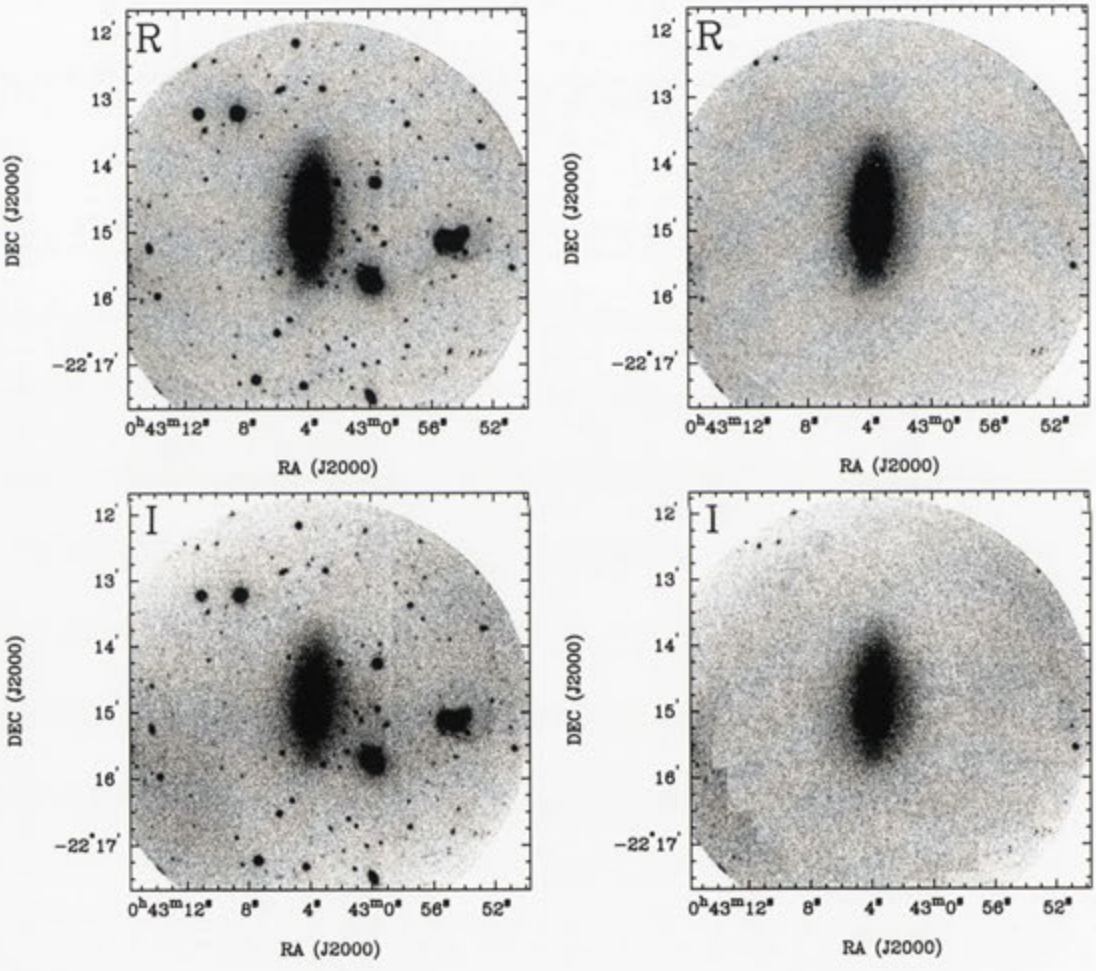

Fig. A.13: continued

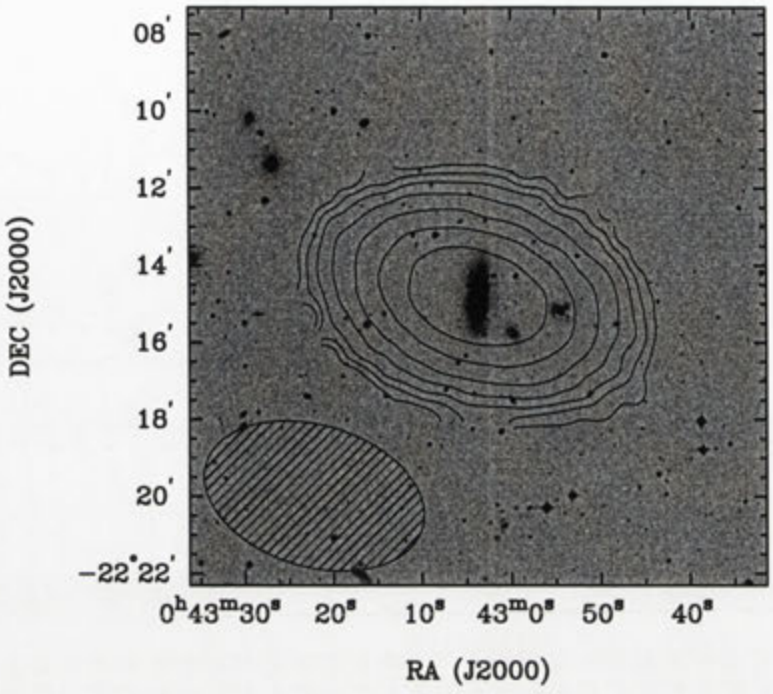

Fig. A.14: Integrated H I intensity distribution of IC 1574 overlaid onto an optical DSS II R band image. The synthesised beam is displayed in the bottom left corner.

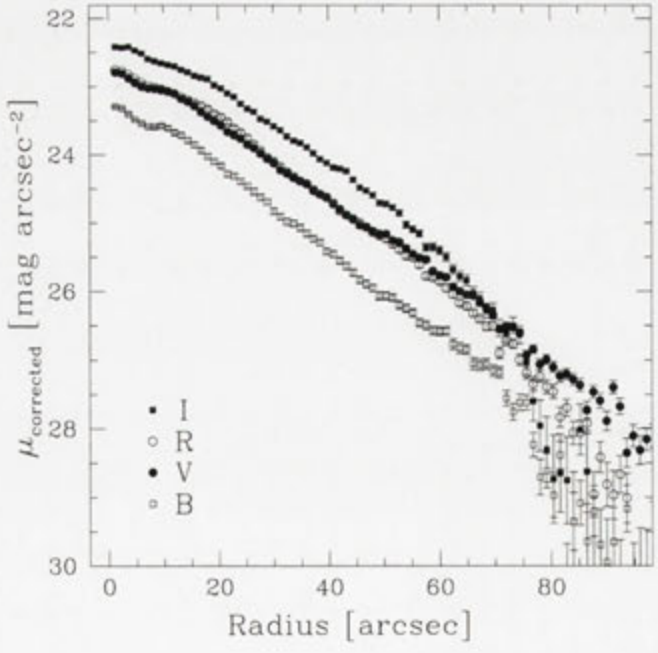

Fig. A.15: *BVRI* surface brightness profiles of IC 1574, corrected for Galactic extinction.

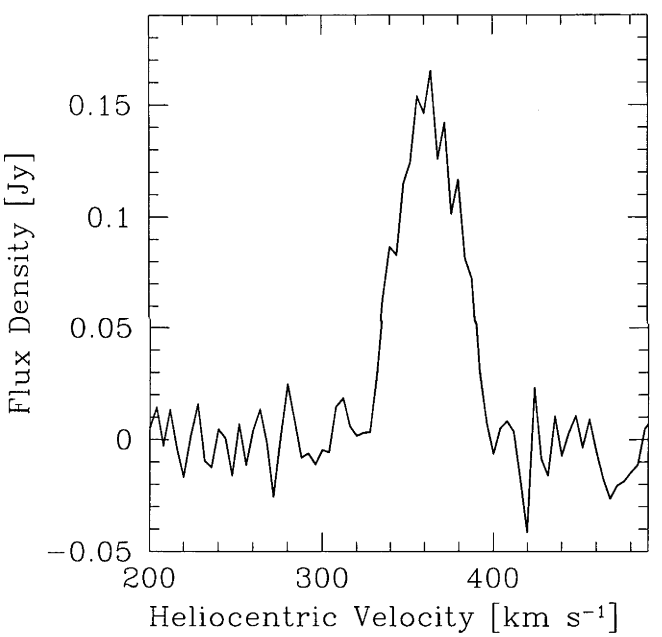

Fig. A.16: Global H I spectra of IC 1574 as obtained from the ATCA.

UGCA 015

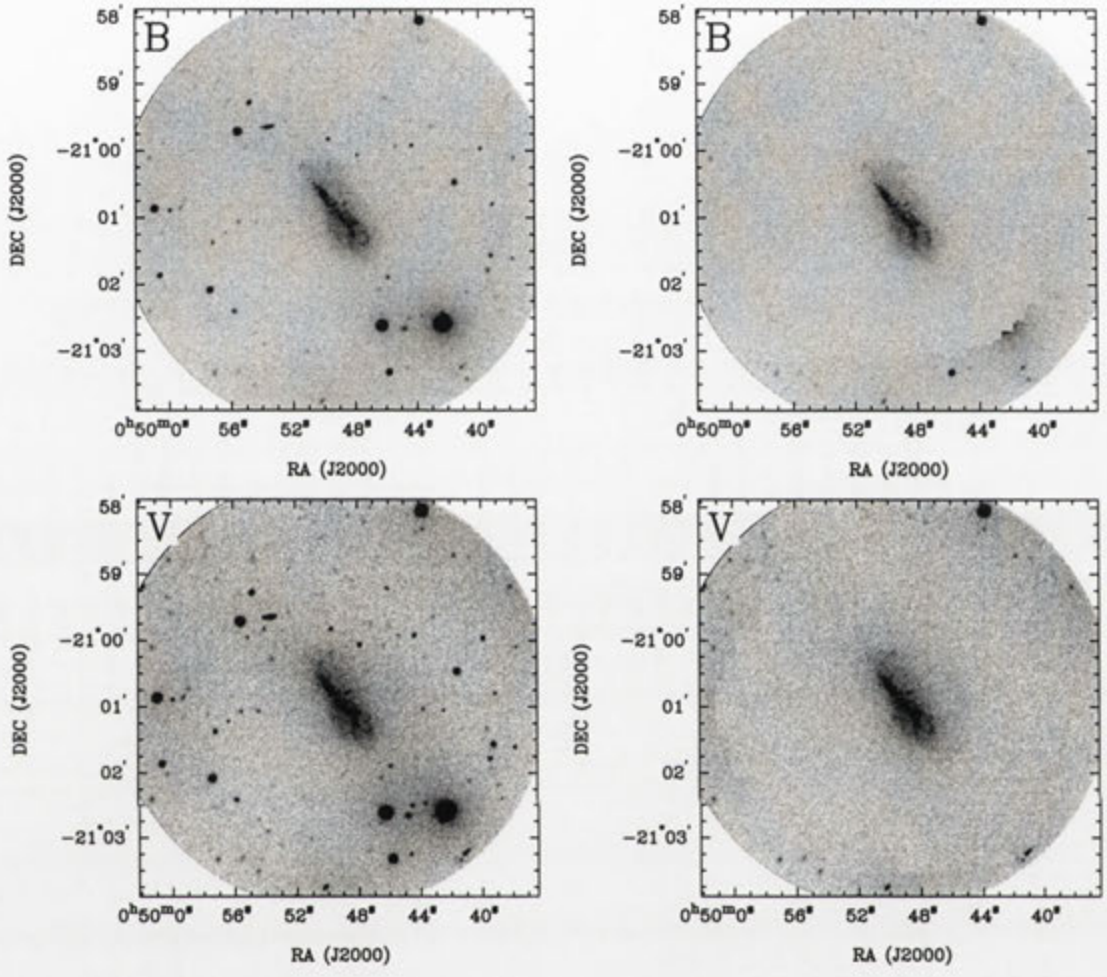

Fig. A.17: Deep *BVRI* images of UGCA 015 before and after subtraction of the foreground stars.

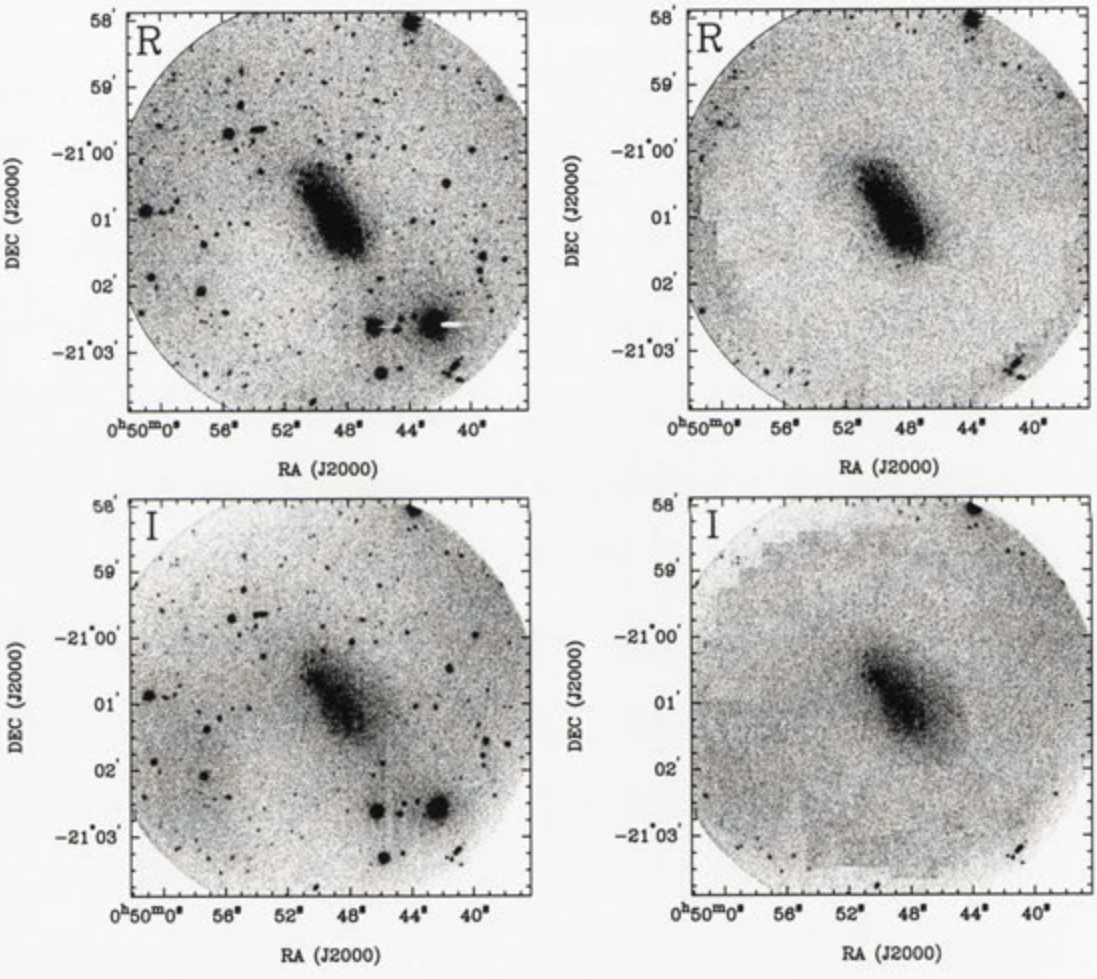

Fig. A.17: continued

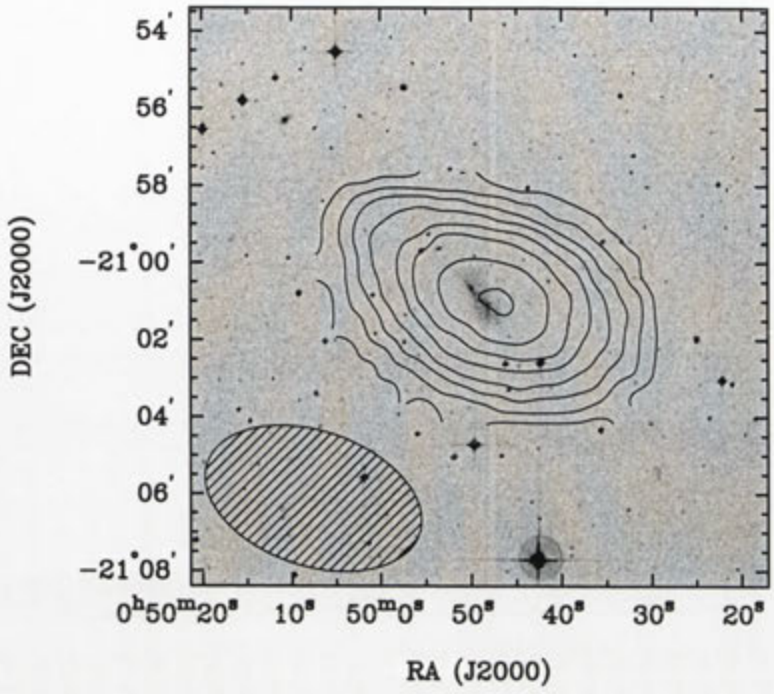

Fig. A.18: Integrated H I intensity distribution of UGCA 015 overlaid onto an optical DSS II R band image. The synthesised beam is displayed in the bottom left corner.

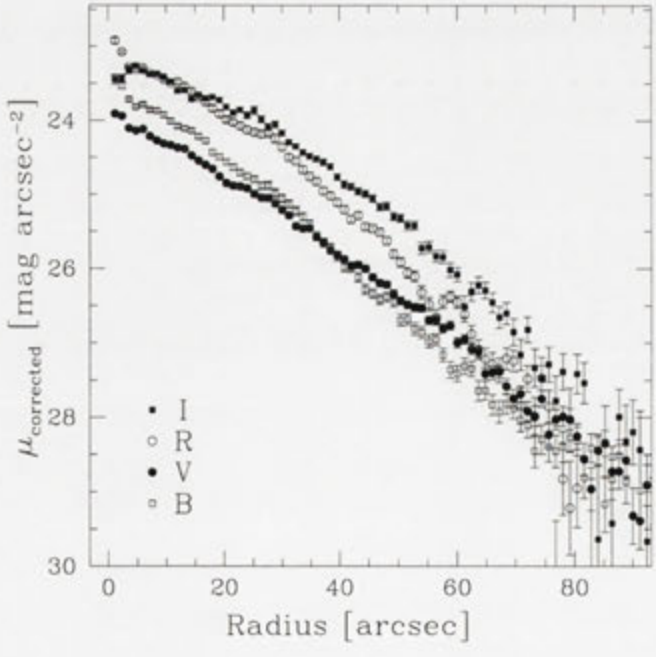

Fig. A.19: *BVRI* surface brightness profiles of UGCA 015, corrected for Galactic extinction.

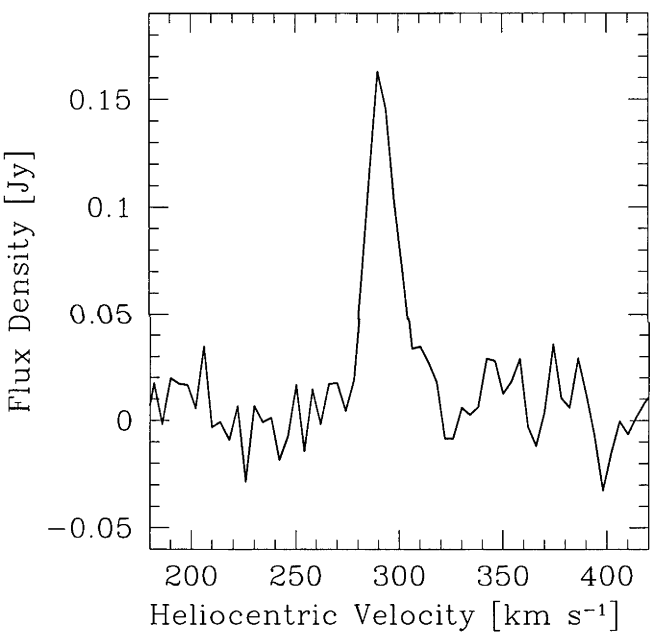

Fig. A.20: Global H I spectra of UGCA 015 as obtained from the ATCA.

ESO 085-G047

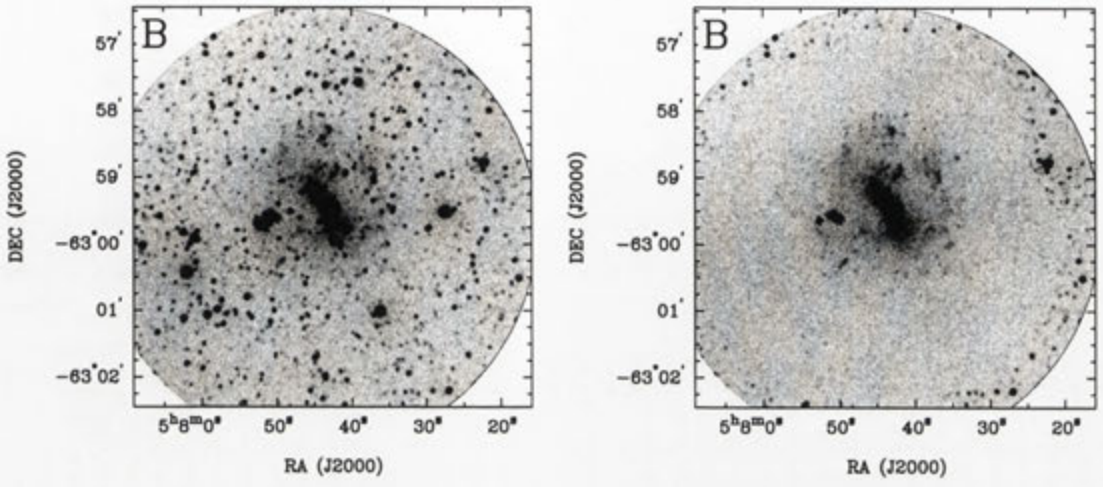

Fig. A.21: Deep B image of ESO 085-G047 before and after subtraction of the foreground stars.

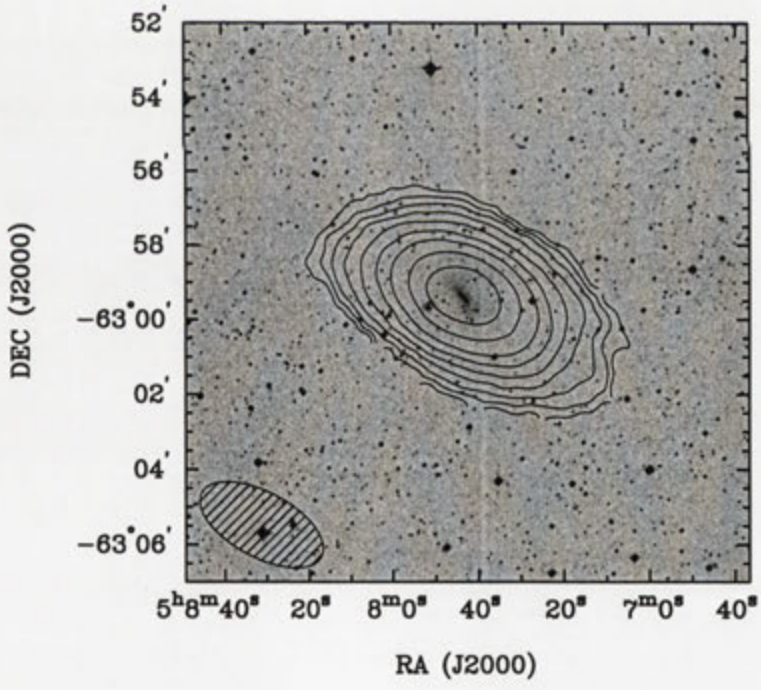

Fig. A.22: Integrated H I intensity distribution of ESO 085-G047 overlaid onto an optical DSS II R band image. The synthesised beam is displayed in the bottom left corner.

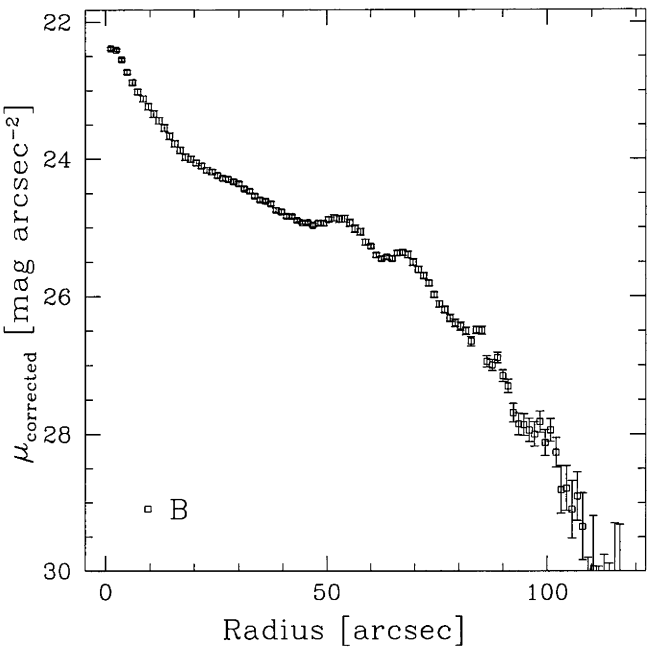

Fig. A.23: *B* surface brightness profile of ESO 085-G047, corrected for Galactic extinction.

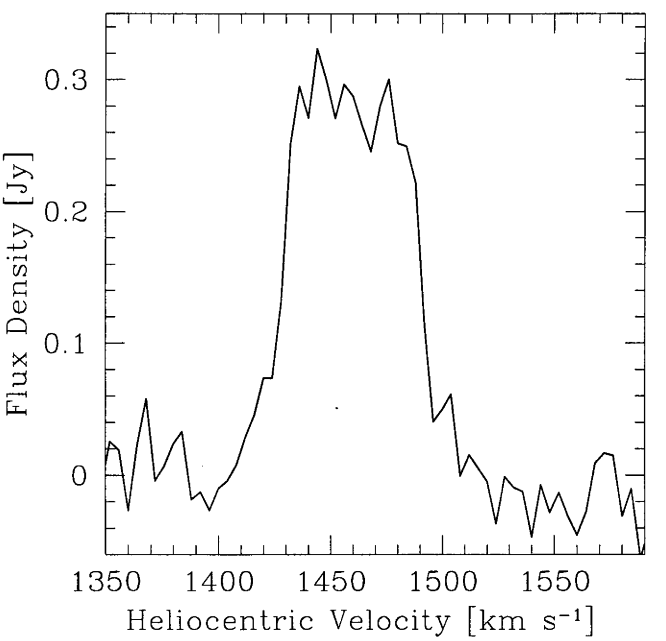

Fig. A.24: Global H I spectra of ESO 085-G047 as obtained from the ATCA.

ESO 120-G021

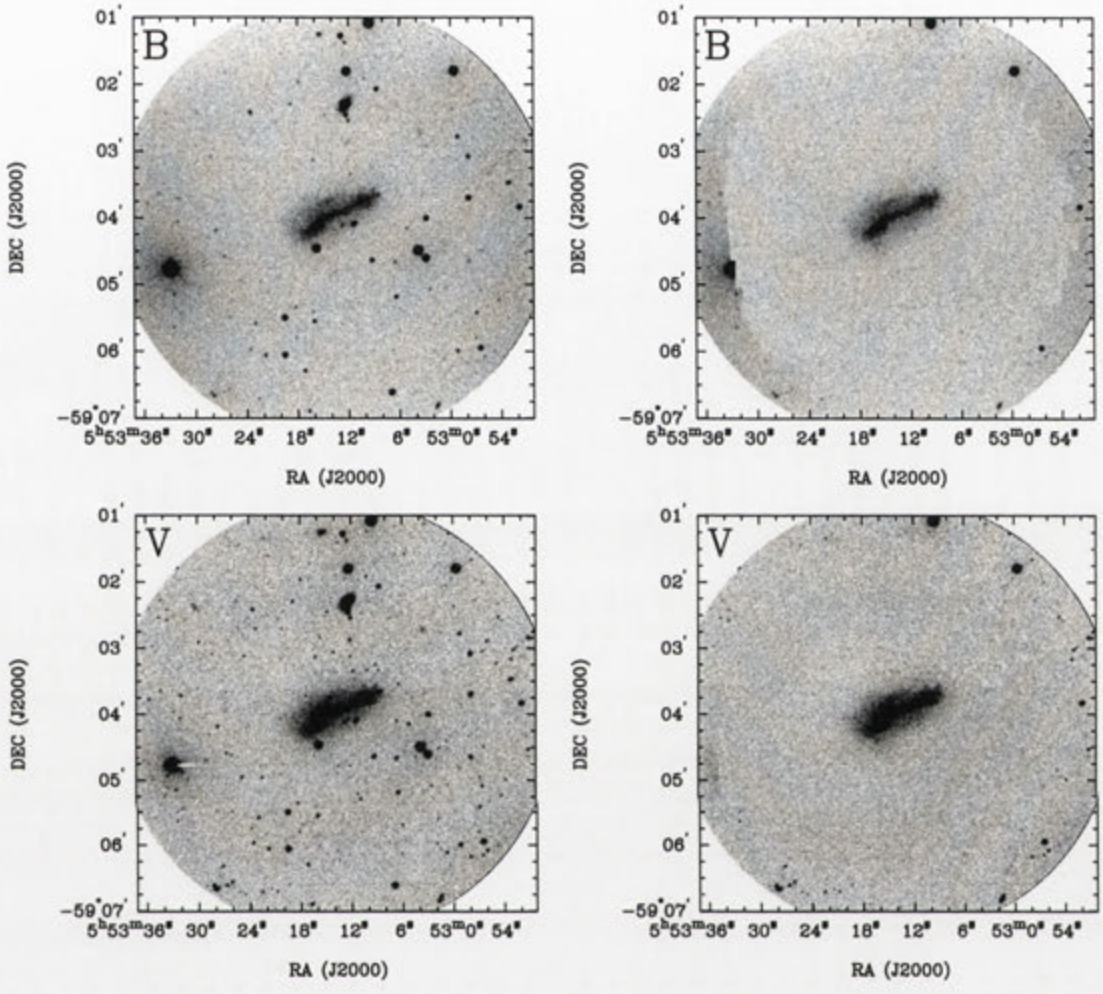

Fig. A.25: Deep *BVRI* images of ESO 120-G021 before and after subtraction of the foreground stars.

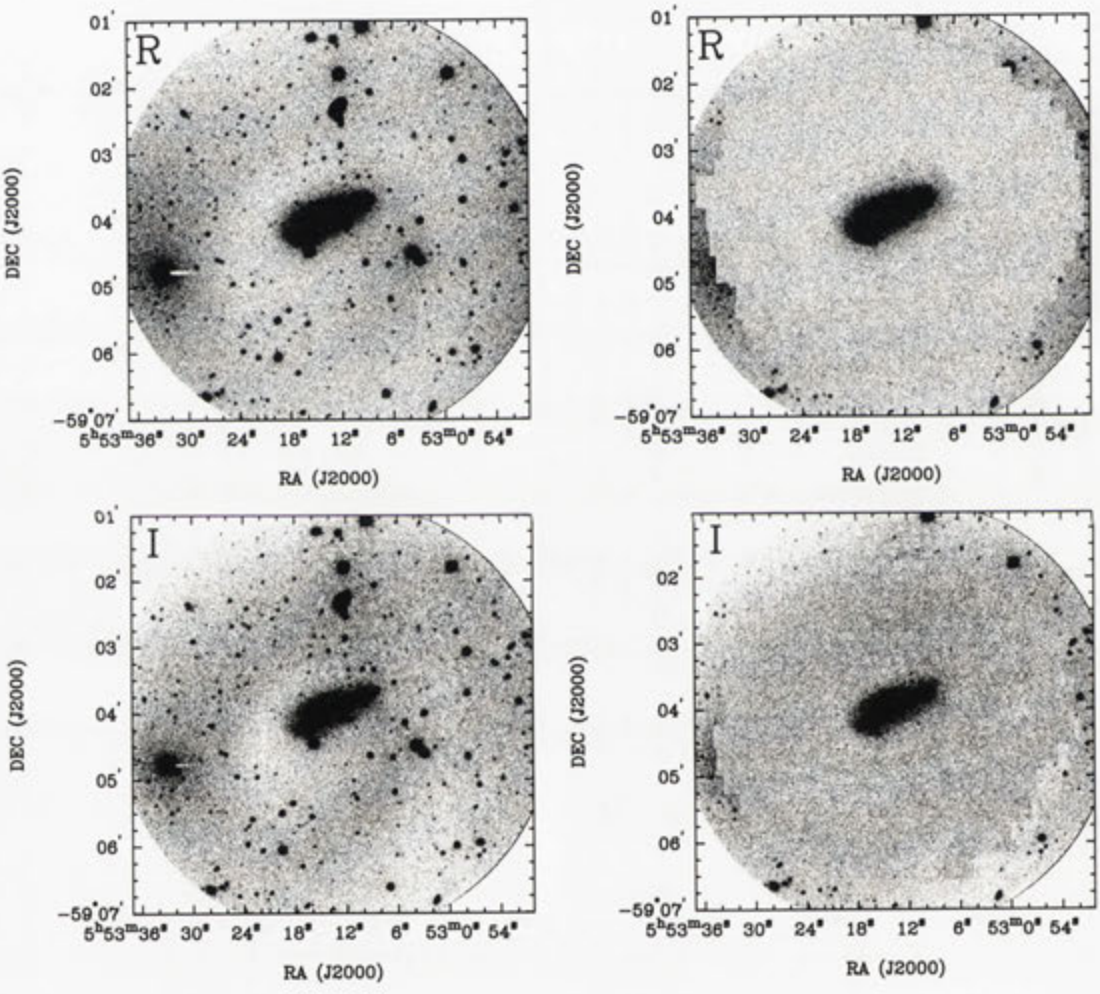

Fig. A.25: continued

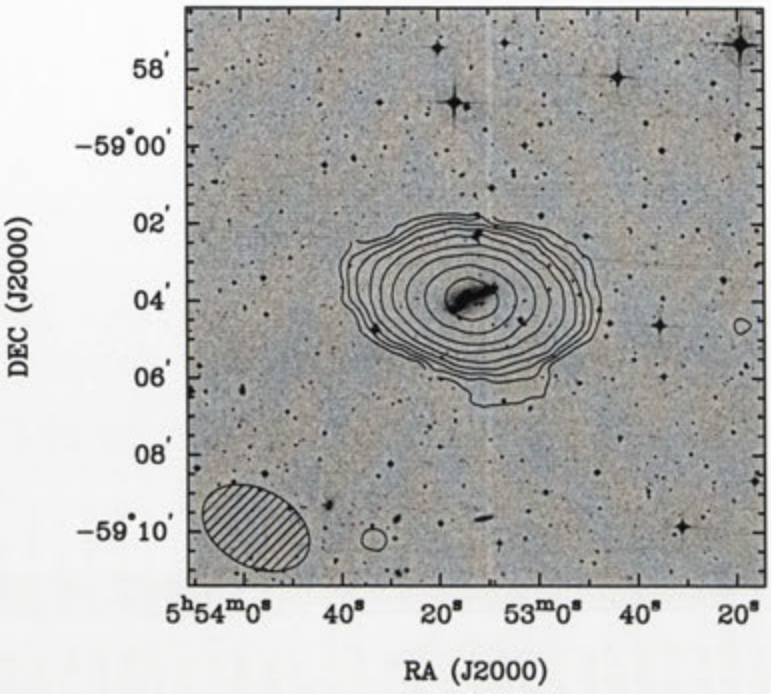

Fig. A.26: Integrated H I intensity distribution of ESO 120-G021 overlaid onto an optical DSS II R band image. The synthesised beam is displayed in the bottom left corner.

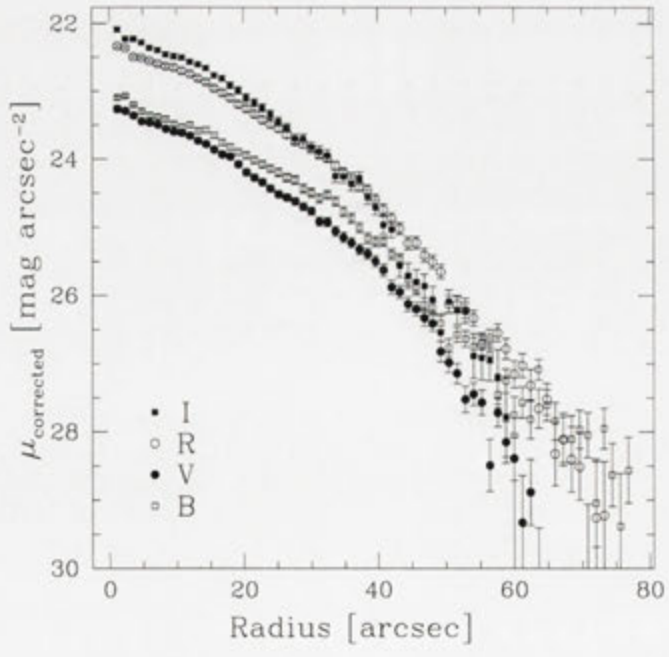

Fig. A.27: *BVRI* surface brightness profiles of ESO 120-G021, corrected for Galactic extinction.

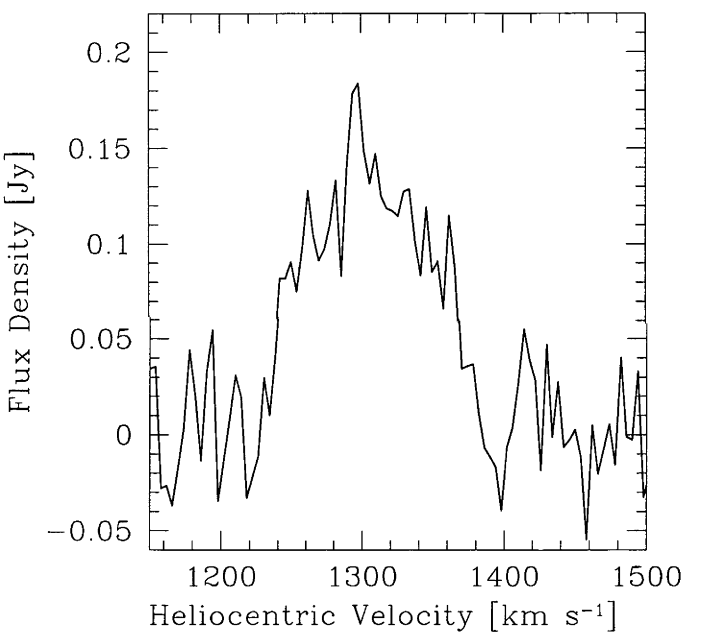

Fig. A.28: Global H I spectra of ESO 120-G021 as obtained from the ATCA.

ESO 425-G001

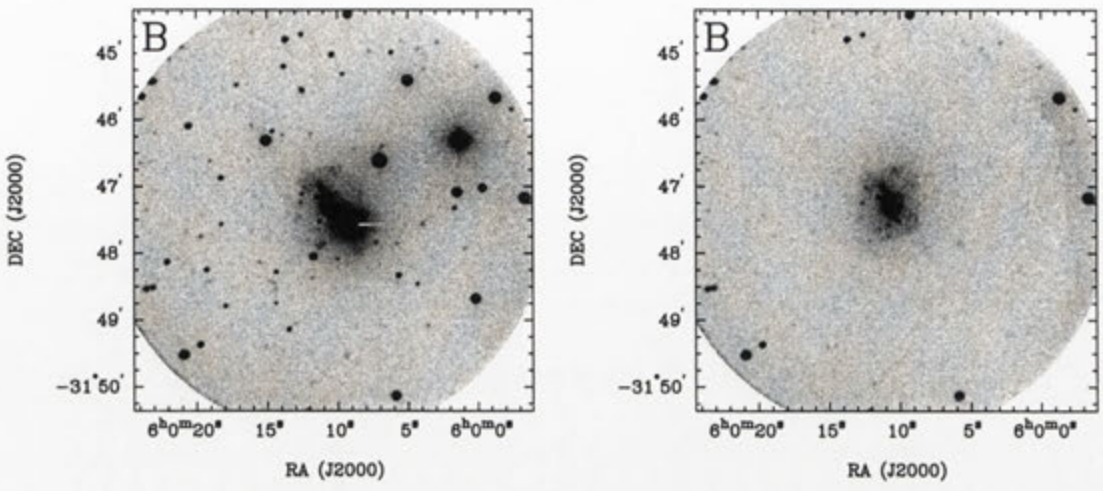

Fig. A.29: Deep B image of ESO 425-G001 before and after subtraction of the foreground stars.

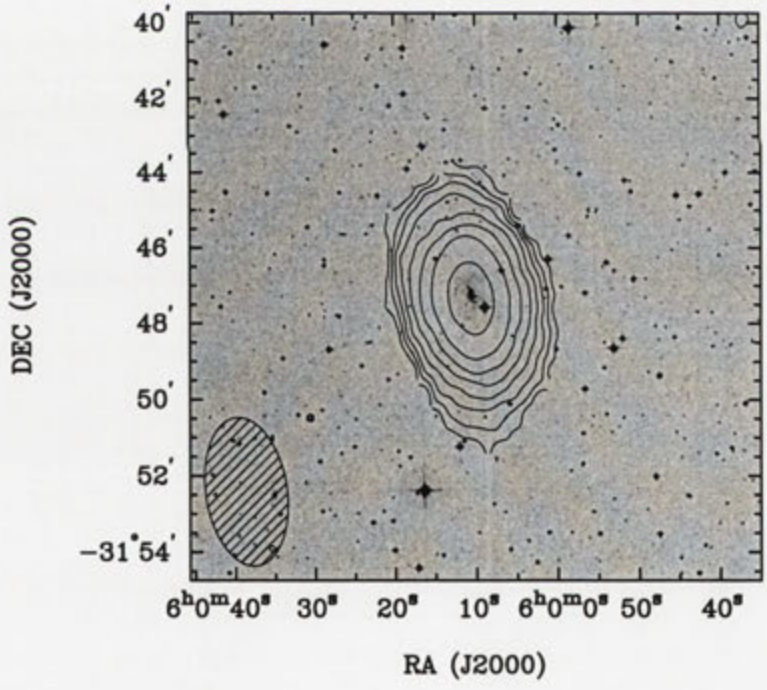

Fig. A.30: Integrated H I intensity distribution of ESO 425-G001 overlaid onto an optical DSS II R band image. The synthesised beam is displayed in the bottom left corner.

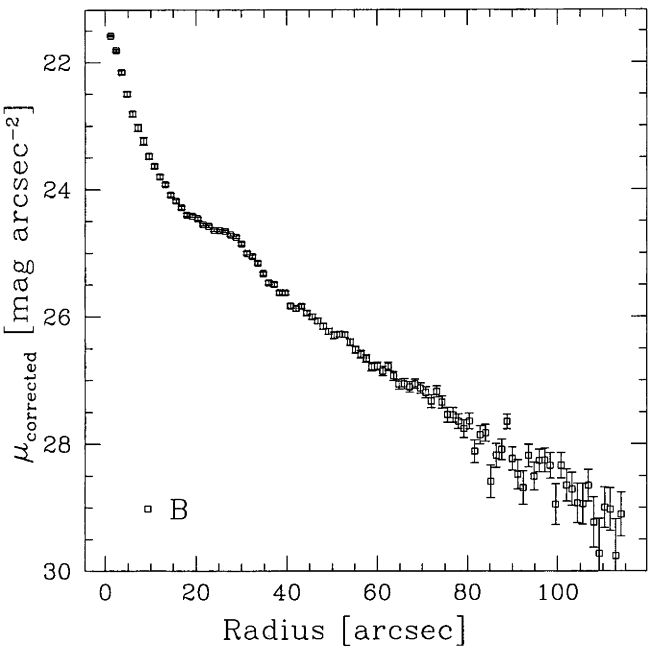

Fig. A.31: *B* surface brightness profile of ESO 425-G001, corrected for Galactic extinction.

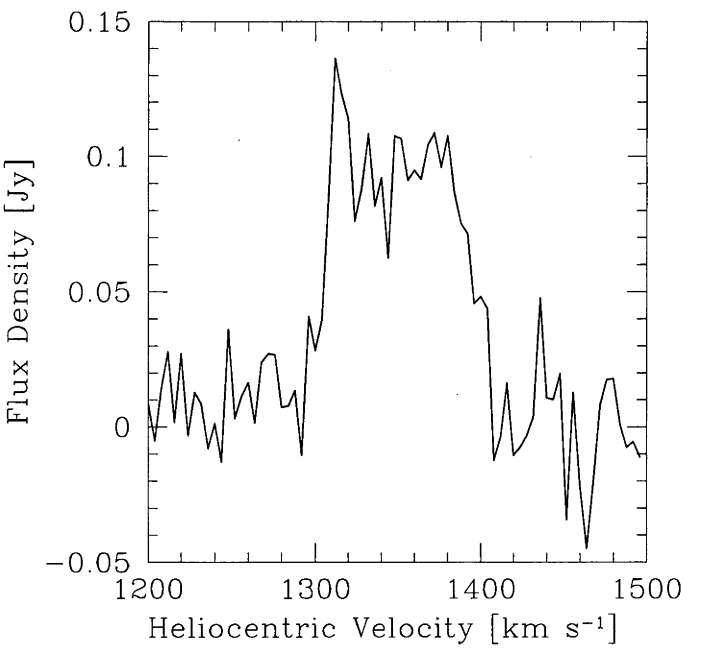

Fig. A.32: Global H I spectra of ESO 425-G001 as obtained from the ATCA.

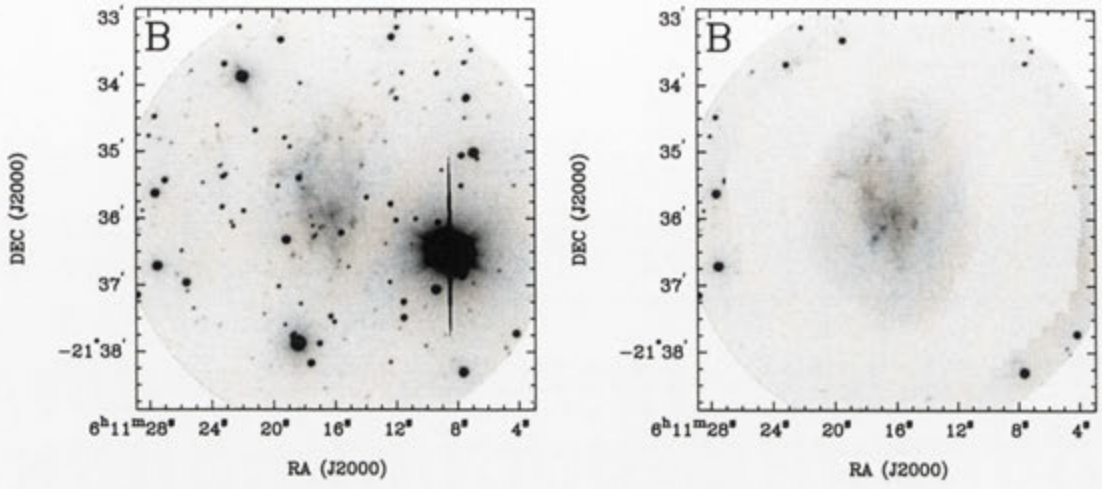

Fig. A.33: Deep B image of UGCA 120 before and after subtraction of the foreground stars.

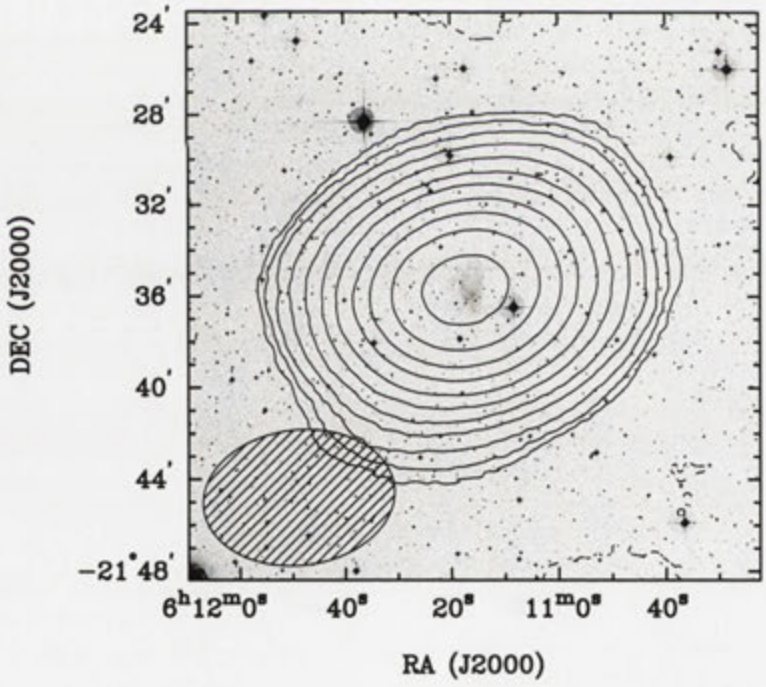

Fig. A.34: Integrated H I intensity distribution of UGCA 120 overlaid onto an optical DSS II R band image. The synthesised beam is displayed in the bottom left corner.

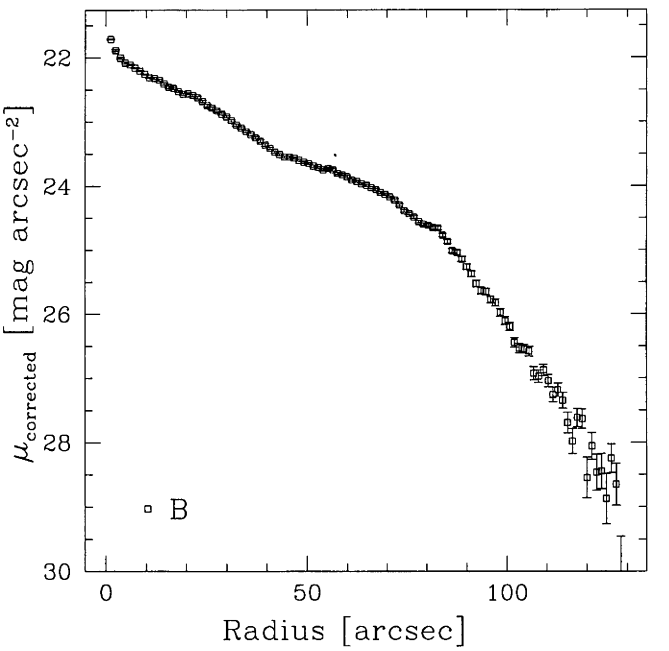

Fig. A.35: *B* surface brightness profile of UGCA 120, corrected for Galactic extinction.

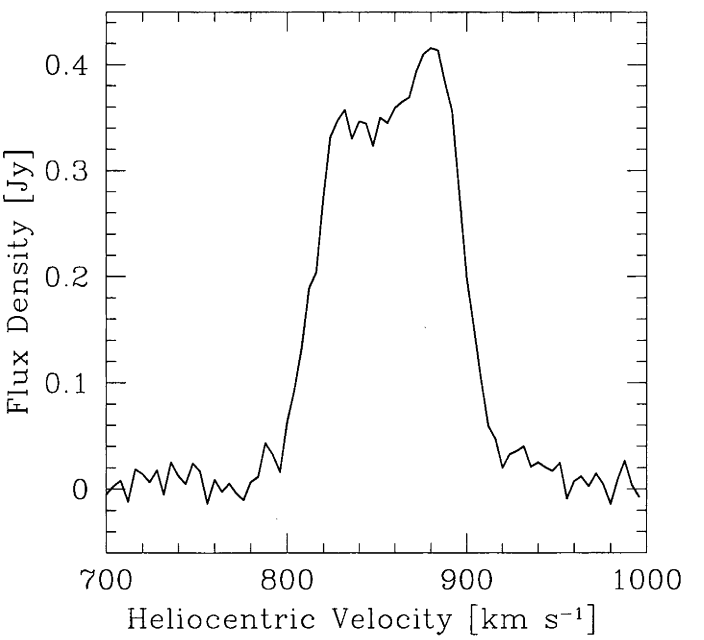

Fig. A.36: Global H I spectra of UGCA 120 as obtained from the ATCA.

ESO 121-G020 and ATCA J061608–574552

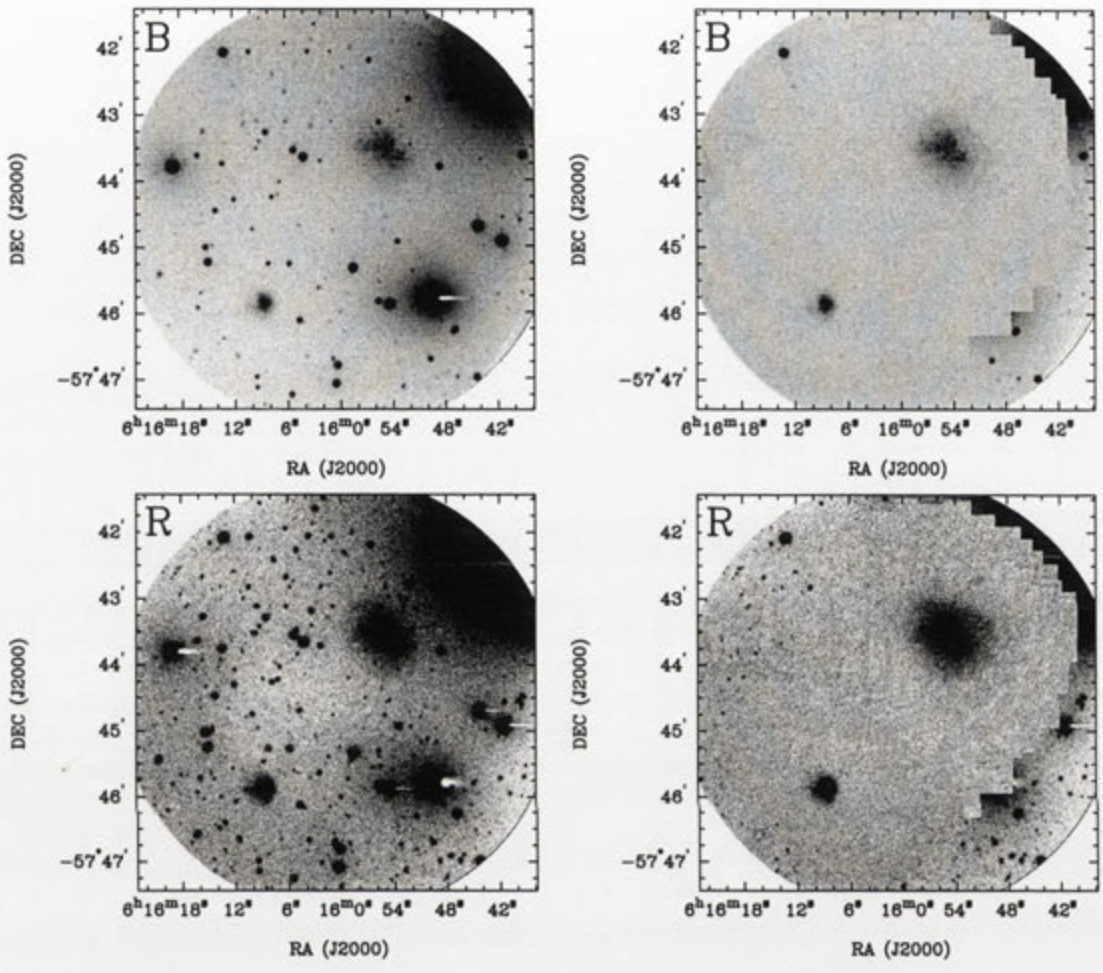

Fig. A.37: Deep *BR* images of ESO 121-G020 (top right galaxy) and ATCA J061608–574552 (bottom left galaxy) before and after subtraction of the foreground stars.

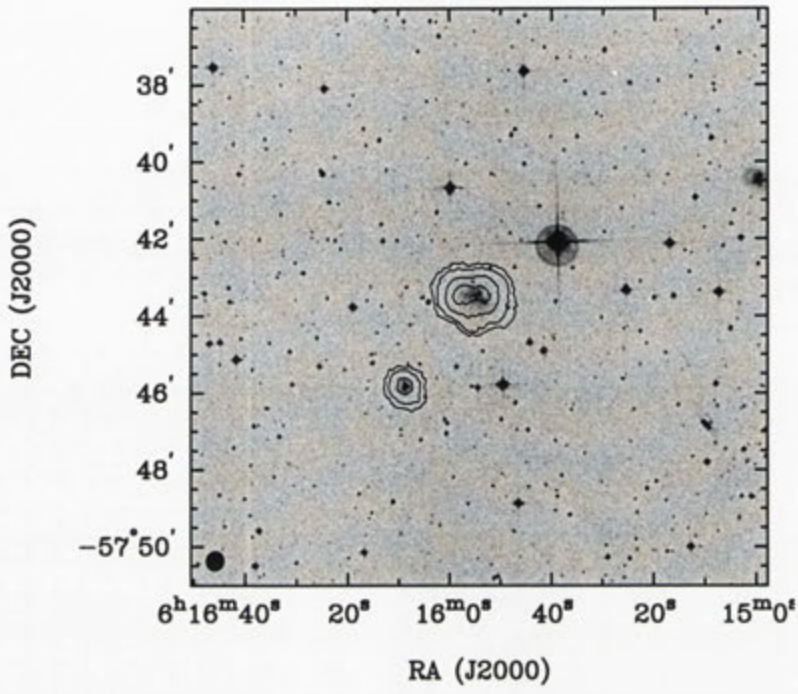

Fig. A.38: Integrated H I intensity distribution of ESO 121-G020 (top right galaxy) and ATCA J061608–574552 (bottom left galaxy) overlaid onto an optical DSS II R band image. The synthesised beam is displayed in the bottom left corner.

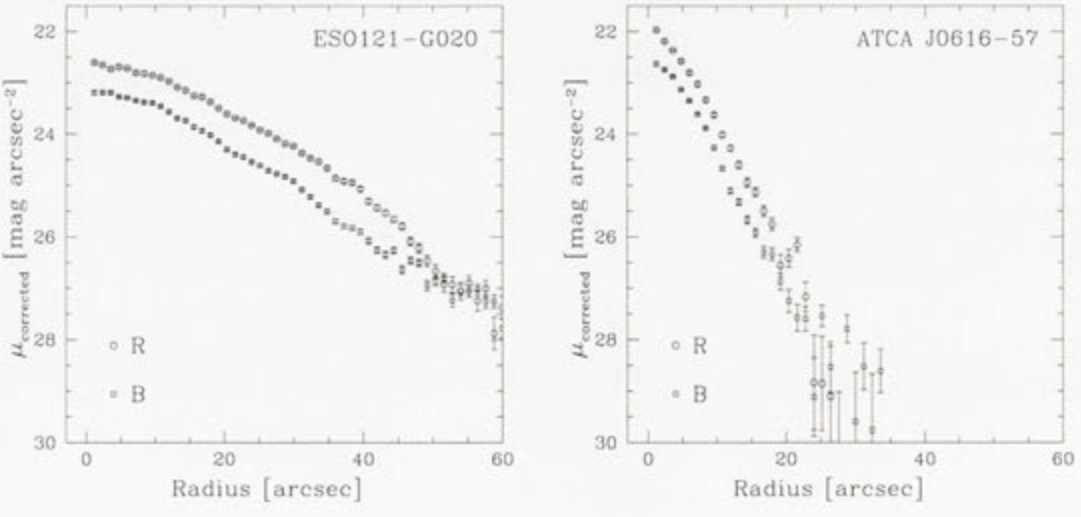

Fig. A.39: *BR* surface brightness profiles of ESO 121-G020 (left) and ATCA J061608–574552 (right), corrected for Galactic extinction.

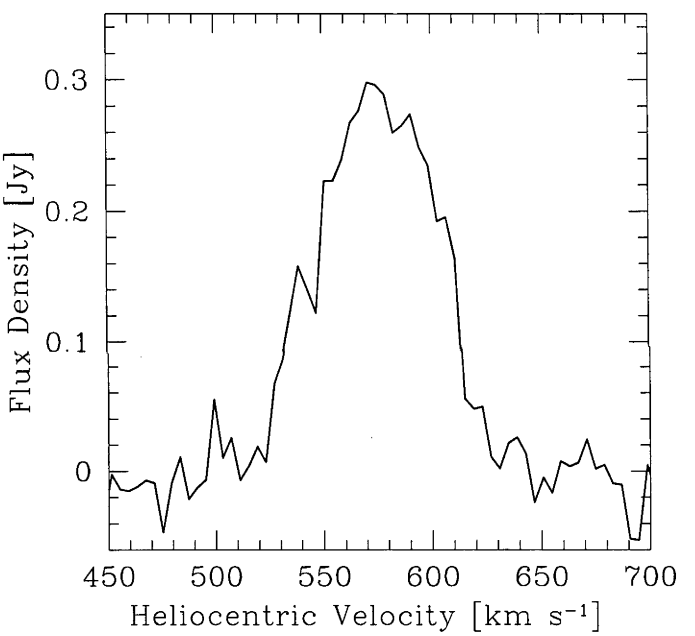

Fig. A.40: Global H I spectra of combined ESO 121-G020/ATCA J061608–574552 system as obtained from the ATCA.

WHI B0619–07

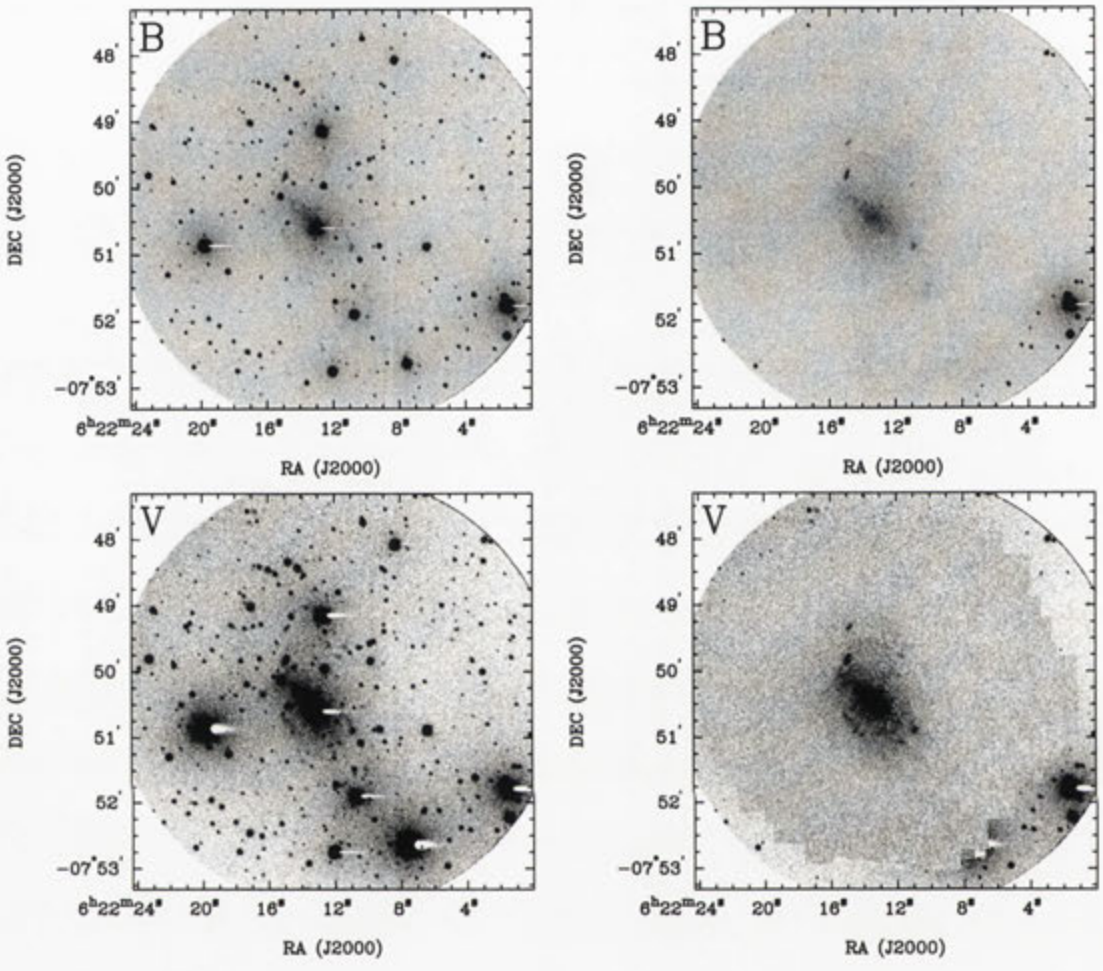

Fig. A.41: Deep *BVRI* images of WHI B0619–07 before and after subtraction of the foreground stars.

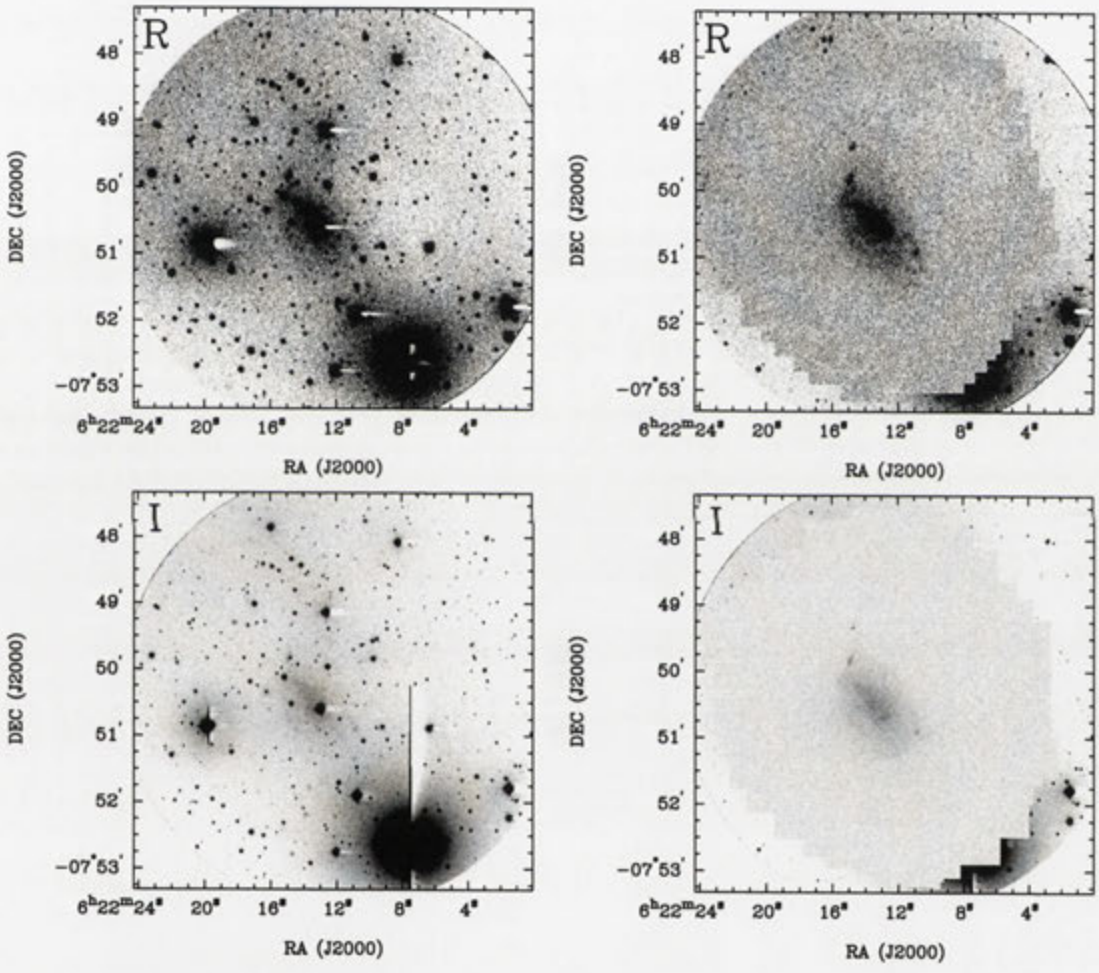

Fig. A.41: continued

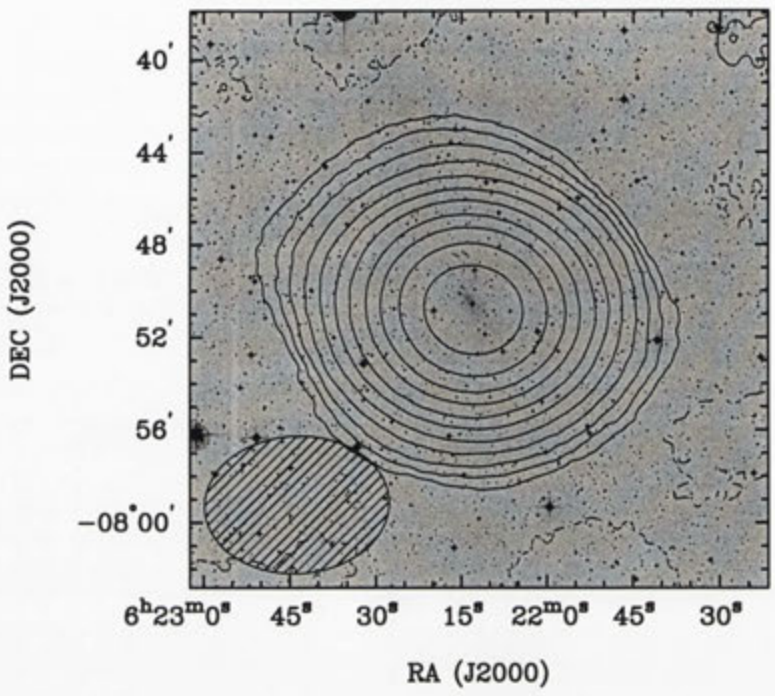

Fig. A.42: Integrated H I intensity distribution of WHI B0619–07 overlaid onto an optical DSS II *R* band image. The synthesised beam is displayed in the bottom left corner.

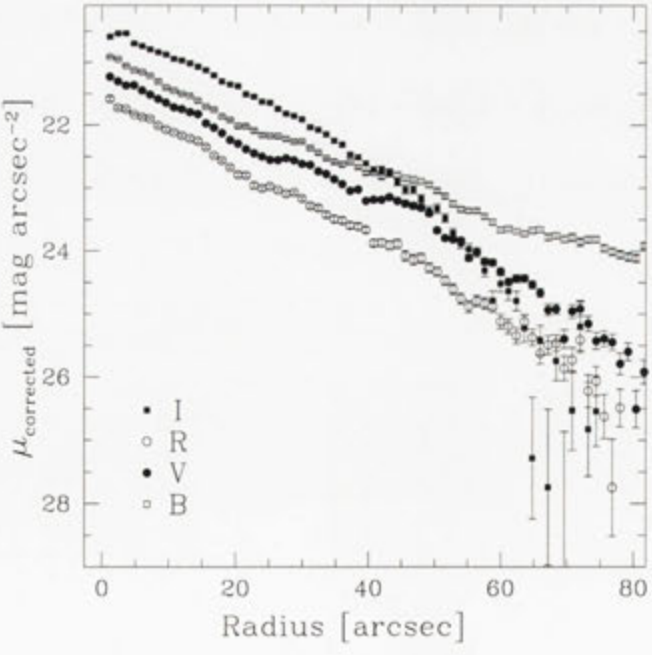

Fig. A.43: *BVRI* surface brightness profiles of WHI B0619–07, corrected for Galactic extinction.

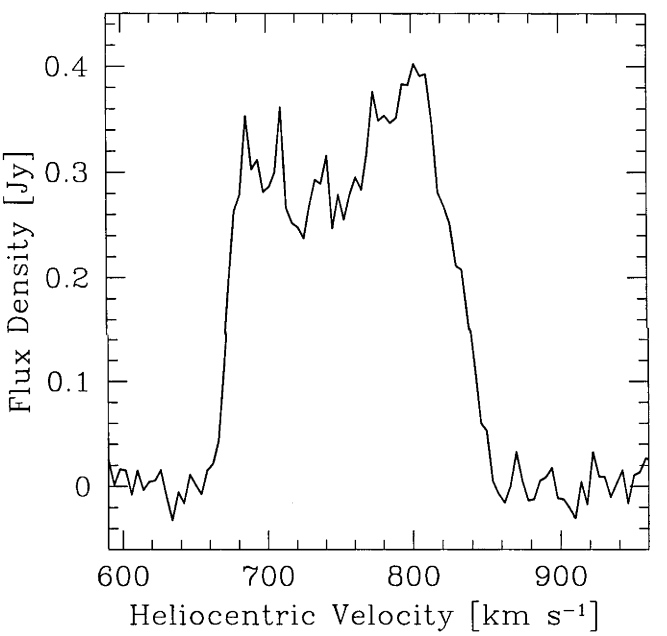

Fig. A.44: Global H I spectra of WHI B0619–07 as obtained from the ATCA.

ESO 490-G017

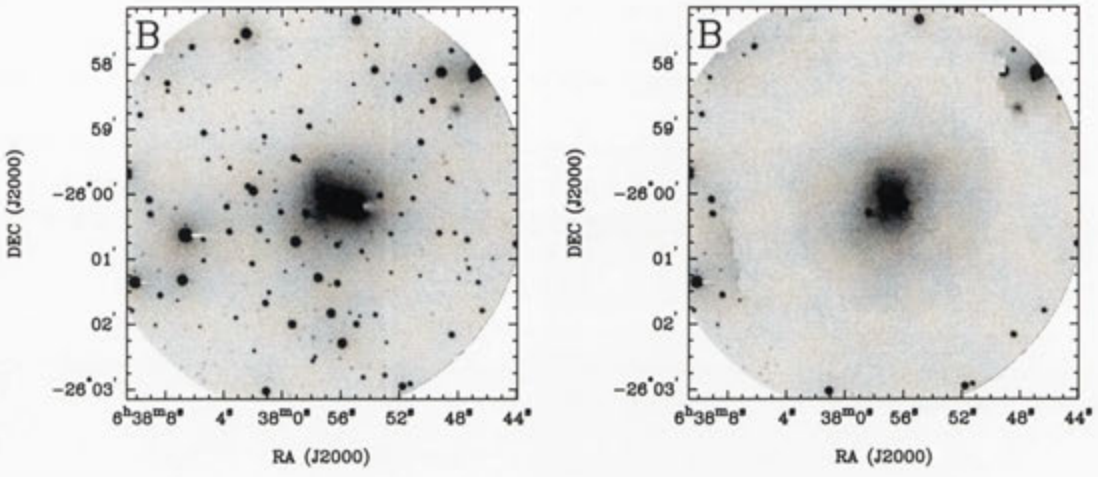

Fig. A.45: Deep B image of ESO 490-G017 before and after subtraction of the foreground stars.

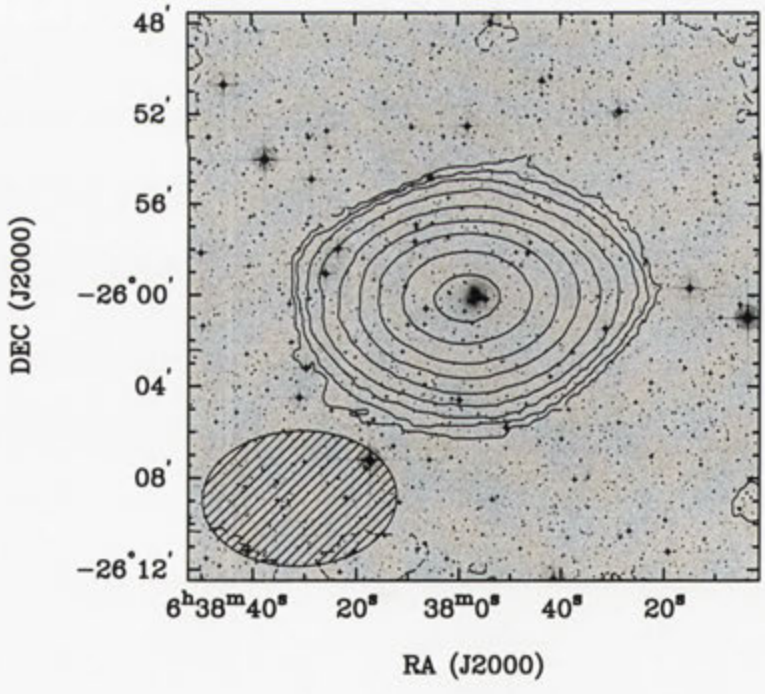

Fig. A.46: Integrated H I intensity distribution of ESO 490-G017 overlaid onto an optical DSS II R band image. The synthesised beam is displayed in the bottom left corner.

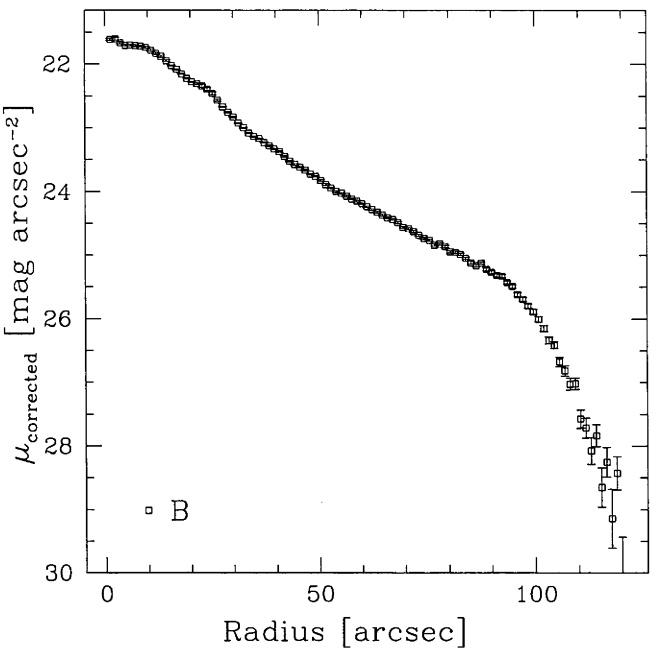

Fig. A.47: *B* surface brightness profile of ESO 490-G017, corrected for Galactic extinction.

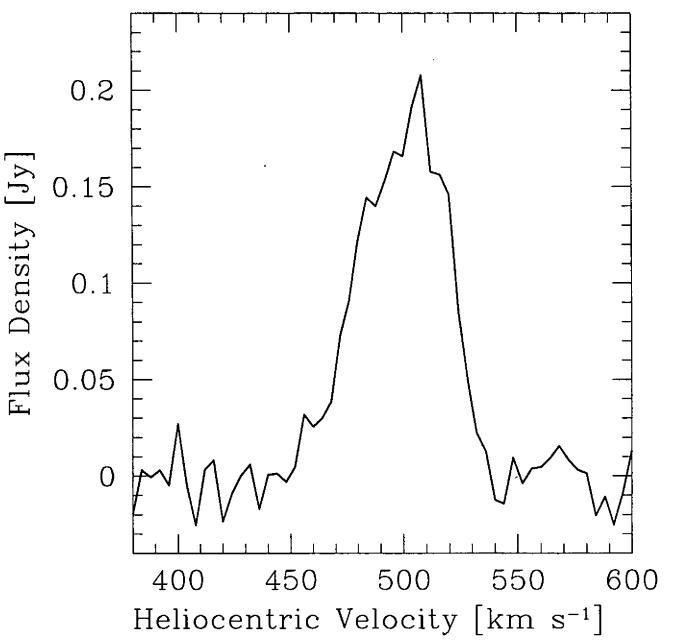

Fig. A.48: Global H I spectra of ESO 490-G017 as obtained from the ATCA.

CGMW 1-0260

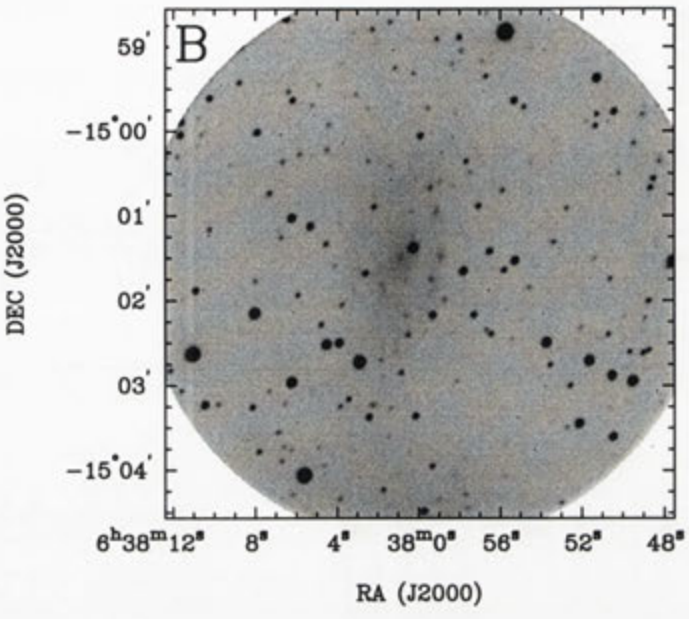

Fig. A.49: Deep B image of CGMW 1-0260.

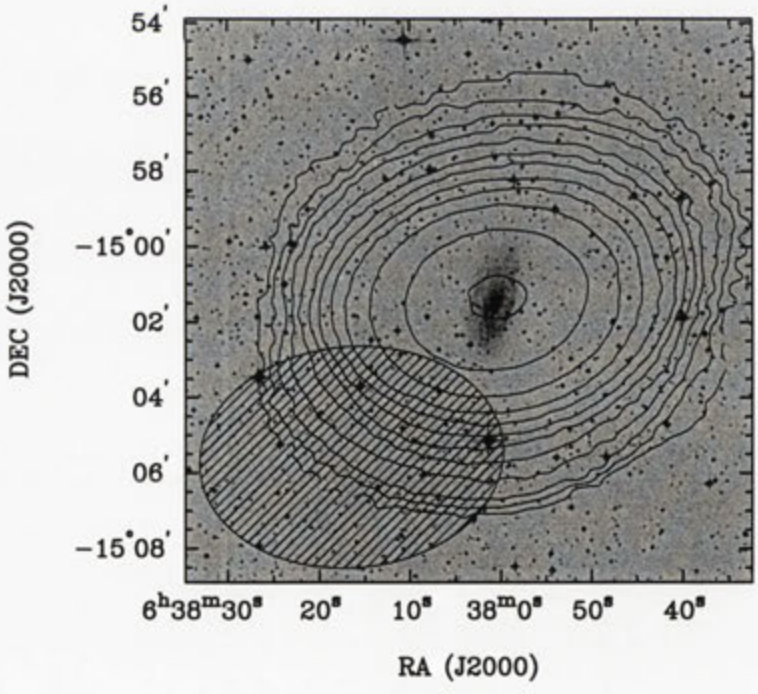

Fig. A.50: Integrated H I intensity distribution of CGMW 1-0260 overlaid onto an optical DSS II R band image. The synthesised beam is displayed in the bottom left corner.

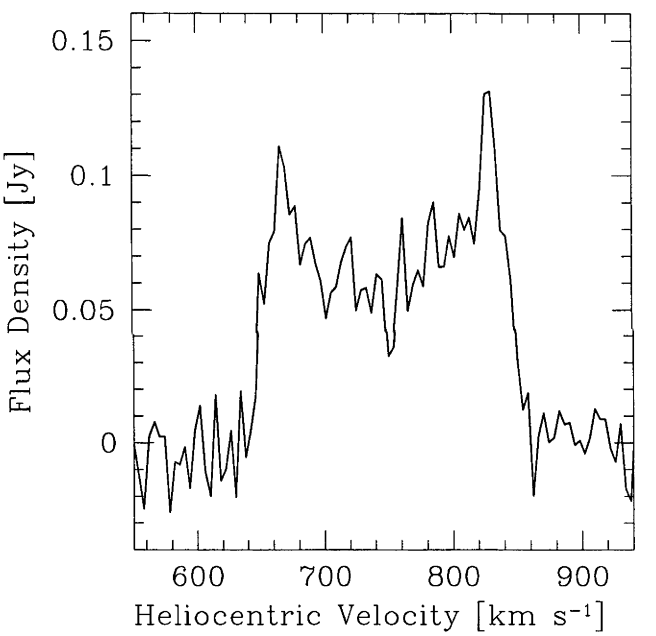

Fig. A.51: Global H I spectra of CGMW 1-0260 as obtained from the ATCA.

ESO 255-G019

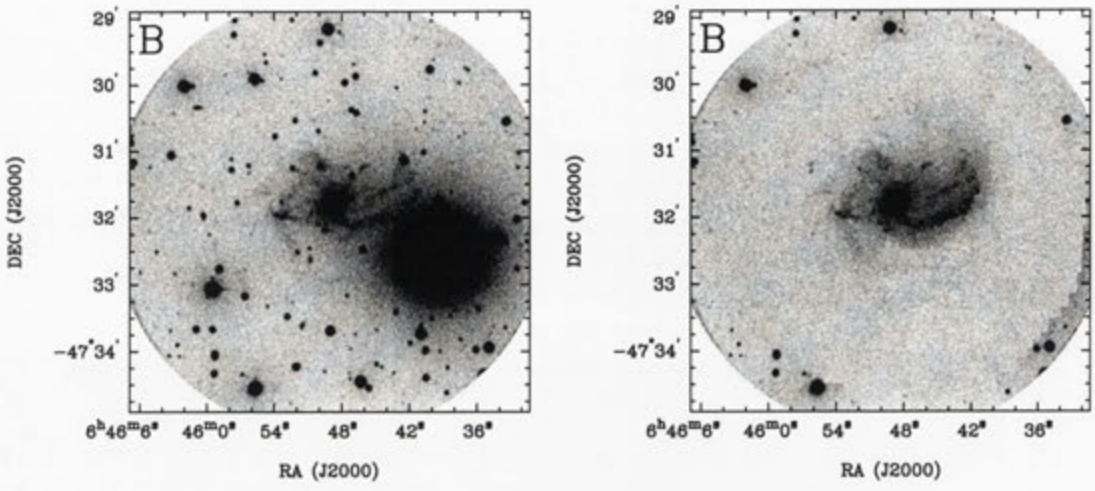

Fig. A.52: Deep *B* image of ESO 255-G019 before and after subtraction of the foreground stars.

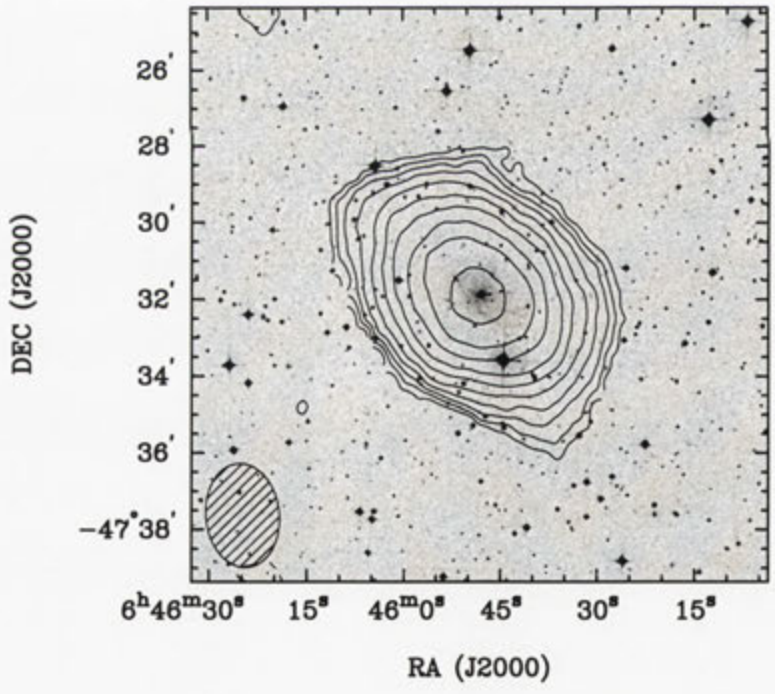

Fig. A.53: Integrated H I intensity distribution of ESO 255-G019 overlaid onto an optical DSS II *R* band image. The synthesised beam is displayed in the bottom left corner.

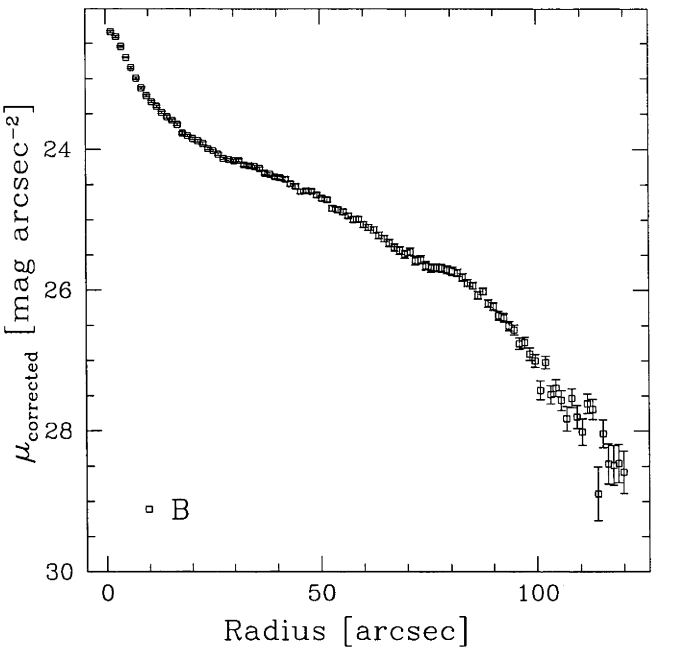

Fig. A.54: *B* surface brightness profile of ESO 255-G019, corrected for Galactic extinction.

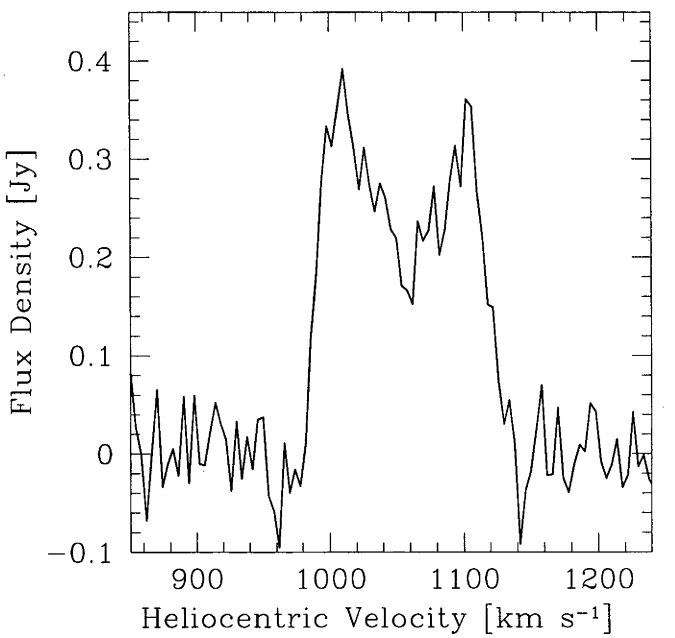

Fig. A.55: Global H I spectra of ESO 255-G019 as obtained from the ATCA.

CGMW 1-0381

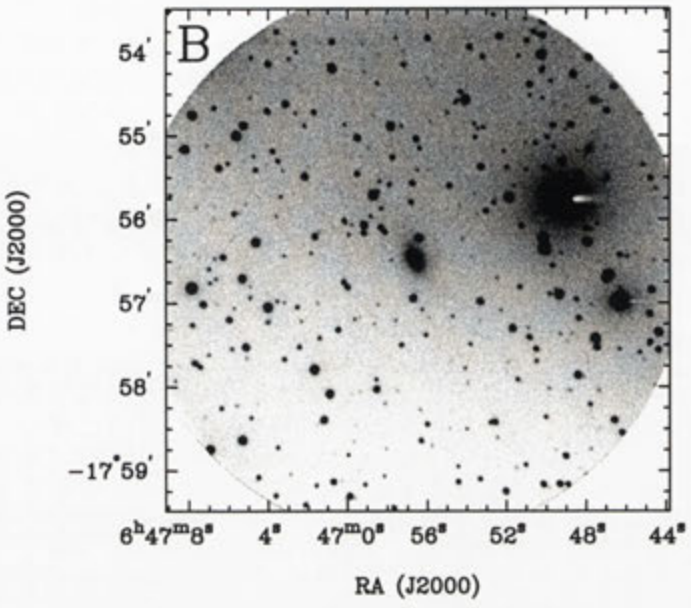

Fig. A.56: Deep B image of CGMW 1-0381.

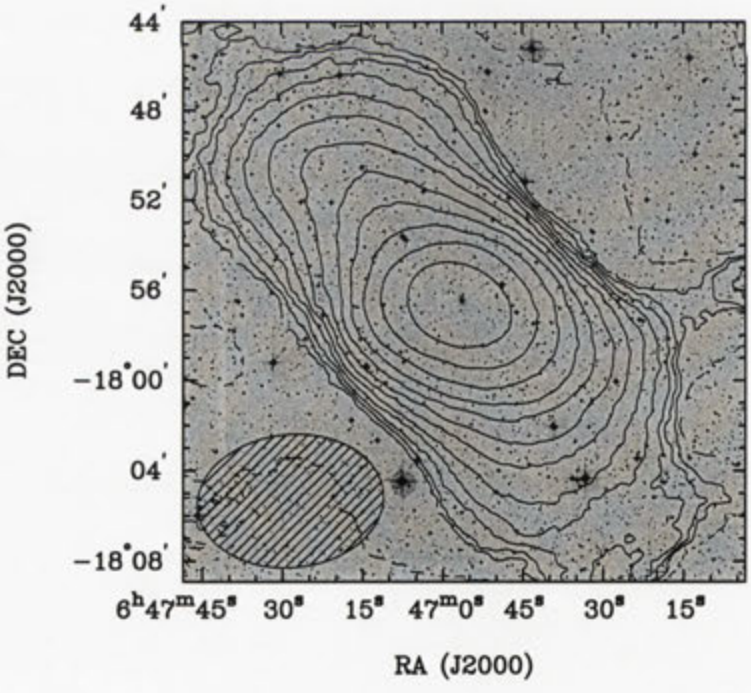

Fig. A.57: Integrated H I intensity distribution of CGMW 1-0381 overlaid onto an optical DSS II R band image. The synthesised beam is displayed in the bottom left corner.

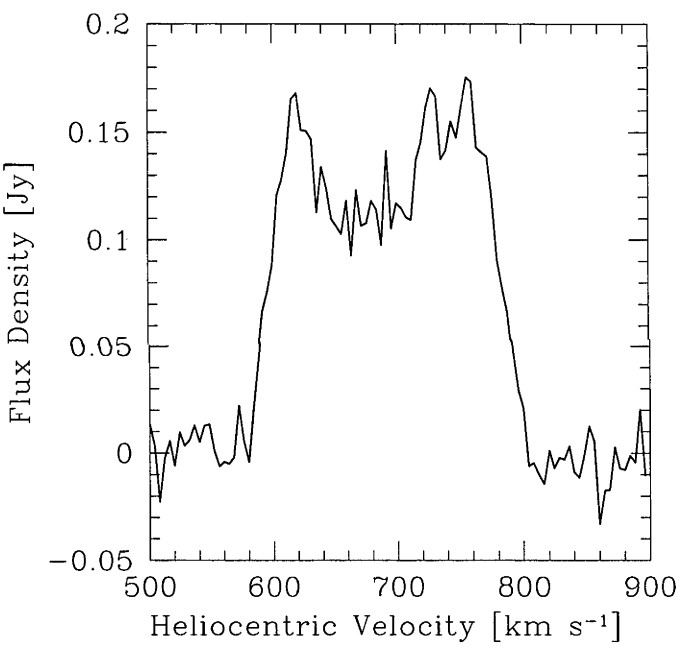

Fig. A.58: Global H I spectra of CGMW 1-0381 as obtained from the ATCA.

ESO 207-G007

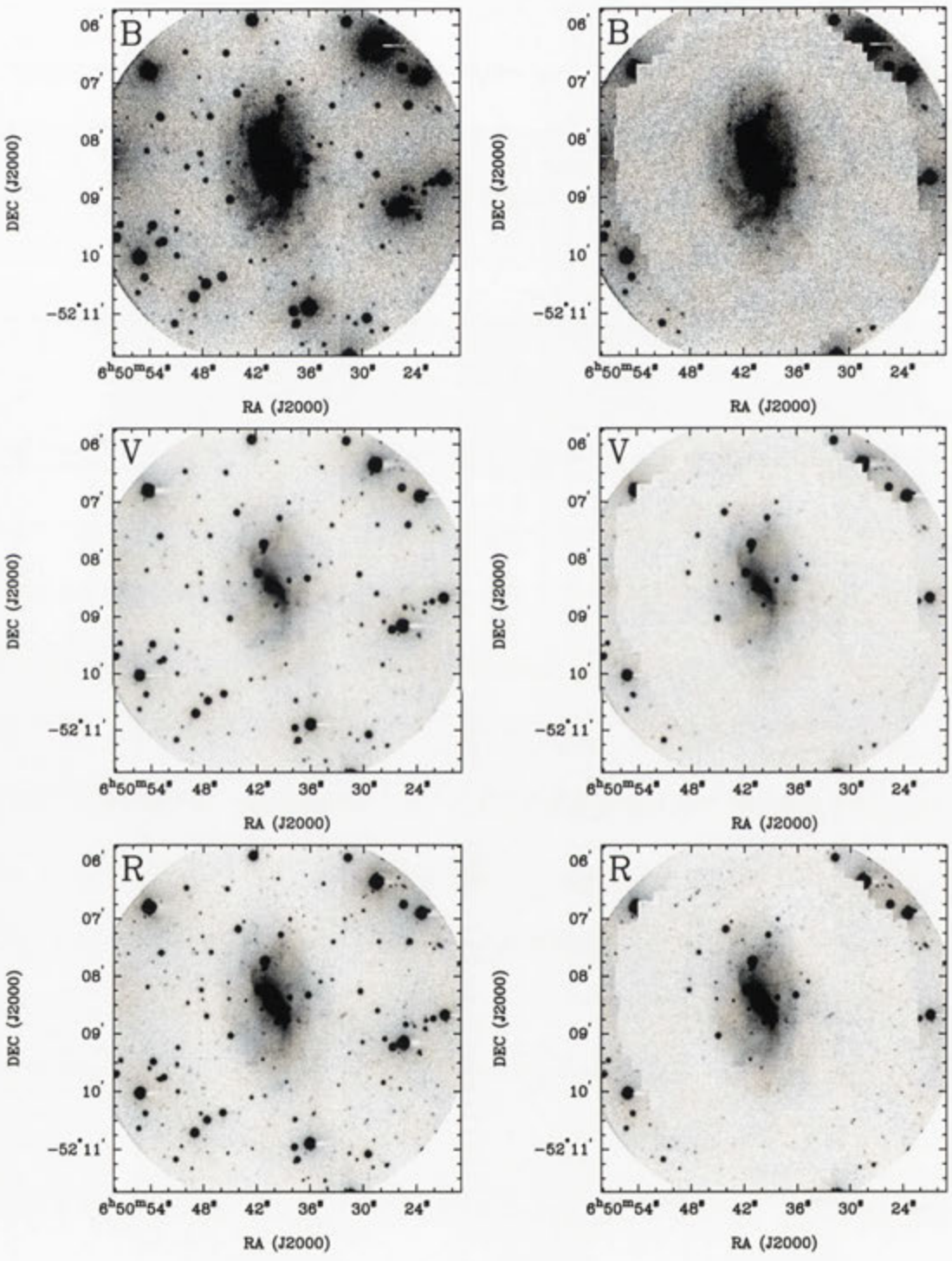

Fig. A.59: Deep *BVR* images of ESO 207-G007 before and after subtraction of the foreground stars.

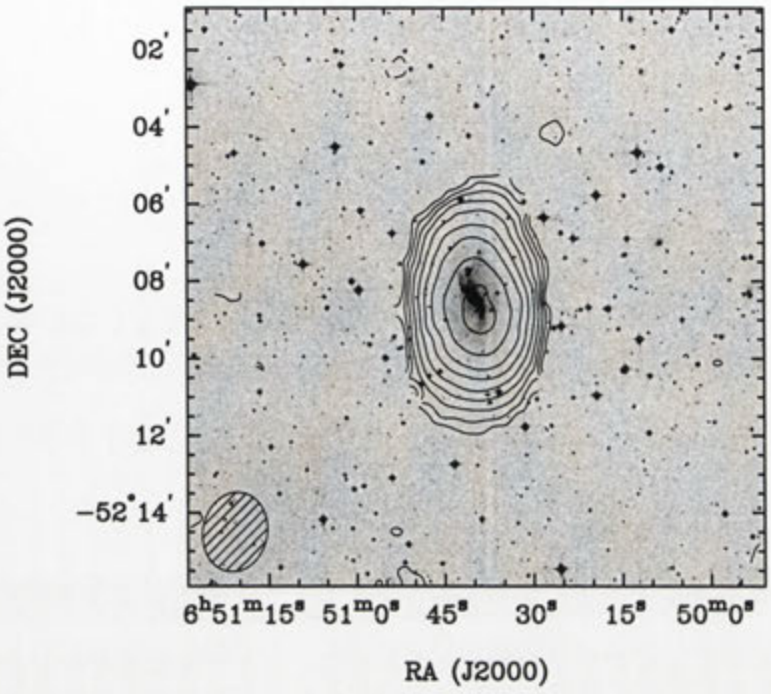

Fig. A.60: Integrated H I intensity distribution of ESO 207-G007 overlaid onto an optical DSS II R band image. The synthesised beam is displayed in the bottom left corner.

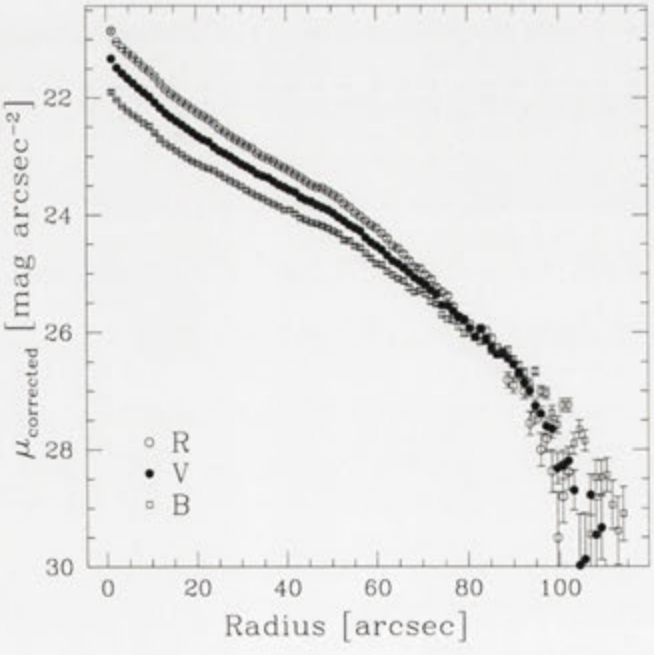

Fig. A.61: BVR surface brightness profiles of ESO 207-G007, corrected for Galactic extinction.

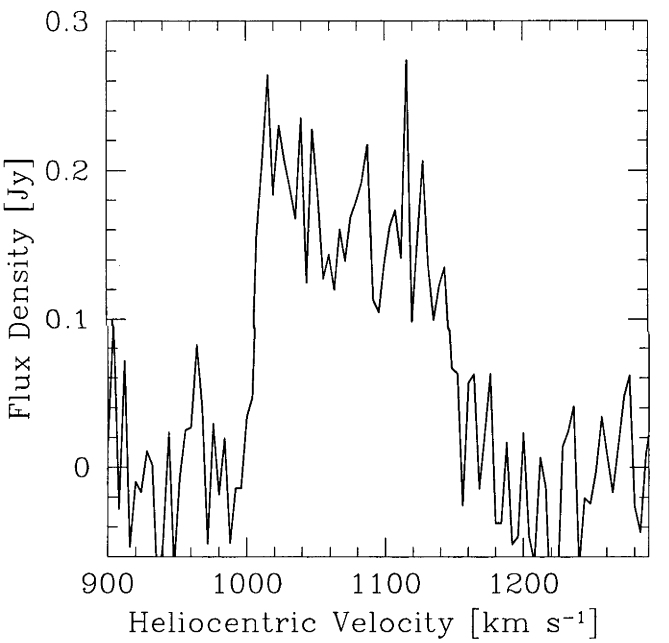

Fig. A.62: Global H I spectra of ESO 207-G007 as obtained from the ATCA.

ESO 207-G022

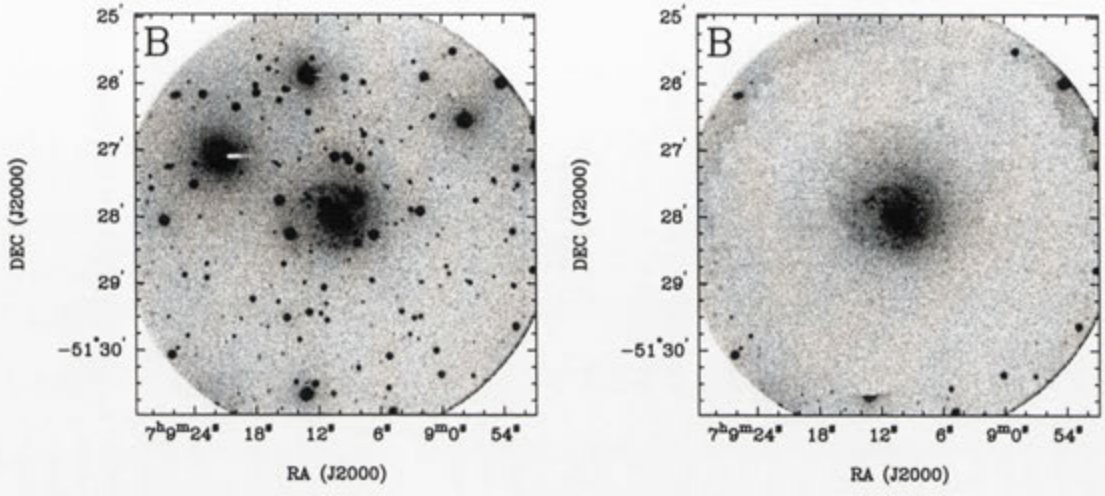

Fig. A.63: Deep B images of ESO 207-G022 before and after subtraction of the foreground stars.

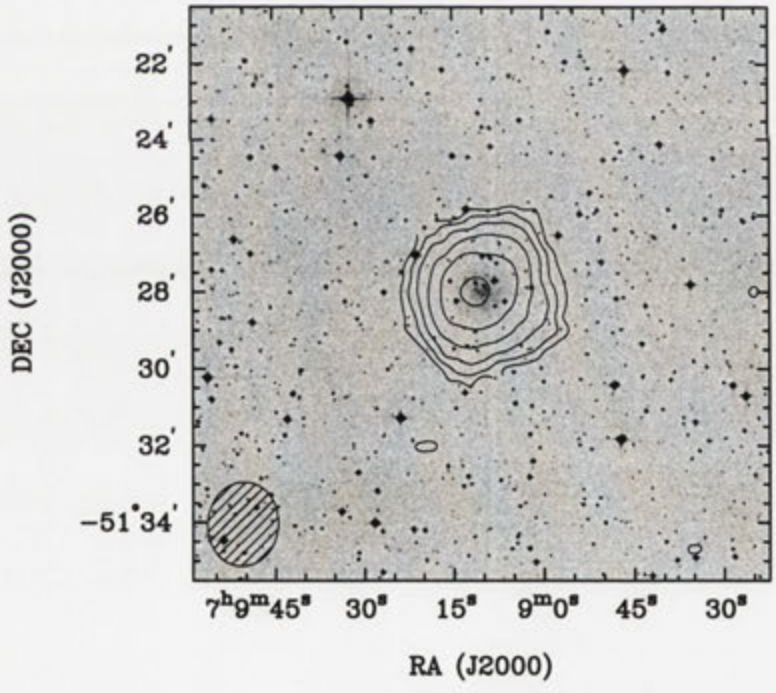

Fig. A.64: Integrated H I intensity distribution of ESO 207-G022 overlaid onto an optical DSS II R band image. The synthesised beam is displayed in the bottom left corner.

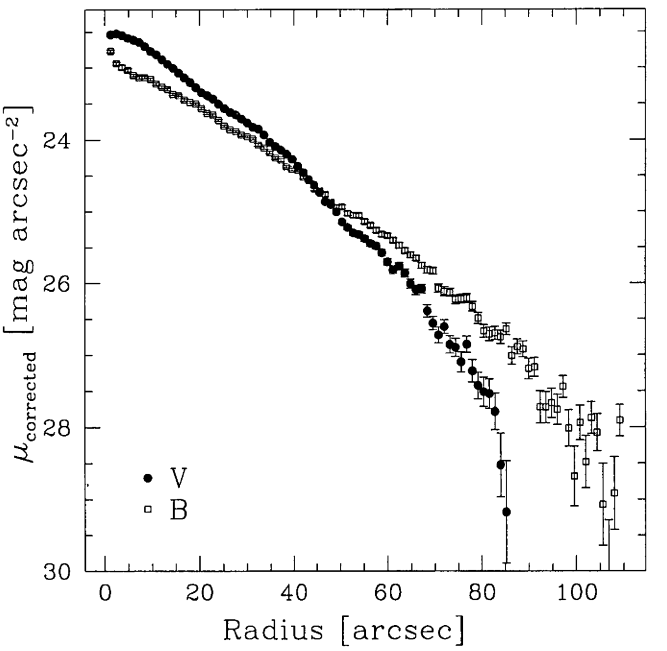

Fig. A.65: BV surface brightness profiles of ESO 207-G022, corrected for Galactic extinction.

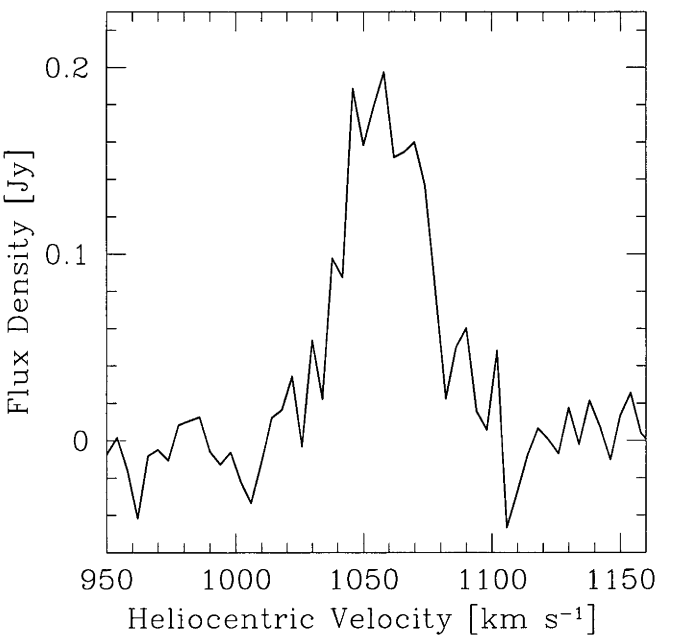

Fig. A.66: Global H I spectra of ESO 207-G022 as obtained from the ATCA.

ESO 428-G033

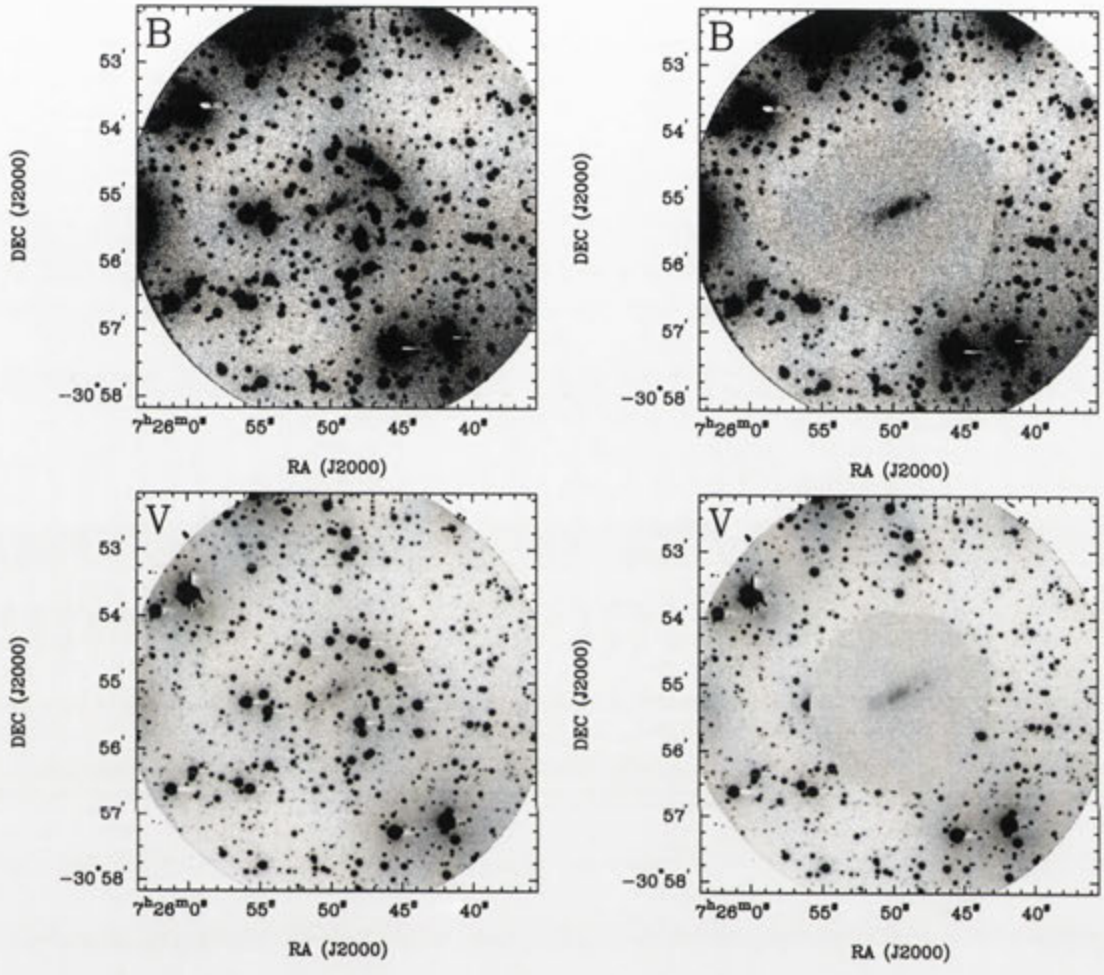

Fig. A.67: Deep *BVRI* images of ESO 428-G033 before and after subtraction of the foreground stars.

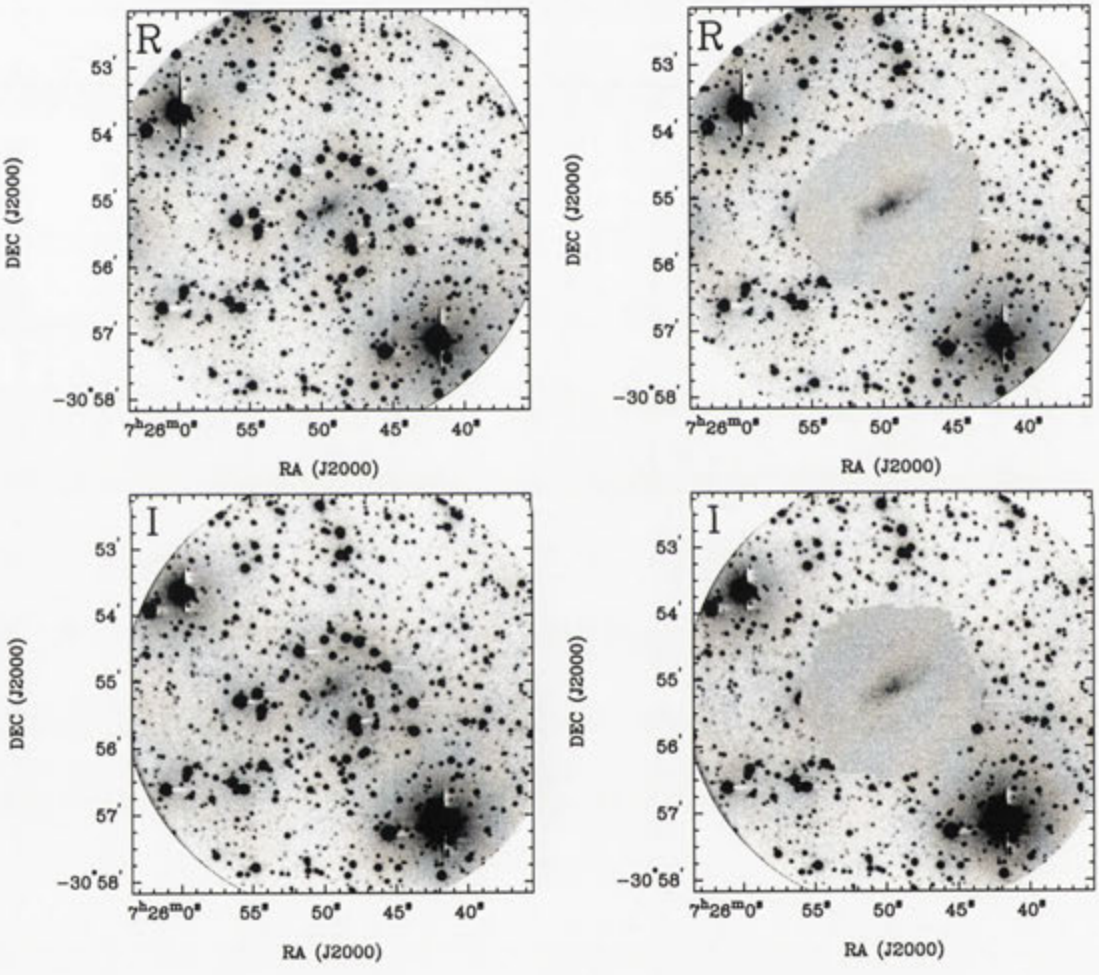

Fig. A.67: continued

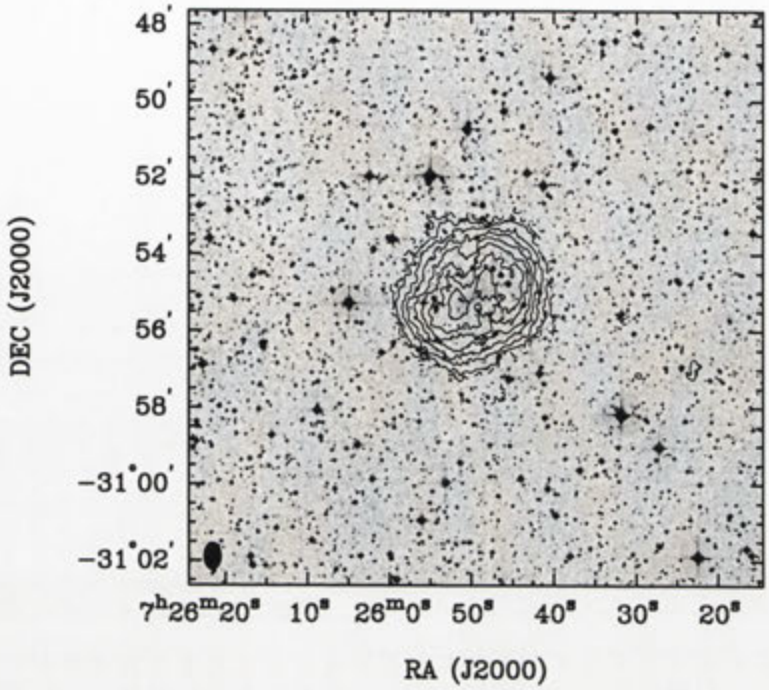

Fig. A.68: Integrated H I intensity distribution of ESO 428-G033 overlaid onto an optical DSS II R band image. The synthesised beam is displayed in the bottom left corner.

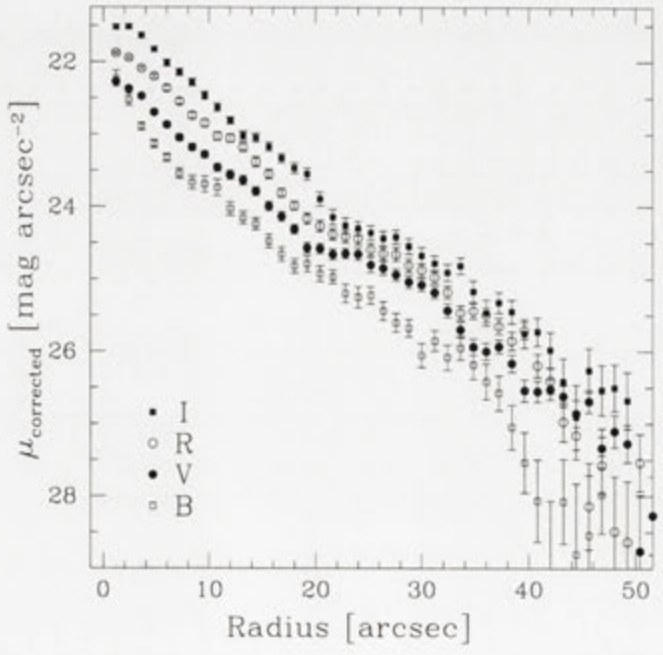

Fig. A.69: *BVRI* surface brightness profiles of ESO 428-G033, corrected for Galactic extinction.

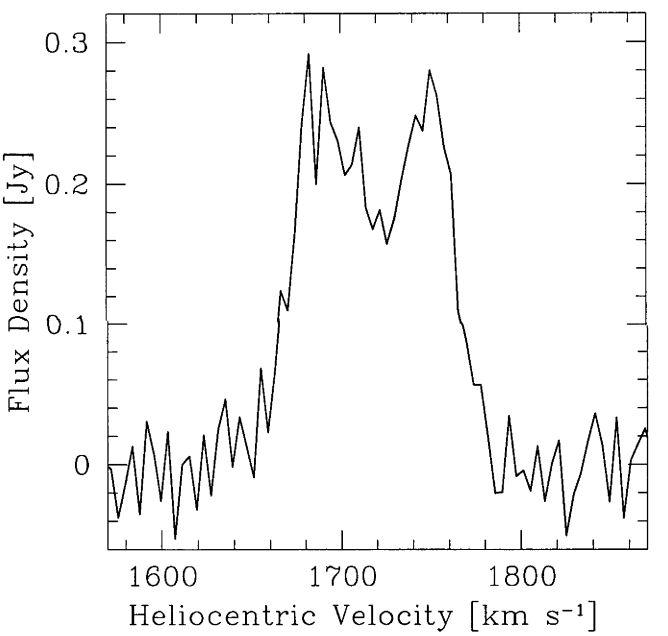

Fig. A.70: Global H I spectra of ESO 428-G033 as obtained from the ATCA.

ESO 257-G?017

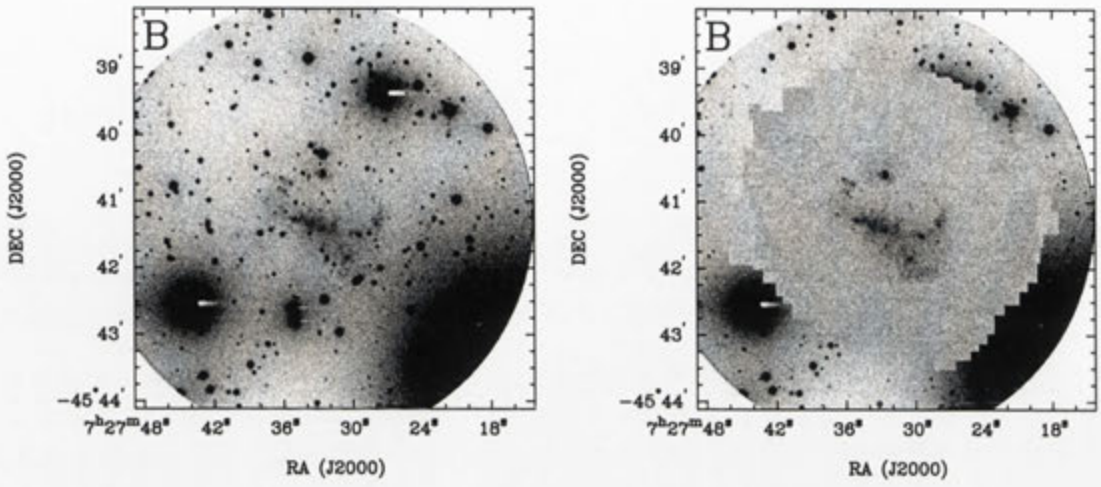

Fig. A.71: Deep B image of ESO 257-G?017 before and after subtraction of the foreground stars.

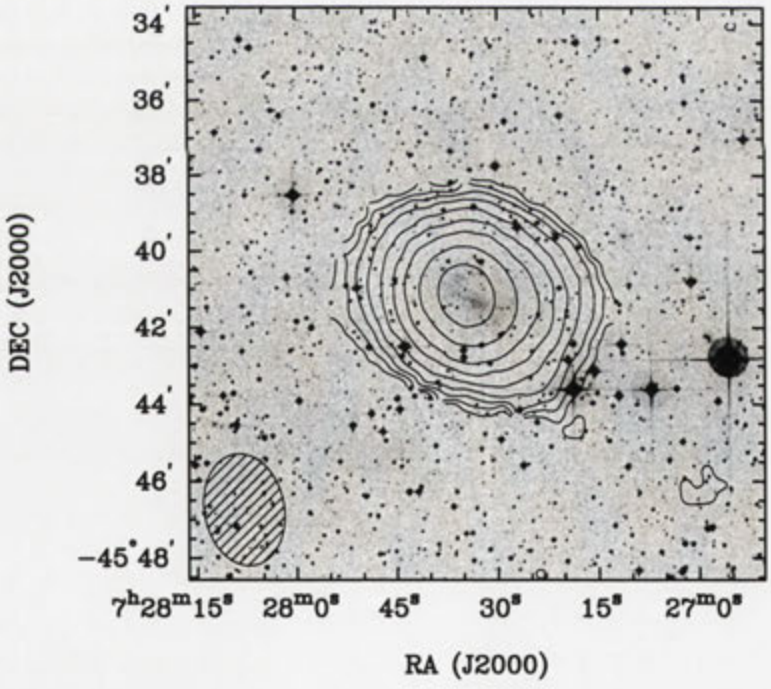

Fig. A.72: Integrated H I intensity distribution of ESO 257-G?017 overlaid onto an optical DSS II R band image. The synthesised beam is displayed in the bottom left corner.

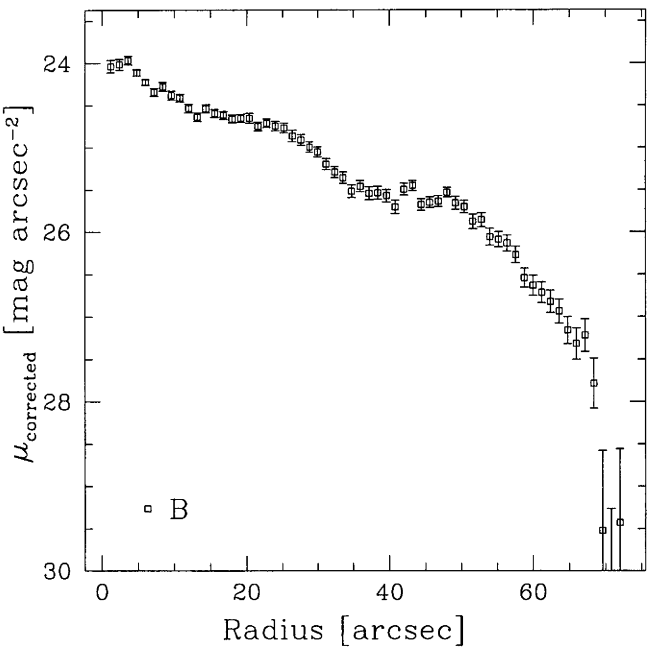

Fig. A.73: *B* surface brightness profile of ESO 257-G?017, corrected for Galactic extinction.

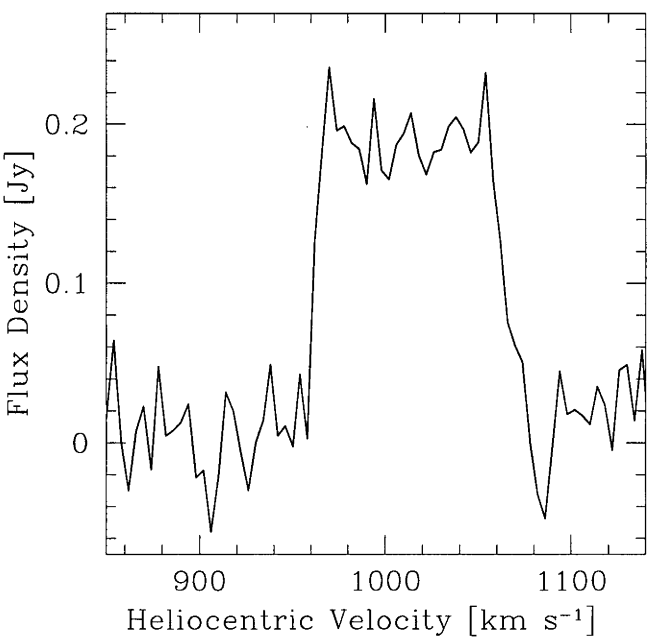

Fig. A.74: Global H I spectra of ESO 257-G?017 as obtained from the ATCA.

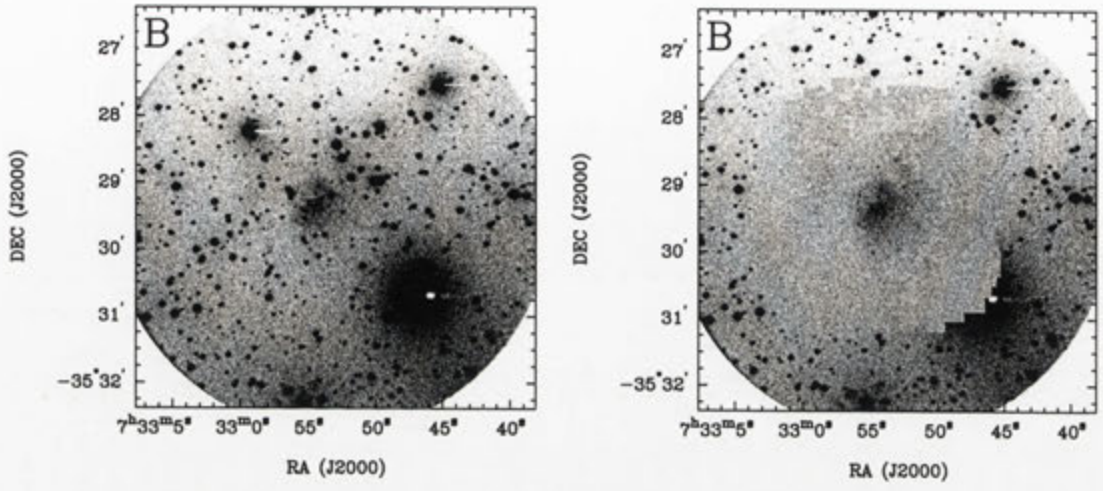

Fig. A.75: Deep *B* image of ESO 368-G004 before and after subtraction of the foreground stars.

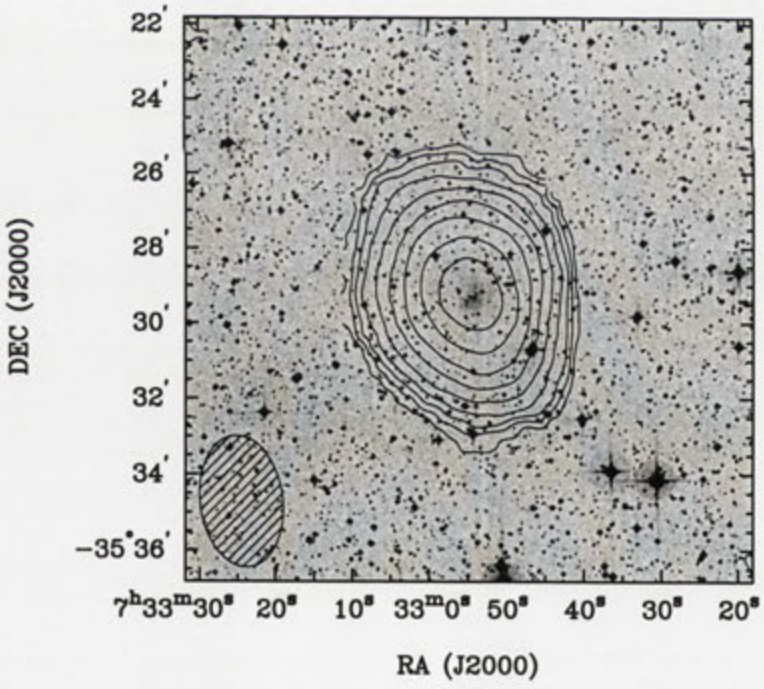

Fig. A.76: Integrated H I intensity distribution of ESO 368-G004 overlaid onto an optical DSS II *R* band image. The synthesised beam is displayed in the bottom left corner.

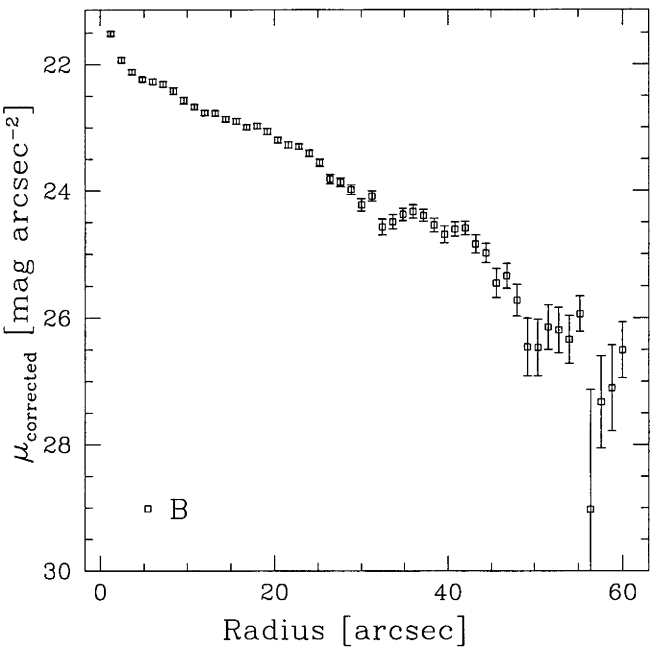

Fig. A.77: *B* surface brightness profile of ESO 368-G004, corrected for Galactic extinction.

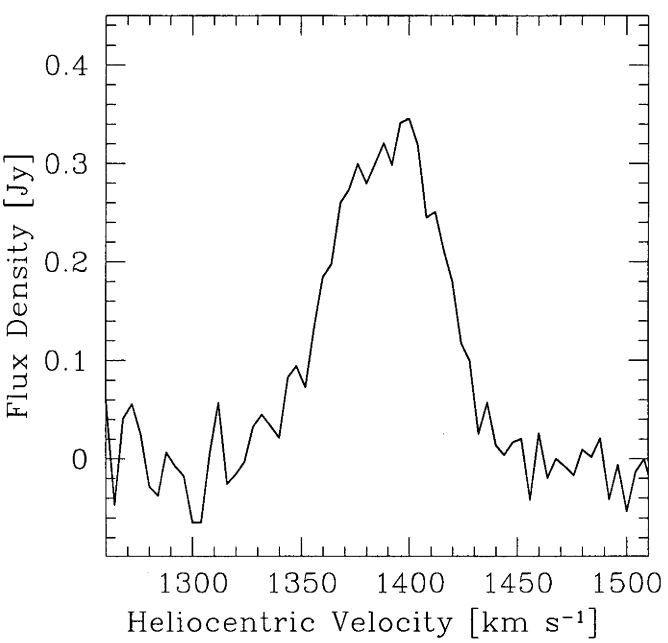

Fig. A.78: Global H I spectra of ESO 368-G004 as obtained from the ATCA.

PGC 023156

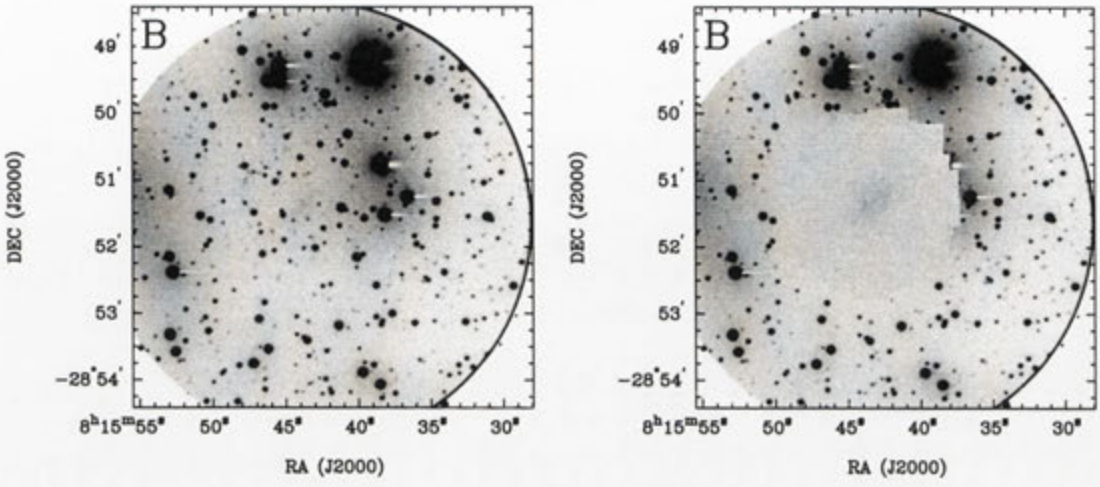

Fig. A.79: Deep B image of PGC 023156 before and after subtraction of the foreground stars.

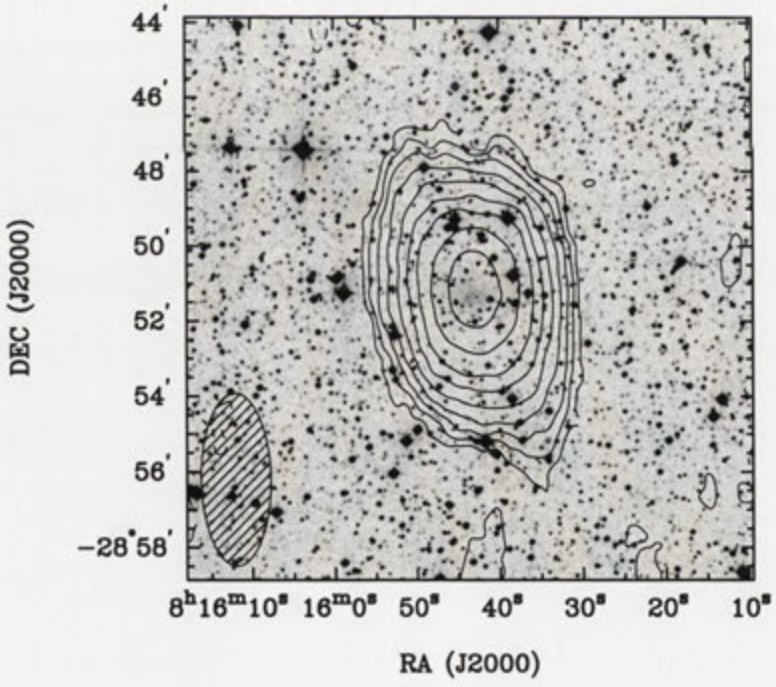

Fig. A.80: Integrated H I intensity distribution of PGC 023156 overlaid onto an optical DSS II R band image. The synthesised beam is displayed in the bottom left corner.

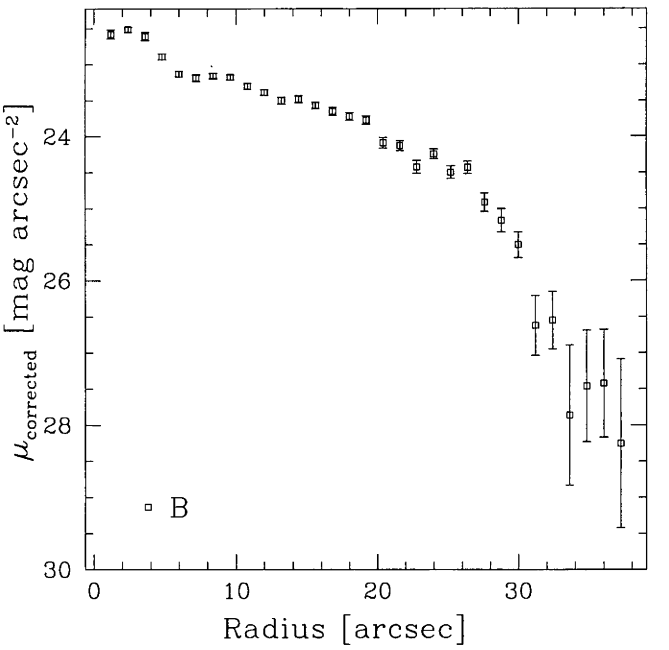

Fig. A.81: *B* surface brightness profile of PGC 023156, corrected for Galactic extinction.

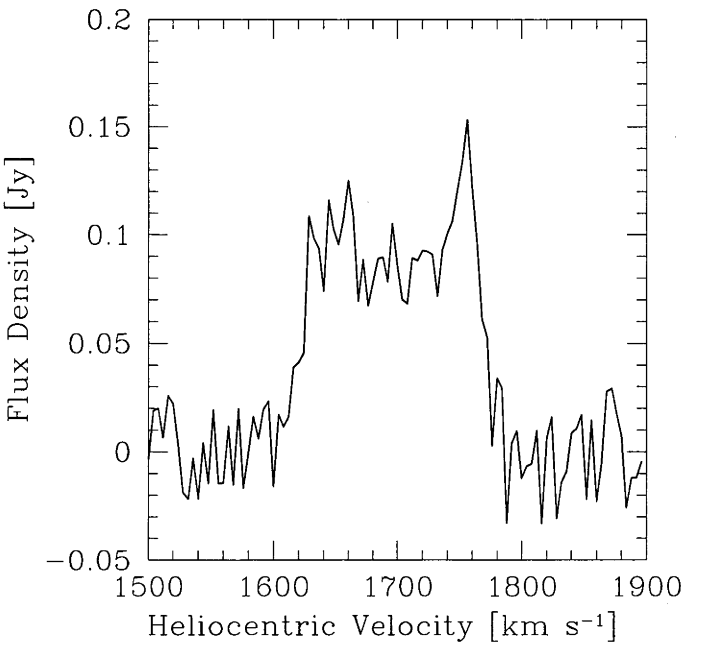

Fig. A.82: Global H I spectra of PGC 023156 as obtained from the ATCA.

ESO 164-G?010

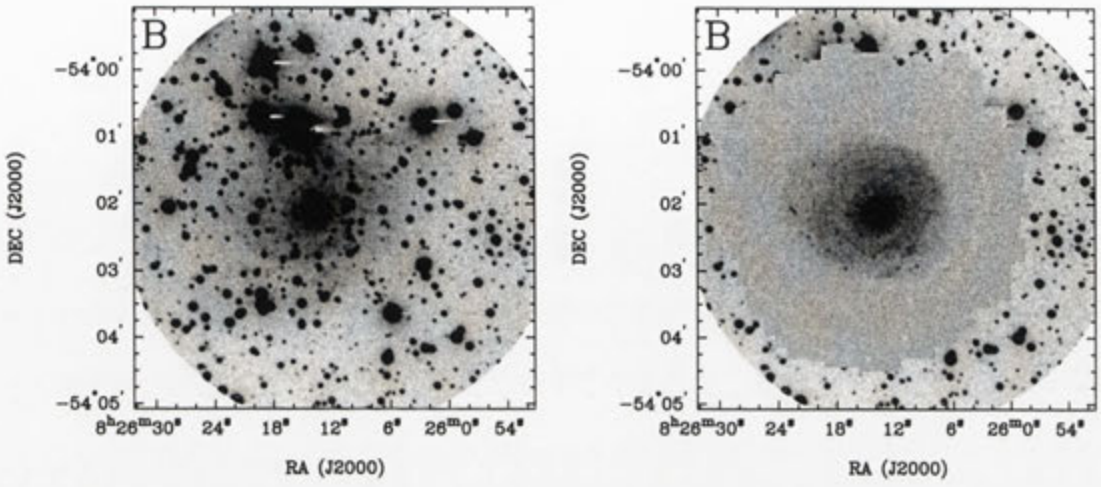

Fig. A.83: Deep B image of ESO 164-G?010 before and after subtraction of the foreground stars.

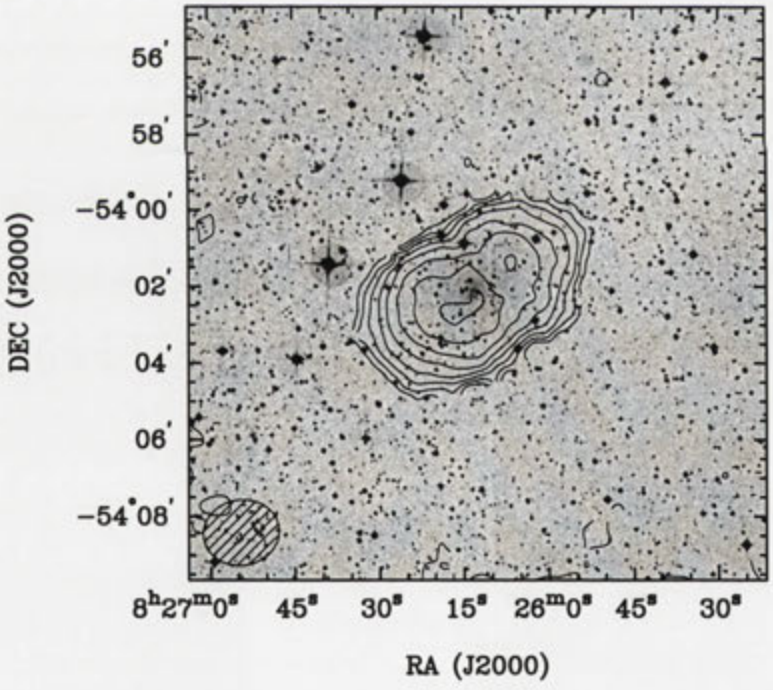

Fig. A.84: Integrated H I intensity distribution of ESO 164-G?010 overlaid onto an optical DSS II R band image. The synthesised beam is displayed in the bottom left corner.

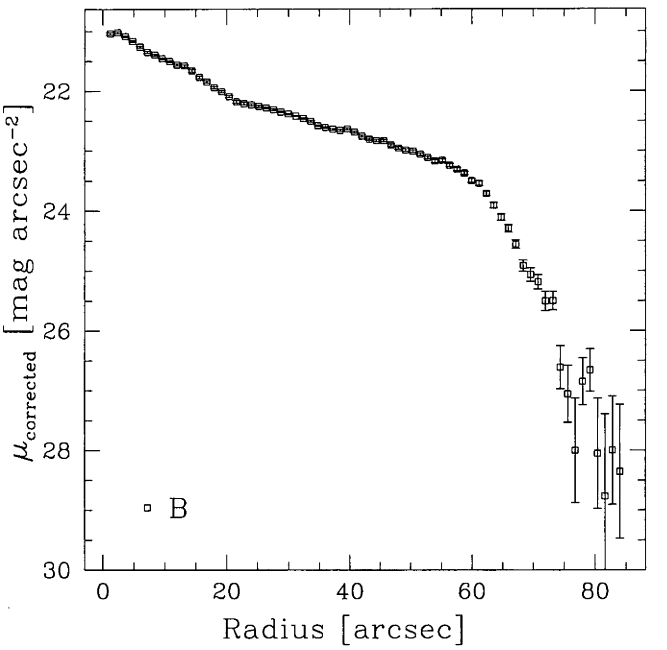

Fig. A.85: *B* surface brightness profile of ESO 164-G?010, corrected for Galactic extinction.

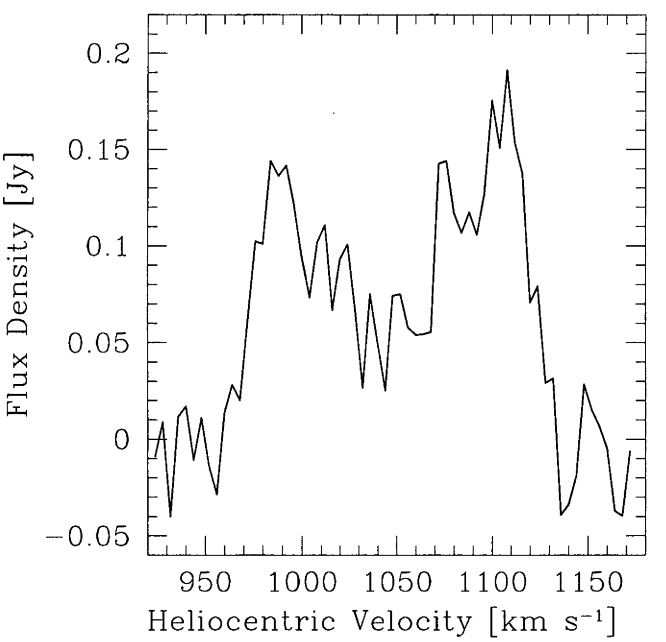

Fig. A.86: Global H I spectra of ESO 164-G?010 as obtained from the ATCA.

ESO 215-G?009

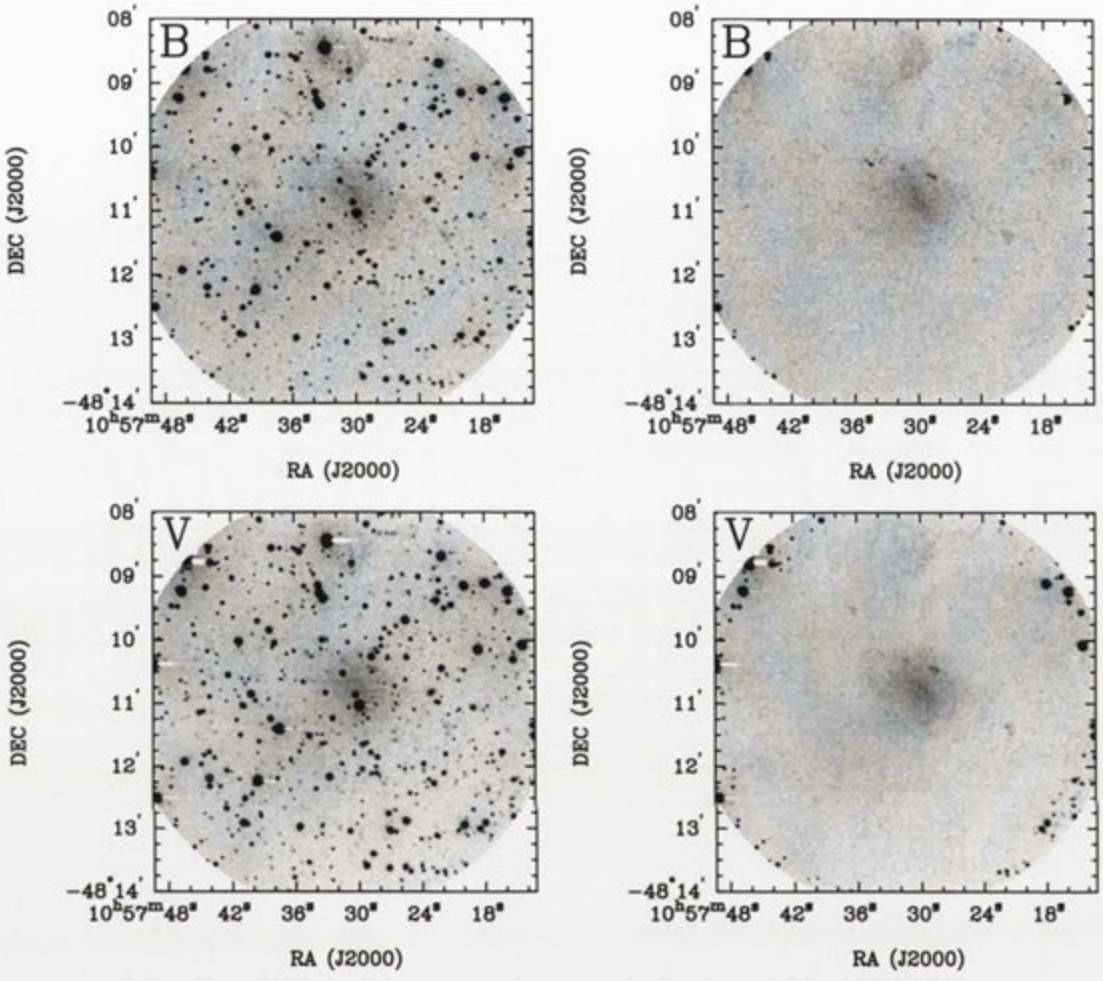

Fig. A.87: Deep *BVRI* images of ESO 215-G?009 before and after subtraction of the foreground stars.

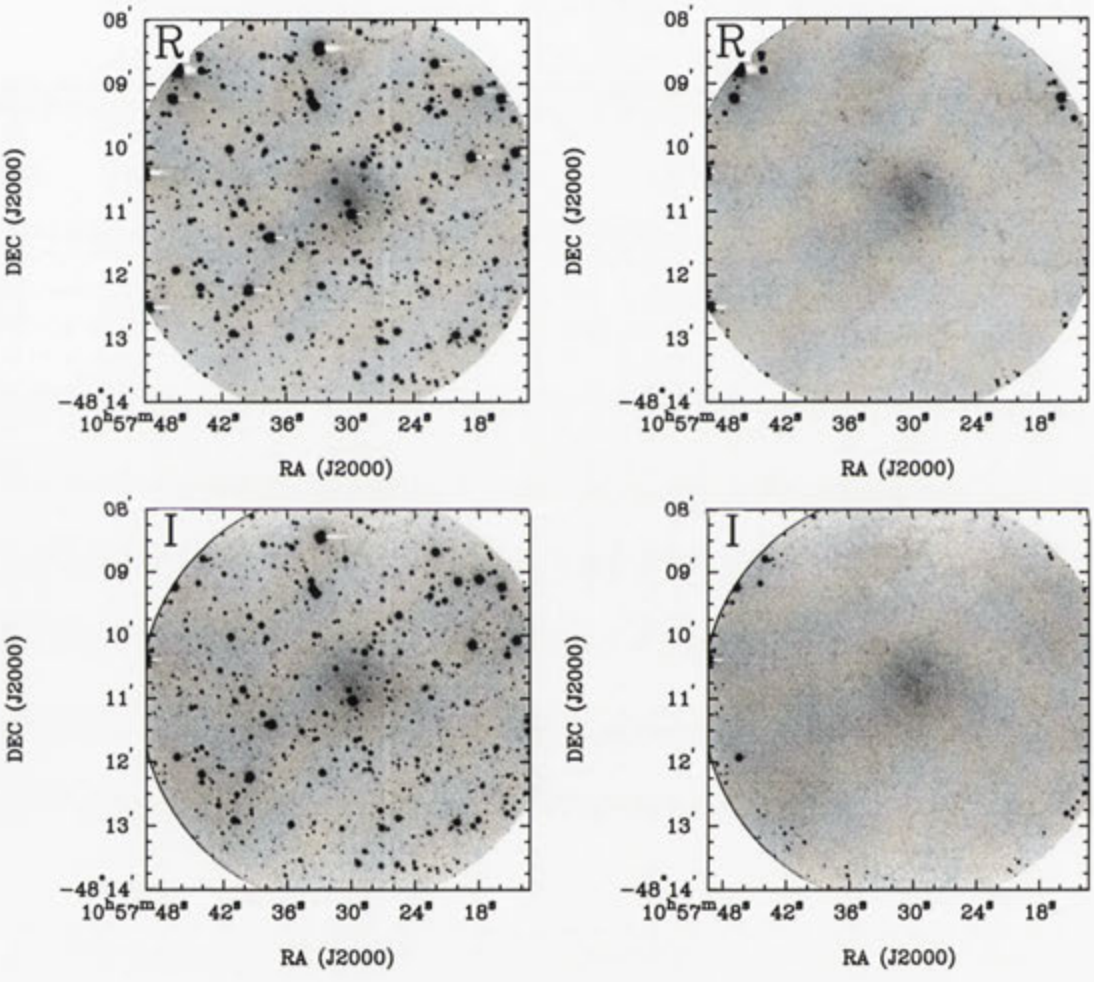

Fig. A.87: continued

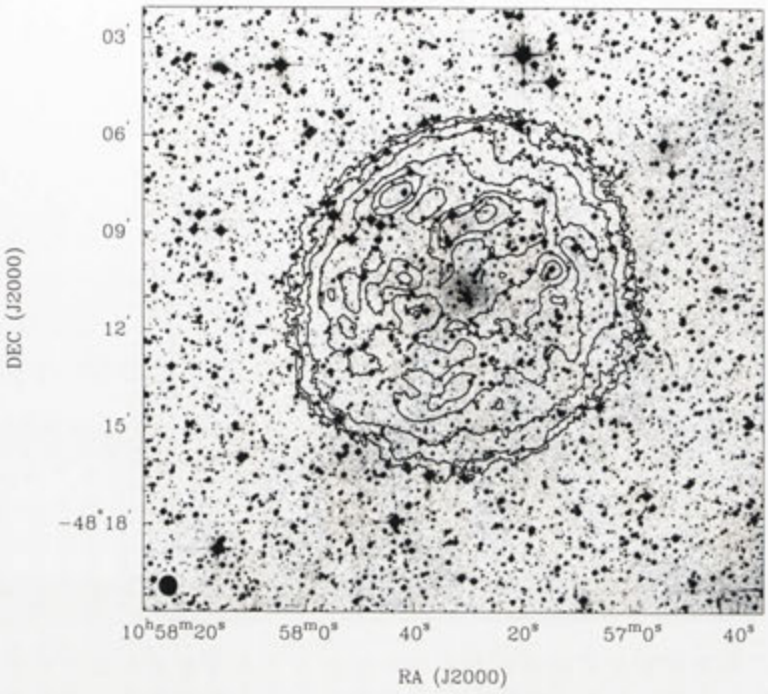

Fig. A.88: Integrated H I intensity distribution of ESO 215-G?009 overlaid onto an optical DSS II *R* band image. The synthesised beam is displayed in the bottom left corner.

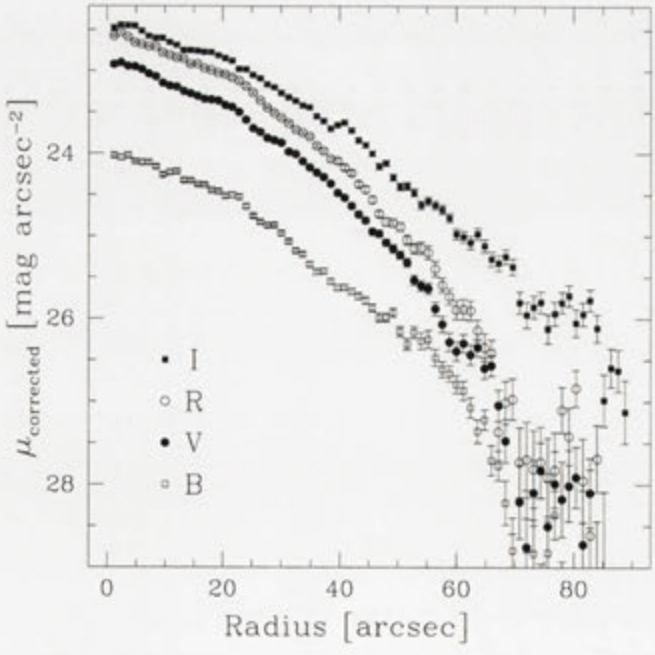

Fig. A.89: *BVRI* surface brightness profiles of ESO 215-G?009, corrected for Galactic extinction.

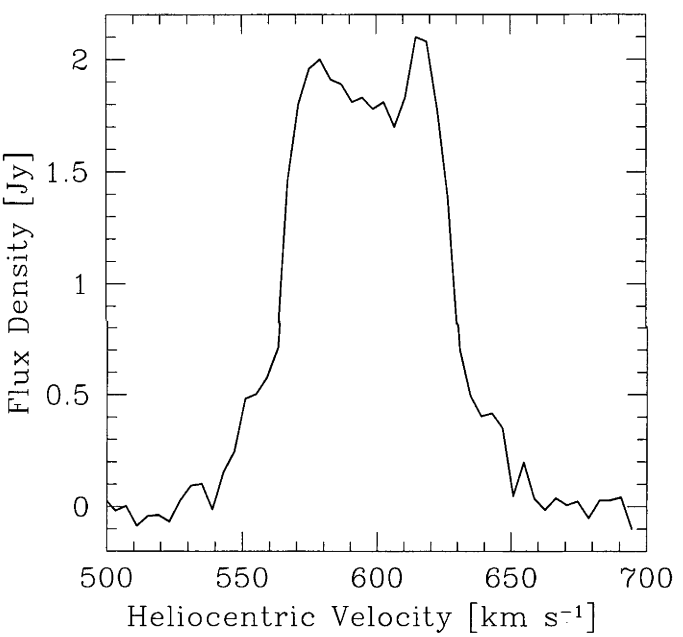

Fig. A.90: Global H I spectra of ESO 215-G?009 as obtained from the ATCA.

CGCG 012-022

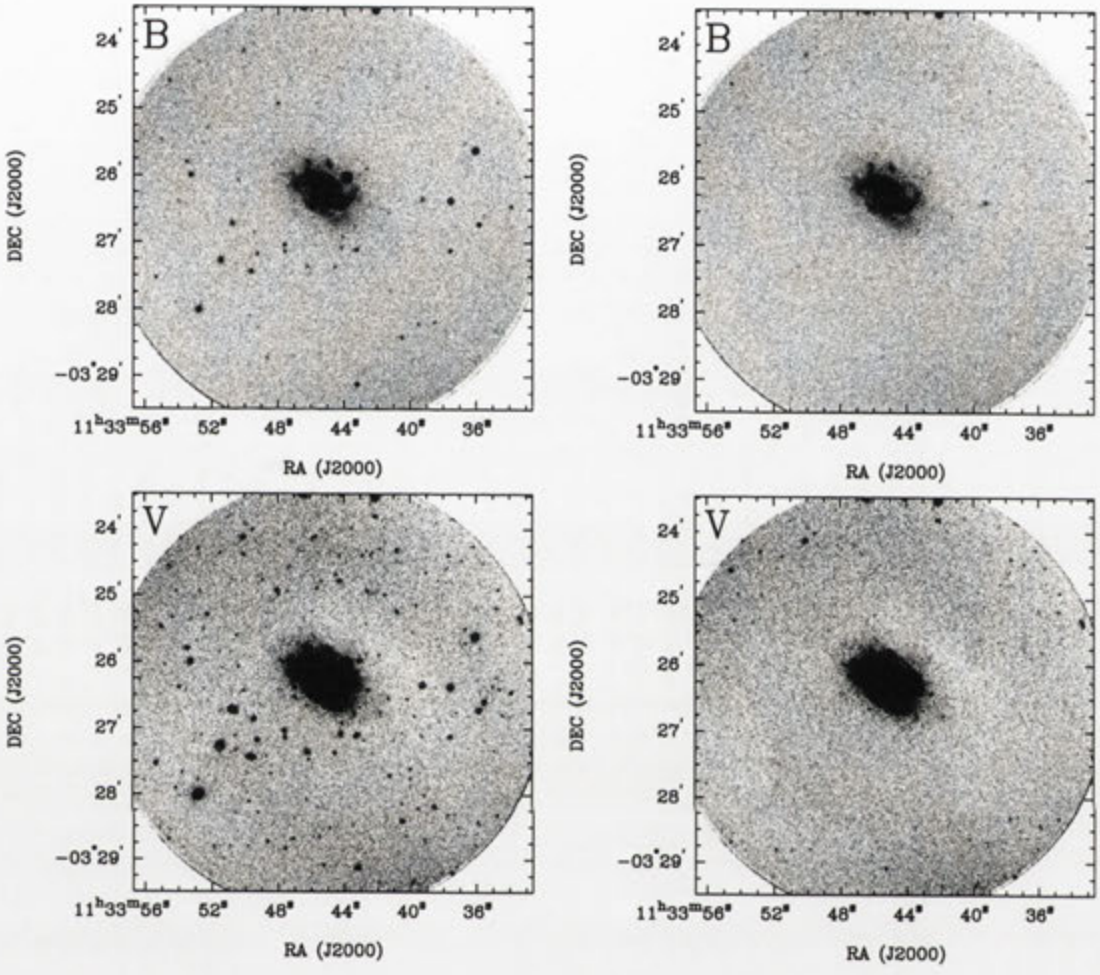

Fig. A.91: Deep *BVRI* images of CGCG 012-022 before and after subtraction of the foreground stars.

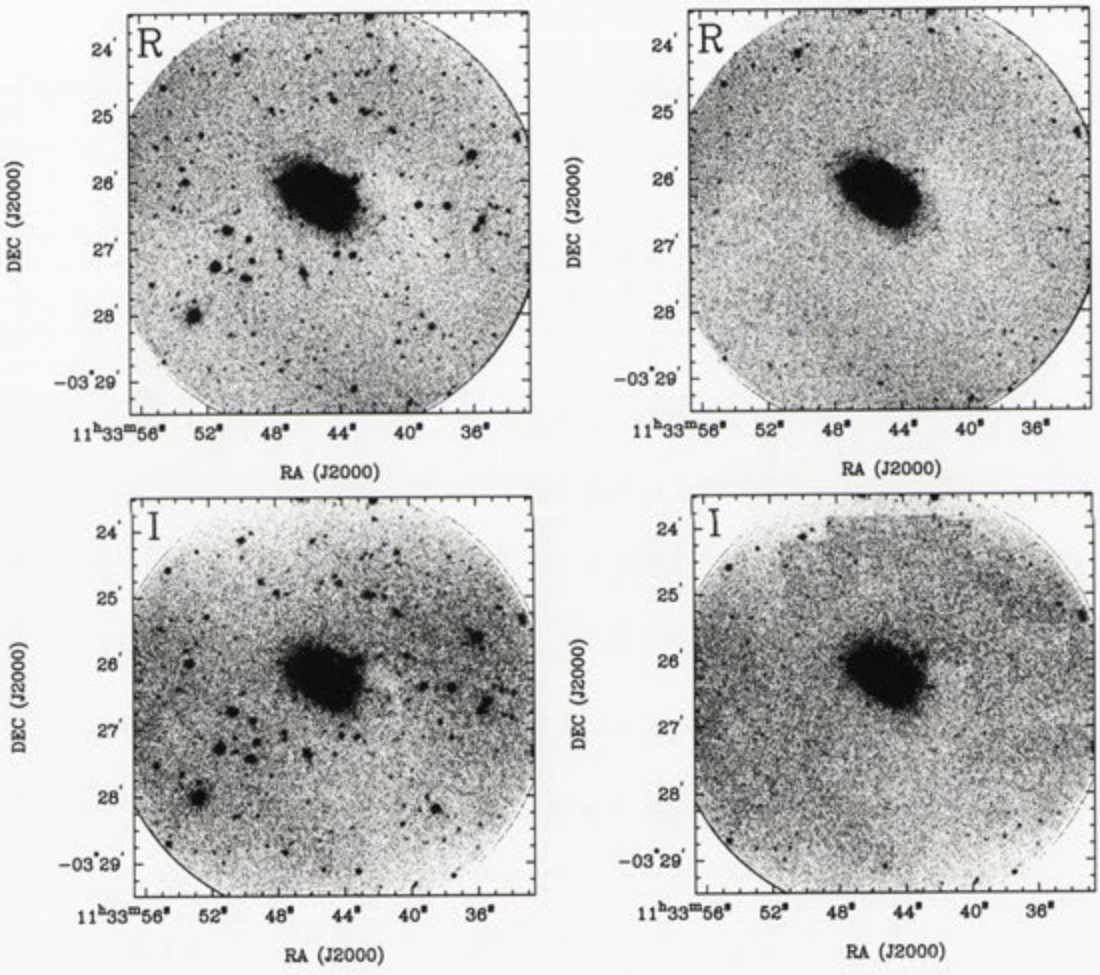

Fig. A.91: continued

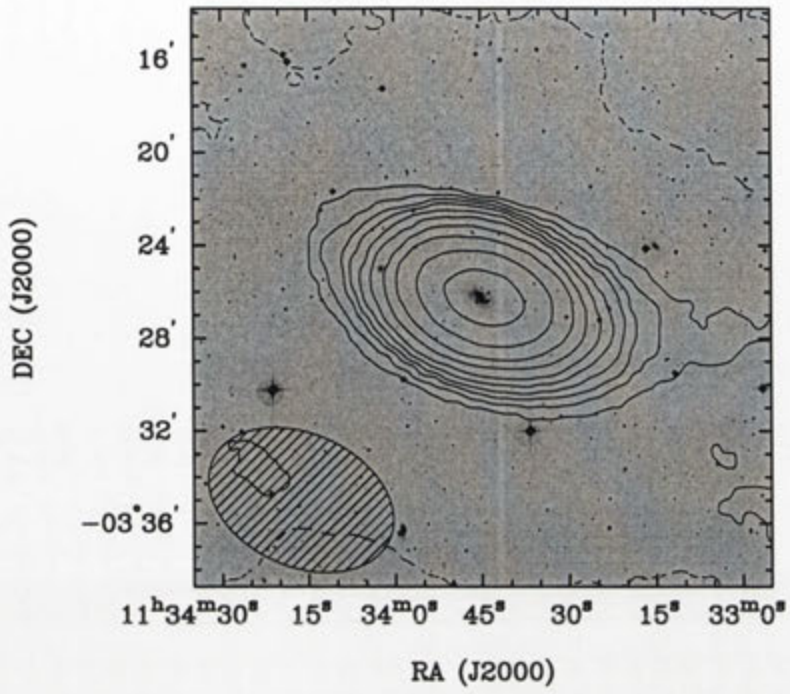

Fig. A.92: Integrated H I intensity distribution of CGCG 012-022 overlaid onto an optical DSS II R band image. The synthesised beam is displayed in the bottom left corner.

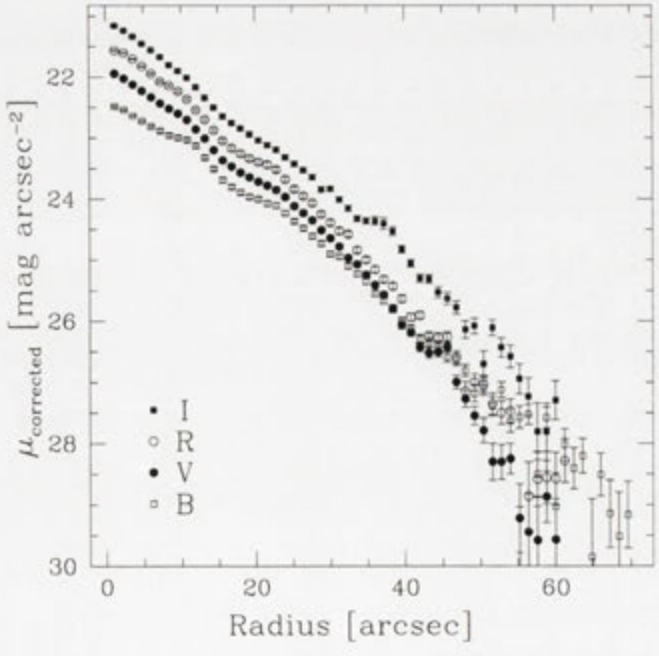

Fig. A.93: *BVRI* surface brightness profiles of CGCG 012-022, corrected for Galactic extinction.

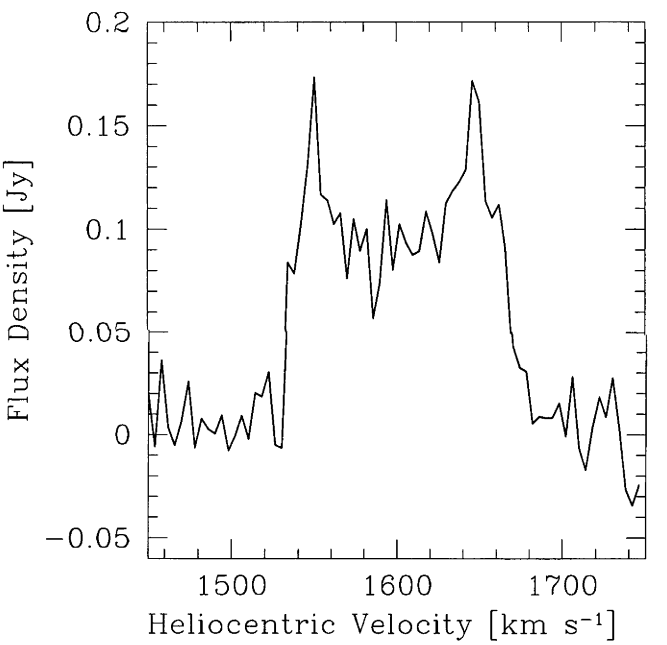

Fig. A.94: Global H I spectra of CGCG 012-022 as obtained from the ATCA.

UGC 06780

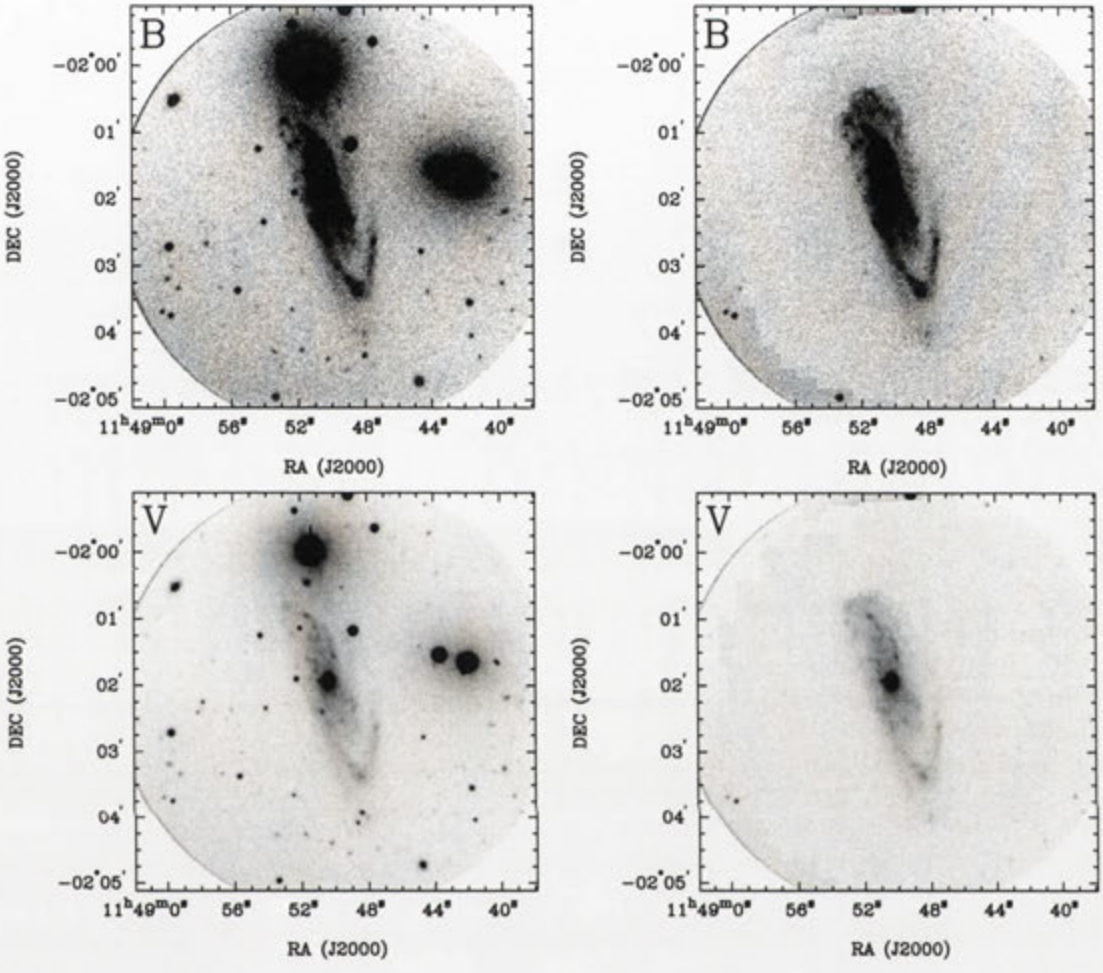

Fig. A.95: Deep *BVRI* images of UGC 06780 before and after subtraction of the foreground stars.

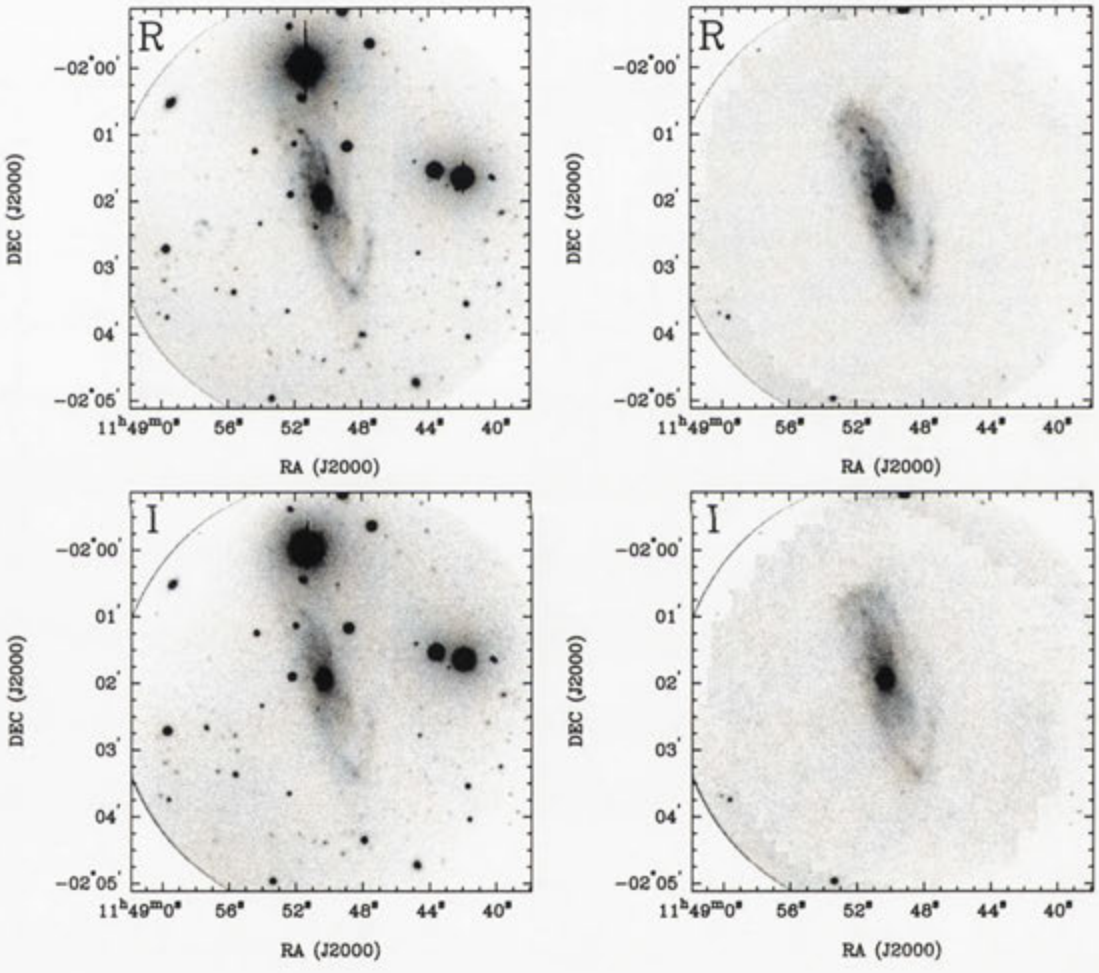

Fig. A.95: continued

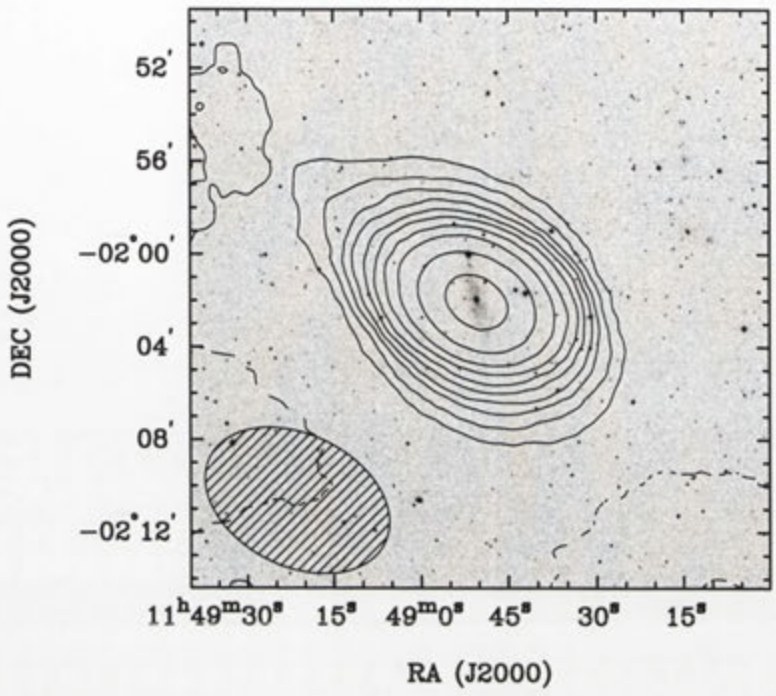

Fig. A.96: Integrated H I intensity distribution of UGC 06780 overlaid onto an optical DSS II R band image. The synthesised beam is displayed in the bottom left corner.

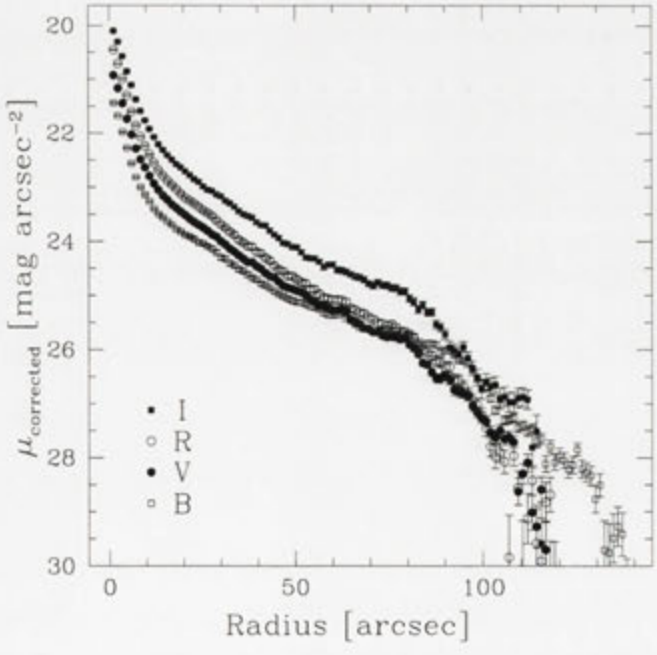

Fig. A.97: *BVRI* surface brightness profiles of UGC 06780, corrected for Galactic extinction.

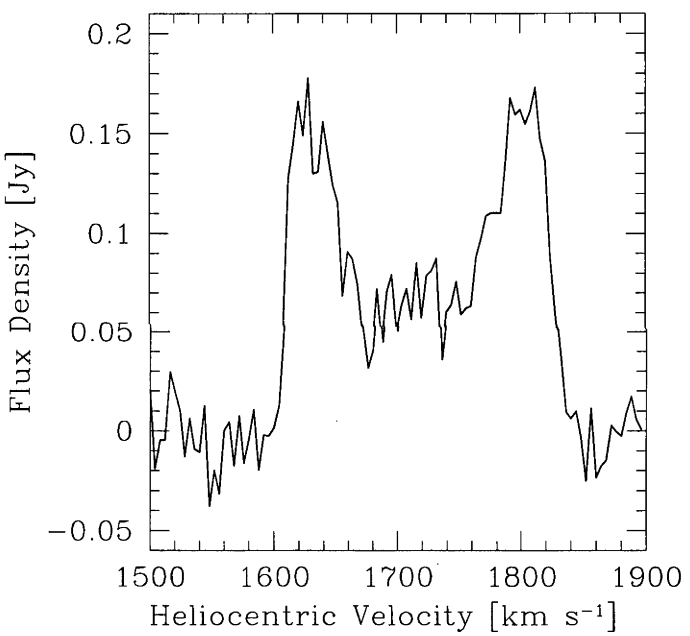

Fig. A.98: Global H I spectra of UGC 06780 as obtained from the ATCA.

ESO 572-G009

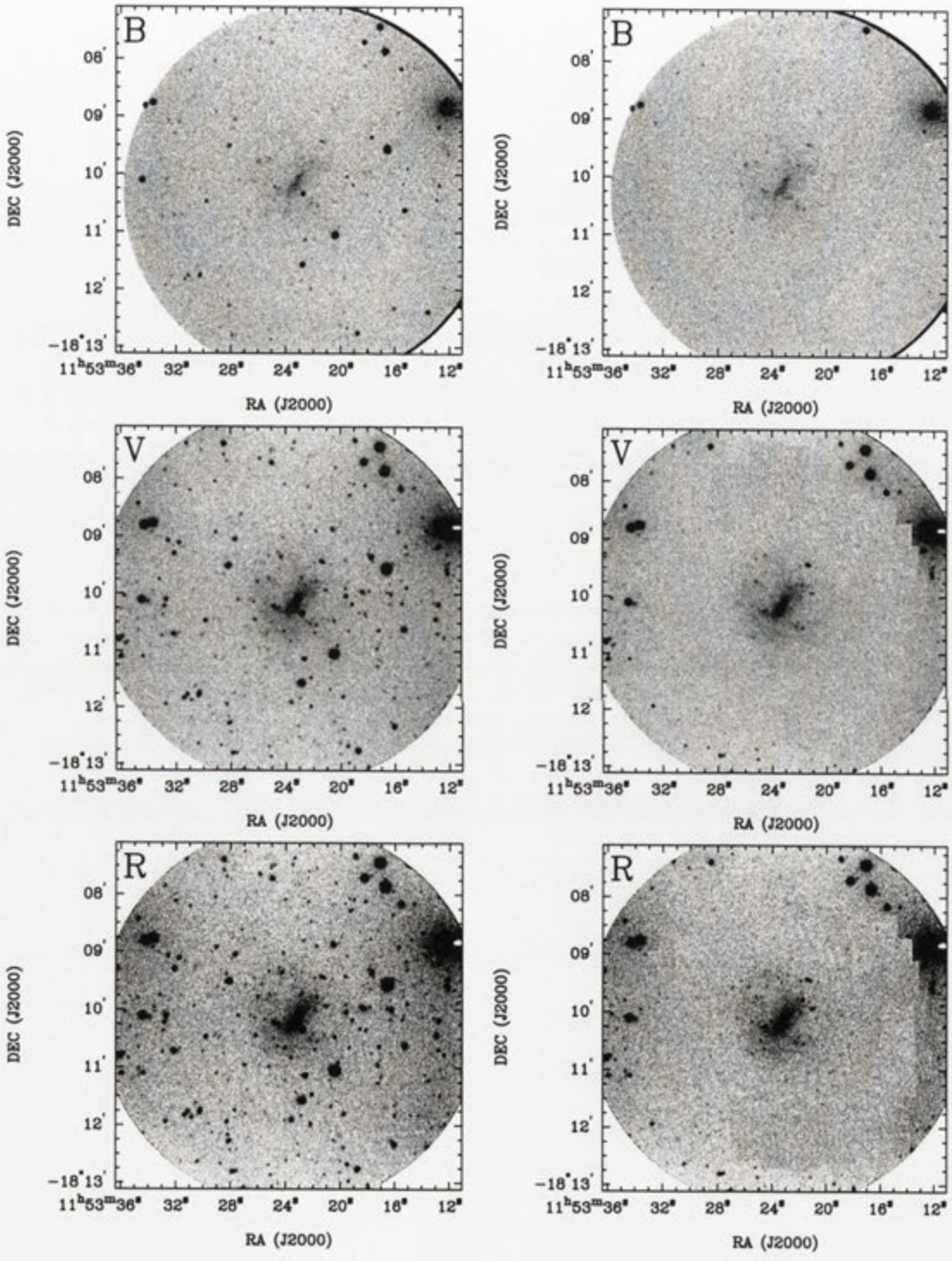

Fig. A.99: Deep *BVR* images of ESO 572-G009 before and after subtraction of the foreground stars.

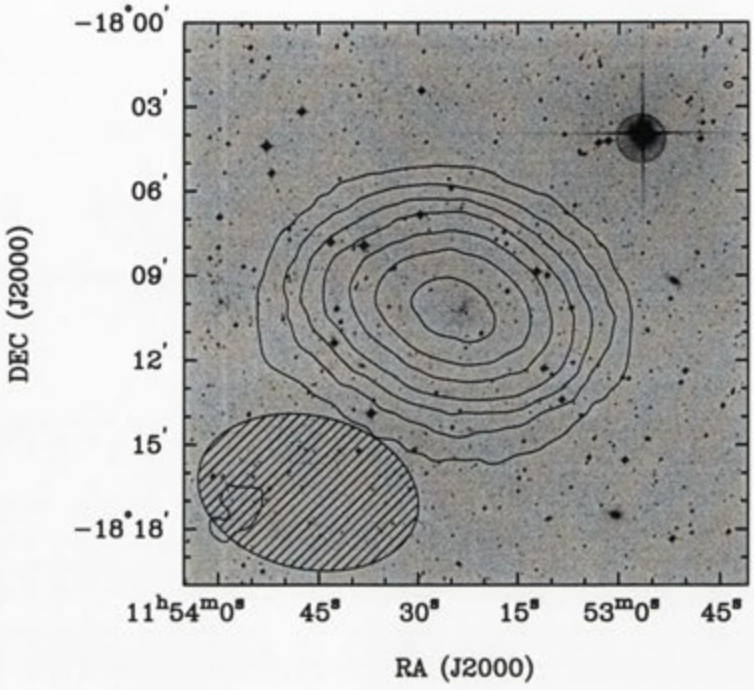

Fig. A.100: Integrated H I intensity distribution of ESO 572-G009 overlaid onto an optical DSS II R band image. The synthesised beam is displayed in the bottom left corner.

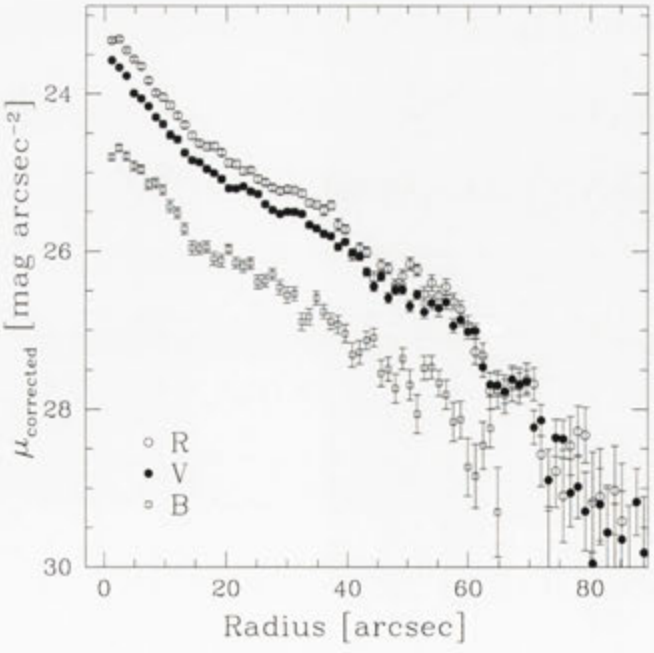

Fig. A.101: *BVR* surface brightness profiles of ESO 572-G009, corrected for Galactic extinction.

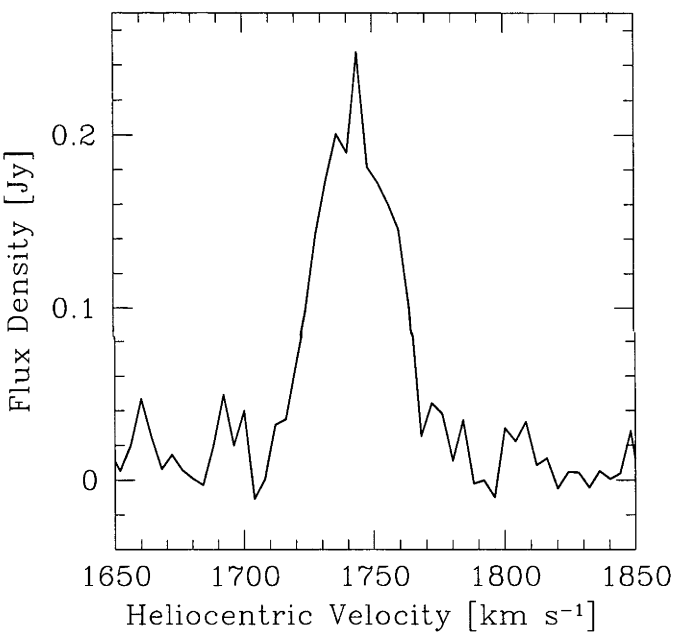

Fig. A.102: Global H I spectra of ESO 572-G009 as obtained from the ATCA.

ESO 505-G007

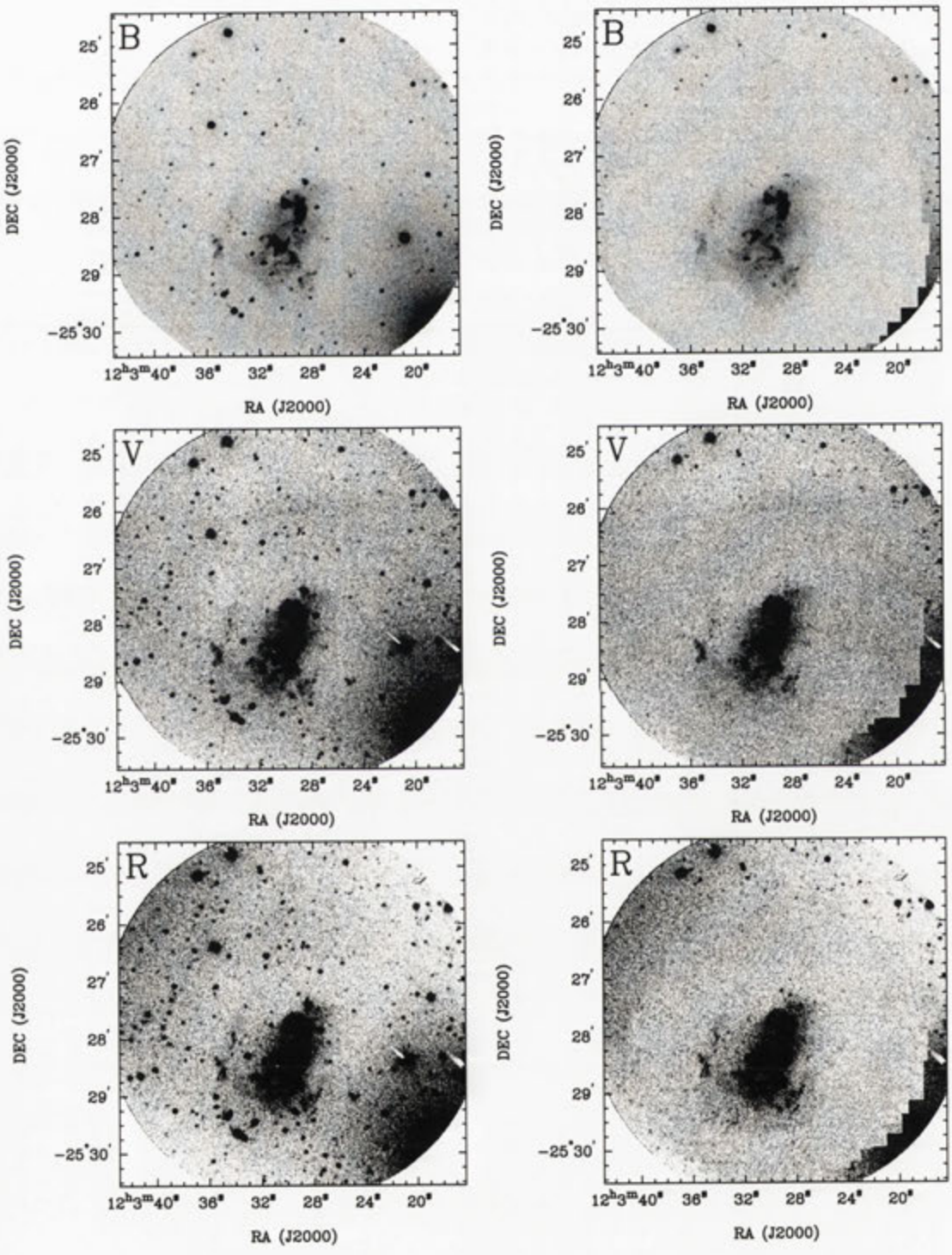

Fig. A.103: Deep *BVR* images of ESO 505-G007 before and after subtraction of the foreground stars.

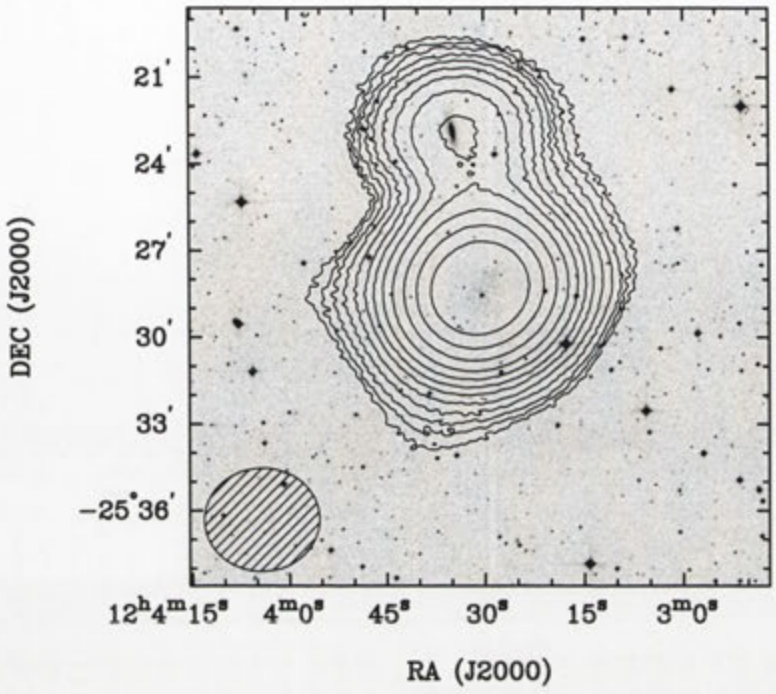

Fig. A.104: Integrated H I intensity distribution of ESO 505-G007 overlaid onto an optical DSS II R band image. The synthesised beam is displayed in the bottom left corner.

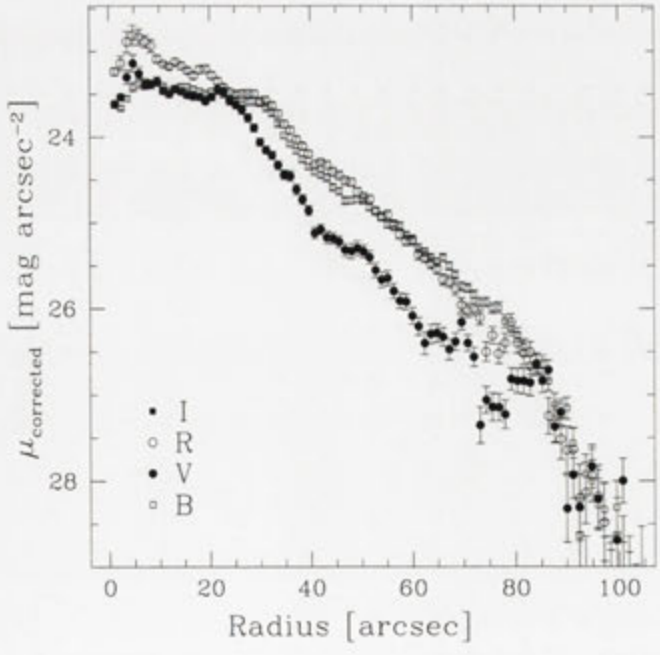

Fig. A.105: BVR surface brightness profiles of ESO 505-G007, corrected for Galactic extinction.

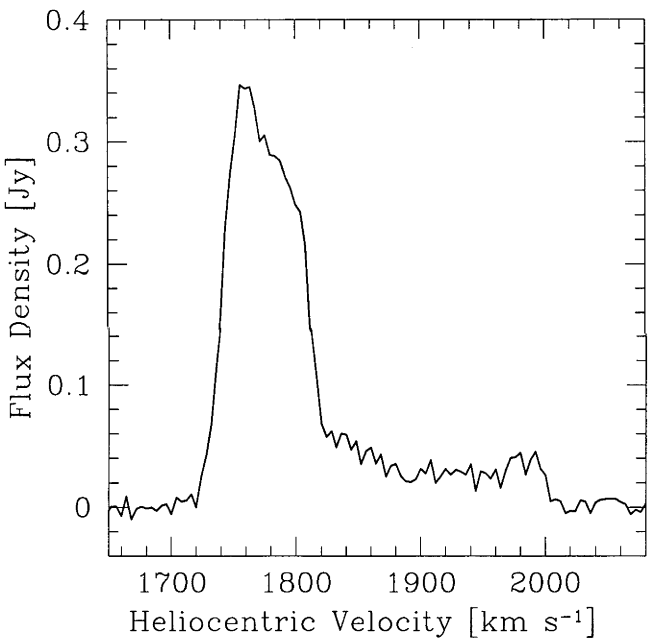

Fig. A.106: Global H I spectra of ESO 505-G007 as obtained from the ATCA.

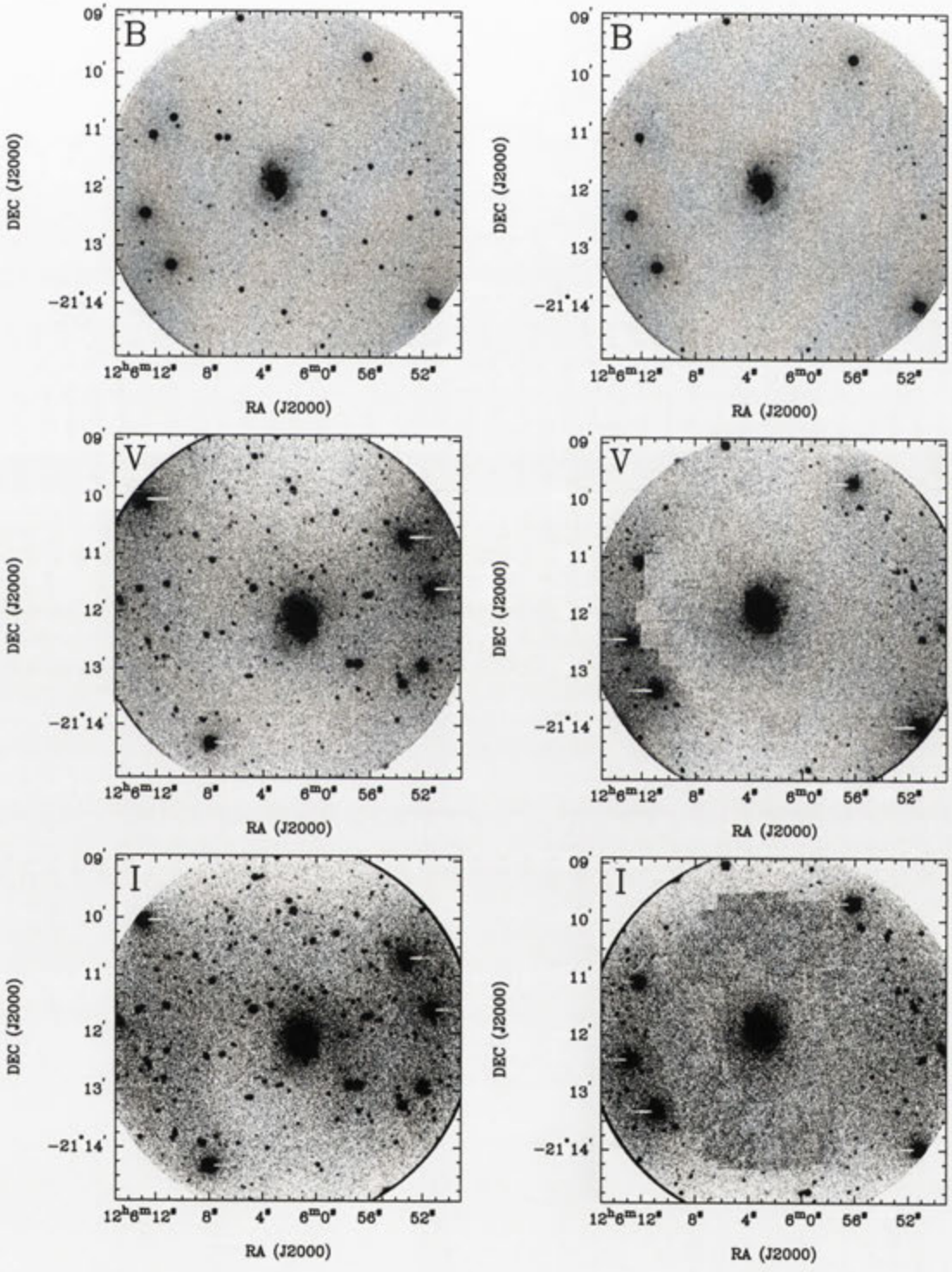

Fig. A.107: Deep *BVI* images of ESO 572-G052 before and after subtraction of the foreground stars.

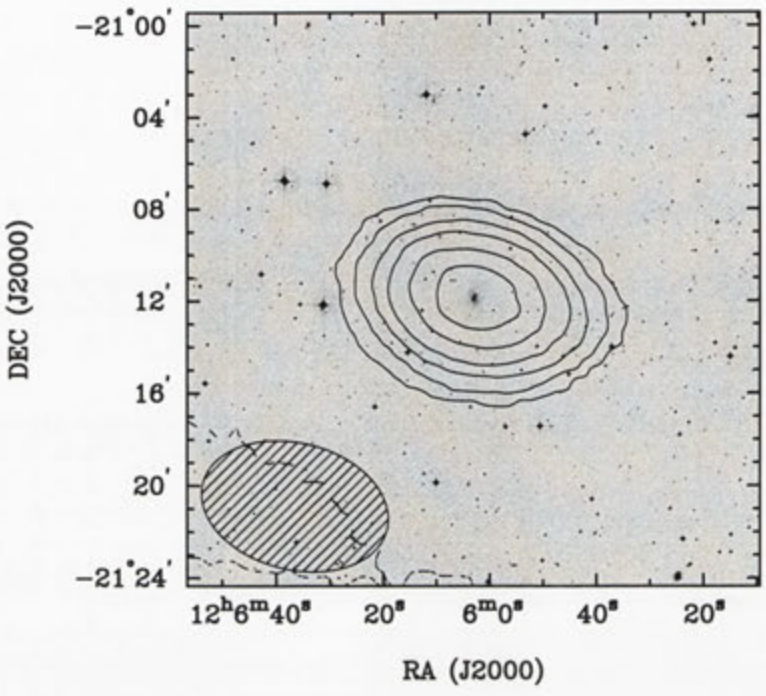

Fig. A.108: Integrated H I intensity distribution of ESO 572-G052 overlaid onto an optical DSS II R band image. The synthesised beam is displayed in the bottom left corner.

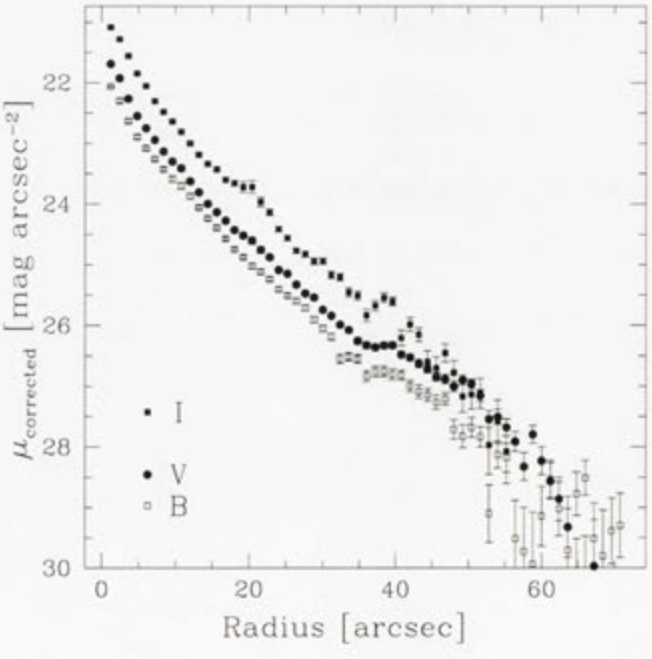

Fig. A.109: BVI surface brightness profiles of ESO 572-G052, corrected for Galactic extinction.

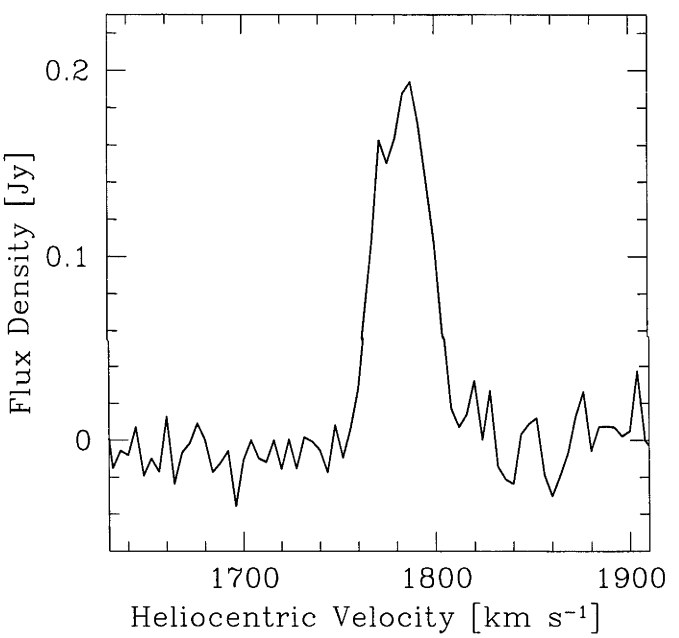

Fig. A.110: Global H I spectra of ESO 572-G052 as obtained from the ATCA.

UGCA 289

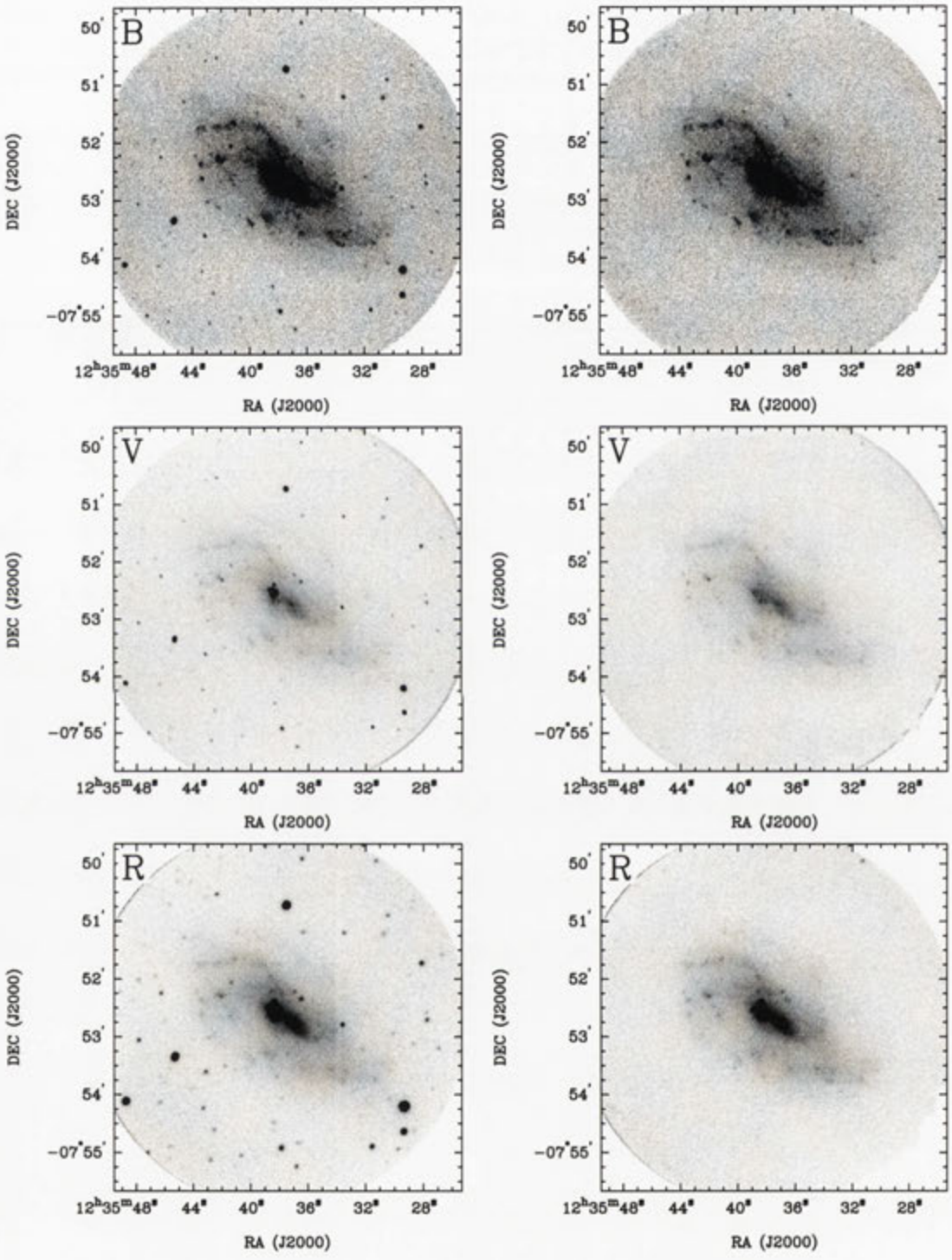

Fig. A.111: Deep *BVR* images of UGCA 289 before and after subtraction of the foreground stars.

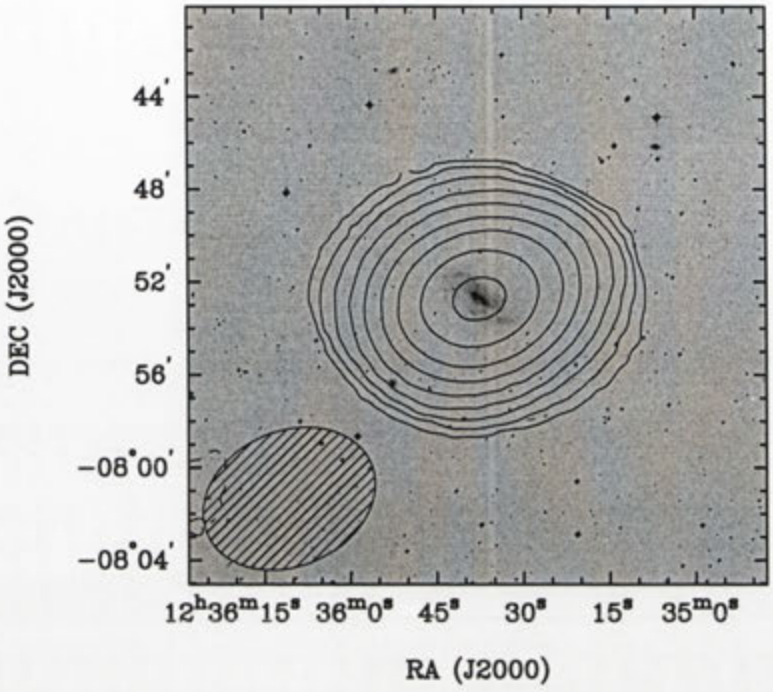

Fig. A.112: Integrated H I intensity distribution of UGCA 289 overlaid onto an optical DSS II R band image. The synthesised beam is displayed in the bottom left corner.

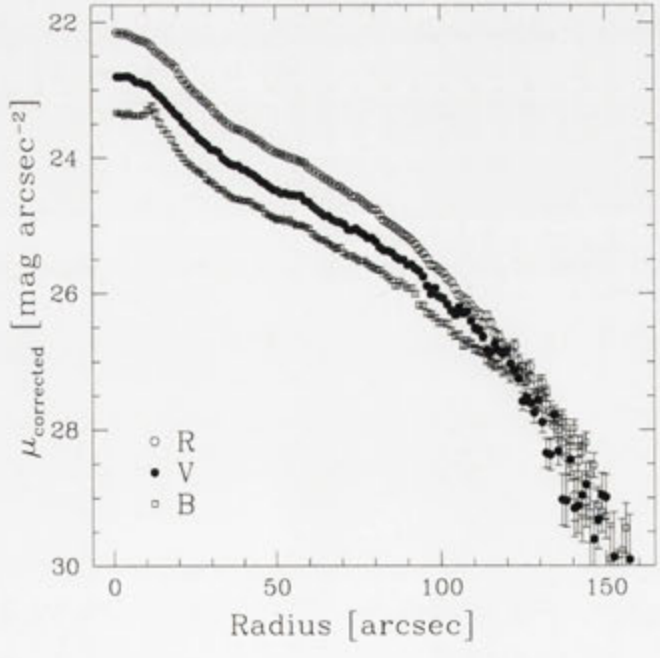

Fig. A.113: BVR surface brightness profiles of UGCA 289, corrected for Galactic extinction.

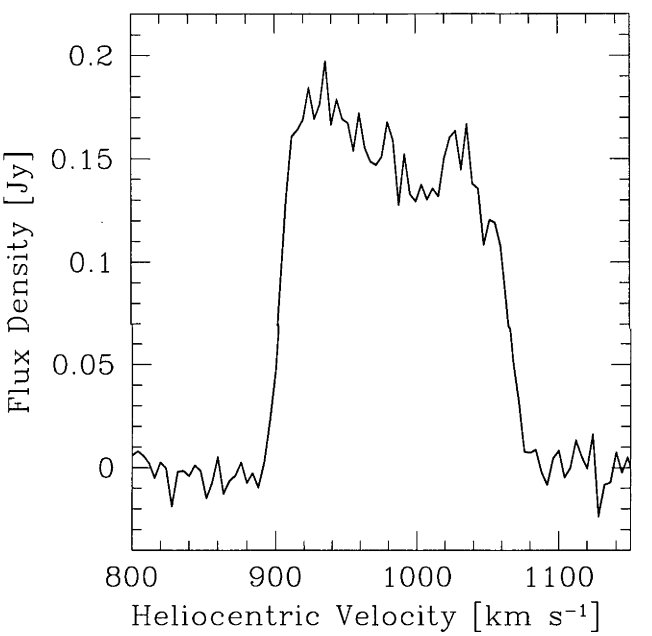

Fig. A.114: Global H I spectra of UGCA 289 as obtained from the ATCA.

UGCA 307

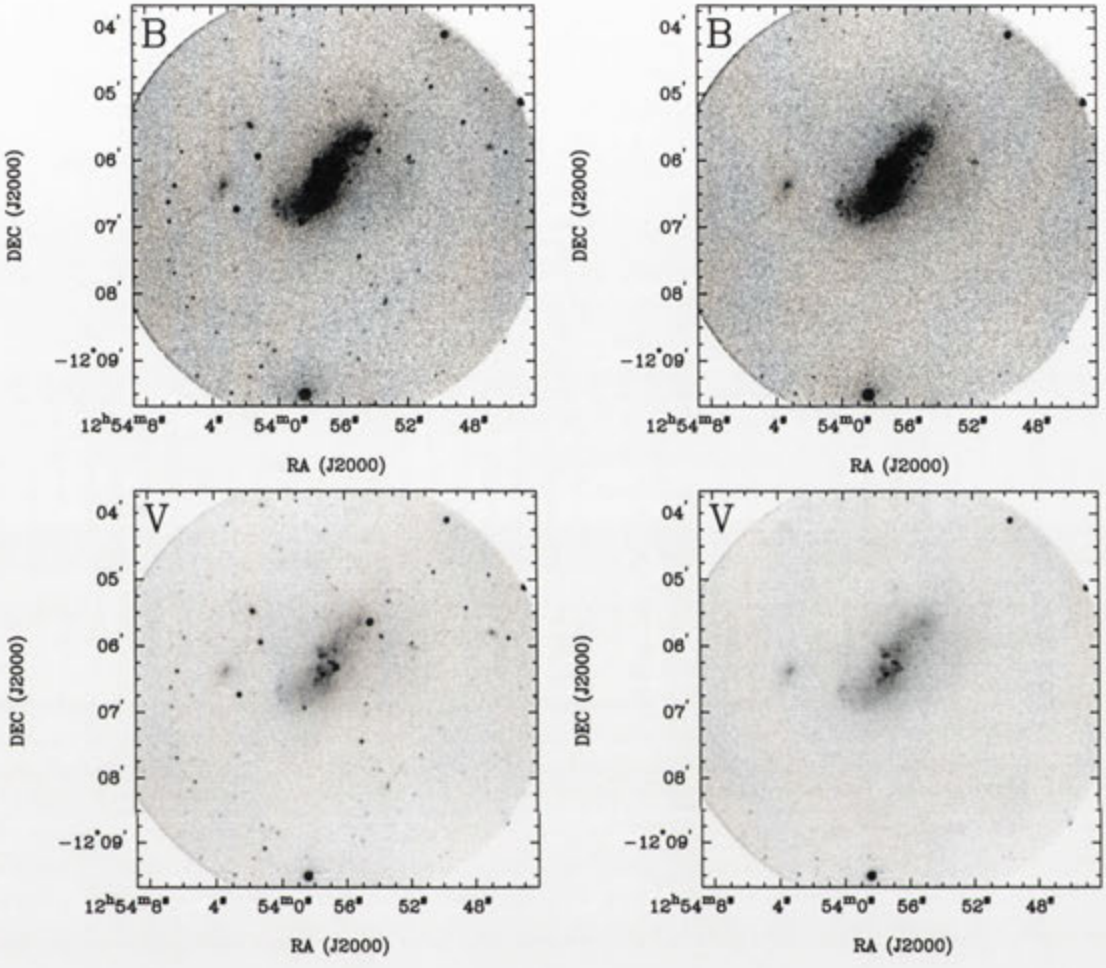

Fig. A.115: Deep *BVRI* images of UGCA 307 before and after subtraction of the foreground stars.

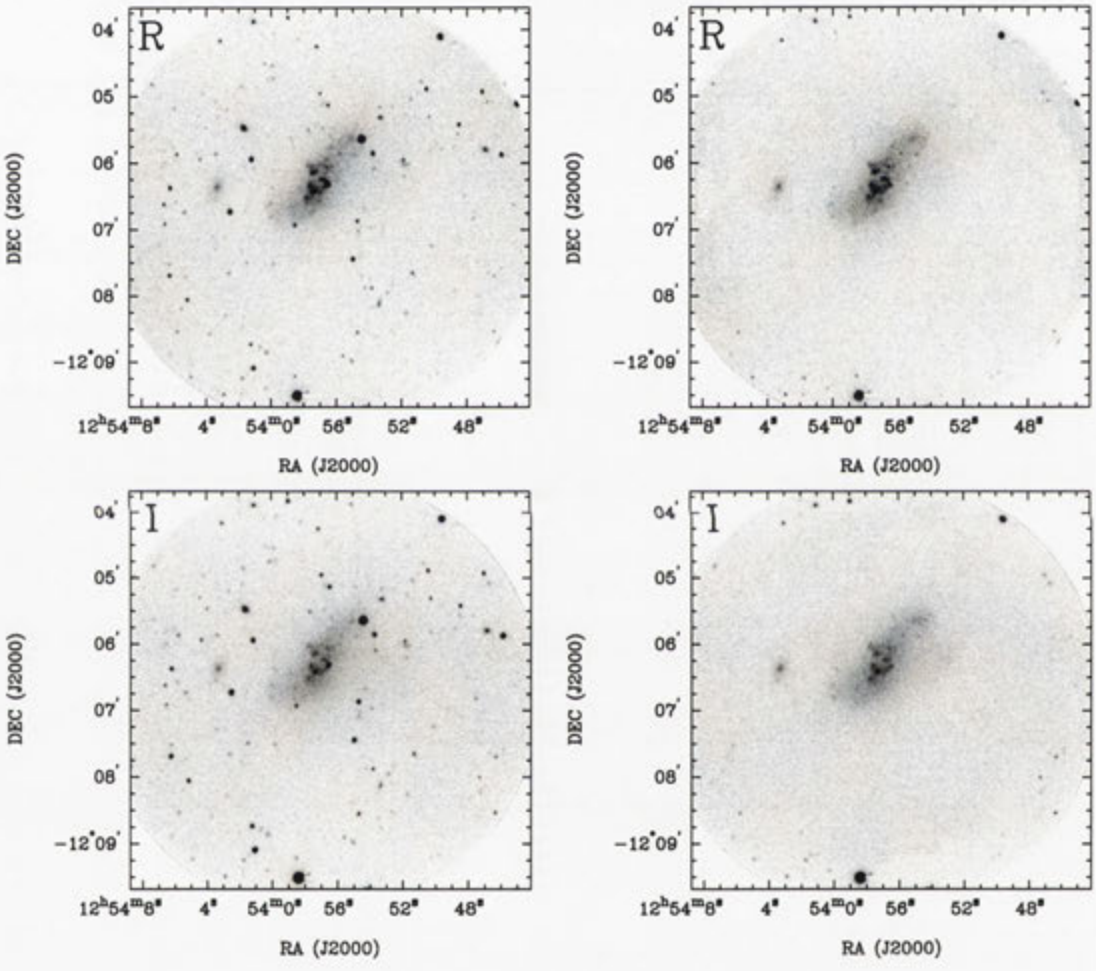

Fig. A.115: continued

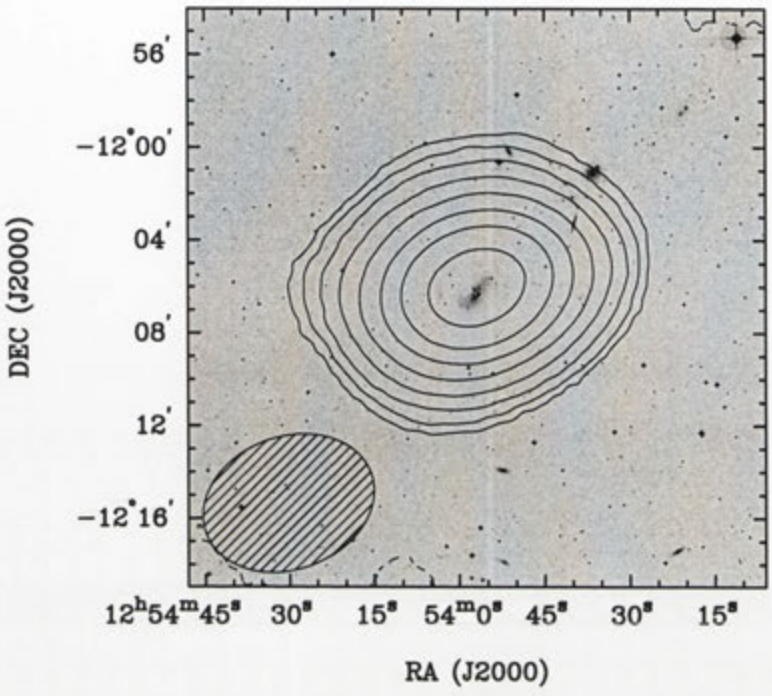

Fig. A.116: Integrated H I intensity distribution of UGCA 307 overlaid onto an optical DSS II R band image. The synthesised beam is displayed in the bottom left corner.

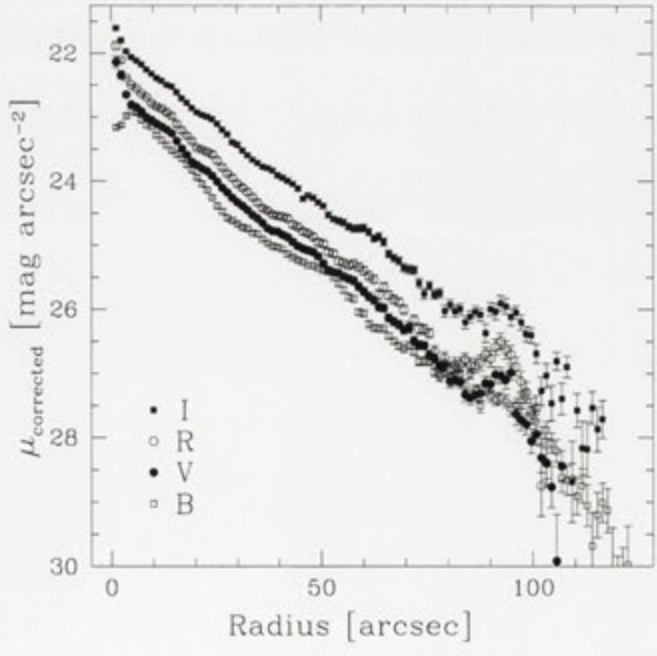

Fig. A.117: *BVRI* surface brightness profiles of UGCA 307, corrected for Galactic extinction.

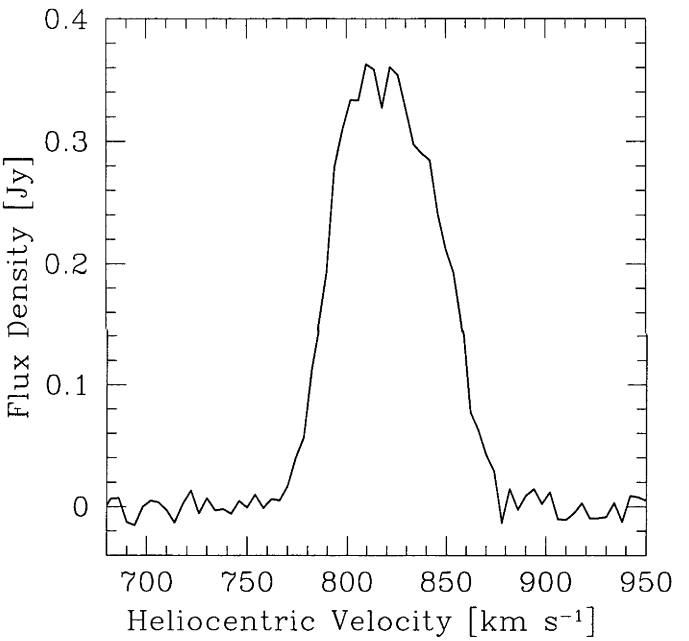

Fig. A.118: Global H I spectra of UGCA 307 as obtained from the ATCA.

UGCA 312

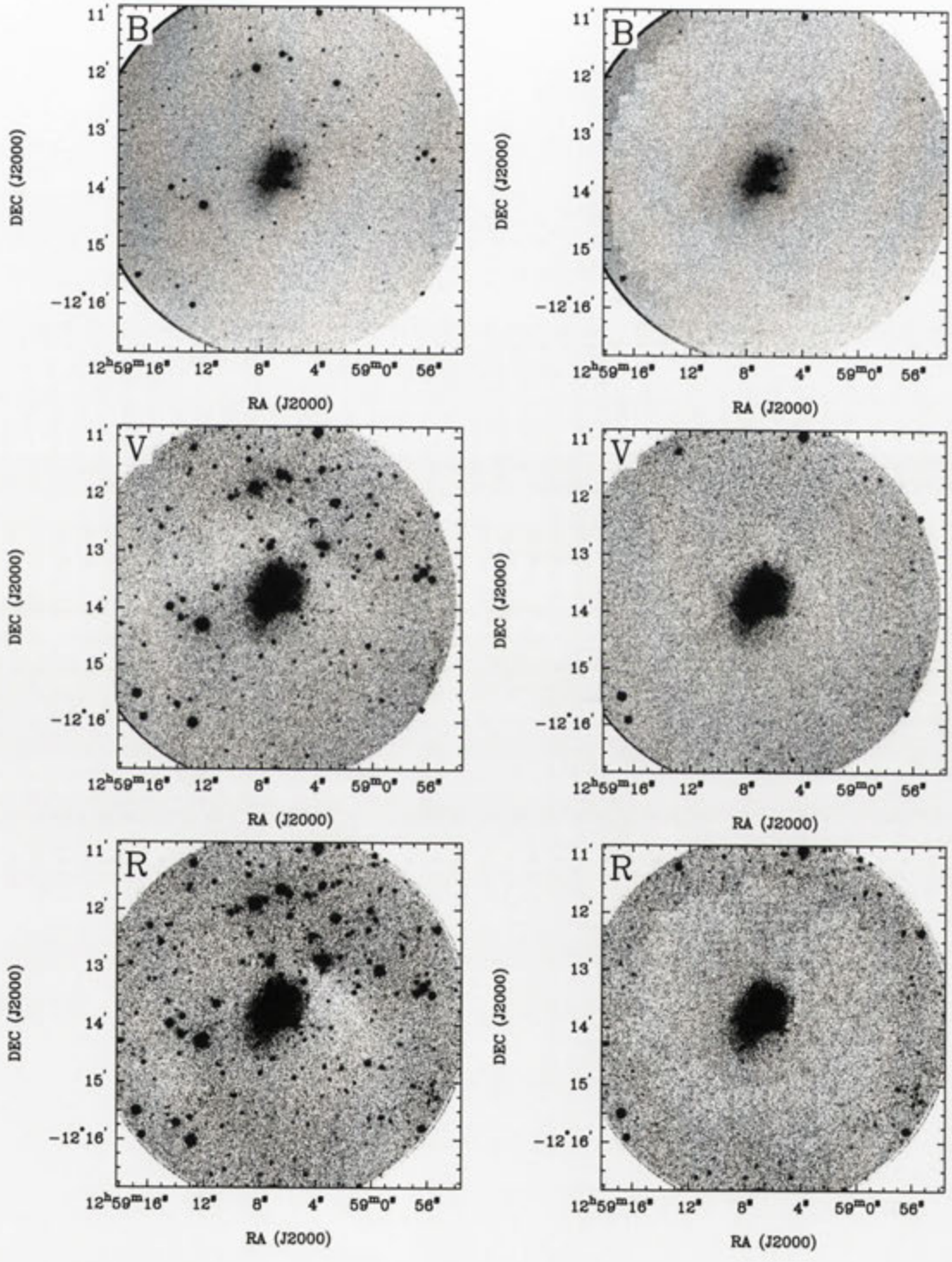

Fig. A.119: Deep *BVR* images of UGCA 312 before and after subtraction of the foreground stars.

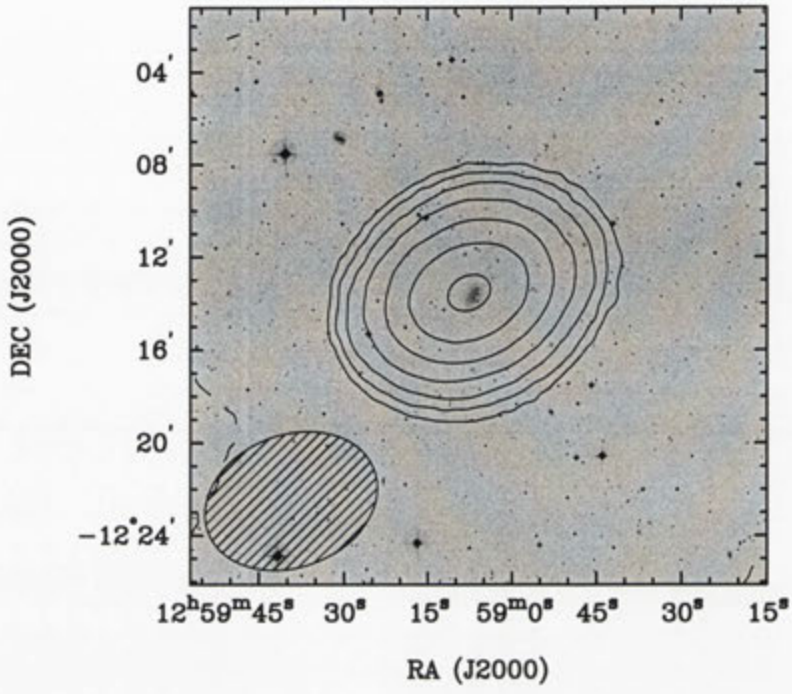

Fig. A.120: Integrated H I intensity distribution of UGCA 312 overlaid onto an optical DSS II R band image. The synthesised beam is displayed in the bottom left corner.

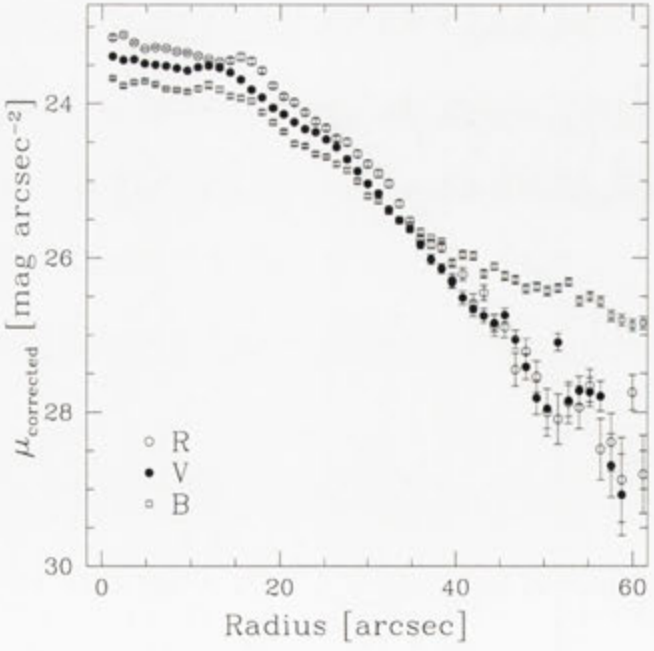

Fig. A.121: BVR surface brightness profiles of UGCA 312, corrected for Galactic extinction.

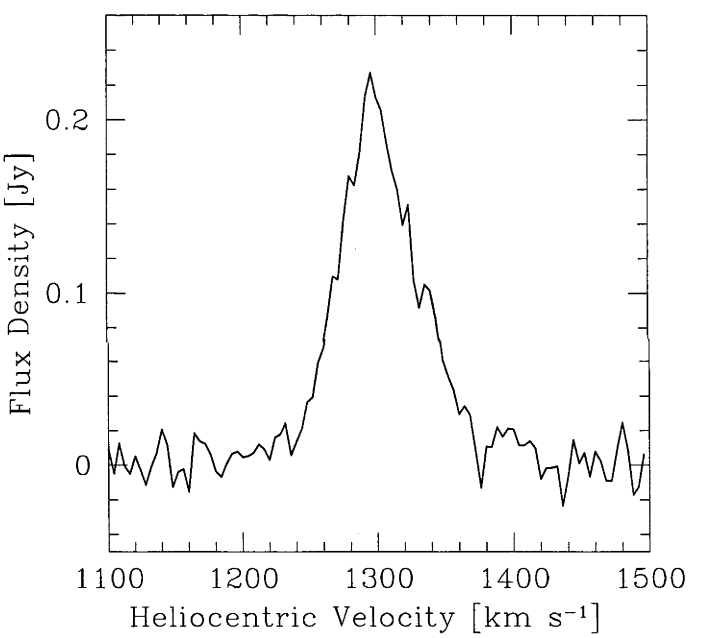

Fig. A.122: Global H I spectra of UGCA 312 as obtained from the ATCA.

UGCA 322

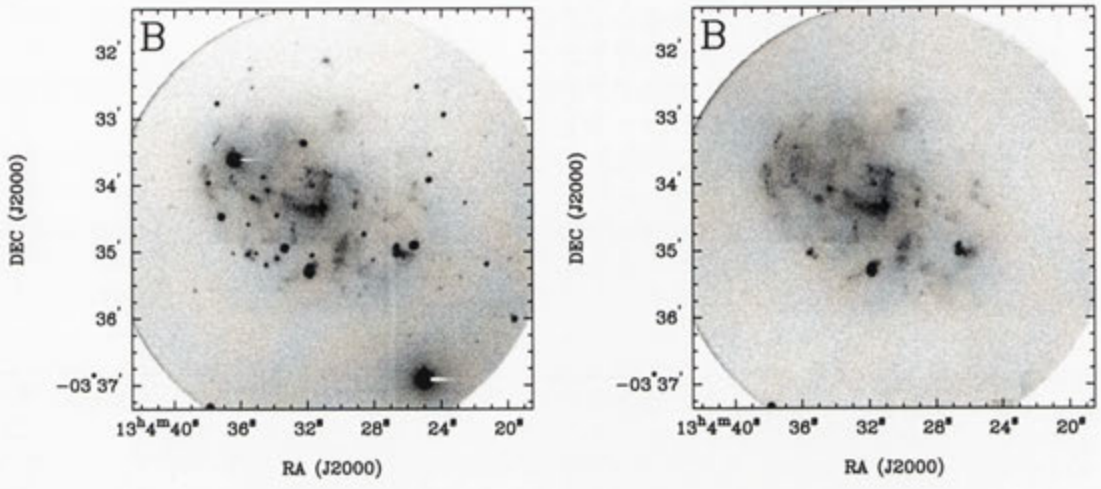

Fig. A.123: Deep B image of UGCA 322 before and after subtraction of the foreground stars.

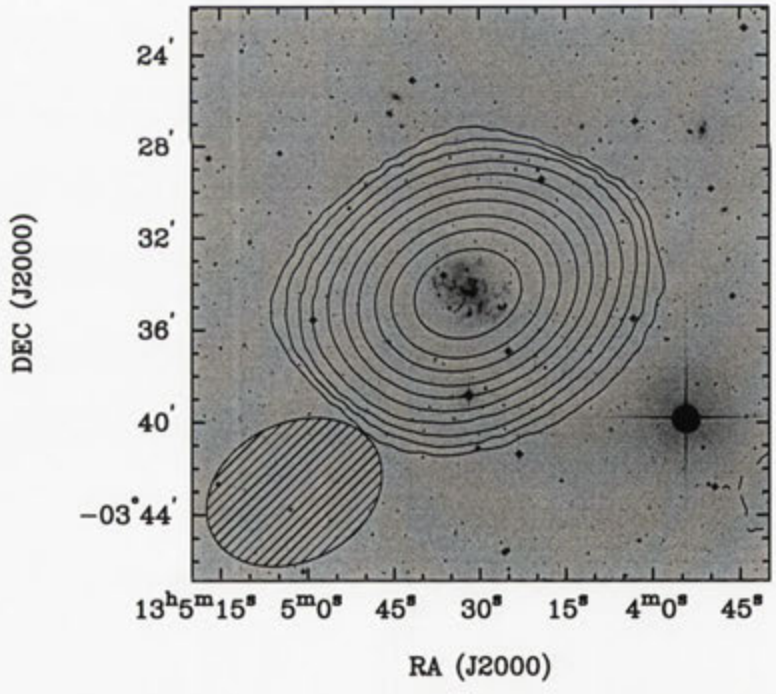

Fig. A.124: Integrated H I intensity distribution of UGCA 322 overlaid onto an optical DSS II R band image. The synthesised beam is displayed in the bottom left corner.

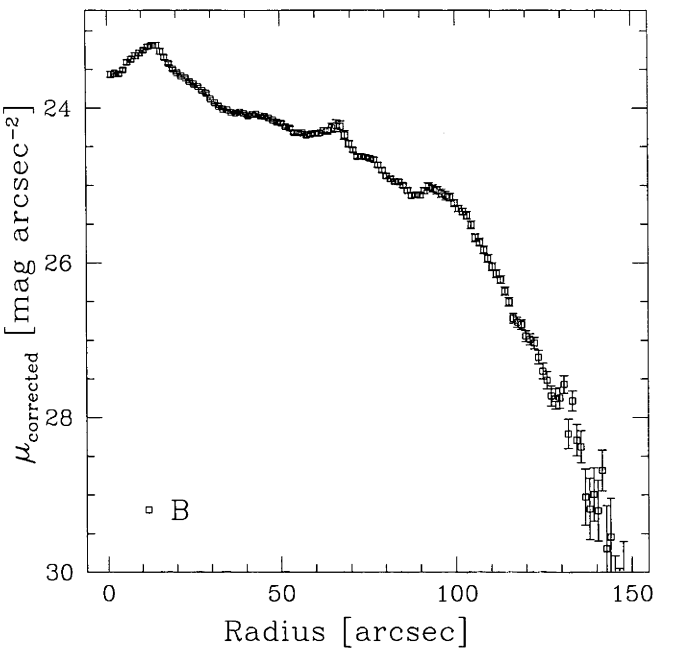

Fig. A.125: *B* surface brightness profile of UGCA 322, corrected for Galactic extinction.

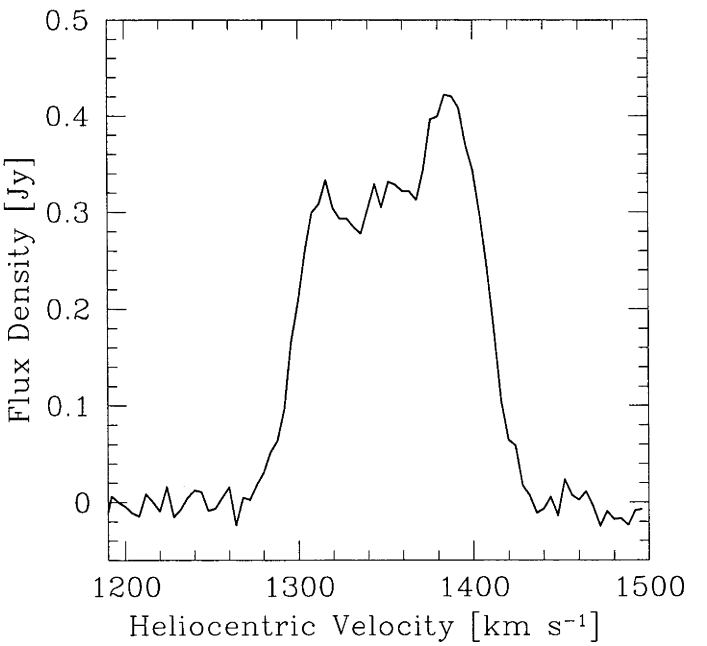

Fig. A.126: Global H I spectra of UGCA 322 as obtained from the ATCA.

IC 4212

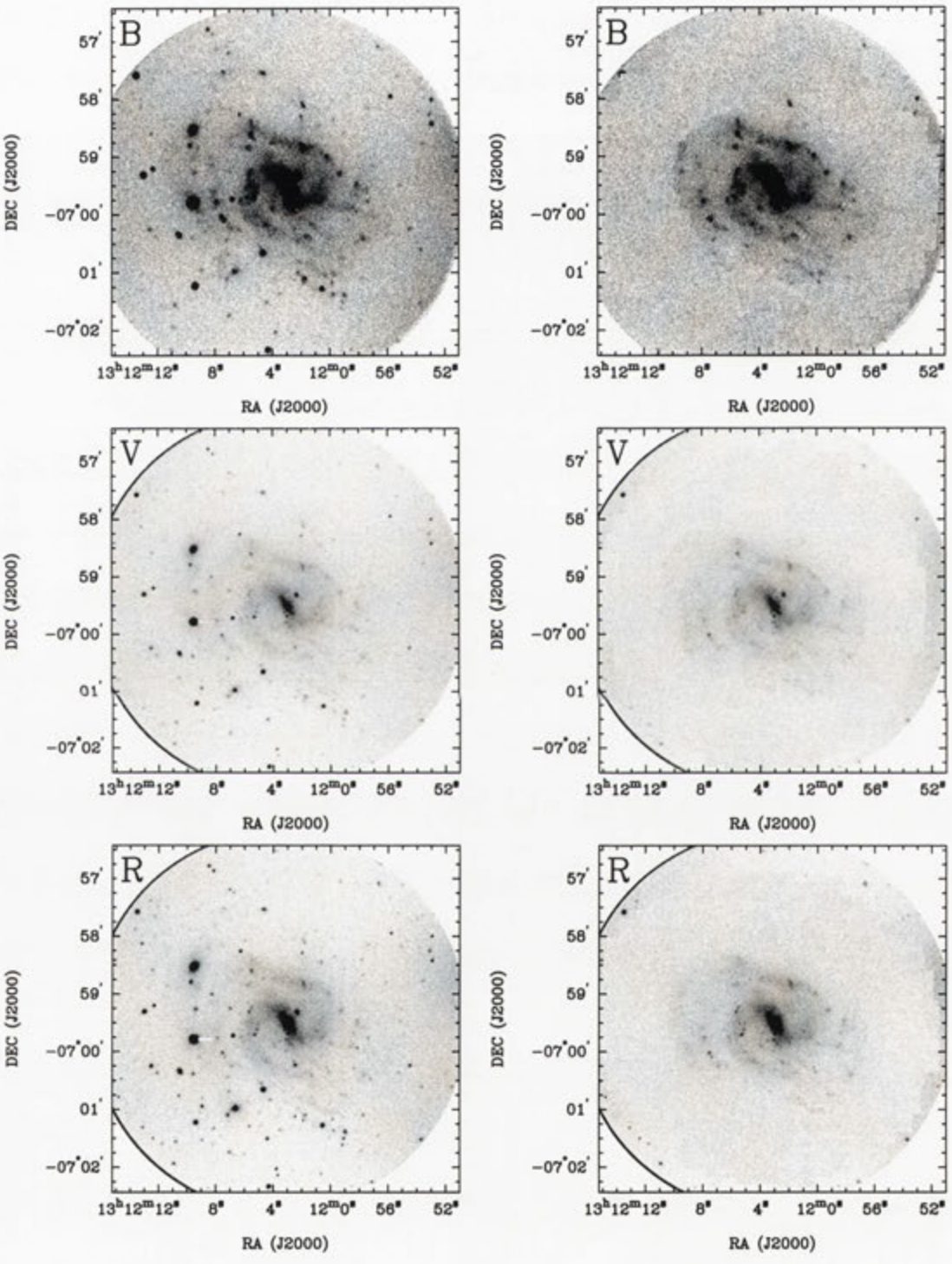

Fig. A.127: Deep *BVR* images of IC 4212 before and after subtraction of the foreground stars.

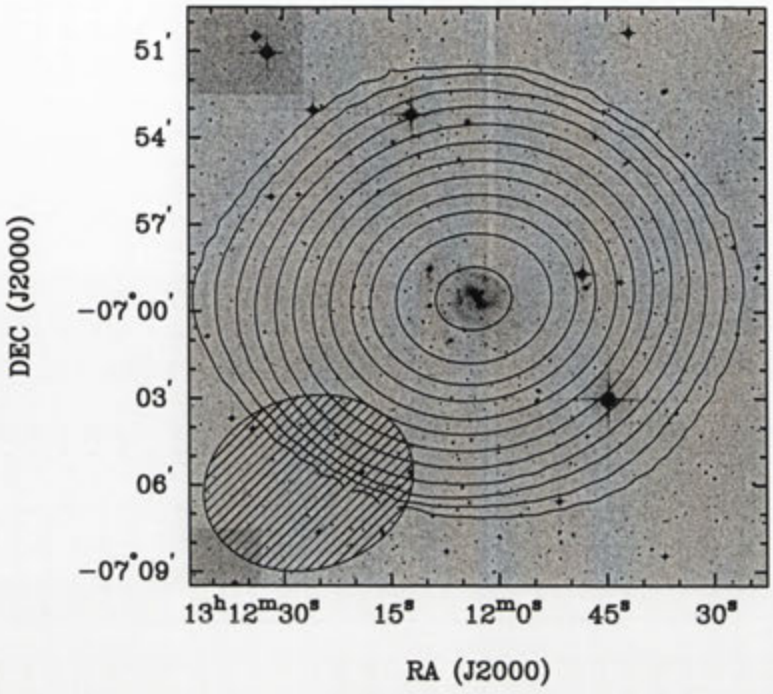

Fig. A.128: Integrated H I intensity distribution of IC 4212 overlaid onto an optical DSS II R band image. The synthesised beam is displayed in the bottom left corner.

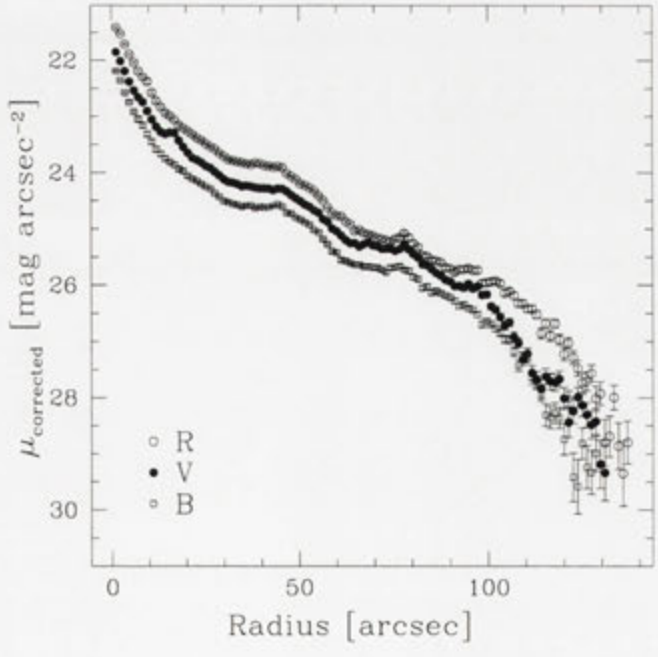

Fig. A.129: BVR surface brightness profiles of IC 4212, corrected for Galactic extinction.

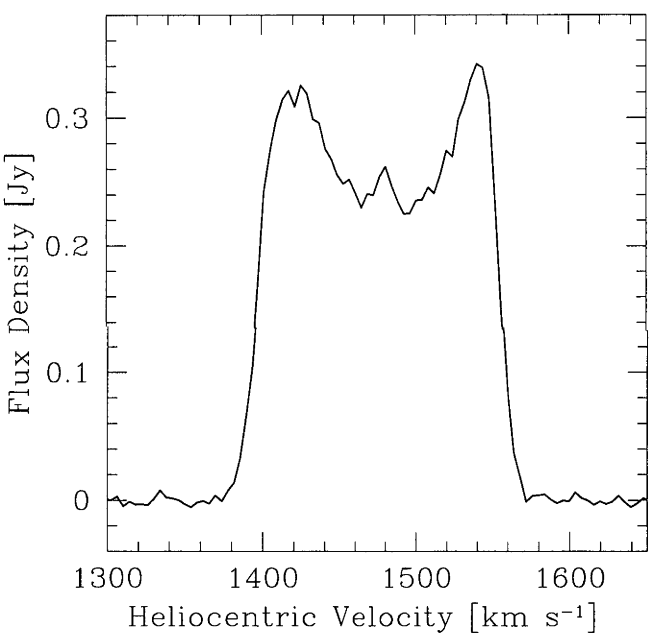

Fig. A.130: Global H I spectra of IC 4212 as obtained from the ATCA.

IC 4824

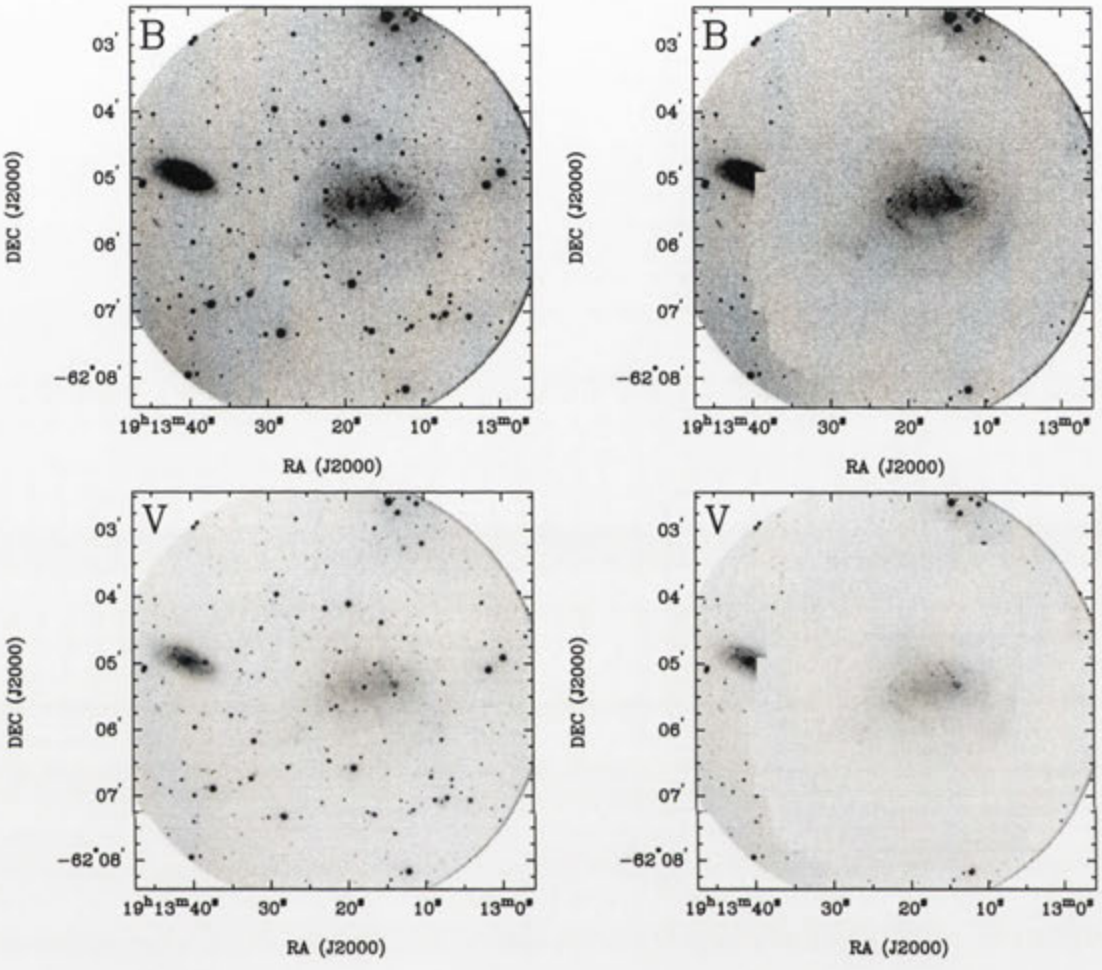

Fig. A.131: Deep *BVRI* images of IC 4824 before and after subtraction of the foreground stars.

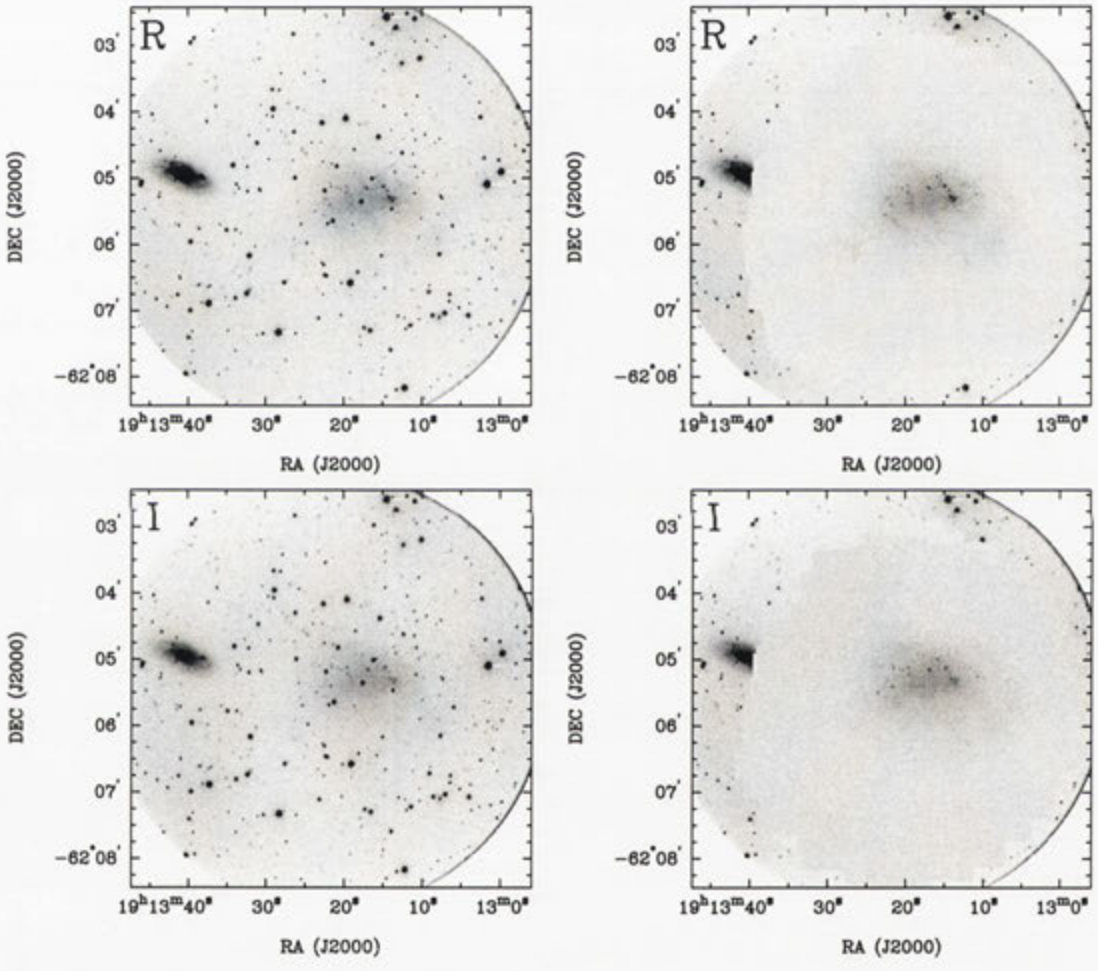

Fig. A.131: continued

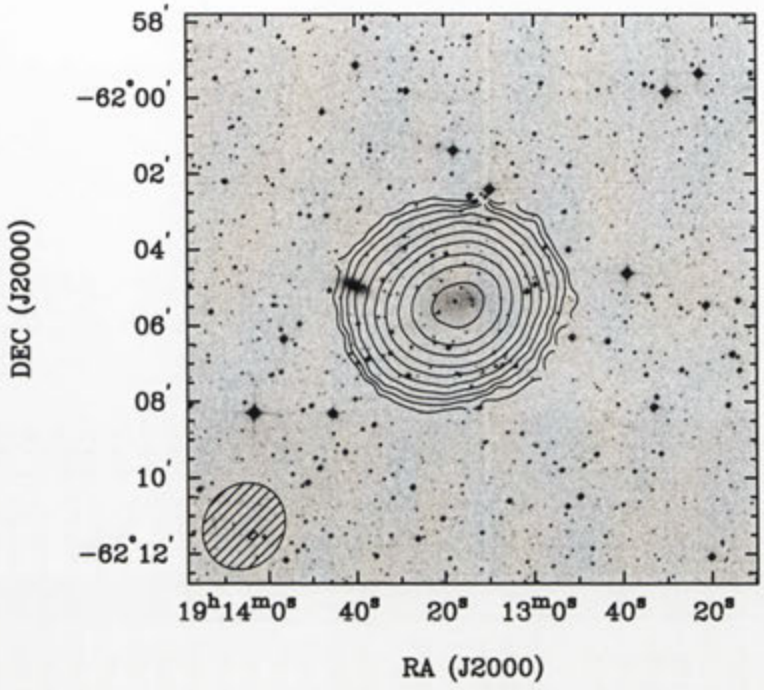

Fig. A.132: Integrated H I intensity distribution of IC 4824 overlaid onto an optical DSS II *R* band image. The synthesised beam is displayed in the bottom left corner.

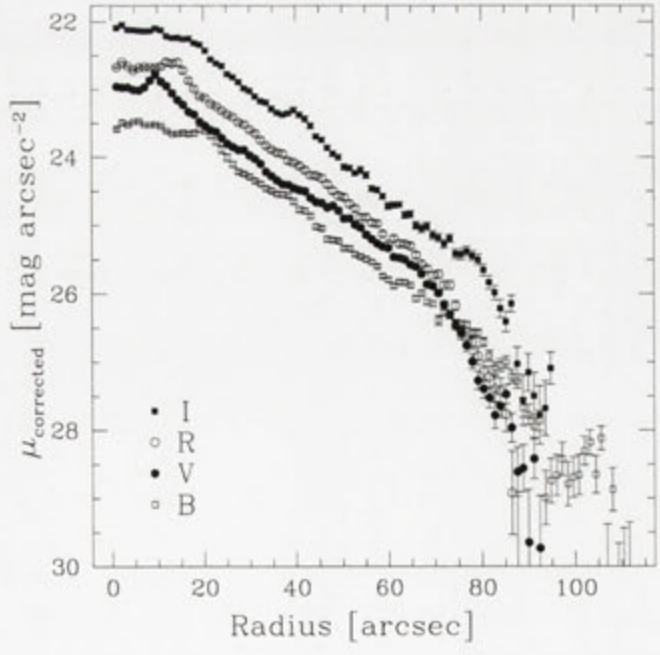

Fig. A.133: *BVRI* surface brightness profiles of IC 4824, corrected for Galactic extinction.

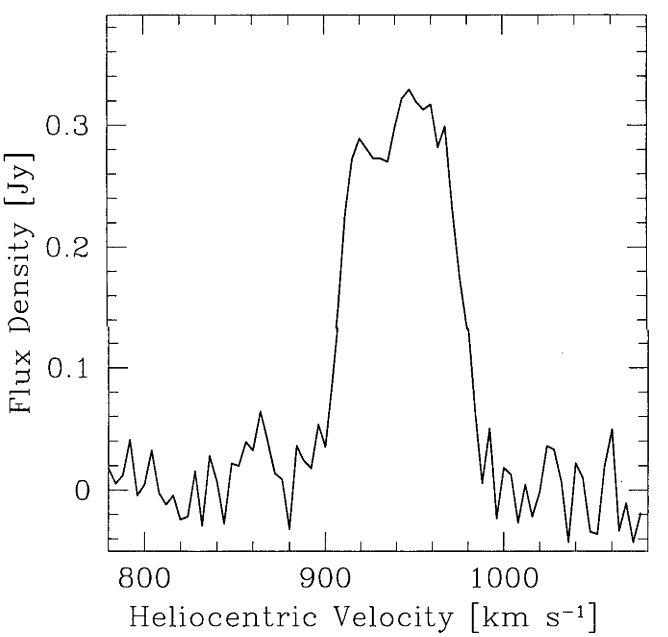

Fig. A.134: Global H I spectra of IC 4824 as obtained from the ATCA.

ESO 141-G042

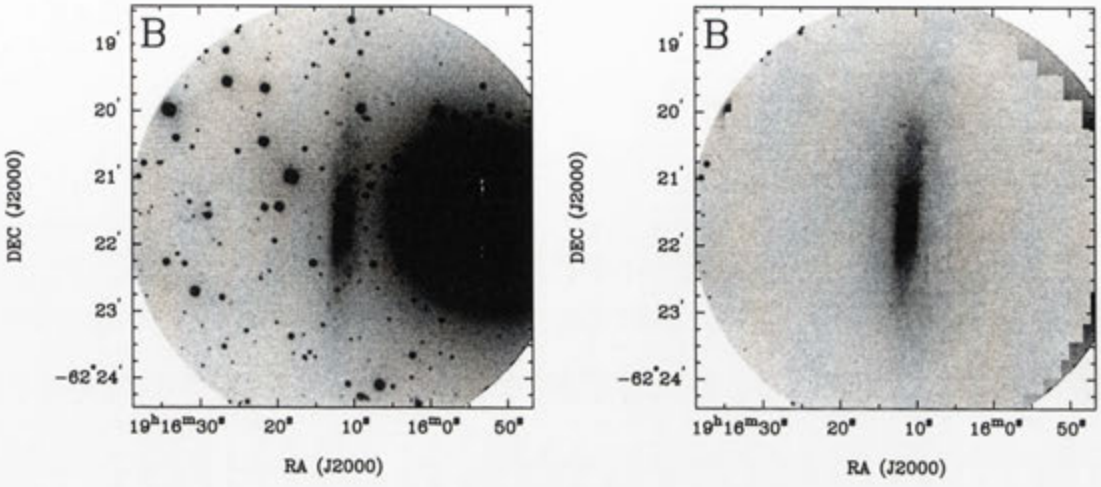

Fig. A.135: Deep B image of ESO 141-G042 before and after subtraction of the foreground stars.

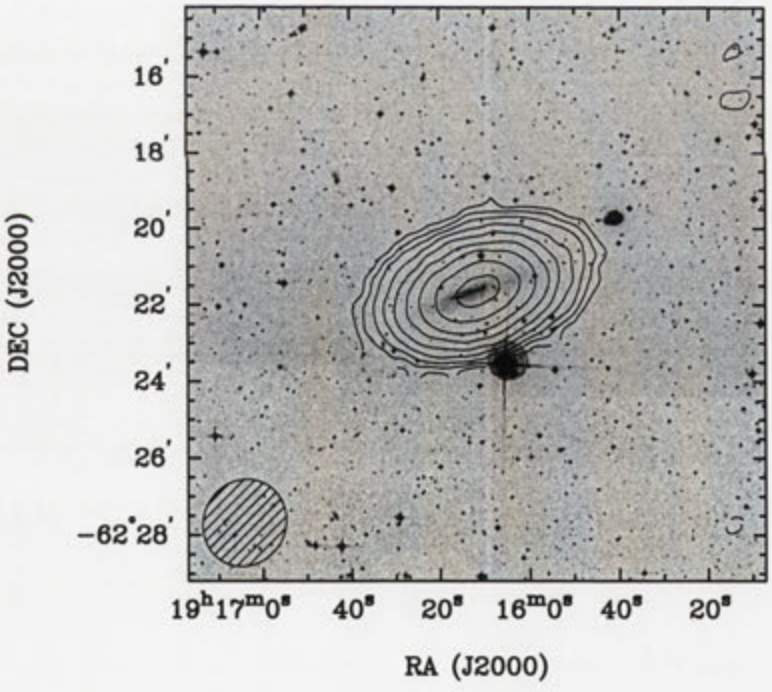

Fig. A.136: Integrated H I intensity distribution of ESO 141-G042 overlaid onto an optical DSS II R band image. The synthesised beam is displayed in the bottom left corner.

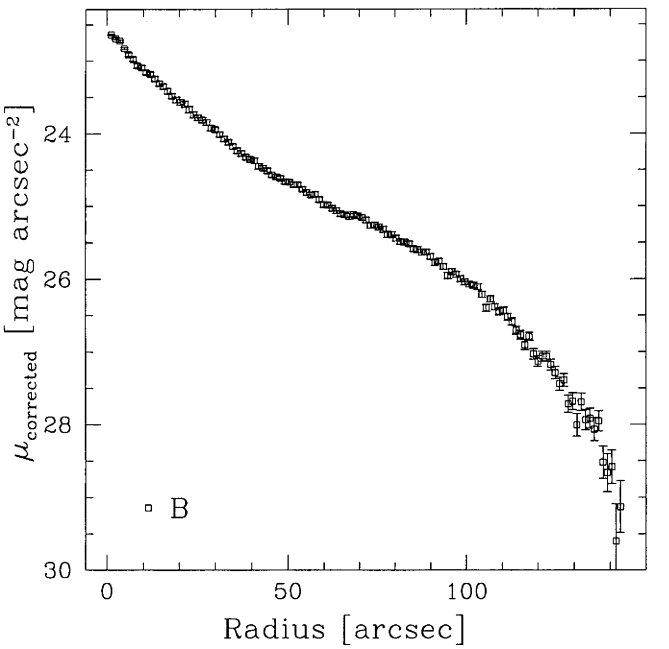

Fig. A.137: *B* surface brightness profile of ESO 141-G042, corrected for Galactic extinction.

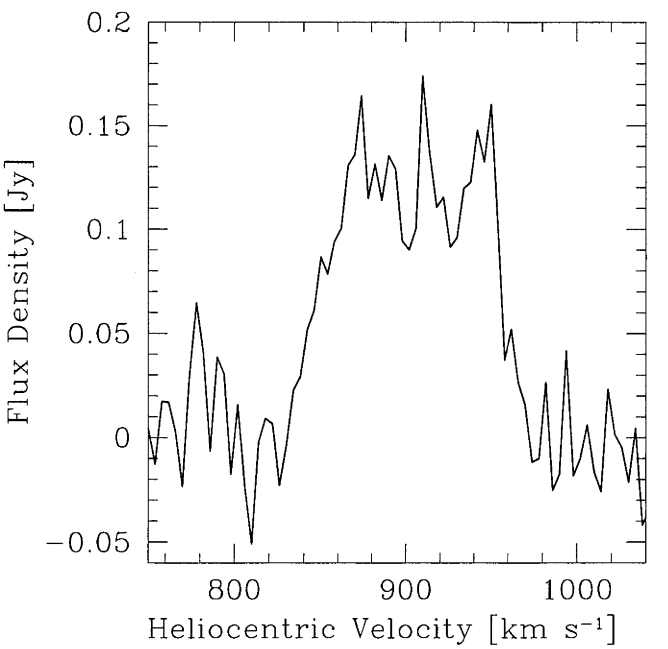

Fig. A.138: Global H I spectra of ESO 141-G042 as obtained from the ATCA.

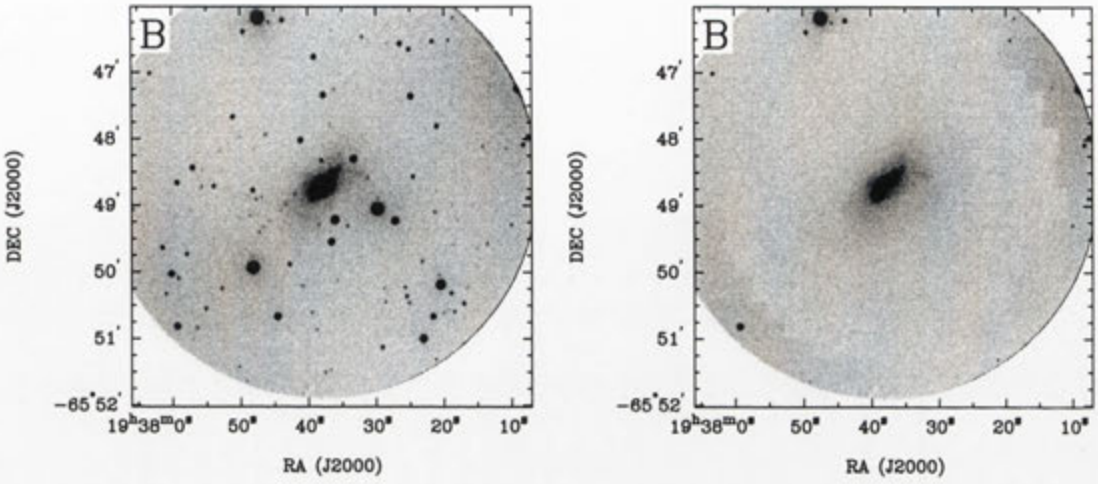

Fig. A.139: Deep B image of IC 4870 before and after subtraction of the foreground stars.

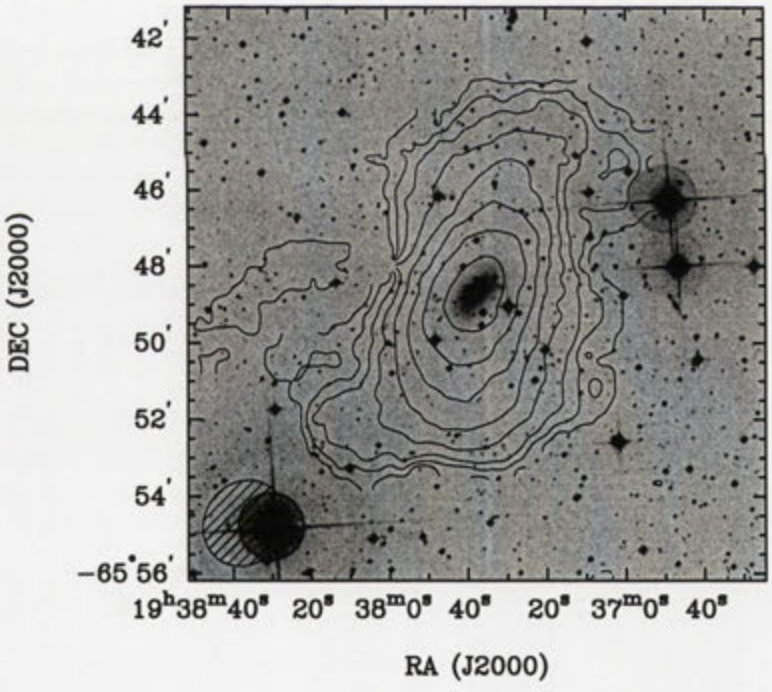

Fig. A.140: Integrated H I intensity distribution of IC 4870 overlaid onto an optical DSS II R band image. The synthesised beam is displayed in the bottom left corner.

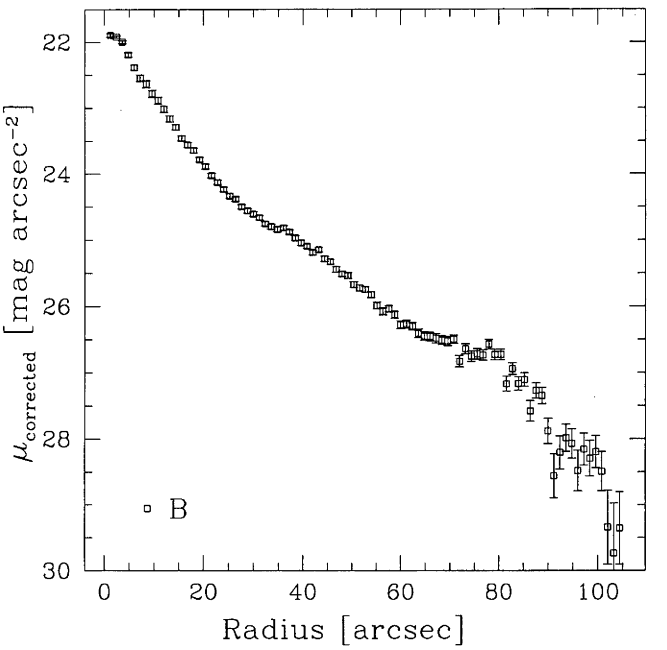

Fig. A.141: *B* surface brightness profile of IC 4870, corrected for Galactic extinction.

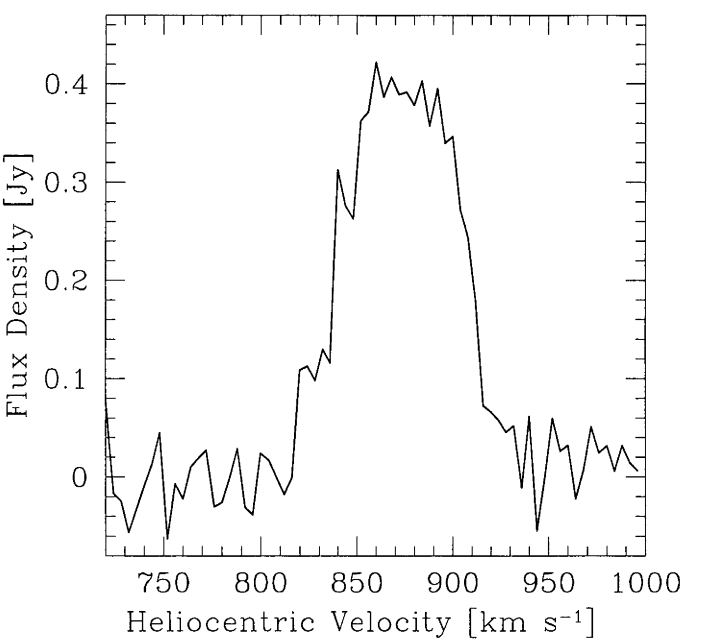

Fig. A.142: Global H I spectra of IC 4870 as obtained from the ATCA.

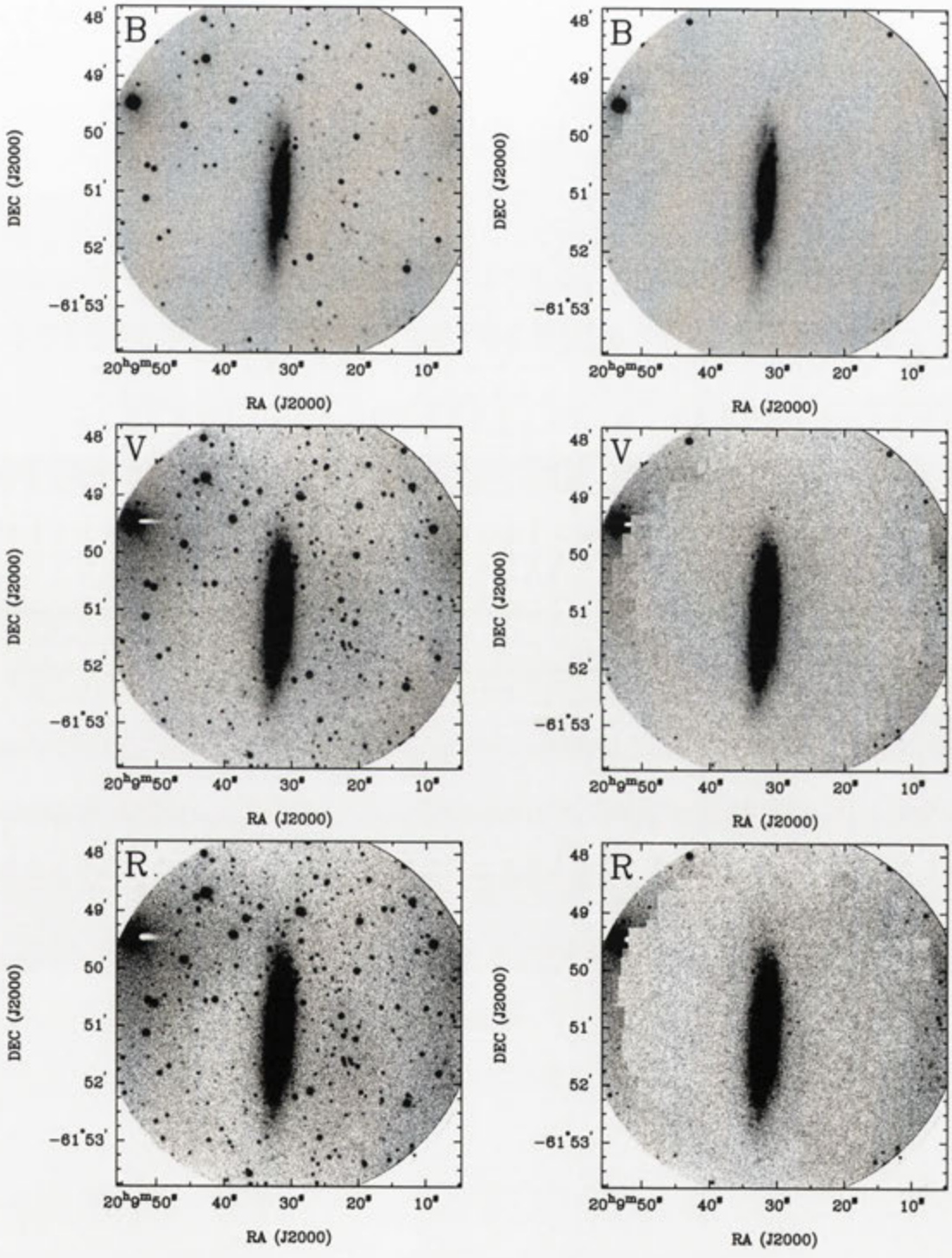

Fig. A.143: Deep *BVR* images of IC 4951 before and after subtraction of the foreground stars.

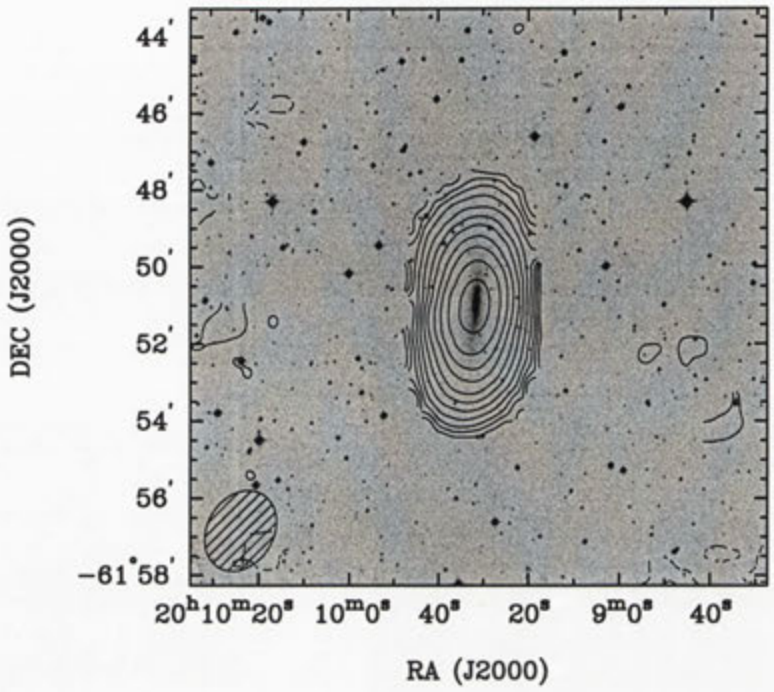

Fig. A.144: Integrated H I intensity distribution of IC 4951 overlaid onto an optical DSS II R band image. The synthesised beam is displayed in the bottom left corner.

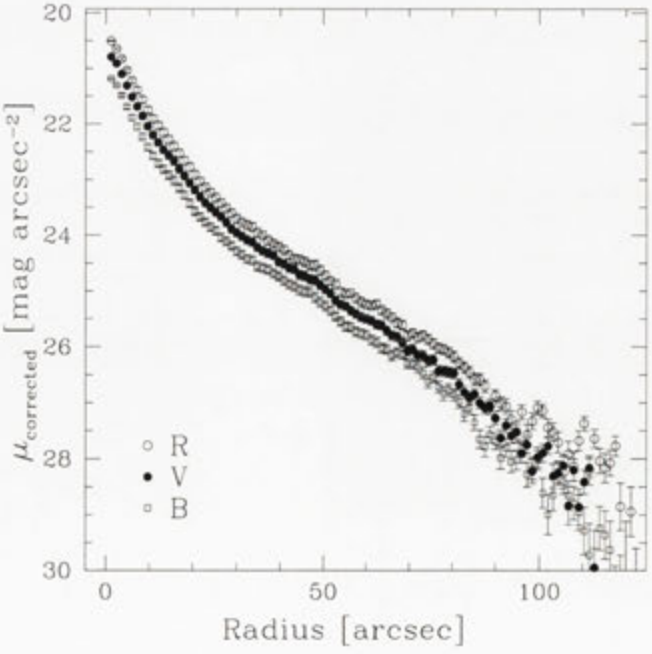

Fig. A.145: BVR surface brightness profiles of IC 4951, corrected for Galactic extinction.

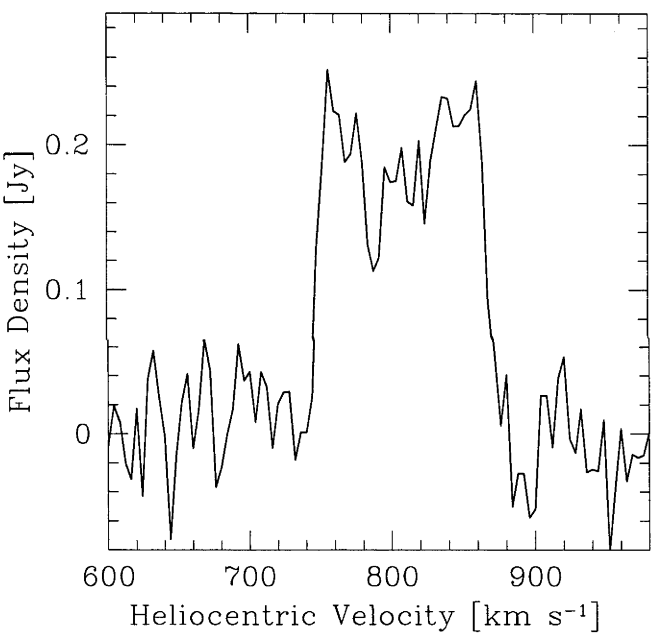

Fig. A.146: Global H I spectra of IC 4951 as obtained from the ATCA.

ESO 347-G017

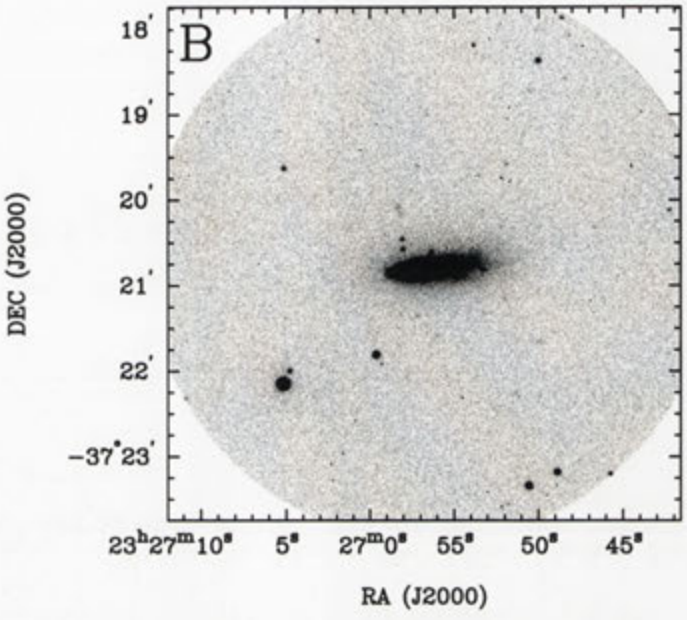

Fig. A.147: Deep B image of ESO 347-G017.

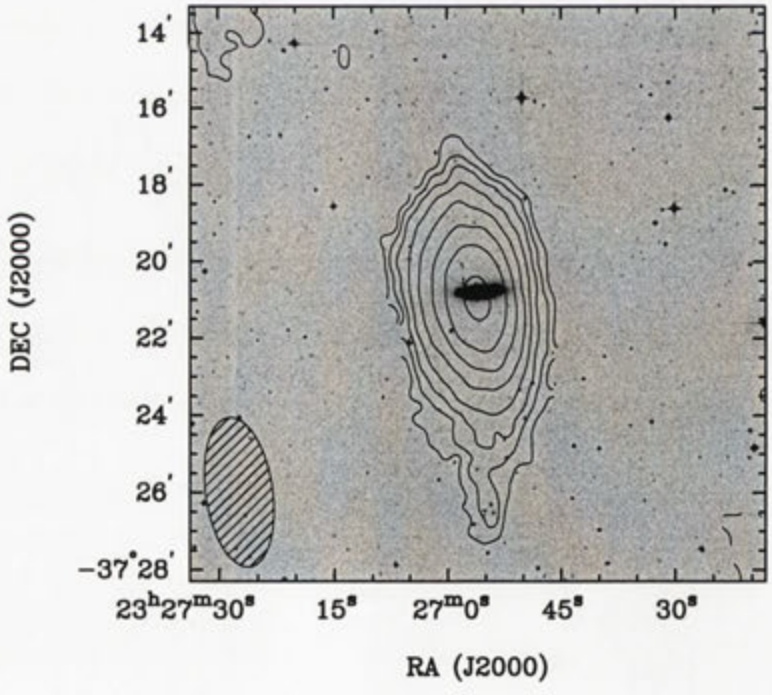

Fig. A.148: Integrated H I intensity distribution of ESO 347-G017 overlaid onto an optical DSS II R band image. The synthesised beam is displayed in the bottom left corner.

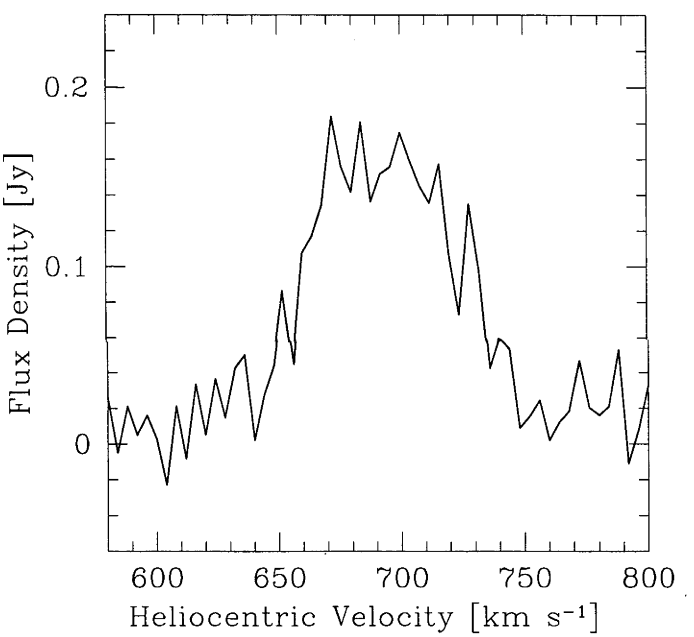

Fig. A.149: Global H I spectra of ESO 347-G017 as obtained from the ATCA.

UGCA 442

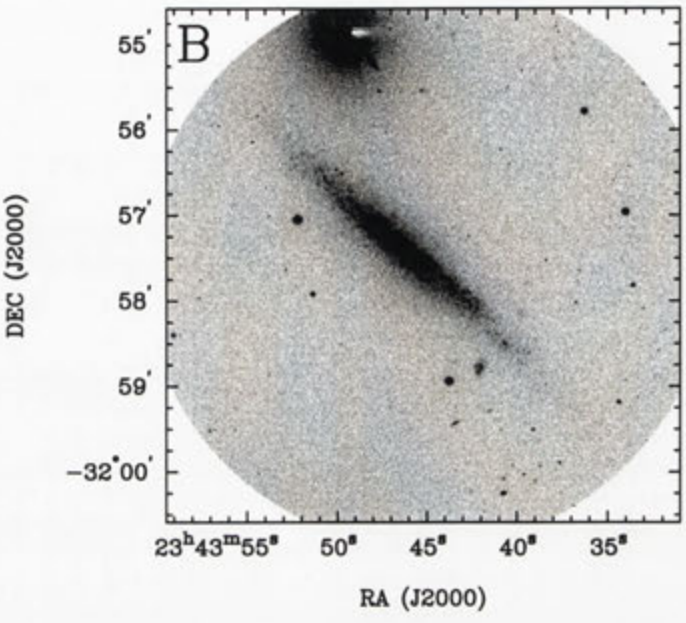

Fig. A.150: Deep B image of UGCA 442.

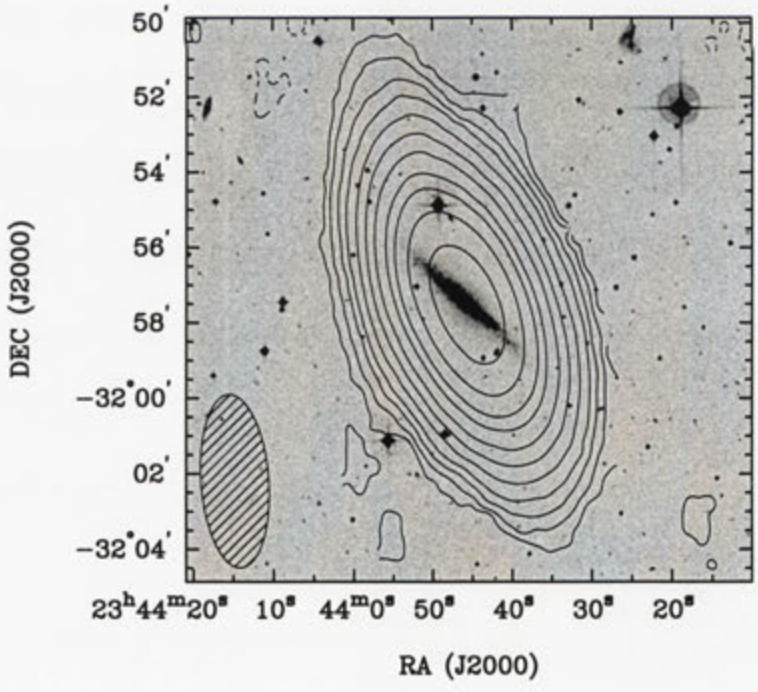

Fig. A.151: Integrated H I intensity distribution of UGCA 442 overlaid onto an optical DSS II R band image. The synthesised beam is displayed in the bottom left corner.

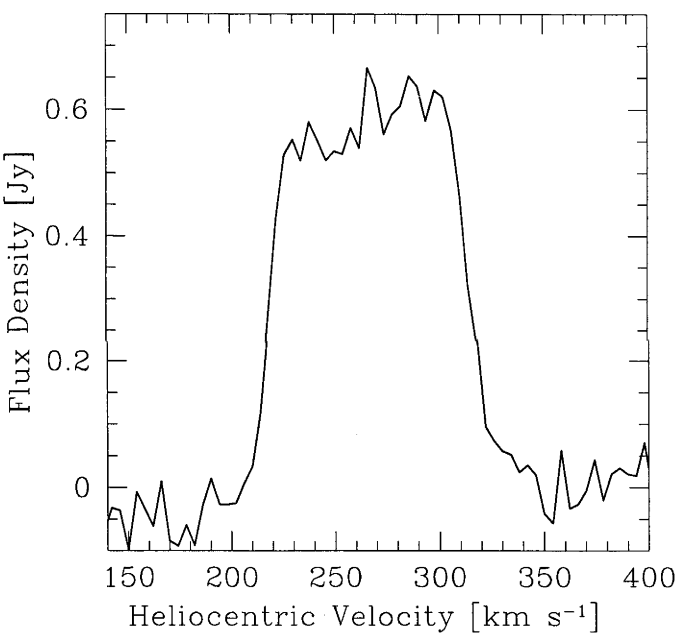

Fig. A.152: Global H I spectra of UGCA 442 as obtained from the ATCA.

ESO 348-G009

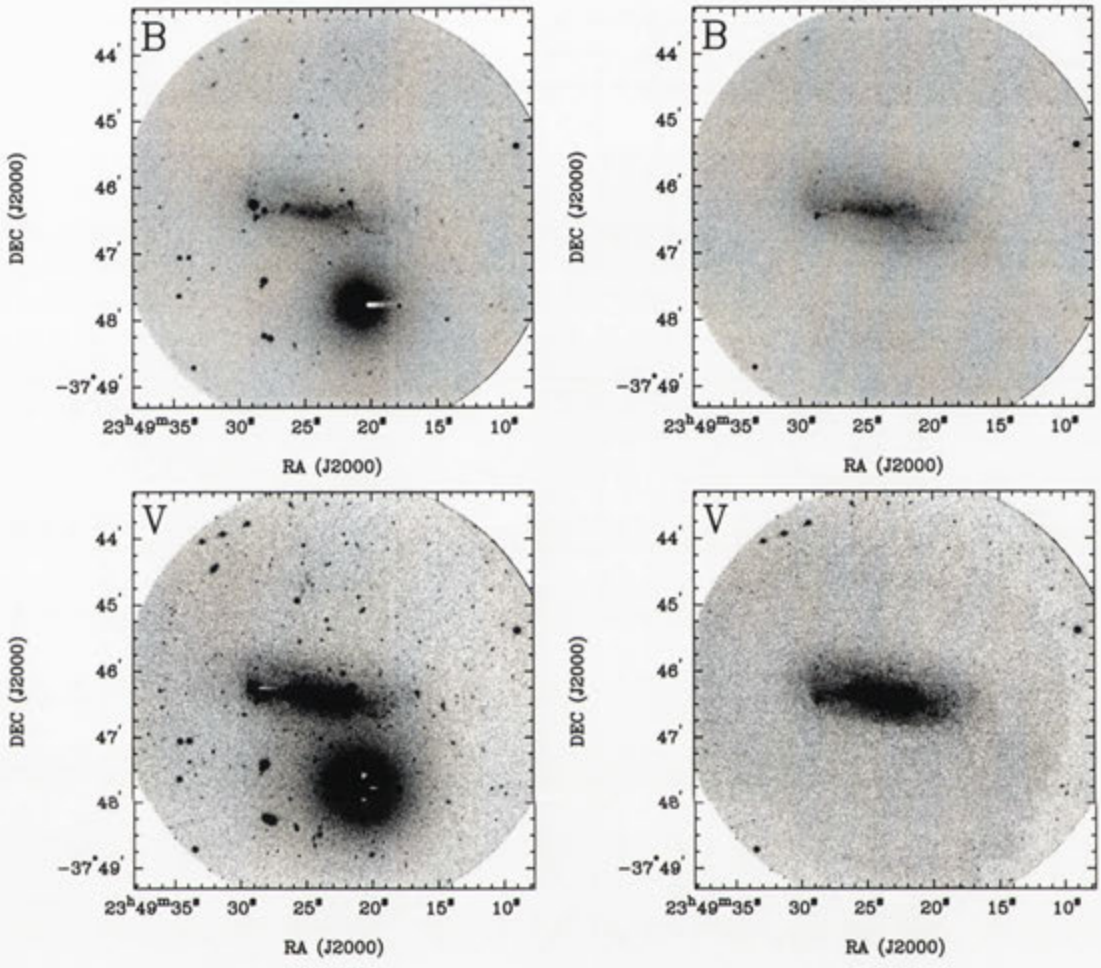

Fig. A.153: Deep *BVRI* images of ESO 348-G009 before and after subtraction of the foreground stars.

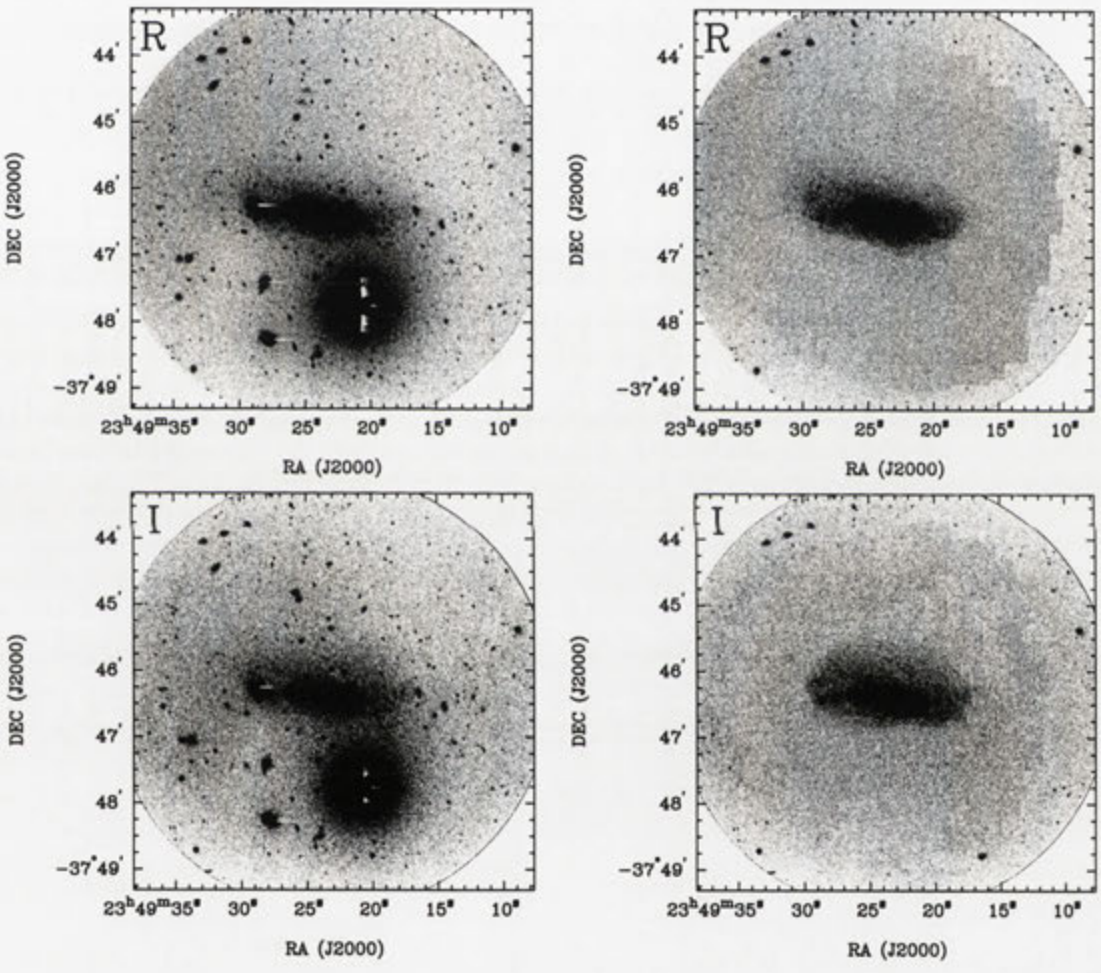

Fig. A.153: continued

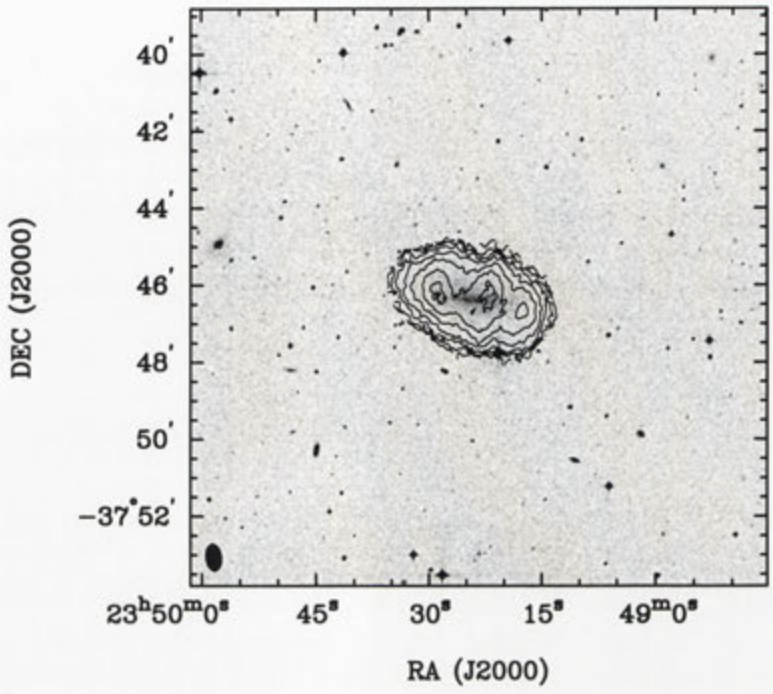

Fig. A.154: Integrated H I intensity distribution of ESO 348-G009 overlaid onto an optical DSS II R band image. The synthesised beam is displayed in the bottom left corner.

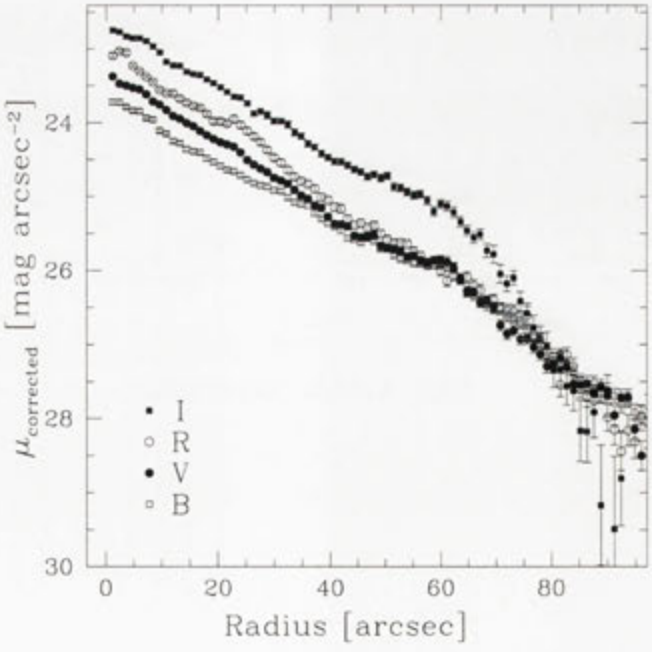

Fig. A.155: *BVRI* surface brightness profiles of ESO 348-G009, corrected for Galactic extinction.

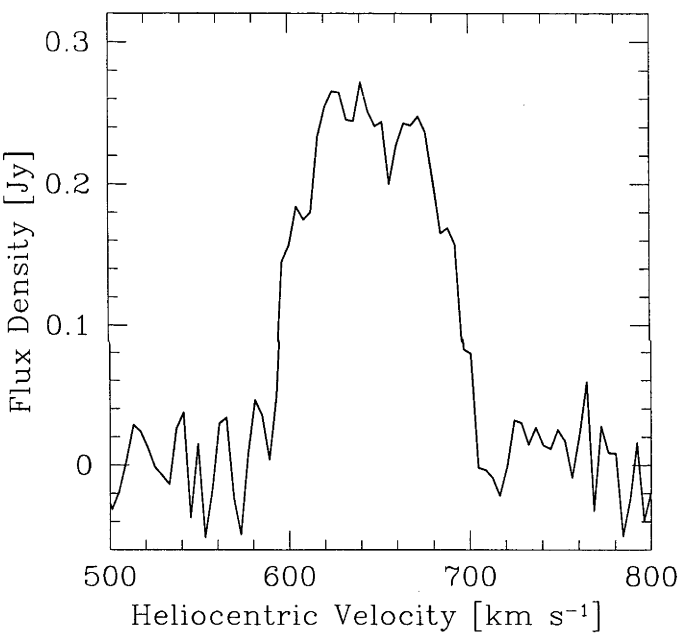

Fig. A.156: Global H I spectra of ESO 348-G009 as obtained from the ATCA.

ESO 149-G003

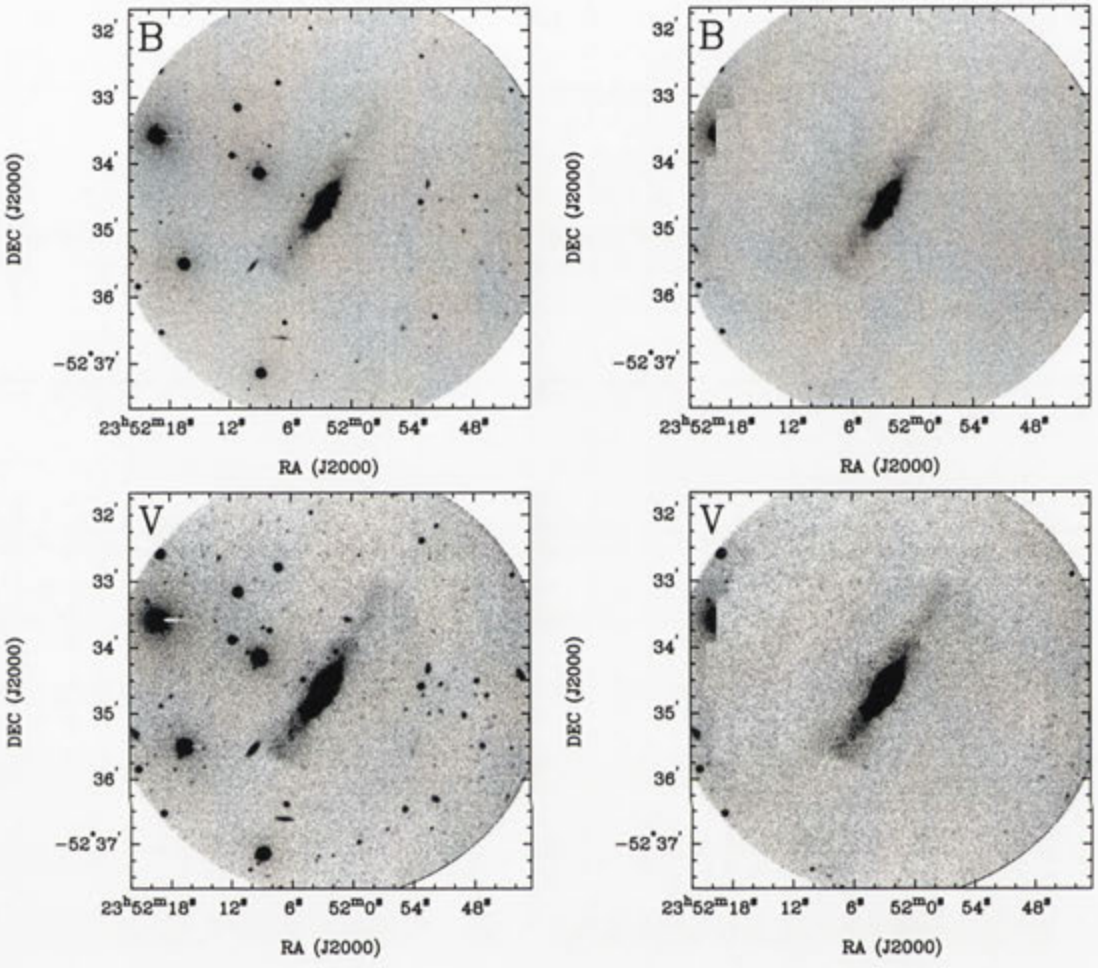

Fig. A.157: Deep *BVRI* images of ESO 149-G003 before and after subtraction of the foreground stars.

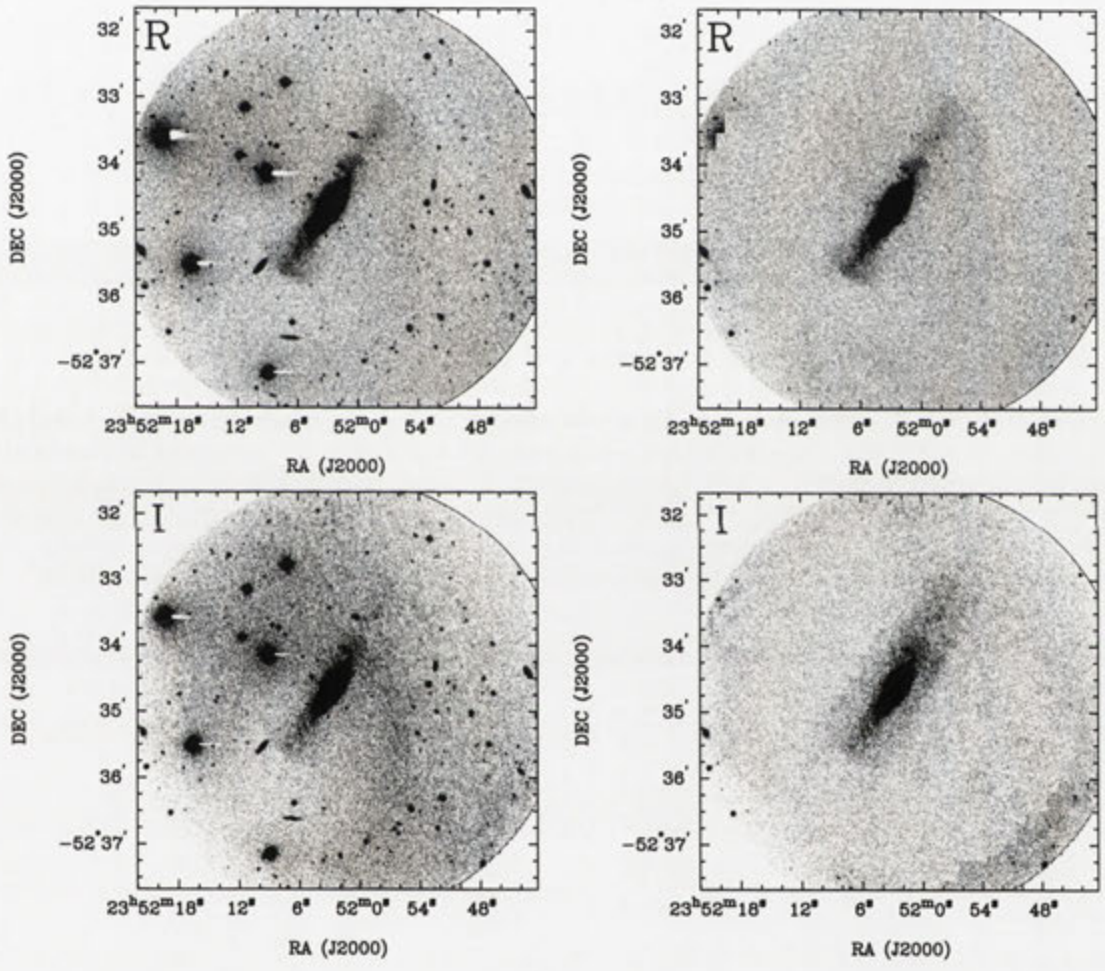

Fig. A.157: continued

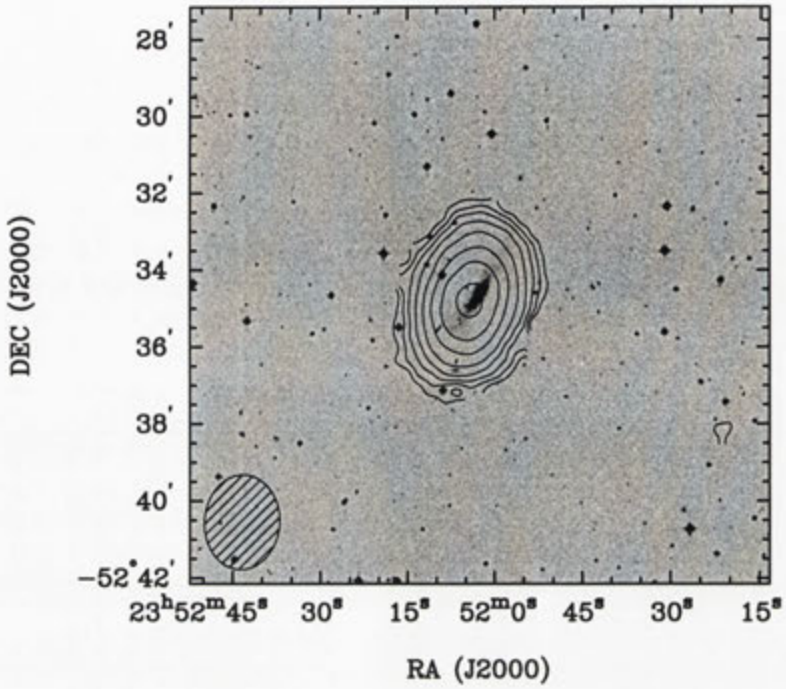

Fig. A.158: Integrated H I intensity distribution of ESO 149-G003 overlaid onto an optical DSS II R band image. The synthesised beam is displayed in the bottom left corner.

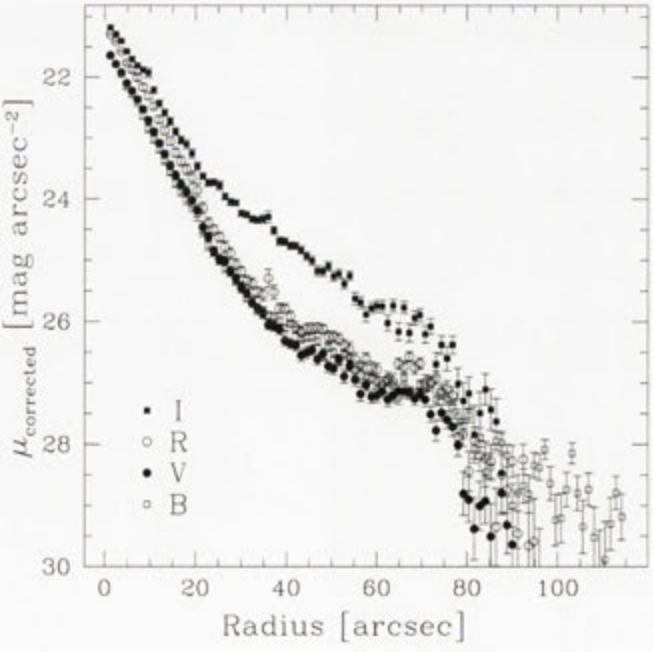

Fig. A.159: *BVRI* surface brightness profiles of ESO 149-G003, corrected for Galactic extinction.

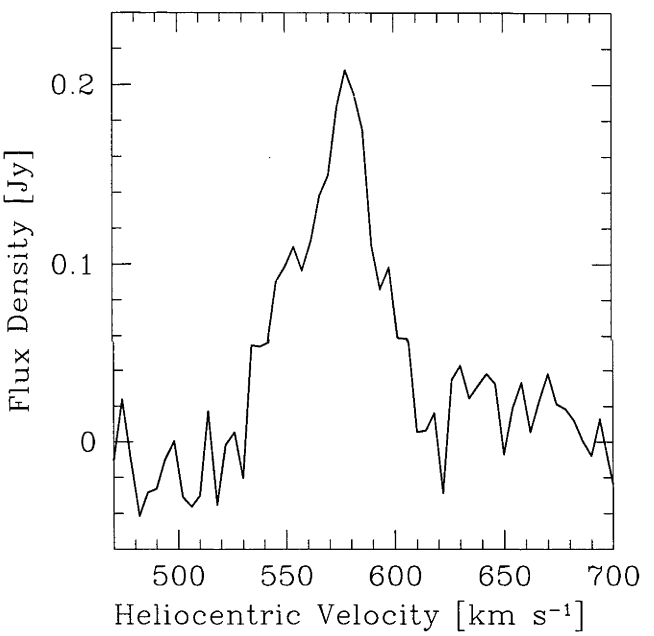

Fig. A.160: Global H I spectra of ESO 149-G003 as obtained from the ATCA.

B. EQUATIONS

- **The H I mass** (Roberts, 1975, Equation 3.1)

$$\mathcal{M}_{\rm HI} = 2.36 \times 10^5 \; D^2 \; F_{\rm HI} \;\; \mathcal{M}_\odot,$$

where $F_{\rm HI}$ is the integrated H I flux density in Jy km s^{-1}, and D is the galaxy distance in Mpc. Hubble flow distances were calculated from the Local Group velocities given in the BGC (using our adopted H_0 of 75 km s^{-1} Mpc^{-1}).

- **The absolute *B* band magnitude** (Equation 3.4)

$$M_{\rm B,0} = m_{\rm B} - A_{\rm B} - 5\log(D) - 25 \;\; {\rm mag},$$

where D is the galaxy distance in Mpc, $m_{\rm B}$ is the B band apparent magnitude, and $A_{\rm B}$ is the B band Galactic extinction.

- **The *B* band luminosity** (Equation 3.2)

$$L_{\rm B} = D^2 \; 10^{10-0.4(m_{\rm B}-A_{\rm B}-M_{\rm B,\odot})} \;\; L_{\odot,{\rm B}},$$

where D is the galaxy distance in Mpc, $m_{\rm B}$ is the B band apparent magnitude, $A_{\rm B}$ is the B band Galactic extinction, and $M_{\rm B,\odot}$ is the absolute Solar B magnitude which is taken as 5.48 mag (Bessell, Castelli, & Plez, 1998).

- **The H I mass-to-light ratio** (Equations 1.1 and 3.3)

$$\frac{\mathcal{M}_{\rm HI}}{L_{\rm B}} = 1.5 \times 10^{-7} F_{\rm HI} \; 10^{0.4(m_{\rm B}-A_{\rm B})} \;\; \frac{\mathcal{M}_\odot}{L_{\odot,{\rm B}}},$$

where $F_{\rm HI}$ is the integrated H I flux density in Jy km s^{-1}, $m_{\rm B}$ is the B band apparent magnitude, and $A_{\rm B}$ is the B band Galactic extinction.

- **The curent star formation rate from the 20 cm continuum** (Condon, 1992; Haarsma et al., 2000, Equation 6.1)

$$SFR_{20\,{\rm cm}} = 0.14 \; D^2 \; S_{20\,{\rm cm}} \;\; \mathcal{M}_\odot \, {\rm yr}^{-1},$$

where D is the distance in Mpc and $S_{20\,{\rm cm}}$ is the 20 cm radio continuum flux density in Jy.

- **The Sérsic profile law (in terms of surface brightness $\mu(r)$)** (Sérsic, 1968, Equation 6.2)

$$\mu(r) = \mu_0 + 1.086(r/r_0)^n \text{ mag arcsec}^{-2},$$

where r is the radius from the center in arcsec, μ_0 is the central surface brightness in mag arcsec^{-2}, r_0 is the scale radius in arcseconds, and n is the shape parameter (where $n = 1$ gives an exponential profile).

- **The average past star formation rate** (Tinsley, 1980, Equation 6.3)

$$\langle SFR \rangle_{past} = \frac{\Gamma_B L_B}{T_{sf}(1-R)} \mathcal{M}_\odot \text{ yr}^{-1},$$

where Γ_B is the B band stellar mass-to-light ratio in $\mathcal{M}_\odot / L_{\odot,B}$, T_{sf} is the time for which the galaxy has been forming stars in years, and R is the recycling fraction (essentially the proportion of the stars formed within the galaxy that are no longer visible).

- **The Toomre (1964) Q criterion** (Martin & Kennicutt, 2001, Equation 6.4)

$$Q(r) \equiv \frac{\sigma(r)\kappa(r)}{\pi G \mu_{gas}(r)},$$

where $\sigma(r)$ is the gas dispersion velocity, $\kappa(r)$ is the epicyclic frequency, G is the normal gravitational constant, and $\mu_{gas}(r)$ is the surface density of the gas in the disk.

- **The Kennicutt (1989) critical gas surface density** (Martin & Kennicutt, 2001, Equation 6.5)

$$\mu_{crit}(r) = \alpha_Q \frac{\sigma(r)\kappa(r)}{\pi G},$$

where $\sigma(r)$ is the gas dispersion velocity, $\kappa(r)$ is the epicyclic frequency, G is the normal gravitational constant, and α_Q is a constant close to unity which is included to account for a more realistic disk ($\alpha_Q = 1$ would return the model to the thin-disk approximation).

- **The epicyclic frequency** (Martin & Kennicutt, 2001, Equation 6.6)

$$\kappa^2(r) = 2\left(\frac{V^2}{R^2} + \frac{V}{R}\frac{dV}{dR}\right) \text{ s}^{-2},$$

where V is the rotation velocity in km s^{-1}, and R is the radius in km.

- **Galactic extinction correction** (Equation 1.2)

$$\begin{aligned} A_{\rm B} &= 4.32E(B-V) \ \ {\rm mag}, \\ A_{\rm V} &= 3.32E(B-V) \ \ {\rm mag}, \\ A_{\rm R} &= 2.68E(B-V) \ \ {\rm mag}, \\ A_{\rm I} &= 1.95E(B-V) \ \ {\rm mag}, \end{aligned}$$

where $A_{\rm B}$, $A_{\rm V}$, $A_{\rm R}$, and $A_{\rm I}$ are the galactic extinction corrections in magnitudes for their respective bands, and $E(B-V)$ is the difference between the extinction corrections in the B and V bands. (Based on the Schlegel, Finkbeiner, & Davis (1998) extinctions as presented in NED[1])

- **The Local Group velocity** (Karachentsev & Makarov, 1996)

$$v_{\rm LG} = v_{\rm sys} + 300 \sin(l) \cos(b) \ \ {\rm km\,s^{-1}},$$

where $v_{\rm sys}$ is the systemic velocity in ${\rm km\,s^{-1}}$, and l and b are the Galactic longitude and latiude, respectively, in degrees.

[1] http://nedwww.ipac.caltech.edu/

C. ACRONYMS AND ABREVIATIONS

The following is a list of acronyms and abreviations used throughout this thesis, including references where appropriate.

2.3m	ANU **2.3-m**eter Telescope at Siding Spring Observatory
ANU	**A**ustralian **N**ational **U**niversity
ATCA	**A**ustralia **T**elescope **C**ompact **A**rray
ATNF	**A**ustralia **T**elescope **N**ational **F**acility, CSIRO
ATT	**A**dvanced **T**echnology **T**elescope (the 2.3m)
BCD	**B**lue **C**ompact **D**warf Galaxy
BGC	The HIPASS **B**right **G**alaxy **C**atalog (Koribalski, 2001; Koribalski et al., 2004)
CSIRO	**C**ommonwealth **S**cientific and **I**ndustrial **R**esearch **O**rganisation
DSS	**D**igitized **S**ky **S**urvey
ESO	**E**uropean **S**outhern **O**bservatory
HIPASS	**H** I **P**arkes **A**ll **S**ky **S**urvey (Staveley-Smith et al., 1996; Barazza et al., 2001)
HSB	**H**igh **S**urface **B**rightness
K89	Kennicutt (1989)
LEDA	**L**yon-Meudon **E**xtragalactic **Da**tabase (Paturel et al., 1997)
LSB	**L**ow **S**urface **B**rightness
MK01	Martin & Kennicutt (2001)
MSO	**M**ount **S**tromlo **O**bservatory, Canberra, Australia (RSAA)
NED	**N**ASA/IPAC **E**xtragalactic **D**atabase
PGC	**C**atalog of **P**rinciple **G**alaxy (Paturel et al., 1989)
RC3	**Third R**eference **C**atalog of Bright Galaxies (de Vaucouleurs et al., 1991)
RSAA	**R**esearch **S**chool of **A**stronomy and **A**strophysics, ANU
SFD98	Schlegel, Finkbeiner, & Davis (1998)
SSO	**S**iding **S**pring **O**bservatory, Coonabarabran, Australia (RSAA)
ZOA	**Z**one **o**f **Avoidance** (the Galactic Plane)

BIBLIOGRAPHY

Allen, R. J., & Shostak, G. S., 1979, A&AS, 35, 163

Barazza, F. D., Binggeli, B., & Prugniel, P., 2001, A&A, 373, 12

Barnes, D. G., Staveley-Smith, L., de Blok, W. J. G., Oosterloo, T., Stewart, I. M., Wright, A. E., Banks, G. D., Bhathal, R., Boyce, P. J., Calabretta, M. R., Disney, M. J., Drinkwater, M. J., Ekers, R. D., Freeman, K. C., Gibson, B. K., Green, A. J., Haynes, R. F., te Lintel Hekkert, P., Henning, P. A., Jerjen, H., Juraszek, S., Kesteven, M. J., Kilborn, V. A., Knezek, P. M., Koribalski, B., Kraan-Korteweg, R. C., Malin, D. F., Marquarding, M., Minchin, R. F., Mould, J. R., Price, R. M., Putman, M. E., Ryder, S. D., Sadler, E. M., Schröder, A., Stootman, F., Webster, R. L., Wilson, W. E., & Ye, T., 2001, MNRAS, 322, 486

Begeman, K. G., 1989, A&A, 223, 47

Begum, A., Chengalur, J. N., & Karachentsev, I. D., 2005, A&A, in press

Bessell, M. S., Castelli, F., & Plez, B., 1998, A&A, 333, 231

Binggeli, B., Tarenghi, M., & Sandage, A., 1990, A&A, 228, 42

Binney, J., & Tremaine, S., 1987, Galactic Dynamics, Princeton University Press, Princeton

Blanton, M. R., Hogg, D. W., Bahcall, N. A., Brinkmann, J., Britton, M., Connolly, A. J., Csabai, I., Fukugita, M., Loveday, J., Meiksin, A., Munn, J. A., Nichol, R. C., Okamura, S., Quinn, T., Schneider, D. P., Shimasaku, K., Strauss, M. A., Tegmark, M., Vogeley, M. S., & Weinberg, D. H., 2003, ApJ, 592, 819

Blanton, M. R., Lupton, R. H., Schlegel, D. J., Strauss, M. A., Brinkmann, J., Fukugita, M., & Loveday, J., 2004, ApJ, submitted, astro-ph/0410164

Bothun, G. D., Impey, C. D., Malin, D. F., & Mould, J. R., 1987, AJ, 94, 23

Bremnes, T., Binggeli, B., Prugniel, P., 2000, A&AS, 141, 211

Bureau, M., Freeman, K. C., Pfitzner, D. W., & Meurer, G. R., 1999, AJ, 118, 2158

Burstein, D., & Heiles, C., 1978, ApJ, 225, 40

Burstein, D., & Heiles, C., 1982, AJ, 87, 1165

Cabanela, J. E., 1999, BAAS, 31, 1404

Carignan, C., & Freeman, K. C., 1988, ApJ, 332, L33

Carignan, C., & Beaulieu, S., 1989, ApJ, 347, 760

Carignan, C., & Purton, C., 1998, ApJ, 506, 125

Chengalur, J. N., Giovanelli, R., & Haynes, M. P., 1995, AJ, 109, 2415

Chung, A., van Gorkom, J. H., O'Neil, K., & Bothun, G. D., 2002, AJ, 123, 2387

Condon, J. J., 1992, ARA&A, 30, 575

Côté, S., Freeman, K. C., Carignan, C., & Quinn, P. J., 1997, AJ, 114, 1313

Côté, S., Carignan, C., & Freeman, K. C., 2000, AJ, 120, 3027

Dalal, N., & Kochanek, C. S., 2002, ApJ, 572, 25

de Blok, W. J. G., McGaugh, S. S., & van der Hulst, J. M., 1996, MNRAS, 283, 18

de Vaucouleurs, G., de Vaucouleurs, A., Corwin, H. G., Buta, R. J., Paturel, G., & Fouqué, P., 1991, Third Reference Catalogue of Bright Galaxies, Springer, New York

Disney, M. J., 1976, Nature, 263, 573

Donley, J. L., Staveley-Smith, L., Kraan-Korteweg, R. C., Islas-Islas, J. M., Schröder, A., Henning, P. A., Koribalski, B. S., Mader, S., & Stewart, I., 2005, AJ, 129, 220

Dressler, A., 1980, ApJ, 236, 351

Dressler, A., 1984, ARA&A, 22, 185

Giovanelli, R., & Haynes, M. P., 1988, in Verschuur, G. L., Kellermann, K. I., eds, Galactic and Extragalactic Radio Astronomy. Springer-Verlag, Berlin, p.522

Giovanelli, R., & Haynes, M. P., 1991, ARA&A, 29, 499

Giovanelli, R., Williams, J. P., & Haynes, M. P., 1991, AJ, 101, 1242

Gurovich, S., McGaugh, S. S., Freeman, K. C., Jerjen, H., Staveley-Smith, L., & de Blok, W. J. G., 2004, PASA, 21, 412

Haarsma, D. B. Partridge, R. B., Windhorst, R. A., Richards, E. A., 2000, ApJ, 544, 641

Hambly, N. C., MacGillivray, H. T., Read, M. A., Tritton, S. B., Thomson, E. B., Kelly, B. D., Morgan, D. H., Smith, R. E., Driver, S. P., Williamson, J., Parker, Q. A., Hawkins, M. R. S., Williams, P. M., & Lawrence, A., 2001, MNRAS, 326, 1279, http://www-wfau.roe.ac.uk/sss/halpha/

Heiles, C., Perillat, P., Nolan, M., Lorimer, D., Bhat, R., Ghosh, T., Lewis, M., O'Neil, K., Salter, C., Stanimirovic, S., 2001, PASP, 113, 1247

Henning, P. A., Kraan-Korteweg, R. C., Rivers, A. J., Loan, A. J., Lahav, O., & Burton, W. B, 1998, AJ, 115, 584

Henning, P. A., Staveley-Smith, L., Ekers, R. D., Green, A. J., Haynes, R. F., Juraszek, S., Kesteven, M. J., Koribalski, B. S., Kraan-Korteweg, R. C., Price, R. M., Sadler, E. M., & Schröder, A., 2000, AJ, 119, 2686

Hilker, M., Mieske, S., & Infante, L., 2003, A&A, 397, L9

Hoffman, G. L., Lu, N. Y., Salpeter, E. E., Farhat, B., Lamphier, C., & Roos, T., 1993, AJ, 106, 39

Hopp, U., & Schulte-Ladbeck, R. E., 1995, A&AS, 111, 527

Hubble, E., & Humason, M. L., 1931, ApJ, 74, 43

Huchtmeier, W. K., & Richter, O.-G., 1989, A General Catalog of H I Observations of Galaxies, Springer-Verlag, Berlin

Huchtmeier, W. K., Karachentsev, I. D., & Karachentseva, V. E., 2001, A&A, 377, 801

Ibata, R. A., Gilmore, G., & Irwin, M. J., 1994, Nature, 370, 194

Impey, C. D., & Bothun, G. D., 1989, ApJ, 341, 89

Jerjen, H., Freeman, K. C., & Binggeli, B., 1998, AJ, 116, 2873

Jerjen, H., Freeman, K. C., & Binggeli, B., 2000, AJ, 119, 166

Kamphuis, J., Sancisi, R., & van der Hulst, T., 1991, A&A, 244, L29

Karachentsev, I. D., & Makarov, D. I., 1996, AJ, 111, 794

Karachentsev, I. D., & Makarov, D. I., 1999, IAU Symp. 186, Galaxy Interactions at High and Low Redshift, ed J. Barnes & D. B. Sanders (Doredrecht: Klewer), 109

Karachentsev, I. D., & Makarov, D. I., & Huchtmeier, W. K., 1999, A&AS, 139, 97

Karachentsev, I. D., & Musella, I., 1996, A&A, 315, 348

Karachentsev, I. D., Sharina, M. E., Dolphin, A. E., Grebel, E. K., Geisler, D., Guhathakurta, P., Hodge, P. W., Karachentseva, V. E., Sarajedini, A., & Seitzer, P., 2002, A&A, 385, 21

Karachentsev, I. D., Karachentseva, V. E., Huchtmeier, W. K., & Makarov, D. I., 2004, AJ, 127, 2031

Karachentseva, V. E., & Karachentsev, I. D., 2000, A&AS, 146, 359

Kauffmann, G., White, S. D. M., & Guiderdoni, B., 1993, MNRAS, 264, 201

Kennicutt, R. C., 1989, ApJ, 344, 685 (K89)

Klypin, A., Kravtsov, A. V., Valenzuela, O., & Prada, F., 1999, ApJ, 552, 82

Koribalski, B. S., 2001, in Gas and Galaxy Evolution, ASP Conference Proceedings, Vol. 240. eds Hibbard, J. E., Rupen, M., van Gorkom, J. H., San Francisco, p. 439

Koribalski, B. S., Staveley-Smith, L., Kilborn, V. A., Ryder, S. D., Kraan-Korteweg, R. C., Ryan-Weber, E. V., Ekers, R. D., Jerjen, H., Henning, P. A., Putman, M. E., Zwaan, M. A., de Blok, W. J. G., Calabretta, M. R., Disney, M. J., Minchin, R. F., Bhathal, R., Boyce, P. J., Drinkwater, M. J., Freeman, K. C., Gibson, B. K., Green, A. J., Haynes, R. F., Juraszek, S., Kesteven, M. J., Knezek, P. M., Mader, S., Marquarding, M., Meyer, M., Mould, J. R., Oosterloo, T., O'Brien, J., Price, R. M., Sadler, E. M., Schröder, A., Stewart, I. M., Stootman, F., Waugh, M., Warren, B. E., Webster, R. L., & Wright, A. E., 2004, AJ, 128, 16 (BGC)

Kraan-Korteweg, R. C., & Huchtmeier, W. K., 1992, A&A, 266, 150

Krumm, N., & Burstein, D., 1984, AJ, 89, 1319

Landolt, A. U., 1992, AJ, 104, 340

Lauberts, A., 1982, ESO-Uppsala survey of the ESO(B) atlas. European Southern Observatory (ESO), Garching

Lauberts, A., Valentijn, E. A., 1989, The surface photometry catalogue of the ESO-Uppsala galaxies. European Southern Observatory (ESO), Garching

Lee, H., McCall, M. L., Kingsburgh, R. L., Ross, R., & Stevenson, C. C., 2003, AJ, 125, 146

Martin, C. L., & Kennicutt, R. C., 2001, ApJ, 555, 301 (MK01)

McGaugh, S. S., Schombert, J. M., Bothun, G. D., & de Blok, W. J. G., 2000, ApJ, 533L, 99

Meurer, G. R., Mackie, G., & Carignan, C., 1994, AJ, 107, 2021

Meurer, G. R., Carignan, C., Beaulieu, S. F., & Freeman, F. C., 1996, AJ, 111, 155

Maddox, S. J., Efstathiou, G., Sutherland, W. J., & Loveday, J., 1990, MNRAS, 243, 692

Mateo, M., 1998, ARA&A, 36, 435

Meyer, M. J., Meyer, M. J., Zwaan, M. A., Webster, R. L., Staveley-Smith, L., Ryan-Weber, E., Drinkwater, M. J., Barnes, D. G., Howlett, M., Kilborn, V. A., Stevens, J., Waugh, M., Pierce, M. J., Bhathal, R., de Blok, W. J. G., Disney, M. J., Ekers, R. D., Freeman, K. C., Garcia, D. A., Gibson, B. K., Harnett, J., Henning, P. A., Jerjen, H., Kesteven, M. J., Knezek, P. M., Koribalski, B. S., Mader, S., Marquarding, M., Minchin, R. F., O'Brien, J., Oosterloo, T., Price, R. M., Putman, M. E., Ryder, S. D., Sadler, E. M., Stewart, I. M., Stootman, F., & Wright, A. E., 2004, MNRAS, 350, 1195

Mo, H. J., Mao, S., & White, S. D. M., 1998, MNRAS, 295, 319

Moore, B., Ghigha, S., Governato, F., Lake, G., Quinn, T., Stadel, J., & Tozzi, P., 1999, ApJ, 524, L19

Monet, D. G., Levine, S. E., Canzian, B., Ables, H. D., Bird, A. R., Dahn, C. C., Guetter, H. H., Harris, H. C., Henden, A. A., Leggett, S. K., Levison, H. F., Luginbuhl, C. B., Martini, J., Monet, A. K. B., Munn, J. A., Pier, J. R., Rhodes, A. R., Riepe, B., Sell, S., Stone, R. C., Vrba, F. J., Walker, R. L., Westerhout, G., Brucato, R. J., Reid, I. N., Schoening, W., Hartley, M., Read, M. A., & Tritton, S. B., 2004, AJ, 125, 984

Oemler, A. Jr., 1974, ApJ, 194, 1

O'Neil, K., Bothun, G. D., & Schombert, J., 2000, AJ, 119, 136

Parodi, B. R., Barazza, F. D., & Binggeli, B., 2002, A&A, 388, 29

Paturel, G., Fouque, P., Bottinelli, L., & Gouguenheim, L., 1989, A&AS, 80, 299

Paturel, G., Andernach, H., Bottinelli, L., di Nella, H., Durand, N., Garnier, R., Gouguenheim, L., Lanoix, P., Marthinet, M. C., Petit, C., Rousseau, J., Theureau, & G., Vauglin, I., 1997, A&AS, 124, 109, http://cismbdm.univ-lyon1.fr/~leda/

Pfenniger, D., & Revaz, Y., 2005, A&A, 431, 511

Postman, M., & Geller, M. J., 1984, ApJ, 281, 95

Quirk, W.J., 1974, ApJ, 176, L9

Roberts, M. S., 1975, Galaxies and the Universe, University of Chicago Press, Chicago

Roberts, M. S., & Haynes, M. P., 1994, ARA&A, 32, 115

Ryan-Weber, E., Koribalski, B. S., Staveley-Smith, L., Jerjen, H., Kraan-Korteweg, R. C., Ryder, S. D., Barnes, D. G., de Blok, W. J. G., Kilborn, V. A., Bhathal, R., Boyce, P. J., Disney, M. J., Drinkwater, M. J., Ekers, R. D., Freeman, K. C., Gibson, B. K., Green, A. J., Haynes, R. F., Henning, P. A., Juraszek, S., Kesteven, M. J., Knezek, P. M., Mader, S., Marquarding, M., Meyer, M., Minchin, R. F., Mould, J. R., O'Brien, J., Oosterloo, T., Price, R. M., Putman, M. E., Sadler, E. M., Schröder, A., Stewart, I. M., Stootman, F., Waugh, M., Webster, R. L., Wright, A. E., & Zwaan, M. A., 2002, AJ, 124, 1954

Salucci, P., & Persic, M., 1999, MNRAS, 309, 923

Schlegel, D. J., Finkbeiner, D. P., & Davis, M., 1998, ApJ, 500, 525 (SFD98)

Schombert, J. M., Bothun, G. D., Schneider, S. E., & McGaugh, S. S., 1992, AJ, 103, 1107

Sérsic, J.-L., 1968, Atlas de galaxias australes, Observatorio Astronomico, Cordoba

Shapiro, P. R., Iliev, I. T., & Raga, A. C., 2004, MNRAS, 348, 753

Sidhu, S. K., & Cabanela, J. E., 2003, AAS, 203, #114.08

Somerville, R. S., Primack, J. R., 1999, MNRAS, 310, 1087

Spitzer, L., 1968, Diffuse Matter in Space, Wiley, New York

Staveley-Smith, L., Wilson, W. E., Bird, T. S., Disney, M. J., Ekers, R. D., Freeman, K. C., Haynes, R. F., Sinclair, M. W., Vaile, R. A., Webster, R. L., & Wright, A. E., 1996, PASA, 13, 243

Stil, J. M., & Israel, F. P., 2002a, A&A, 389, 29

Stil, J. M., & Israel, F. P., 2002b, A&A, 389, 42

Tinsley, B. M., 1980, Fundam. Cosmic Phys., 5, 287

Toomre, A., 1964, ApJ, 139, 1217

Trentham, N., Möller, O., & Ramirez-Ruiz, E., 2001, MNRAS, 322, 658

Tully, R. B., & Fisher, J. R., 1977, A&A, 54, 661

van Zee, L., Haynes, M. P., & Giovanelli, R., 1995, AJ, 109, 990

van Zee, L., Haynes, M. P., Salzer, J. J., & Broeils, A. H., 1996, AJ, 112, 129

van Zee, L., Haynes, M. P., Salzer, J. J., & Broeils, A. H., 1997, AJ, 113, 1618

van Zee, L., 2000, AJ, 119, 2757

van Zee, L., 2001, AJ, 121, 2003

Verde, L., Oh, S. P., & Jimenez, R., 2002, MNRAS, 336, 541

Verheijen, M. A. W., 2001, ApJ, 563, 694

Warren, B. E., Jerjen, H., & Koribalski, B. S., 2004, AJ, 128, 1152

Warren, B. E., Jerjen, H., & Koribalski, B. S., 2005a, MNRAS, in preparation

Warren, B. E., Jerjen, H., & Koribalski, B. S., 2005b, MNRAS, in preparation

Whiting, A. B., Hau, G. K. T., & Irwin, M., 2002, ApJS, 141, 123

Widrow, L. M., & Dubinski, J., 1998, ApJ, 504, 12

Willick, J. A., 1999a, ApJ, 516, 47

Willick, J. A., 1999b, ApJ, 522, 647

Willick, J. A., & Batra, P., 2001, ApJ, 548, 564

Young, L. M., van Zee, L., Lo, K. Y., Dohm-Palmer, R. C., Beierle, M. E., 2003, ApJ, 592, 111

Zwaan, M. A., Staveley-Smith, L., Koribalski, B. S., Henning, P. A., Kilborn, V. A., Ryder, S. D., Barnes, D. G., Bhathal, R., Boyce, P. J., de Blok, W. J. G., Disney, M. J., Drinkwater, M. J., Ekers, R. D., Freeman, K. C., Gibson, B. K., Green, A. J., Haynes, R. F., Jerjen, H., Juraszek, S., Kesteven, M. J., Knezek, P. M., Kraan-Korteweg, R. C., Mader, S., Marquarding, M., Meyer, M., Minchin, R. F., Mould, J. R., O'Brien, J., Oosterloo, T., Price, R. M., Putman, M. E., Ryan-Weber, E., Sadler, E. M., Schröder, A., Stewart, I. M., Stootman, F., Warren, B. E., Waugh, M., Webster, R. L., & Wright, A. E., 2003, AJ, 125, 2842

Zwaan, M. A., Meyer, M. J., Webster, R. L., Staveley-Smith, L., Drinkwater, M. J., Barnes, D. G., Bhathal, R., de Blok, W. J. G., Disney, M. J., Ekers, R. D., Freeman, K. C., Garcia, D. A., Gibson, B. K., Harnett, J., Henning, P. A., Howlett, M., Jerjen, H., Kesteven, M. J., Kilborn, V. A., Knezek, P. M., Koribalski, B. S., Mader, S., Marquarding, M., Minchin, R. F., O'Brien, J., Oosterloo, T., Pierce, M. J., Price, R. M., Putman, M. E., Ryan-Weber, E., Ryder, S. D., Sadler, E. M., Stevens, J., Stewart, I. M., Stootman, F., Waugh, M., & Wright, A. E., 2004, MNRAS, 350, 1210

Erratum

Detailed Corrections

- Page 20, line 13 - follow a sinusoidal curve $\rightarrow$ follow a $\sin^2$ distribution
- Chapter 3 - An examiner has asked for a clarification of the selection criteria for the control sample, in particular whether they cover the same range for key parameters as the target sample (especially environment). The only such criteria applied was for the luminosity range of the galaxies as stated in the text. Otherwise they were chosen at random, with slight favour to galaxies close to other sample objects (which applies to most of the high $\mathcal{M}_{\rm HI}/L_{\rm B}$ galaxies as well as all the control sample, see § 3.2).
- Page 66 and Fig. 6.11 (Page 84) - To recover the extended H I emission from ESO 215-G?009 we followed the general procedure of excluding the long baselines (the five baselines using CA06) which do not contain extended line signal. These baselines were not excluded from the continuum map, where the sources are generally unresolved and so the inclusion of the longer baselines increases the signal-to-noise. Hence the angular resolution of the 20cm continuum data is higher than for the H I maps.
- Table 6.2 (Page 69) - Table 1 of this erratum (following page) gives the parameters for the Sérsic profiles fit to the surface brightness profiles of ESO 215-G?009. The parameters are as defined in eqn. 6.2
- Fig. 6.8 (Page 76) - The high peak in the velocity dispersion near the centre of the galaxy is most likely due to beam smearing rather than a true increase in the velocity dispersion. It should be noted that the highest velocity dispersion region in the galaxy, as seen by the 10 $\rm km\,s^{-1}$ contour in Fig. 6.6d (Page 74), extends north beyond the central region.
- Page 132, starting line 21 - The text unintentionally suggests that the velocity difference between ESO 505-G007 and ESO 505-G008 ($\sim$200 $\rm km\,s^{-1}$) indicates they are well separated. This is not the case as the velocity separation could indicate interaction between the two galaxies, so that ESO 505-G008 could in fact be closer to ESO 505-G007 than the galaxy which is designated as the nearest neighbour (UGCA 263). The intention was to illustrate the difficulty in calculating the separation between neighbouring galaxies without good distance measurements.
- Fig. A.135 (Page 247) - The optical image of ESO 141-G042 was rotated at the telescope to avoid overflow from the overexposed star within the field, but was not rotated back for this figure and the axes are incorrect as a result. The images should be rotated clockwise 65°, as in Fig. 1 of this erratum.

Typographical Corrections

- Page vi, line 4 - initial $\rightarrow$ initially
- Page 1, line 8 - theorist $\rightarrow$ theorists

Table 1. *BVRI* Sérsic parameters for the surface brightness profiles of ESO 215-G?009.

Band	μ_0 [a] (mag arcsec^{-2})	r_0 (arcsec)	n
(1)	(2)	(3)	(4)
B	24.97 ± 0.04	32.2 ± 1.0	1.56 ± 0.08
V	23.69 ± 0.11	32 ± 3	1.7 ± 0.3
R	23.19 ± 0.02	32.5 ± 0.5	1.74 ± 0.04
I	22.90 ± 0.02	36.7 ± 0.5	1.61 ± 0.04

(1) Cousins broad band filters.
(2) Central surface brightness.
(3) Scale radius.
(4) Shape parameter.

[a]Galactic extinction not applied.

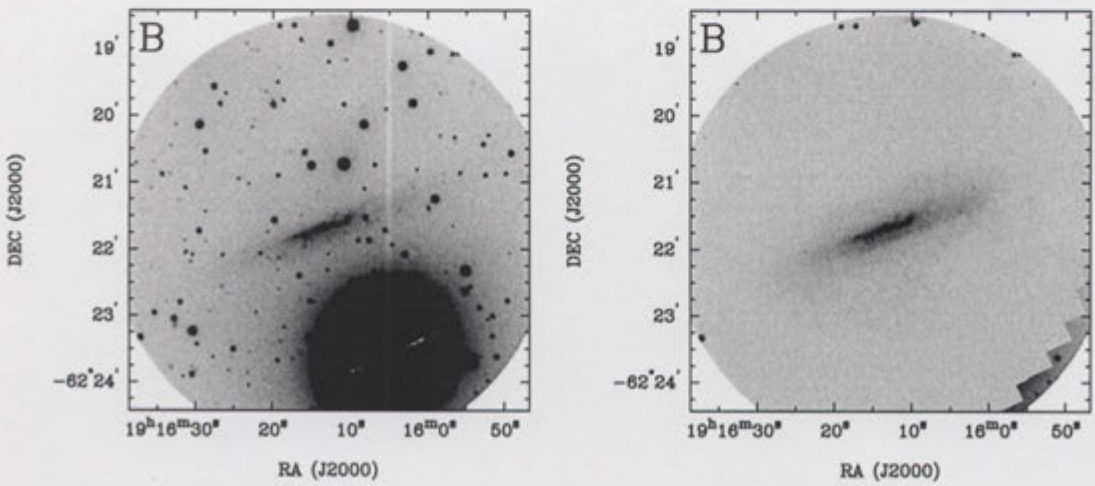

Figure 1 Deep *B* image of ESO 141-G042 before and after foreground stars subtraction (correct orientation).

- Page 1, line 18 - galaxy → galaxies
- Page 1, line 21 - object → objects
- Page 3, line 5 - function for → functions based on
- Page 4, line 21 - know → known
- Page 6, line 24 - need → needed
- Page 12, line 19 - seach → search
- Page 15, line 9 - others → other
- Page 30, line 9/10 - dwarf galaxies have high → dwarf galaxies which have high
- Page 30, line 37 - because their → because of their
- Page 31, line 30 - look an → look at an
- Page 36, line 7 - had → hand
- Page 43, line 23 - although a the occasional → although the occasional
- Page 44, line 2 - the the → the

- Page 44, line 15 - Cassergrain → Cassegrain
- Page 47, line 16 - 1st order maps → 1st moment maps
- Page 47, line 17 - 2nd order maps → 2nd moment maps
- Table 5.1 (Page 52), Column 3 header - (Jy → (Jy)
- Table 5.5 (Page 58), Column 6 - remove ± after ESO 085-G047 Galactic extinction.
- Page 60, line 14 - (see Chapter 7, § 7.4.2, and Chapter 8, § 7.4.2) → (see § 7.4.2 and § 8.1)
- Page 60, line 36 - (page 261) → (page 262)
- Page 77, line 11 - turn down → down turn
- Page 80, line 23 - $EB-V \rightarrow E(B-V)$
- Page 104, line 4 - like BCD → like a BCD
- Page 104, line 13 - the other had → the other hand
- Page 104, line 33 - group, however, → group. However,
- Page 105, line 4 - with the many → with many
- Page 105, line 6 - ratio → ratios
- Page 105, line 9 - of HIPASS → of the HIPASS
- Page 106, line 14 - right angle → correct angle
- Page 106, line 33 - along → a long
- Page 107, line 10 - brighter, about 25 times more emission. → brighter (corresponding to a 25 times higher luminosity).
- Page 111, line 4 - appears → appear
- Page 111, line 13 - where → was
- Page 112, line 3 - galaxies → galaxy
- Page 113, line 12 - object → objects
- Page 115, line 2 - stratergy → strategy
- Page 122, line 6 - used → use
- Page 122, line 18 - of of → of
- Page 123, line 12 - area lower → area of lower
- Page 123, line 18 - in general that the → in general the
- Page 126, line 36 - very a high → very high
- Page 126, line 39 - looked a sample → looked at a sample
- Page 129, line 9 - best method to measure → best method is to measure
- Page 130, line 1 - brightness' → brightnesses

- Page 130, line 7 - sensibility → sensitivity
- Page 131, line 6 - has been seen to extend out several orders lower in space density → has been seen to extend to regions with space densities that are several orders of magnitude lower
- Page 131, line 19 - effectivness → efficiency
- Page 131, line 31 - indexes → indices
- Page 132, line 31 - as an rough → as a rough
- Page 135, line 31 - crutial → crucial
- Page 135, line 36 - dimentional → dimensional
- Page 139, line 20 - multiwavelenght → multiwavelength
- Page 139, line 26 - By why → But why
- Page 141, line 1 - efficent → efficient
- Appendix A, all H I Spectra captions - spectra → spectrum

Other Comments Made by Examiners

- Fig. 5.2 (Page 61) - An examiner has asked for a discussion on why we are convinced that our magnitudes are correct, and what could cause the LEDA magnitudes to be so different. Such a discussion regarding our magnitudes is already provided in the first paragraph on the previous page (Page 60), and a reference is given to later discussions on the LEDA magnitudes (§ 7.4.2 and § 8.1, see typographical correction above).
- Page 72 - An examiner has suggested multiplying the ATCA map for ESO 215-G?009 by the Parkes main beam pattern to mimic a single pointing single dish observation and check the H I flux density discrepancy. However, due to HIPASS being composed of scanning strips rather than single pointings, and the methods used to obtain the flux densities (Barnes et al. 2001), this method would probably not resolve this difference (Koribalski, priv. comm.).
- I would like to thank the examiners for a suggestion regarding the use of gaussian rather than Poisson statistics for the uncertainty in the H I profiles (Fig. 6.7 and 6.8) which will be considered for use in future publications.
- Page 79 - An examiner has suggested further discussion on the Galactic extinction in the region of ESO 215-G?009. However, such a discussion is already provided two pages later in § 6.5.3, and further discussion is given in the following chapter (§ 7.4.3 and Fig. 7.5).
- Page 46, line 4 - An examiner has suggested to change the CCD dimensions to 1024 × 1024 pixels (believing this to be a typographical error). However, the dimensions stated in the Thesis, 1124 × 1024 pixels, are the correct numbers.

Bradley Evan Warren
13 May, 2005